Search for Non-Pointing Photons in the Diphoton and Missing Transverse Energy Final State in 7 TeV pp Collisions Using the ATLAS Detector

Nikiforos K. Nikiforou

Submitted in partial fulfillment of the
requirements for the degree
of Doctor of Philosophy
in the Graduate School of Arts and Sciences

COLUMBIA UNIVERSITY

2014

ABSTRACT

Search for Non-Pointing Photons in the Diphoton and Missing Transverse Energy Final State in 7 TeV pp Collisions Using the ATLAS Detector

Nikiforos K. Nikiforou

A search for photons originating in the decay of a neutral long-lived particle produced in proton–proton collisions at $\sqrt{s} = 7$ TeV is presented. The search was performed in the diphoton plus missing transverse energy final state, using the full data sample of 4.8 fb^{-1} of 7 TeV proton–proton collisions collected in 2011 with the ATLAS detector at the CERN Large Hadron Collider. The analysis exploits the capabilities of the ATLAS electromagnetic calorimeter to make precise measurements of the flight direction of photons, and utilizes the excellent time resolution of the calorimeter as an independent cross-check of the results. The search was conducted in the context of Gauge Mediated Supersymmetry Breaking models, where the lightest neutralino is the next-to-lightest supersymmetric particle and has a finite lifetime. In the family of models investigated, supersymmetric particles are produced in pairs due to R-parity conservation, eventually decaying to a pair of neutralinos, each subsequently decaying to a photon and a gravitino. The gravitinos escape the detector, giving rise to missing energy, while the photons can appear not to originate from the primary vertex of the event, and are measured with a delay with respect to the collision time. No excess was observed above the background expected from Standard Model processes. The results were used to set exclusion limits at 95% CL in the two-dimensional parameter space defined by the supersymmetry breaking scale and the lifetime of the lightest neutralino.

Table of Contents

List of Figures

List of Tables

Acknowledgments

I wish to express my tremendous gratitude to my advisor John Parsons for his invaluable guidance and for his sincere concern and support for my progress in both my career and personal life. His knowledge, patience, kindness, and his genuine interest for his students, set very high standards and an example which I will do my best to follow.

The work presented here would not have been possible without the help and excellent cooperation with several ATLAS colleagues, including Sergey Burdin, Mark Cooke, Helen Hayward, and Allan Lehan. I also thank all the professors, post-docs, and students in the Columbia University ATLAS group, for the fruitful discussions, their help, advice, and for creating a friendly working atmosphere. I would especially like to thank Gustaaf Brooijmans for his advice and guidance in the course of my work on the LAr electronics upgrade, as well as throughout my time as a graduate student. Further, I gratefully acknowledge the support of the staff at the Columbia University Department of Physics and the staff at Nevis Laboratories, for all their efforts in ensuring I had every resource needed for my education and the performance of my research. I also appreciate thankfully the work and time invested by the members of the thesis examination committee, James Applegate, Andy Haas, Alberto Nicolis, and Mike Shaevitz, in the review of this thesis.

In addition, I wish to thank Martin Aleksa, Paolo Iengo, Emmanuel Monnier, Isabelle Wingerter-Seez, and everybody in ATLAS LAr Operations, for a remarkable cooperation and for their trust, confidence, and the opportunity to work and learn productively in tremendously exciting and challenging positions and projects. Special thanks goes to my undergraduate studies advisor, Theo Alexopoulos, for his continuous encouragement and for making sure I have every opportunity to advance in this field.

The last few years have been made more meaningful, and certainly more exciting, due to the genuine friends, both old and new, I am lucky to have in my life. I would particularly like to thank my dear friends Christos, Constantinos, Louiza, Marina, and Zenonas for their valuable advice, openhanded and continuous support and, most importantly, for making life at the CERN area feel like home. Warmest thanks are due to my close friends and colleagues at Columbia University, Alessandro, Andrej, and Christopher, who made studying and living in New York City an even more fascinating and unique experience. For my friends back home, I am grateful for never making me feel forgotten, and just picking up where we had left off, each time I went back. Last but not least, I thank Natalie, my greatest discovery, for sharing my ups and enduring my downs, and for her selfless love and encouragement.

Finally, I am indebted to my parents, my grandmother, my uncles, and my entire family, for teaching me the first and most important lessons in life. Pursuing these studies meant being away for so long, but this did not limit your endless love and infinite support. This thesis is dedicated to you.

Στην Άρτεμις
και τον Κλεάνθη

Foreword

I moved to New York in August 2008 to begin my graduate studies at the Dept. of Physics, Columbia University, with the specific intent of joining the ATLAS group there. Upon joining the Columbia ATLAS group, I was assigned a very interesting project in the context of the liquid argon (LAr) calorimeter Front End Board (FEB) electronics upgrade. The project involved testing the radiation hardness of commercial ADCs as well as a custom-made chip designed at Columbia University's Nevis Laboratories. The chip was one in a series of custom-designed and built devices being developed at Nevis towards an ADC suitable for the LAr upgrade. I assisted in the development of a testing procedure and infrastructure and had a very active role in the organization, setup and carrying-out of the irradiation tests of the electronics at a medical proton accelerator in Boston. With these tests, we determined that commercially available ADCs were not likely candidates for the upgrade [1]. Conversely, we demonstrated that the fabrication technology and design used in the custom-made chips were suitable for a custom-made ADC in the next generation LAr FEB.

In June 2010, I moved to Geneva and joined the LAr Operations group. I trained as an expert for the Online and Calibration Systems and regularly served as the Expert On-call for that post. My work in Operations, besides day-to-day problem solving, involved mainly software development for the Online System, to make the operation of the calorimeter and the data taking more efficient. In addition, I was involved in the preparations for the 2010 shutdown period, where a significant number of FEBs as well as Back-End equipment were replaced. During the 2011 data taking period, I served as LAr Run Coordinator, the first student to be entrusted with this important position. The LAr Run Coordinator is expected to be available around the clock and coordinates the work of all the LAr shifters and experts and has the final word on any decision regarding the detector safety and data taking efficiency of the calorimeter. As a member of the LAr Operations group, I was asked to present the status and performance of the ATLAS

LAr calorimeter during the 2012 LHCC meeting [2] and at the ANIMMA 2013 conference in Marseille [3].

For this thesis, I decided to perform a search for supersymmetry with non-pointing photons, with the understanding that it would be a particularly challenging analysis, though all the more interesting and exciting both as a demonstration of the remarkable capabilities of the detector and as a novel search for new physics. Initial work on the analysis begun during the spring of 2011 and a small analysis team was formed. In parallel to the physics analysis, my advisor and I launched an extensive investigation of the LAr timing performance, with the intent of improving it for use in our search as well as in future analyses. The timing study [4] yielded a significant improvement in the LAr timing resolution and uniformity and, in addition, provided us with valuable experience concerning the timing of electromagnetic clusters. For this first iteration of the non-pointing photon search, we decided to use the full 2011 dataset, using calorimeter pointing as the primary discriminating variable of the search. The analysis method and strategy were developed with the bulk of the 2011 data blinded, using only a subset of the data corresponding to approximately 12% of the total. The analysis method was frozen in August 2012 after which point the full dataset was investigated. The results were documented in an internal ATLAS note [5] and the analysis was reviewed and approved within the collaboration in fall 2012. Since then, the results have been presented in various conferences, including *Pheno-2013*, during which I presented the non-pointing photon analysis along with other recent ATLAS supersymmetry searches on behalf of the collaboration. A publication [6] describing the analysis and its results was submitted in April 2013 to *Physical Review D* and was published in July 2013. This thesis describes in detail the analysis of the 2011 dataset.

In parallel with the final stages of the 2011 data analysis, I started preparations and initial work for the analysis of the 2012 data. With the experience and confidence in the timing observable gained from the 2011 data timing calibration, we implemented a complete overhaul of the non-pointing analysis, moving to a more powerful two-dimensional search in which the timing has a more elevated role. For this reason, the timing calibration procedure for the 2012 dataset was further refined and optimized, achieving an even better timing resolution and uniformity [7]. The improved timing is already being used in the 2012 data non-pointing photon analysis, the method of which, at the time of writing of this thesis, is being finalized.

Chapter 1

Introduction

This thesis presents a search for new phenomena that are not described by the Standard Model of particle physics (SM), performed within the ATLAS [8] collaboration at the CERN Large Hadron Collider (LHC) [9, 10]. The analysis presented uses the full data sample of 4.8 fb^{-1} of proton–proton (pp) collisions collected by ATLAS in 2011 at a center-of-mass energy of 7 TeV.

The SM has been very successful in describing all known particles and interactions except gravity and has managed to explain experimental observations for more than forty years with remarkable precision. However, there are several issues with the SM that make it unsatisfactory as a theory of nature. The main physics objective of the LHC and the associated experiments is therefore to probe into unexplored high-energy regions and try to complete our understanding of the physical world. A possible theoretical path to that goal is offered by supersymmetry (SUSY), a class of theories providing interesting solutions to some of the shortcomings of the SM.

The LHC and the experiments effectively started physics operations in 2010, after more than two decades of planning, development and construction, providing access to unprecedented center-of-mass energies and particle production rates. The accelerator and the experiments, the best tools currently available for particle physics research, are considered themselves remarkable achievements of science and are undoubtedly modern marvels of technology. The two general-purpose experiments, ATLAS and CMS [11], employ state-of-the-art detector technologies, feeding millions of readout channels, while breakthroughs in data acquisition and computing efficiently process and record the produced collision data. Coupled with the unparalleled energies and formidable rates provided by the LHC, the design and quality of the detectors and their remarkable performance allow the study of the rarest of processes and allow the development of novel analysis techniques to investigate challenging experimental signatures. The analysis described in the following chapters is an example of one such challenging experimental topology, one that required the development of a non-standard analysis technique.

The main feature exploited in this analysis is that most SM processes produce intermediate particles that decay promptly, or almost immediately, therefore resulting in final state particles which are observed emanating from the primary production vertex (PV). Conversely, various models for physics beyond the SM (BSM) predict the production of heavy long-lived intermediate particles, the decay of which gives rise to objects that are detected with a delay with respect to the collision time and are not pointing towards the PV. Accordingly, the measurement of the arrival times and point of origin along the beam axis of physics objects can be powerful discriminating tools for new physics signals against the challenging background levels in the LHC environment. Perhaps more importantly, if new physics lies at the TeV-scale, the potential existence of such topologies may hold the answer to why no light BSM particles have yet been directly observed at the LHC, since direct searches may not be as sensitive to long-lived states. As a consequence, exotic topologies, such as the one presented in this thesis, have the potential to mitigate the constraints for BSM physics already imposed by the LHC, and are therefore even more interesting.

The analysis searches in particular for events with two photons in association with large missing transverse energy, $E_{\mathrm{T}}^{\mathrm{miss}}$, where at least one photon is non-pointing back to the PV. As photons leave no track in the inner tracker system, the novel pointing capabilities of the ATLAS liquid argon (LAr) electromagnetic (EM) calorimeter system are exploited. More specifically, the fine segmentation of the LAr calorimeter is used to determine the position of the EM cluster barycenters in two calorimeter layers, and from these two points the photon direction is calculated. The precise measurement of the arrival time of the photons is used as an independent cross-check of the results. Consequently, the analysis relies heavily on the capabilities and performance of the ATLAS EM calorimeter system.

The novel LAr calorimeter pointing capabilities had previously been employed in the ATLAS $H \rightarrow \gamma\gamma$ analysis [12, 13] for the determination of the position of the PV of the event, thereby improving the diphoton mass resolution. As part of the work performed for the non-pointing photon analysis, the calorimeter pointing performance was studied extensively and its response for objects not originating from the PV was determined. In terms of timing, the calorimeter had been calibrated with a typical resolution of ~ 1 ns, which is sufficient for the detector operation and the needs of most physics analyses. Anticipating the use of the timing in long-lived particle searches, an extensive study of the calorimeter timing performance was performed, using collision data from $W \to e\nu$ and $Z \to ee$ candidate events. Several corrections were determined and applied in order to improve the timing performance. As a result of this campaign, the timing resolution for collision data recorded in 2011 was shown to reach values of ~ 290 ps, which includes an irreducible contribution from the finite length of the LHC beam proton bunches, estimated to be approximately 220 ps.

The search is performed within the theoretical context of Gauge Mediated Supersymmetry Breaking (GMSB) scenarios, for which limits at 95% confidence level (CL) are set. In the GMSB models considered here, the Next-to-Lightest Supersymmetric Particle (NLSP), the lightest neutralino, decays to a stable Lightest Supersymmetric Particle (LSP), the gravitino, and a photon. The NLSPs can be long-lived and slow moving, giving rise to delayed and non-pointing photons, while the LSPs escape the detector without being measured, contributing to missing energy. Under certain assumptions, supersymmetric particles have to be produced in pairs at the LHC, resulting in a characteristic diphoton plus $E_{\mathrm{T}}^{\mathrm{miss}}$ signature. While the diphoton plus $E_{\mathrm{T}}^{\mathrm{miss}}$ topology for prompt NLSP decays has been studied in ATLAS, this is the first analysis where this signature is explored using calorimeter pointing and timing to probe longer-lived NLSP scenarios.

The material in the subsequent chapters is organized as follows: Some elements of theory are provided in Chapters 2 and 3, discussing basic concepts of the SM and SUSY, respectively, and documenting the theoretical motivation behind this analysis. The experimental setup is described next, with Chapters 4 and 5 outlining the design and characteristics of the LHC accelerator and the ATLAS detector, respectively. In Chapter 6, the reconstruction of the physics objects representing particles and observables is discussed. In Chapter 7 the calorimeter pointing and timing measurement and performance are described. The analysis strategy and event selection are outlined in Chapter 8, and the expected signal yields are described in Chapter 9. The modeling of signal and sources of background is described in Chapter 10. Chapter 11 summarizes the various systematic uncertainties relevant for this analysis. The template fitting method for the extraction of the results and limits is described in Chapter 12. The final results of the analysis and their interpretation in the context of GMSB are presented in Chapter 13. Finally, Chapter 14 presents some conclusions and discusses briefly the outlook and future work using data collected in 2012.

Chapter 2

The Standard Model of Particles and Interactions

In this chapter, a brief introduction to the Standard Model (SM) of particle physics is provided. The SM describes the elementary particles which constitute matter and their mutual interactions, which proceed through the exchange of force mediating particles. The particle content and the basic properties of the SM are discussed in Section 2.1. The SM describes three of the four identified fundamental forces: the strong force, the weak force, and electromagnetism. Gravitational interactions are not described by the SM, which is one of the significant limitations of the model. Some of the most important shortcomings of the SM are discussed in Section 2.2.

2.1 General Properties of the Standard Model

According to the SM, ordinary matter is composed of spin-1/2 fermions, classified according to their interactions as *leptons* and *quarks*. The fermions are further organized in three so-called generations. The first lepton generation contains the electron, e, which carries one negative unit of elementary electric charge. and the electron neutrino, ν_e, which is electrically neutral. Both leptons participate in the weak interaction, while the former, being electrically charged, can also interact electromagnetically. Quarks carry fractional electric charge and participate in all three of the SM forces. The first quark generation contains the up quark, u, carrying an electrical charge of $2/3$ and the down quark, d, with an electrical charge of $-1/3$.

The additional two generations of leptons and quarks contain almost identical copies of the particles, differing only in their masses. The electron and its neutrino are complemented by two negatively charged leptons, the muon, μ, and the tau, τ, and their corresponding neutrinos, the muon neutrino, ν_μ, and the tau neutrino, ν_τ. The up quark is complemented by the charm and top quarks (c and t, respectively), while the strange and bottom quarks (s and b, respectively), correspond to the down quark. A minimal particle organization of the SM is summarized in Fig. 2.1.

The fundamental forces are mediated through the exchange of spin-1 gauge bosons. The electrically neutral and massless gluon, g, and photon, γ, mediate the strong and electromagnetic force, respectively. The weak force is mediated by the massive $W^\pm$ and Z^0 bosons, with the former carrying one unit of elementary electric charge and the latter carrying no electric charge. The final component of the SM is the recently discovered spin-0 and electrically neutral Higgs boson, H, which is a remnant of the electroweak symmetry breaking mechanism that generates the masses of the SM particles.

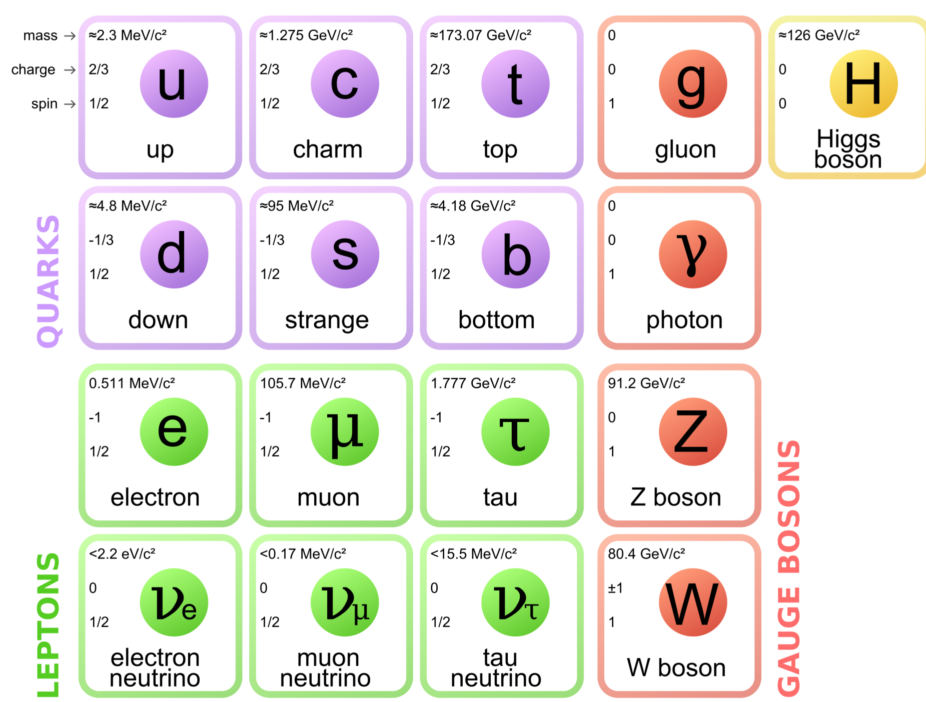

Figure 2.1: Particle content of the Standard Model.

Mathematically, the SM is a quantum field theory described by the local gauge symmetry group [14] obtained by the direct product of three groups:

$$G_{SM} = SU(3)_{\mathrm{C}} \times SU(2)_{\mathrm{L}} \times U(1)_{\mathrm{Y}} \tag{2.1}$$

The $SU(3)_C$ group describes Quantum Chromodynamics (QCD) [15–17], which is the theory of the strong interaction, charged under a property called "color". Color charge can have three possible values, usually denoted by *red*, *green* and *blue*. The generators of this group are eight independent fields corresponding to eight different gluon states, which mediate the interactions between quarks and other gluons.

The product $SU(2)_{\mathrm{L}} \times U(1)_{\mathrm{Y}}$ describes the unified theory of electroweak interactions, where $SU(2)_{\mathrm{L}}$ represents the symmetry of weak isospin, I, acting only on the left-handed components of fermions and $U(1)_{\mathrm{Y}}$ represents the symmetry of weak hypercharge, Y. The three generators of $SU(2)_{\mathrm{L}}$ correspond to three vector gauge bosons, W^1, W^2, and W^3, while the generator of $U(1)_{\mathrm{Y}}$ corresponds to the vector gauge field B. The experimentally observed particles W^+ and W^- can be identified with the W^1 and W^2 gauge bosons:

$$W^{\pm} = \frac{1}{\sqrt{2}}\left(W^1 \mp i W^2\right) . \tag{2.2}$$

The neutral fields W^3 and B mix to form the physical states:

$$Z = \cos\theta_{\mathrm{W}} W^3 - \sin\theta_{\mathrm{W}} B \tag{2.3}$$

$$A = \sin\theta_{\mathrm{W}} W^3 + \cos\theta_{\mathrm{W}} B \tag{2.4}$$

where θ_{W} is the weak mixing angle, which is a parameter that has to be determined experimentally. The two physical states Z and A are the mass eigenstates associated with the massive Z boson and massless photon, γ, respectively.

Explicit mass terms for the fermions and gauge bosons in the SM are not gauge invariant and therefore are forbidden. Consequently, the electroweak $SU(2)_{\mathrm{L}} \times U(1)_{\mathrm{Y}}$ symmetry is apparently broken. It is believed that the so-called Higgs mechanism is responsible for the generation of the masses of the SM particles, via the spontaneous breaking of the electroweak symmetry. In brief, the theory postulates that a complex scalar doublet field, ϕ, exists, which has non-zero vacuum expectation value (VEV), ϕ_0:

$$\phi_0 = \frac{1}{\sqrt{2}}\begin{pmatrix} 0 \\ v \end{pmatrix} \tag{2.5}$$

where v is a constant measured to be $v = 246$ GeV. With an appropriate parametrization, allowed by gauge invariance, the field ϕ can be expanded about the vacuum. Three of the four degrees of freedom of the ϕ field are absorbed by the $W^{\pm}$ and Z bosons to create their longitudinal polarizations and become massive, with masses proportional to v. The photon remains massless as result of a residual $U(1)_{em}$ gauge invariance. The fourth degree of freedom is identified as a new massive scalar field, the Higgs boson, H, with its mass remaining as an experimentally determinable parameter. Finally, fermion masses, m_f, are generated by so-called Yukawa terms, which also introduce couplings to the Higgs boson proportional to m_f/v.

The particle content described in Fig. 2.1 is a minimal description of the particles in the SM, with additional copies of the particles predicted by the model. More specifically, each fermion is complemented by an anti-particle with identical mass and opposite quantum numbers. Further, as described above, quarks and gluons carry color, which leads to the need for three distinct copies of the quarks and eight copies of the gluon. In total, 61 fundamental particles are predicted by the SM. Since gravity is not described by the SM, the model does not include the graviton, G, which is the proposed and hitherto unobserved massless spin-2 mediator of gravitational interactions.

2.2 Limitations of the Standard Model

Even with the obvious shortcoming of not describing gravity, the SM is remarkably successful in describing our understanding of the particles and interactions accessible to us. The SM has withstood extensive scrutiny from experiments conducted over the last 50 years, with the discovery of the Higgs boson in July 2012 figuring prominently as the crown jewel of the theory. However, the SM is still not considered a complete theory, and is certainly far from the “theory of everything” physicist strive to determine. Some of the main limitations of the SM are discussed below, providing the motivation for the postulation of new theories and the search for new physics beyond the SM (BSM).

A first limitation is the failure of the SM to explain the large differences between the various mass scales of the theory. The so-called “gauge hierarchy problem” raises the question of why the electroweak scale $m_{\text{EWK}} \approx 100$ GeV, determined by the Higgs field VEV, is so much smaller than the Planck scale, $m_{\text{P}} \approx 1.22 \times 10^{19}$ GeV. We could choose to ignore this vast gap between the two scales and introduce an ultraviolet cutoff scale, Λ_{UV}, up to which the SM is valid. However, an even more worrisome problem manifests that threatens the "naturalness" of the theory. It can be shown that fermion one-loop corrections to m_H^2 will diverge quadratically with m_{P}. Since m_H sets the scale of the masses for the particles of the electroweak model, corrections to these masses potentially much larger than the values themselves are possible. For example, if Λ_{UV} is at the Planck scale, the corrections would be more than 30 orders of magnitude larger than m_H^2 [18].

A further complication concerns the question of the unification of forces [19]. The electroweak model is in impressive agreement with experimental results. However, it does not explain the relative strength of the electromagnetic force coupling, e, with the coupling for the $SU(2)_{\mathrm{L}}$ and $U(1)_{\mathrm{Y}}$ groups, g_2 and g_1, respectively. These are related through the experimentally determined weak mixing angle θ_{W}:

$$e = g_2 \sin\theta_{\mathrm{W}} = g_1 \cos\theta_{\mathrm{W}}. \tag{2.6}$$

If a larger "unifying" group is found to describe the electroweak interactions, the theory should predict this parameter. This reasoning can be extended to search for a larger grand unifying group G to incorporate the $SU(3)_C$ strong interaction with coupling g_3 as well. Assuming G exists, a Grand Unified Theory (GUT) can describe all the interactions with the couplings g_i related and converging to a common single coupling, g_G, at some energy scale m_{GUT}. The obvious hurdle to such an endeavor is the apparent large discrepancy between the strong coupling constant and the electroweak couplings. However, the realization of "asymptotic freedom" of the strong interaction and the dependence of the couplings with the energy scale make their convergence at the GUT-scale feasible. The evolution of the coupling constants depends on the particle content of the theory, in this case the SM. Using the evolution of the coupling constants from values accessible by the experiments, the three coupling constants fail to converge to a single point. It is therefore intriguing to search for a theory that can provide a prediction of a more precise unification at a particular energy scale.

The SM also fails to address questions posed by astrophysical observations: Non-luminous and non-absorbing matter in the universe, called Dark Matter, is considered responsible for the discrepancies between predicted and observed gravitational effects on the luminous matter [19]. The SM does not provide a candidate for Dark Matter, and therefore BSM theories attempt to provide a stable, non-interacting or only weakly interacting particle that could constitute the bulk of the Dark Matter. In addition, the SM provides no mechanism for Dark Energy, which is hypothesized to explain the observed acceleration of the expansion of the Universe. Further, the SM fails to explain the observed asymmetry between ordinary matter and antimatter.

The limitations described above are only part of the set of deficiencies of the SM, for some of which Supersymmetry, described in the next chapter, provides elegant solutions. In addition to the outlined limitations and despite its tremendous success, the SM suffers from additional problems which make it clear that it is only a part of the picture that describes nature [20]. For example, the SM fails to explain why there are three distinct copies of the quarks and leptons and why the weak interactions between them proceed in the way observed. Further, a feature of the SM that makes it unpleasant as a theory is the need for at least 19 independent parameters to be determined by experiment. For the advancement of our understanding of nature, there is strong motivation to search for evidence of physics that cannot be explained by the SM, that may point in the right direction towards the formulation of a more complete theory.

Chapter 3

Supersymmetry

In this chapter, the basic theoretical elements relevant to the work presented in this thesis are discussed. The idea of supersymmety (SUSY) is introduced, which is one of the major classes of theories attempting to explain physics beyond the SM. Given the tremendous success of the SM, it is natural to attempt to capitalize on these achievements and build upon the principles of the SM. The minimal supersymmetric extension to the SM, the MSSM, and its attractive properties are discussed next, followed by a general discussion of SUSY breaking. Subsequently, the characteristics of the GMSB signal scenarios under investigation are discussed. Finally, previous results of searches for evidence of GSMB models are briefly presented.

3.1 Introduction to Supersymmetry

Supersymmetry (SUSY) [21–29] is a family of theoretical models well motivated to provide solutions to some of the issues that remain unanswered by the SM. SUSY postulates the existence of a symmetry between fermions and bosons, in addition to the full space-time symmetry described by the Poincaré group. The additional symmetry is described with an operator, Q, transforming the fermionic states to bosonic states and vice versa:

$$Q|\text{Boson}\rangle = |\text{Fermion}\rangle, \quad Q|\text{Fermion}\rangle = |\text{Boson}\rangle \tag{3.1}$$

Both Q and its hermitian conjugate, $Q^\dagger$, are generators of SUSY [30, 31]. In its most general form, SUSY theories can realize more than one supersymmetric transformation, which translates to more than one distinct copy of the generator pairs Q and $Q^\dagger$. In this thesis, we consider only the case where the number of generators, N, is equal to 1. It can be shown [18] that, for the simplest realistic SUSY extension of the SM, the application of the SUSY operators on a particular state produces a state with the same mass and identical gauge quantum numbers. It can further be shown that the two states will have spin differing by 1/2, which satisfies the original requirement for Q to transform between fermions and bosons.

The important consequence of the results above is that, in a SUSY theory, for each fermionic (bosonic) degree of freedom in the SM, there has to exist a corresponding bosonic (fermionic) degree of freedom identical in every aspect but its spin. The corresponding SUSY counterparts are called *superpartners* and the SM particles and their superpartners are typically arranged in *supermultiplets*, which are irreducible representations of the SUSY algebra. Taking into account experimental observations, it can be deduced that, in realistic SUSY theories, the superpartners of SM particles are in fact new particles that are not contained in the SM. We can form supermultiplets by considering the spin of the SM particles and pairing them with supersymmetric particles, or *sparticles*, of appropriate spin, with the constraint that the number of fermionic degrees of freedom in the supermultiplets has to be equal to the number of bosonic degrees of freedom. For a $N = 1$ SUSY extension to the SM, the simplest case would be to consider scalar particles (spin-0) as superpartners of the SM fermions (spin-1/2) and therefore called *sfermions*. The SM fermions and sfermions form together a *chiral supermultiplet*. The superpartners for the SM vector gauge bosons (spin-1) are spin-1/2 particles called *gauginos*, arranged together in a vector or *gauge supermultiplet*. In the case of scalars, such as the SM Higgs boson, the appropriate superpartners are spin-1/2 particles called *Higgsinos*. Finally, if the theory includes gravity, the graviton (spin-2) has to be assigned a superpartner with spin-3/2, called the *gravitino*. From these considerations, it is clear that, in a SUSY theory, the particle content of the SM needs to be extended to include at least as many new particles.

3.2 The Minimal Supersymmetric Standard Model

A generalization of the SM with the minimal introduction of new particles is provided by the Minimal Supersymmetric SM (MSSM). The SM gauge bosons are naturally organized in gauge supermultiplets, with the gluon, the W bosons and the B boson partnered by the gluino, the winos and the bino, respectively. In the case of the SM fermions, left-handed fields are arranged as $SU(2)_L$ doublets in chiral supermultiplets together with their superpartners, whereas right-handed fields are arranged as singlets in different chiral supermultiplets, with their own superpartners. The naming convention for the supersymmetric partners of fermions is to add the prefix "s" the fermion name to obtain the sfermion name. For example, the SUSY partner of an electron is the *selectron*, while the SUSY partner of the top quark is the *stop*.

A more complicated treatment of the Higgs mechanism is required in SUSY extensions of the SM [32], primarily since its is necessary in SUSY models to generate masses independently for the up- and down-type quarks. The Higgs sector extension is further necessitated to conserve the renormalizability of the theory, since the introduction of new fermions via a single Higgsino doublet carrying weak hypercharge would create a gauge anomaly [18]. Consequently, in the MSSM, the Higgs sector has to be extended to include two scalar Higgs-doublets, each partnered by a fermionic Higgsino doublet.

The particle content of the MSSM and their properties under the SM groups are summarized in Table 3.1. Even though a graviton is not predicted by the SM, it is often included in the MSSM with its superpartner, the gravitino, in their own supermultiplet, and is included in Table 3.1 for completeness.

With the introduction of new particles that correspond to the SM particles, but satisfying complementary spin-statistics, an elegant solution to the hierarchy problem is provided. More specifically, the introduction of heavy charged scalars in supersymmetric theories has the potential to cancel the fermionic contributions to loop corrections of the Higgs mass, since fermions and scalars contribute with the opposite sign.

An additional attractive feature of the MSSM is the prediction of unification of the fundamental forces. With the increased particle content, the running coupling constants in the MSSM are shown to converge [18] at some scale $m_U \approx 2 \times 10^{16}$ GeV. Within the MSSM, the evolution of the coupling constants is shown to be much more precise compared to the imperfect unification at high energy in the non-supersymmetric SM.

The existence of renormalizable baryon and lepton number violating couplings in the MSSM introduces the problem of proton decay, which has not been observed experimentally [19]. In or-

Chiral Supermultiplets			
Content	$SU(3)_C \times SU(2)_L \times U(1)_Y$	Spin-1/2	Spin-0
quarks - squarks	$(3, 2, \frac{1}{6})$	(u_L, d_L)	$(\tilde{u}_L, \tilde{d}_L)$
	$(3, 1, -\frac{2}{3})$	$\bar{u}_R$	$\tilde{u}_R^*$
	$(3, 1, \frac{1}{3})$	$\bar{d}_R$	$\tilde{d}_R^*$
leptons - sleptons	$(1, 2, -\frac{1}{2})$	(ν_L, e_L)	$(\tilde{\nu}_L, \tilde{e}_L)$
	$(1, 1, 1)$	$\bar{e}_R$	$\tilde{e}_R^*$
Higgsinos - Higgs	$(1, 2, \frac{1}{2})$	$(\tilde{H}_u^+, \tilde{H}_u^0)$	(H_u^+, H_u^0)
	$(1, 2, -\frac{1}{2})$	$(\tilde{H}_d^0, \tilde{H}_d^-)$	(H_d^0, H_d^-)
Gauge Supermultiplets			
Content	$SU(3)_C \times SU(2)_L \times U(1)_Y$	Spin-1	Spin-1/2
gluon - gluino	$(8, 1, 0)$	g	$\tilde{g}$
W bosons - winos	$(1, 3, 0)$	$W^\pm$, W^0	$\tilde{W}^\pm$, $\tilde{W}^0$
B boson - bino	$(1, 1, 0)$	B	$\tilde{B}$
Graviton Supermultiplet			
Content	$SU(3)_C \times SU(2)_L \times U(1)_Y$	Spin-2	Spin-3/2
graviton - gravitino	$(1, 1, 0)$	G	$\tilde{G}$

Table 3.1: The chiral and gauge supermultiplets of the MSSM with their representations in $SU(3)_C \times SU(2)_L \times U(1)_Y$. Only the first generation of quarks and leptons is shown, with identical arrangements understood for the second and third generations. The graviton supermultiplet is also included for completeness.

der to conserve the stability of the proton, the conservation of a multiplicative quantum number called *R-parity* is imposed in many SUSY models [33–37]. For a given particle, R-parity is defined as

$$P_R = (-1)^{3(B-L)+2S} \tag{3.2}$$

where B and L are the baryon- and lepton- numbers, respectively and S is the spin of the particle. With this definition, SM particles have an R-parity of $+1$, while SUSY particles have an R-parity of -1. The conservation of R-parity has interesting consequences: First, SUSY particles at a hadron collider have to be produced in pairs. Secondly, the conservation of R-parity enforces the existence of at least one stable Lightest Supersymmetric Particle (LSP), to which all produced SUSY particles will cascade. Since the LSP cannot interact via SM processes, a stable LSP is an excellent candidate for Dark Matter. Further, if SUSY particles are produced in a hadron collider, in certain scenarios, the LSPs will escape the detector undetected, giving rise to missing energy.

It is worth mentioning that models which introduce R-parity Violating (RPV) terms in the MSSM have been proposed [18]. RPV models often produce interesting topologies and challenging experimental signatures and are studied extensively in ATLAS. For the remaining of this thesis, however, R-parity is assumed to be conserved.

3.3 SUSY as a Broken Symmetry

An immediate conclusion arising from the previous sections is that, even in the most minimal realizations of SUSY, several new particles are expected with masses equal to their SM counterparts. Since no such particles have been observed, for SUSY to be a property of nature one has to assume that it is not an exact symmetry, but is broken, through an unknown mechanism, at some scale, Λ. It has been shown [37] that SUSY can be broken explicitly by the inclusion of "soft" breaking terms in the Lagrangian, which preserve the ultraviolet properties of the theory. With soft SUSY-breaking, and with the further assumption of SUSY masses at the TeV-scale, the convenient solution to the hierarchy problem is maintained.

In the MSSM, electroweak symmetry breaking occurs in a manner analogous to that in the SM. Since the MSSM prescribes two Higgs doublets, each one obtains a non-zero VEV. The ratio of the two VEVs, parametrized as $\tan\beta$, and the sign of the Higgsino mass term in the superpotential, denoted as sign(μ), are important parameters controlling the behavior of the theory. Three of the original eight degrees of freedom in the Higgs supermultiplets are absorbed by the gauge bosons to provide their longitudinal polarizations and to acquire masses, while the remaining degrees of freedom are associated with four scalar and one pseudoscalar Higgs boson (h^0, H^0, $H^\pm$, A^0). SUSY imposes several requirements on the masses of the Higgs bosons, and with the inclusion of radiative corrections, an upper bound for the mass of the lightest Higgs boson, h^0, is estimated at $m_h^{\max} \approx 140$ GeV [32]. Such a bound is certainly compatible with the recent discovery of a Higgs boson at the LHC with a mass of approximately 125 GeV and, if the discovered boson is assumed to coincide with the lightest Higgs boson predicted by the MSSM, strong constraints on MSSM parameters can be imposed [38].

With the electroweak symmetry broken, some SUSY fields mix, giving rise to new mass eigenstates. The two neutral gauginos (the neutral wino, $\tilde{W}^0$, and the Bino, $\tilde{B}$) and the two neutral Higgsinos ($\tilde{H}_u^0$ and $\tilde{H}_d^0$) mix to form so-called neutralinos ($\tilde{\chi}_1^0$, $\tilde{\chi}_2^0$, $\tilde{\chi}_3^0$, $\tilde{\chi}_4^0$). Similarly the charged winos mix with the charged Higgsinos to form charginos ($\tilde{\chi}_1^\pm$, $\tilde{\chi}_2^\pm$). The subscripts of the neutralino and chargino symbols denote the relative masses, with $\tilde{\chi}_1^0$ denoting the lightest neutralino and $\tilde{\chi}_1^\pm$ the lightest charginos. Finally, sfermion mixing is generally considered only for the third generation sfermions, which have relatively large Yukawa couplings and mix to create new mass eigenstates, whereas the lower generation fermions are often considered almost degenerate and constitute their own mass eigenstates. Table 3.2 catalogs the mass eigenstates together with the relevant SUSY fields that mix to produce them, summarizing the new particles predicted by the MSSM [18].

For the theory to include gravity, SUSY has to be promoted from a global to a local symmetry [18]. Such a theory is called *supergravity* and includes the graviton and its superpartner, the gravitino, $\tilde{G}$, which acquire mass when SUSY is broken. The spontaneous breaking of SUSY, due to a non-zero VEV, F_0, gives rise to a *goldstino*, which is analogous to the Nambu-Goldstone boson of the Higgs mechanism in electroweak symmetry breaking. In this "super-Higgs" mechanism, the gravitino absorbs the goldstino and acquires a mass given by:

$$m(\tilde{G}) = \frac{F_0}{\sqrt{3}m_{\mathrm{P}}} \tag{3.3}$$

Names	Spin	P_R	Gauge Eigenstates	Mass Eigenstates
Higgs bosons	0	+1	$H_u^0\ H_d^0\ H_u^+\ H_d^-$	$h^0\ H^0\ A^0\ H^\pm$
squarks	0	−1	$\tilde{u}_L\ \tilde{u}_R\ \tilde{d}_L\ \tilde{d}_R$	(same)
			$\tilde{s}_L\ \tilde{s}_R\ \tilde{c}_L\ \tilde{c}_R$	(same)
			$\tilde{t}_L\ \tilde{t}_R\ \tilde{b}_L\ \tilde{b}_R$	$\tilde{t}_1\ \tilde{t}_2\ \tilde{b}_1\ \tilde{b}_2$
sleptons	0	−1	$\tilde{e}_L\ \tilde{e}_R\ \tilde{\nu}_e$	(same)
			$\tilde{\mu}_L\ \tilde{\mu}_R\ \tilde{\nu}_\mu$	(same)
			$\tilde{\tau}_L\ \tilde{\tau}_R\ \tilde{\nu}_\tau$	$\tilde{\tau}_1\ \tilde{\tau}_2\ \tilde{\nu}_\tau$
neutralinos	1/2	−1	$\tilde{B}\ \tilde{W}^0\ \tilde{H}_u^0\ \tilde{H}_d^0$	$\tilde{\chi}_1^0\ \tilde{\chi}_2^0\ \tilde{\chi}_3^0\ \tilde{\chi}_4^0$
charginos	1/2	−1	$\tilde{W}^\pm\ \tilde{H}_u^+\ \tilde{H}_d^-$	$\tilde{\chi}_1^\pm\ \tilde{\chi}_2^\pm$
gluino	1/2	−1	$\tilde{g}$	(same)
gravitino	3/2	−1	$\tilde{G}$	(same)

Table 3.2: The particle content of the MSSM (with sfermion mixing for the first two generations assumed to be negligible).

where m_P is the Planck mass. Since F_0 represents the SUSY breaking scale, if SUSY breaks at a relatively low scale, the gravitino can be expected to have a low mass and to be the LSP.

Several different possible mechanisms of soft SUSY breaking have been proposed. In most of these theories, a "hidden sector" is postulated which couples to the rest of the theory via renormalizable interactions. The hidden sector comprises fields that do not have any gauge or superpotential couplings with the "visible sector" containing the MSSM. SUSY breaking occurs in the hidden sector and, with the help of "messenger" fields, is communicated to the MSSM. Several classes of theories have been proposed, primarily based on the nature of the mediation mechanism. For example, in Gravity Mediated SUSY Breaking, SUSY breaking is mediated through gravitational interactions. In Gauge Mediated SUSY Breaking (GMSB), the gauge interactions of the Standard Model are used. The scenario investigated in this thesis is a part of the GMSB family of models, and is therefore discussed in more detail below.

3.4 Gauge Mediated Supersymmetry Breaking

GMSB [39–44] models are soft SUSY breaking models in which the symmetry breaking occurs in a TeV-scale hidden sector and is transmitted to the MSSM particles in the visible sector via messenger fields which transform as a representation under the ordinary $SU(3)_C \times SU(2)_L \times U(1)_Y$ SM gauge group. These messenger particles acquire mass in the hidden sector through Yukawa couplings with the goldstino superfield, whose non-zero VEV generates the SUSY breaking. The masses of the messenger particles are characterized by an overall mass scale, M_m and a mass-splitting, $\sqrt{F}$. The mass splitting in the visible sector arises because of gauge interactions between the observable and messenger fields. The masses of SM particles are protected by gauge invariance, but sparticles acquire mass through loops, with the gauginos acquiring mass at one-loop and scalars at the two-loop level [18]. The soft masses are controlled by their SM couplings together with just two additional parameters: the number of generations in the messenger sector, N_m, and the effective SUSY breaking scale in the visible sector, defined as $\Lambda = F/M_m$. The gaugino masses are shown to be $\tilde{M} \propto N_m \Lambda$, while the sfermion masses are $\tilde{m} \propto \sqrt{N_m}\Lambda$. It can also be shown that, in order for the masses to be in the TeV range, Λ values of the order of 100 TeV are required.

In GMSB models, the gravitino, $\tilde{G}$, will be the LSP for any reasonable choice of F, with gravitino masses typically at the keV-level. The ratio $C_{\text{grav}} = F_0/F$ depends on the details of the mechanism which transmits the SUSY breaking to the messengers and is such that $C_{\text{grav}} > 1$, with the possibility that $C_{\text{grav}} >> 1$. C_{grav} is treated as a free parameter in the model description. Therefore, in the minimal GMSB scenario considered here, the model is completely fixed by the six parameters:

$$\left\{ \Lambda \, , \, N_m \, , \, M_m \, , \, \tan\beta \, , \, \text{sign}(\mu) \, , \, C_{\text{grav}} \right\}.$$

The coupling of the gravitino to particles and their SUSY partners leads to the decay of the NLSP into its SM partner and a gravitino. Consequently, the phenomenology of various GMSB models depends on the nature of the NLSP. The latter is largely determined by the parameter N_m, which has typical values between 1 and 5. For low values, the NLSP is the lightest neutralino, $\tilde{\chi}_1^0$. The parameter C_{grav} determines not only the gravitino mass but also, crucially for this analysis, the lifetime of the NLSP:

$$c\tau(\tilde{\chi}_1^0) \propto C_{\text{grav}}^2 \frac{F^2}{m(\tilde{\chi}_1^0)^5} \tag{3.4}$$

The Snowmass Points and Slopes (SPS) [45] benchmark SUSY scenarios consist of strategically selected parameter sets in which all but one or two parameters are fixed. This thesis concentrates on the SPS8 set, which describes a set of minimal GMSB models with a bino-like neutralino as the NLSP. In this set, Λ and C_{grav} (or equivalently $\tau(\tilde{\chi}_1^0)$) are free parameters, while the rest of the parameters satisfy the relations $M_m = 2\Lambda$, $N_m = 1$, $\tan\beta = 15$ and $\mu > 0$. Fig. 3.1 shows the SUSY mass spectra for SPS8 parameter sets with Λ values of 120 and 180 TeV, indicating the relative mass scales of the neutralinos with respect to the charginos and the lightest sleptons and squarks.

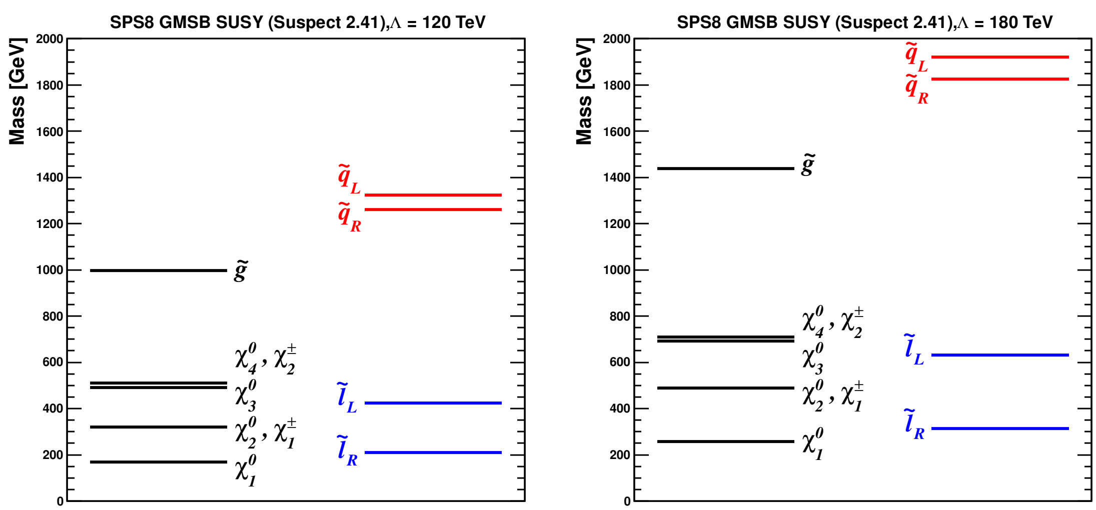

Figure 3.1: Spectrum of SUSY particle masses in the SPS8 GMSB model for $\Lambda = 120$ TeV (left) and $\Lambda = 180$ TeV (right).

The bino-like nature of the lightest neutralino leads to the decay $\tilde{\chi}_1^0 \rightarrow \tilde{G} + \gamma\,(Z^0)$. As the SUSY particles will be produced in pairs in pp collisions, topologies such as the ones represented by the Feynman diagrams in Fig. 3.2 are expected. This analysis considers only NLSP decays to a gravitino and photon. The experimental signature therefore comprises a pair of high transverse momentum photons, together with missing transverse energy due to the escaping gravitinos ($\gamma\gamma + E_{\text{T}}^{\text{miss}}$). Furthermore, the lifetime of this decay, controlled by C_{grav}, can take a very large range of

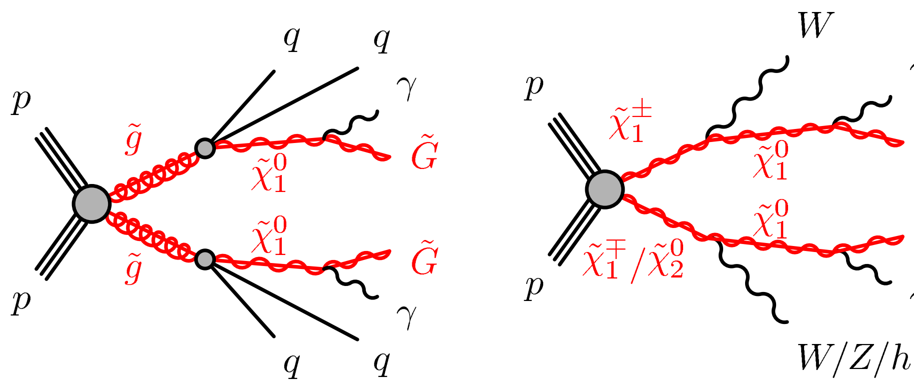

Figure 3.2: Leading order Feynman diagrams contributing to the production of two photon and gravitino pairs in the context of GMSB. The left diagram shows an example of a strongly-produced event, while the right diagram shows typical topologies for electroweak production.

values. At one extreme, the NLSPs decay promptly at their production vertex. At the other they survive long enough to escape undetected. Of special interest in this thesis is the intermediate range where the decays occur within the detector, but significantly displaced so that the decay photons fail to point back to the neutralino production vertex.

Fig. 3.3 (left) shows for 7 TeV pp collisions the SUSY total production cross section for SPS8 GMSB models as a function of Λ, as well as a function of the NLSP and lightest chargino masses. The production of SUSY particles can occur either via strong pair-production of colored super-particles, such as gluinos or squarks, or via the electroweak production of gaugino pairs. The cross section is calculated at next-to-leading order (NLO) using `PROSPINO` [46] version 2.1. For the contribution to the cross section due to strong production, the calculation includes resummations at the next-to-leading-logarithmic (NLL) accuracy, as described in Ref. [47]. Fig. 3.3 (right) shows the fraction of SUSY events that are due to gluino/squark pair-production as a function of Λ, as well as as a function of the gluino and typical squark masses. For lower values of Λ, corresponding to lighter gluinos and squarks, strong production dominates. However, as Λ increases and the gluino and squark masses become heavier, electroweak production of gaugino pairs becomes dominant. The final state topology depends on the production process, with strong production events often having large jet multiplicities, whereas electroweak production tends to produce fewer jets and instead, in some cases, charged leptons. To reduce the model-dependence of the results, this analysis performs an inclusive search of the $\gamma\gamma + E_{\mathrm{T}}^{\mathrm{miss}}$ final state, and therefore does not make any explicit requirements on the multiplicities of jets or leptons in the final state.

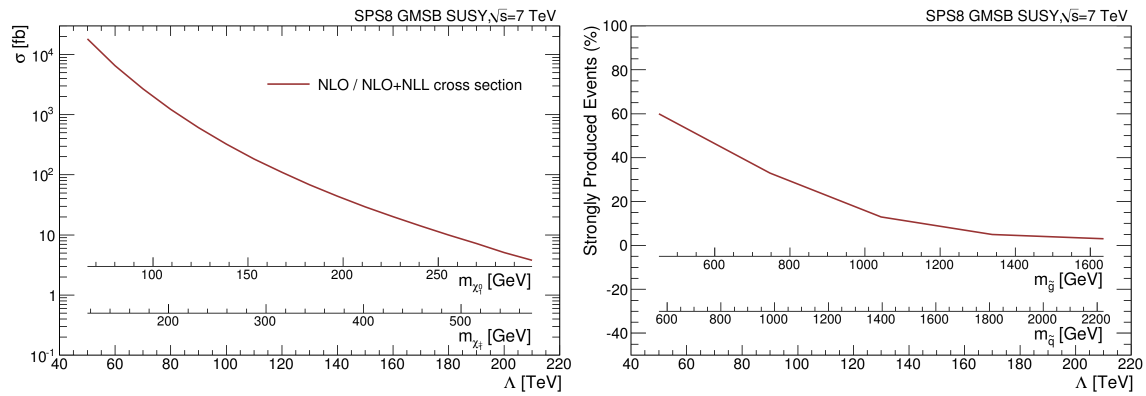

Figure 3.3: (Left) The total SUSY cross section for the SPS8 GMSB model as a function of Λ. (Right) The fraction of strongly produced SUSY events as a function of Λ. On the interior axes, the dependence as function of the mass of the lightest neutralino and chargino is shown for the left plot, and as a function of the gluino mass and typical squark mass for the right plot.

The final state kinematics depend on Λ. Fig. 3.4 shows, as a function of Λ, the distribution of the NLSP momentum in the plane transverse to the beam direction (p_{T}), as well as the distribution of the NLSP speed (β). As Λ increases, the SUSY particle masses tend to increase, the p_{T} spectrum becomes harder, and the β spectrum softer.

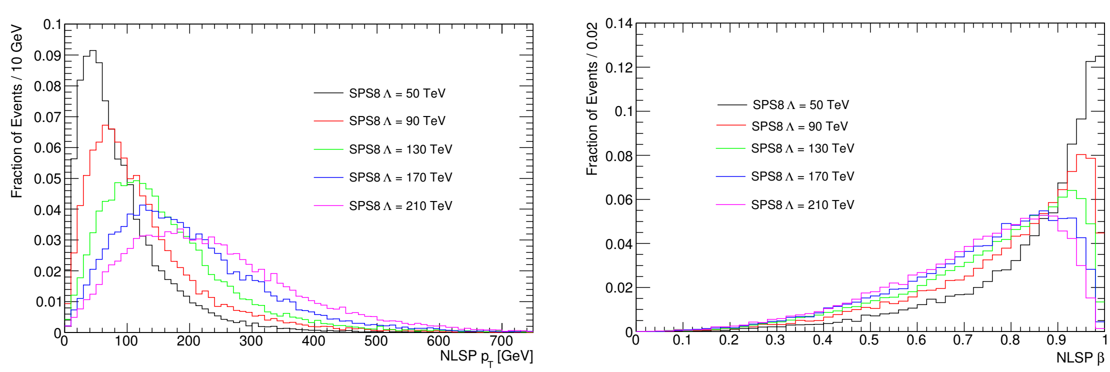

Figure 3.4: Unit-normalized distributions of the NLSP transverse momentum (left) and the NLSP speed (right), for several Λ values on the SPS8 GMSB model line.

A toy Monte Carlo (MC) simulation, which included the expected SUSY kinematics, was used to estimate, as a function of the NLSP lifetime, the fraction of NLSPs which would decay within a cylinder of radius of 1.5 m and length of 3 m. The size of the cylinder corresponds approximately to the volume of the ATLAS inner detector (ID). The result is shown in Fig. 3.5 for some sample Λ values. As can be seen, due to the differences in kinematics, there is some Λ dependence. However, the main effect is due to the exponential NLSP decay length. Typically 20% of the NLSPs decay within the ID for an NLSP lifetime of 20 ns. Since this analysis searches in the $\gamma\gamma + E_{\mathrm{T}}^{\mathrm{miss}}$ final state, it is therefore sensitive only to those SUSY events in which both NLSPs decay within the volume of the ID. An estimate of the rate of such events can be obtained by squaring the result in Fig. 3.5; for example, for an NLSP lifetime of 20 ns, only $\sim (0.20)^2 = 4\%$ of the total SUSY events would be expected in the diphoton final state. This effect limits the reach of the current analysis for longer NLSP lifetimes. However, in the regime of intermediate NLSP lifetime values, the $\gamma\gamma + E_{\mathrm{T}}^{\mathrm{miss}}$ final state provides a fairly well understood topology with which to conduct this first search for evidence of non-prompt NLSP decays.

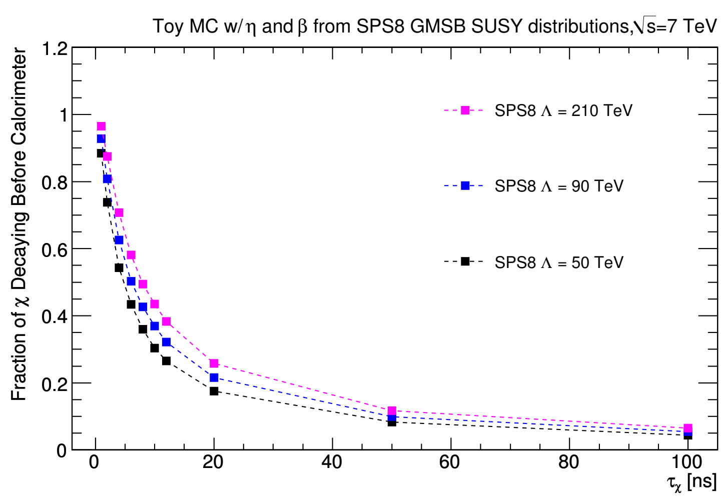

Figure 3.5: The fraction of NLSPs decaying before the calorimeter as a function of the NLSP lifetime. Curves are shown for three different Λ values.

3.5 Most Recent Previous Results

Previous ATLAS analyses investigating SPS8 models have assumed prompt NLSP decays, with $c\tau(\tilde{\chi}_1^0) < 0.1$ mm. Such analyses therefore search for an excess production of diphoton events with significant $E_{\mathrm{T}}^{\mathrm{miss}}$ due to the escaping gravitinos. The latest such ATLAS results [48] use the full 2011 dataset and, within the context of SPS8 models, exclude values of $\Lambda < 196$ TeV, corresponding to $m(\tilde{\chi}_1^0) > 280$ GeV, at the 95% CL. An earlier result by the D0 Collaboration [49] had excluded values of $\Lambda < 124$ TeV at 95% CL, which corresponds to a limit on the mass of the lightest neutralino of $m(\tilde{\chi}_1^0) > 175$ GeV. The CMS Collaboration has performed a search for SUSY in events with photons and $E_{\mathrm{T}}^{\mathrm{miss}}$ [50], using its full 2011 dataset and setting limits on SUSY production; however, the CMS analysis does not evaluate the results within the context of SPS8 GMSB models, therefore their results are not directly comparable with the results in this thesis.

The limits on SPS8 models are less stringent in the case of a longer-lived NLSP. For example, a recent CMS analysis [51] determined 95% CL limits on the mass of the NSLP, $m(\tilde{\chi}_1^0)$, and its proper decay length, $c\tau(\tilde{\chi}_1^0)$, using the $E_{\mathrm{T}}^{\mathrm{miss}}$ spectrum of events with at least three jets and one or two photons, coupled with measurements of the photon arrival time. The CMS results impose the requirements $m(\tilde{\chi}_1^0) > 220$ GeV for $c\tau(\tilde{\chi}_1^0) < 500$ mm, and $c\tau(\tilde{\chi}_1^0) > 6000$ mm for $m(\tilde{\chi}_1^0) < 150$ GeV. It should be noted, however, that the event selection requirement of at least three jets for the CMS result does introduce a model dependence, since final states with multiple jets are favored in strongly-produced events. Finally, a CDF analysis [52] performed a search sensitive to NLSP lifetimes up to 2 ns, excluding values of $m(\tilde{\chi}_1^0) \lesssim 146$ GeV for $\tau(\tilde{\chi}_1^0) = 2$ ns, and $m(\tilde{\chi}_1^0) < 146$ GeV for $\tau(\tilde{\chi}_1^0) << 1$ ns.

Chapter 4

The Large Hadron Collider

The Large Hadron Collider (LHC) [9, 10] is a circular particle accelerator located at CERN, the European Organization for Nuclear Research, in the border region of France and Switzerland near Geneva. The LHC is currently the highest-energy collider in the world, and is designed to accelerate protons or heavy-ions. Inside the LHC, two counter-circulating proton beams collide with a center-of-mass energy of up to 14 TeV, providing collisions to four experiments, ATLAS [8], CMS [11], LHCb [53] and ALICE [54], distributed along its perimeter. ATLAS and CMS are two large, general-purpose experiments with a broad physics program, whereas LHCb and ALICE are specialized experiments, designed to study B-physics and heavy-ion collisions, respectively. The work presented in this thesis uses data recorded by the ATLAS detector, which is described in detail later. In this chapter, the design and operation of the LHC are briefly described, and the environment presented by the machine during the relevant data taking period is summarized.

4.1 Concepts of Accelerator Physics

In a particle accelerator, charged particles are accelerated under the influence of an electric field, creating a stream of particles called a *particle beam*. Most modern accelerators provide *bunched* beams, containing packets, or *bunches*, of particles instead of a continuous stream. In synchrotron accelerators, the acceleration is usually provided by Radio-Frequency (RF) cavities. The electromagnetic field in the cavities oscillates at a particular frequency so properly timed particles will experience an acceleration when passing through them, grouping in the troughs of the electromagnetic waves. The troughs are frequently called RF *buckets* and effectively trap the particle bunches [55]. In a circular accelerator, the particles can pass many times through the cavities and can be timed so that they gradually increase their energy up to the design limit of the machine. The particles are kept in their trajectory by a suitably tuned magnetic field, usually provided by dipole magnets. Additional multipole magnets are used for the beam optics, focusing, constraining and applying other corrections to the beam in the transverse direction.

As the particles move along their nominal trajectory, s, they undergo *betatron oscillations* in the transverse direction. The amplitude of those oscillations is described by the machine *beta function*, $\beta(s)$, which depends on the multipole configuration in the machine. The beam size in the transverse direction is often characterized by their RMS and, under the assumption of a Gaussian distribution, the standard deviation, σ, is used. It is customary to use one standard deviation to define the *transverse emittance* as:

$$\epsilon \equiv \pi \frac{\sigma^2(s)}{\beta(s)}. \tag{4.1}$$

It is also useful to define the *normalized emittance*, $\epsilon_n = \beta_r \gamma_r \epsilon$ where β_r and γ_r are the usual relativistic functions.

For high energy physics research, one of the most important properties of a particle accelerator is arguably the center-of-mass collision energy, usually denoted by $\sqrt{s}$. For a symmetric particle collider, the upper limit of the center-of-mass energy is the sum of the two individual beam energies. For a given machine radius (R), the beam energy is dictated by the strength of the magnetic field (B) providing the beam steering:

$$p[\mathrm{TeV}] = 0.3B[\mathrm{T}] \cdot R[\mathrm{km}] \tag{4.2}$$

and therefore technologies such as superconducting magnets are employed in modern particle accelerators. The maximum energy attainable in a circular machine is also limited by the loss of energy due to synchrotron radiation. In a hadron machine, this is normally negligible since the power lost via synchrotron radiation is inversely proportional to the fourth power of the mass of the accelerated particle. In the case of the LHC, however, this phenomenon is expected to provide a significant challenge for the first time in a hadron collider as the machine energy approaches its design value [19].

An equally important parameter for a collider is the instantaneous *luminosity*, $\mathscr{L}$, which is proportional to the particle production rate for any given process. The total number of expected events for a process with cross section σ_{exp} is:

$$N_{exp} = \sigma_{exp} \times \int \mathscr{L}(t)dt \tag{4.3}$$

The factor $\int \mathscr{L}(t)dt$ is called the *integrated luminosity*. The instantaneous luminosity in a collider can, in principle, be calculated from the beam characteristics. In a circular collider, two beams are usually brought together to cross in one or more Interaction Points (IP). For a machine with two similar beams, revolving around the ring with frequency f_{rev}, the luminosity at the IP is given by:

$$\mathscr{L} = f_{rev}\frac{N_b^2 n_b \gamma_r}{4\pi\epsilon_n \beta^*}F \tag{4.4}$$

where N_b is the number of particles per bunch, n_b is the number of bunches per beam, γ_r is the relativistic γ-factor, ϵ_n is the normalized emittance, and β^* is the beta-function at the IP [55]. Finally, F is a geometric factor arising from the fact that the beams do not collide head-to-head, but instead cross at a non-zero angle. From these equations, it is evident that, to achieve high luminosity in a collider, a high number of high population bunches with low emittance is needed. In addition, tuning of the beam optics is needed to obtain low values of the amplitude function at the IP. However, these can be very challenging and many factors, such as beam-beam interaction effects, can hinder this effort.

The determination of the luminosity from Eq. 4.4 using beam characteristics in the IP is not performed during data taking since it can cause undesired interference. Further, the precision of this method is rather poor, with uncertainties exceeding $\sim 10\%$. Specialized runs called "van der Meer Scans" [56] are used instead to obtain an absolute measurement of the luminosity and to calibrate specialized equipment and methods used by the experiments for the determination of the luminosity. These methods usually rely on the knowledge of the cross section and the measurement of the observed rate for a certain process. For a pp collider, Eq. 4.3 can be rewritten as

$$\mathscr{L} = \frac{R_{inel}}{\sigma_{inel}} \tag{4.5}$$

where R_{inel} is the rate of inelastic collisions and σ_{inel} is the pp inelastic cross section. Eq. 4.5 can further be recast to

$$\mathscr{L} = \frac{\mu n_b f_{rev}}{\sigma_{inel}} \tag{4.6}$$

where $\mu =< N_{inel}/n_b >$ is the *average number of inelastic interactions per bunch crossing*. The equations above are frequently used in the determination of the instantaneous and integrated luminosity by the experiments, including ATLAS.

4.2 LHC Design and Operation

The LHC is built in the same tunnel previously housing the Large Electron-Positron Collider (LEP) that operated from 1989 until 2000. The tunnel has a circumference of approximately 27 km and lies between 45 m and 170 m below the ground, in a plane with a slope of 1.4%. The availability of this already excavated tunnel, and the cost reduction associated with using it, was a significant factor in the decision to design and construct the LHC as is.

The LHC machine is a two-ring, superconducting alternating gradient synchrotron [57, 58] designed to accelerate protons to energies up to 7 TeV, as well as heavy ions to energies up to 2.76 TeV per nucleon. The specifics of the heavy ion program are not relevant to the work presented in this thesis and will not be discussed further. The machine is not a perfect circle, and is instead made of eight arcs and eight straight segments. The arcs contain dipole magnets that are used to steer the particles in the circular orbit. The setup in the straight segments depends on their specific use, which includes beam cleaning, injection and dump facilities, and IPs, where the beams are steered to cross and provide collisions for the four experiments. The bunches in the two beams are suitably arranged and timed so as to provide higher instantaneous luminosity to the two general purpose experiments, ATLAS and CMS, compared to the specialized experiments, LHCb and ALICE.

Particle-antiparticle colliders like LEP or the Tevatron [59] can have their two counter-rotating beams share the same beamline in different orbits. In contrast, in the LHC, two individual rings are needed. Due to the limited space in the LEP/LHC tunnel, which has an inner diameter of 3.7 m in the arcs, the construction of two completely separate rings was not feasible. Instead, a twin-bore dipole magnet was developed which provides a uniform magnetic field with opposite directions to the center of each of two beam pipes sharing the same cold vessel. The LHC uses 1,232 main dipole magnets to bend the beams and 392 main quadrupoles for focusing. Several other types of magnets complete the beam optics system. The dipole magnets employ coils using niobium-titanium (NbTi) cables and superfluid helium is used to cool the magnets to 1.9 K. At this temperature, using an electrical current of 11.85 kA, the dipoles are able to provide the magnetic field of 8.33 T required for operation at 7 TeV per beam.

The pre-existing accelerators in the CERN complex (see Fig. 4.1) act as injectors for the LHC, while they are also serving non-LHC experiments. Protons are obtained by stripping the electrons from molecular hydrogen gas, and are initially accelerated to an energy of 50 MeV by the LINAC2 linear accelerator. The protons are then fed into a series of circular accelerators with increasing energies, to be accelerated to the LHC injection energy of 450 GeV. The protons from LINAC2 are divided to the four superimposed synchrotron rings of the Proton Synchrotron Booster (PSB), where they obtain an energy of 1.4 GeV. Subsequently they are injected to the Proton Synchrotron (PS), where the protons are assembled into a train of proton bunches which are approximately 25 ns apart and nominally contain 1.15×10^{11} protons. The proton energy is increased to 25 GeV and, at the last step of the injection chain, typically three or four bunch trains are fed to the Super Proton Synchrotron (SPS). The protons are accelerated to 450 GeV during the 21.6 s SPS cycle and then injected to one of the LHC rings. The procedure is typically repeated 12 times to fill one LHC ring with a total of nominally 2,808 bunches, assembled in bunch trains. When both LHC rings are filled, the beam energy is ramped up to an energy of 7 TeV, in a procedure that takes at least ~ 20 minutes. The beams are brought into collision and, after some beam adjustments, *stable beams* are declared and the experiments take data suitable for physics analysis. The beams are slowly depleted while circulating and providing collisions at the IPs. The beam lifetime is of the order of 10 h, after which time the beams are dumped and the machine is ramped down so a new LHC fill can start.

The LHC employs eight superconducting RF cavities per beam using niobium-on-copper technology, each providing a 5 MV/m accelerating field. The machine operates a 400 MHz RF

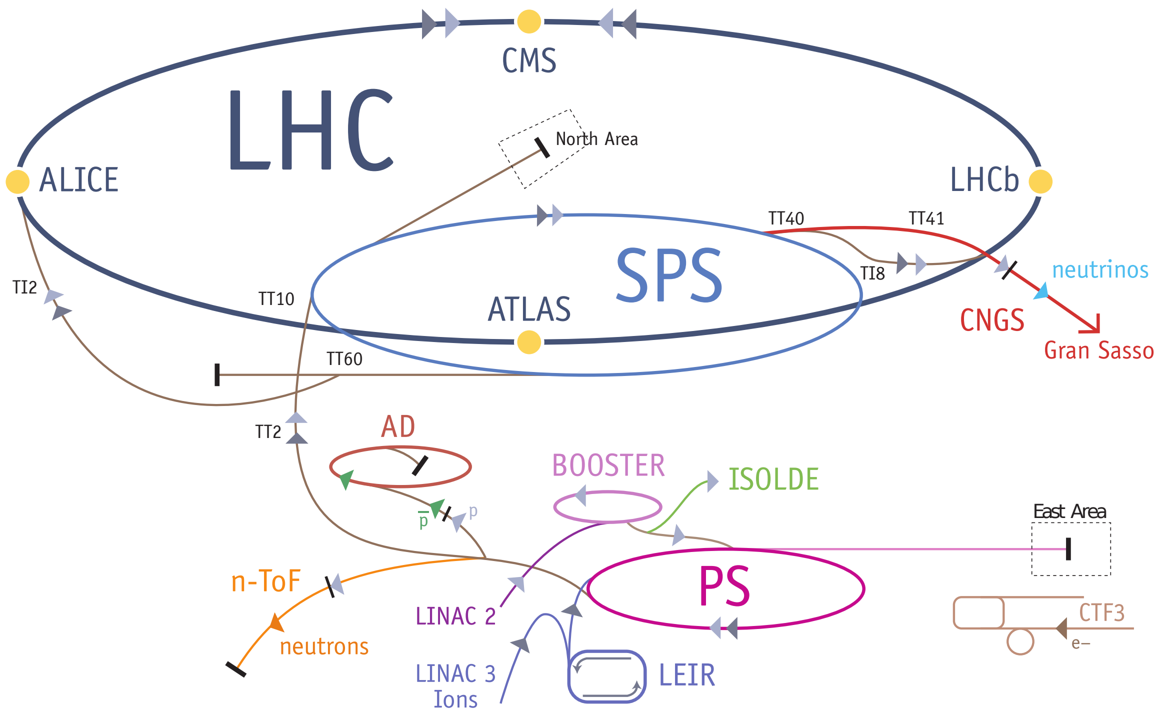

Figure 4.1: Schematic of the accelerator complex at CERN and the relative location of the experiments. The series of machines that constitute the LHC accelerator chain, as well as additional setups for non-LHC experiments, are visible [60].

system, which translates to 2.5 ns-wide RF buckets. As described in the previous section, filled buckets contain and constrain the proton bunches. A sufficient number of empty buckets is arranged between the bunch trains to allow for the reaction time of the injection and dumping systems and to provide the minimum 25 ns spacing between the filled buckets[1]. The minimum bunch spacing corresponds to a maximum bunch crossing frequency of 40 MHz, to which all the experiments are synchronized. As discussed later, for the 2011 and 2012 data-taking periods, the minimum bunch spacing used was 50 ns. Empty bunch crossings, when empty bunches overlap and no collisions are expected, are used by the experiments to estimate non-collision backgrounds during data taking under stable beams.

As a consequence of the narrow spacing between beam crossings, there is a possibility to have

[1]The actual nominal bunch spacing is 24.95 ns which corresponds to a bunch crossing frequency of 40.08 MHz and an RF frequency of 400.8 MHz. However, for simplicity, multiples of 25 ns and 40 MHz will be used throughout this thesis.

an event triggered in a particular beam crossing overlapping with events from neighboring crossings. This phenomenon is known as *out-of-time pileup*. A similar phenomenon is *in-time pileup* where many pp interactions occur in the same bunch crossing. Pileup can have a detrimental effect on the identification and reconstruction of physics objects in the detectors, since events originating from different interaction vertices overlap with a triggered event. The effects and potential impact of pileup are studied and taken into account in the analysis, as discussed later.

4.3 Operating Conditions in 2011 and 2012

The LHC started operations on September 10th, 2008. Unfortunately, after only a few days of operation an incident [61] occurred when an superconducting electrical connection failed between a dipole and a quadrupole. This caused the development of a resistive load across the connection and the dissipation of heat, raising the temperature, which in turn caused the cable to lose its superconducting properties, or *quench*. An arc developed across the connection, destroying the helium enclosure. The rapid expansion of the escaping helium gas caused severe mechanical and electrical damage to at least 53 cryomagnets, as well as contamination of the vacuum beam pipes. The LHC subsequently underwent a period of several months repairs and connection inspections to return to operation in November 2009 with pp collision energies up to $\sqrt{s} = 2.36$ TeV. As a precaution, it was decided to operate the LHC at a beam energy lower than design for the first few years of operation, leading up to the first long shutdown period of 2013, during which a lengthy program of electrical interconnection replacement and inspection was planned and is now underway. In 2010 and 2011, the machine operated at $\sqrt{s} = 7$ TeV, while in 2012 it was considered safe to increase the energy to $\sqrt{s} = 8$ TeV.

During the 2010 data taking period the LHC delivered a modest integrated luminosity of approximately 48 pb^{-1} of pp collisions. The delivered luminosity evolved rapidly over the following two years, made possible by an increase of the number bunches in the beams, as well as the gain in operation experience which allowed the operators to fine tune the machine parameters and optimize the peak luminosity. The LHC has performed excellently, operating at unprecedented instantaneous luminosities and delivering a remarkable amount of collision data to the experiments. In 2011 and 2012, the LHC delivered to ATLAS approximately 5.6 fb^{-1} and 23.3 fb^{-1} of

pp collisions, respectively.

The high integrated luminosities and the associated high instantaneous luminosities come at the cost of in-time pileup. For the 2011–2012 data taking period, this effect is further amplified by the high number of protons per bunch employed, which was above the design specifications of the machine and experiments. The increased proton density was a compromise between the need for high integrated luminosity while operating the machine with a wider, 50 ns minimum bunch spacing. The wider spacing was deemed by the machine operators a more stable mode of operation for these first years of running. The mean number of interactions per bunch crossing, μ, as recorded by ATLAS in the 2011 and 2012 data taking periods is shown in Fig. 4.2. For 2011, the mean number of interactions per bunch crossing was on average 9.1, while for 2012 this value rose to 20.7.

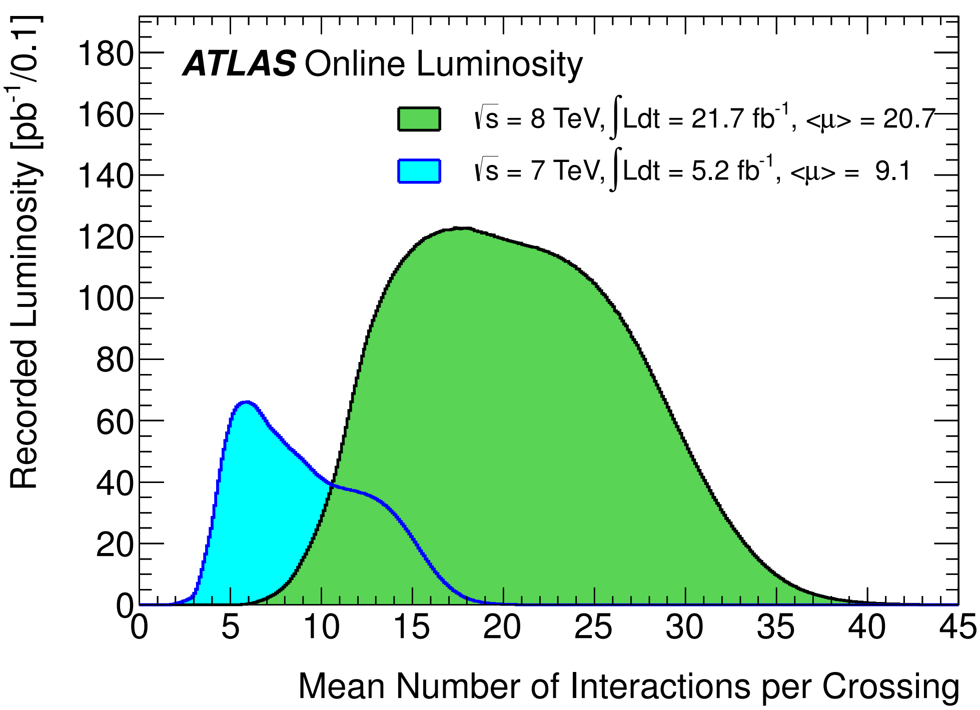

Figure 4.2: Distribution of mean number of interactions per bunch crossing, μ, weighted by the bunch instantaneous luminosity, as recorded by ATLAS during 2011 and 2012.

Chapter 5

The ATLAS Experiment

ATLAS (A Toroidal LHC Apparatus) is the largest of four experiments running at the LHC. In this chapter, the ATLAS detector is described in general. Detailed descriptions of the detector design and performance are available in Ref. [8]. The ATLAS Liquid Argon (LAr) Electromagnetic (EM) calorimeter [62] is described in more detail, since the analysis presented in this thesis relies on the novel capabilities of that particular subsystem.

5.1 Overview of the ATLAS Detector

The ATLAS detector is a general purpose apparatus engineered to exploit the full discovery potential of the LHC, and is designed to be sensitive to a broad selection of physics processes. The physics goals and the harsh environment of the LHC impose severe requirements for the detector in terms of performance and operation in a radiation environment.

The ATLAS detector has a cylindrical geometry with forward-backward symmetry with a diameter of approximately 25 m and a length of approximately 44 m, as shown in Fig. 5.1. The ATLAS detector consists of a series of concentric subdetectors and systems: In the innermost section of the detector, and within a solenoid magnet, lies the Inner Detector (ID), consisting of the Pixel Detector, the Semiconductor Tracker (SCT), and the Transition Radiation Tracker (TRT). The Calorimeter System surrounds the solenoid and consists of LAr Electromagnetic, Hadronic, and Forward Calorimeters, as well as a Tile Hadronic Calorimeter. In the outermost layers of the detector, several technologies of muon chambers make up the Muon Spectrometer,

Detector component	Required resolution (p_T and E in GeV)	Coverage in η	
		Measurement	Trigger
Tracking	$\sigma_{p_T}/p_T = 0.05\%/p_T \oplus 1\%$	$\pm$ 2.5	—
EM calorimetry	$\sigma_E/E = 10\%/\sqrt{E} \oplus 0.7\%$	$\pm$ 3.2	$\pm$ 2.5
Hadronic calorimetry			
- Barrel and endcap	$\sigma_E/E = 50\%/\sqrt{E} \oplus 3\%$	$\pm$ 3.2	$\pm$ 3.2
- Forward	$\sigma_E/E = 100\%/\sqrt{E} \oplus 10\%$	$3.1 < \|\eta\| < 4.9$	$3.1 < \|\eta\| < 4.9$
Muon Spectrometer	$\sigma_{p_T}/p_T = 10\%/p_T$ at $p_T = 1$ TeV	$\pm$ 2.7	$\pm$ 2.4

Table 5.1: General performance goals of the ATLAS detector. The $\oplus$ symbol denotes the addition of the surrounding terms in quadrature.

which is supported by a toroidal magnet system. The detector is complemented by a sophisticated Trigger and Data Acquisition (DAQ) system.

The right-handed ATLAS coordinate system is depicted in Fig. 5.2. The x-axis points to the center of the accelerator ring, while the y-axis points upwards. The z-axis is matched with the beamline axis and the $x-y$ plane is transverse to the beam direction. The transverse momentum, the transverse energy (E_T), and the missing transverse energy are therefore defined in the $x-y$ plane. The nominal interaction point (IP) is considered to be at the nominal center of the detector, where $x = y = z = 0$. Using cylindrical coordinates, the azimuthal angle ϕ is measured with respect to the positive x-axis and the polar angle θ is measured with respect to the positive z-axis. The pseudorapidity η is commonly used instead of θ and is defined as:

$$\eta \equiv -\ln\left[\tan\left(\frac{\theta}{2}\right)\right]. \tag{5.1}$$

The distance in the pseudorapidity-azimuthal angle space (ΔR) is used for matching between objects reconstructed in the detector and is defined as

$$\Delta R = \sqrt{\Delta\eta^2 + \Delta\phi^2} \tag{5.2}$$

The general performance goals of the various components of the ATLAS detector are shown in Table 5.1. The component coverage is also shown, for both the η-range where the subdetector can provide measurements, as well as the range where it provides information to the first level of the ATLAS trigger system.

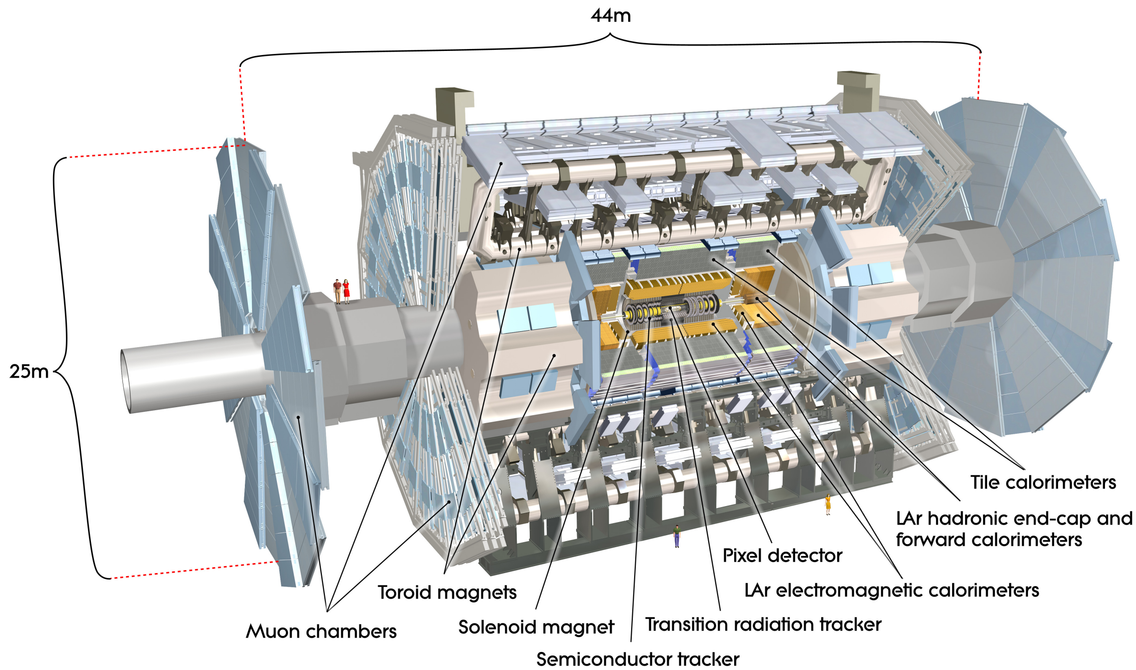

Figure 5.1: A three-dimensional visualization of the ATLAS detector.

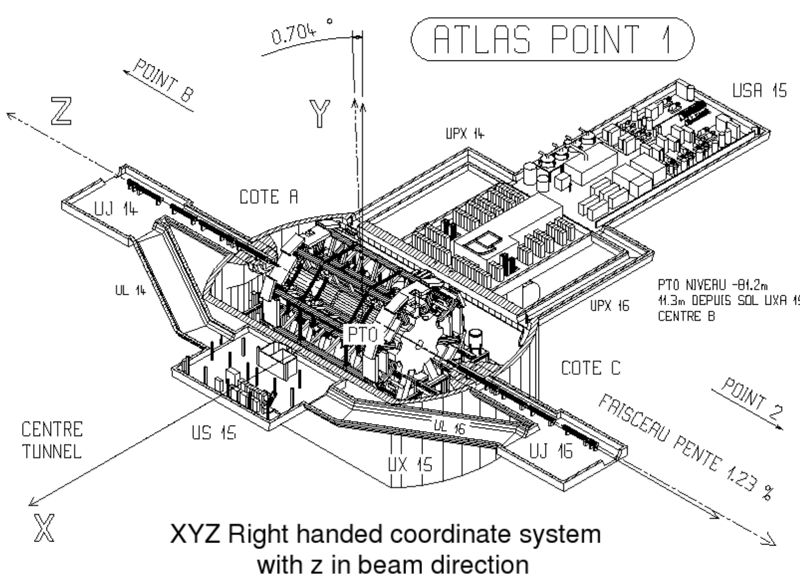

Figure 5.2: Schematic of the ATLAS detector and installation with respect to the LHC ring. The ATLAS right-handed coordinate system is also indicated.

5.2 Inner Detector

The basic function of the ATLAS ID [63, 64] is the reconstruction, above a given momentum threshold, of the trajectory and momentum of tracks of charged particles from the collision. From the set of reconstructed tracks, a set of common track intersection points along the beamline is produced, and the positions of primary vertex (PV) candidates are measured. The ID is able to provide a measurement of the z-position of a PV with at least four tracks with a resolution better than 1 mm. In addition, the ID measures with high efficiency the positions of vertices of the decay products of long-lived particles like neutral kaons or mesons containing c- and b-quarks. Further, the ID provides electron identification information up to $|\eta| < 2$, over energies ranging between 0.5 GeV and 150 GeV.

The cylindrical ID (see Fig. 5.3) is approximately 6.2 m long, has a diameter of 2.1 m and is contained in a superconducting solenoidal magnet with a central field of 2 T. The ID is composed of three sections, one central section and one endcap at each end, with total pseudorapidity coverage up to $|\eta| < 2.5$.

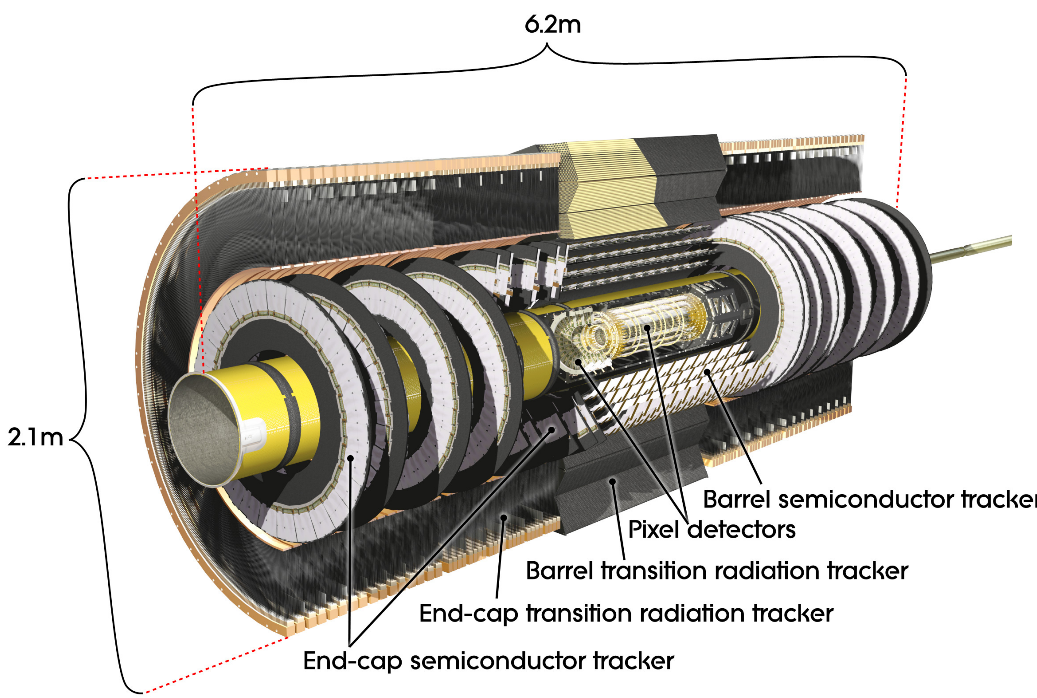

Figure 5.3: Cut-away view of the ATLAS Inner Detector.

The innermost part of the ID is the pixel detector, which comprises three cylindrical barrel layers and, on either side, three forward disk layers completing the total coverage. With this setup, the pixel detector provides typically three spatial point measurements for a charged track emanating from the interaction region. The pixel detector has the finest granularity and thus provides the best position resolution of 10 μm in the $R-\phi$ direction and 115 μm in the $R(z)$ direction for the barrel (disk) layers. The nominal pixel size is 50 μm in the ϕ direction and 400 μm in z (R) in the barrel (endcap) region. The barrel layer closest to the beam is situated at a radius $R_0 = 50.5$ mm and, owing to its importance in b-tagging, it is often referred to as the *B-layer*. The following two pixel barrel layers are situated at radii $R_1 = 88.5$ mm and $R_2 = 120.5$ mm, respectively. The three endcap disks are perpendicular to the beam axis, with an inner radius of 89 mm, and are situated at points with $|z_0| = 495$ mm, $|z_1| = 580$ mm and $|z_2| = 650$ mm. Each cylindrical layer and each disk supports a different number of pixel modules, which are composed of silicon sensors bump-bonded to front-end electronics chips as well as control circuitry. Each module services 46,080 pixel electronics channels and the total number of pixel channels is of order 81 million.

The second part of the ID is the SCT, where silicon microstrip sensors are used. With a geometry similar to the pixel detector, the SCT consists of four barrel layers at radii $R_3 = 299$ mm, $R_4 = 371$ mm, $R_5 = 443$ mm, and $R_6 = 514$ mm, as well as nine endcap disks on each side at positions ranging from $|z| = 853.8$ mm to $|z| = 2720.2$ mm. Each SCT component consists of a different number of SCT modules: the surface of the barrel layers is tiled with 2,112 identical square modules whereas the endcap disks are tiled with 1,976 wedge-shaped modules from five different module types. Most of the modules consist of two layers of sensors, each comprising 768 strips with an approximate length of 12 cm, and organized so as to provide sensor pairs with a stereo rotation angle of 40 mrad. In the barrel modules, the strip sensors have a constant pitch of 80 μm and are mounted so that one side has its strips parallel to the beam axis, resulting in a precision of 17 μm in the $R-\phi$ coordinate and 580 μm in the z coordinate. In the endcap disks, the strips are radial with a varying pitch due to the wedge geometry, which results in a mean precision of 17 μm in the $R-\phi$ coordinate and 580 μm in the radial direction.

The third part of the ID is the TRT consisting of more than 300,000 gas-filled straw tubes with a diameter of 4 mm each. In the barrel, the straws are 144 cm long and are oriented parallel to the beam. In the endcaps, the straws are 37 cm in length, assembled radially in wheels. This geometry is capable of providing a resolution of 170 μm per straw and allows for a continuation of the track measurement of the pixel detector and SCT, up to $|\eta| = 2$, with typically 36 hits per track. The TRT also provides particle identification via the transition radiation photons produced in a polypropylene radiator interleaved with the straws. The transition radiation photons are absorbed by the gas in the straws, significantly increasing the amplitude of the ionization signal. The TRT straws are read out with two thresholds. Electrons traversing the TRT produce more transition radiation photons compared to charged hadrons, such as pions, and therefore are expected to have more high-threshold hits.

The use of high resolution detectors at smaller radii and continuous tracking elements at larger radii provides a precise measurement of the ϕ and z coordinates and a robust pattern recognition. The number of precision layers is limited to keep the material budget and the cost of the ID within acceptable limits.

5.3 Calorimetry

The purpose of the ATLAS calorimeter system (Fig. 5.4) is the measurement of the energy and position of particles, and to assist in their identification. Further, the calorimeter system contributes to the precise estimation of the missing energy. In order to meet the design specifications, the calorimeter can measure the energy of a 100 GeV EM cluster with resolution of the order of 1%, depending on η. Similarly, for a jet with energy 100 GeV, the design goals require an energy resolution of the order of 6%.

The calorimeter system covers the pseudorapidity range $|\eta| < 4.9$. Sampling calorimeters based on LAr technology are used for the detection of EM objects, such as electrons and photons, up to $|\eta| = 3.2$, as well as hadronic objects in the $|\eta|$ range of $1.5 - 4.9$. Hadronic calorimetry within $|\eta| < 1.7$ is provided by a steel/scintillator-tile calorimeter. The thickness of the EM calorimeter in terms of radiation lengths (X_0) is larger than $22X_0$ in the EMB and larger than $24X_0$ in the EMEC, while in terms of interaction lengths (λ), the entire calorimeter presents a thickness of $\sim 11\lambda$ to hadronic objects at $\eta = 0$.

5.3.1 The Liquid Argon calorimeter system

In ATLAS, EM calorimetry is provided by barrel ($|\eta| < 1.475$) and endcap ($1.375 < |\eta| < 3.2$) accordion geometry lead/LAr sampling calorimeters. An additional thin LAr presampler (PS) covering $|\eta| < 1.8$ allows for corrections of energy losses in material upstream of the EM calorimeters. The EM barrel (EMB) calorimeter [62] consists of two half-barrels housed in the same cryostat. Each half-barrel is 3.2 m long and has an inner (outer) radius of 1.4 m (2 m). The EM endcap calorimeter (EMEC) [65] comprises two wheels, one on each side of the EMB. Each wheel is 63 cm thick and has an inner (outer) radius of 0.33 m (2.1 m). The EMEC wheels are contained in independent endcap cryostats, together with the hadronic endcap and forward calorimeters described later. The wheels themselves consist of two co-axial wheels, with the outer wheel (OW) covering the region $1.375 < |\eta| < 2.5$ and the inner wheel (IW) covering the region $2.5 < |\eta| < 3.2$.

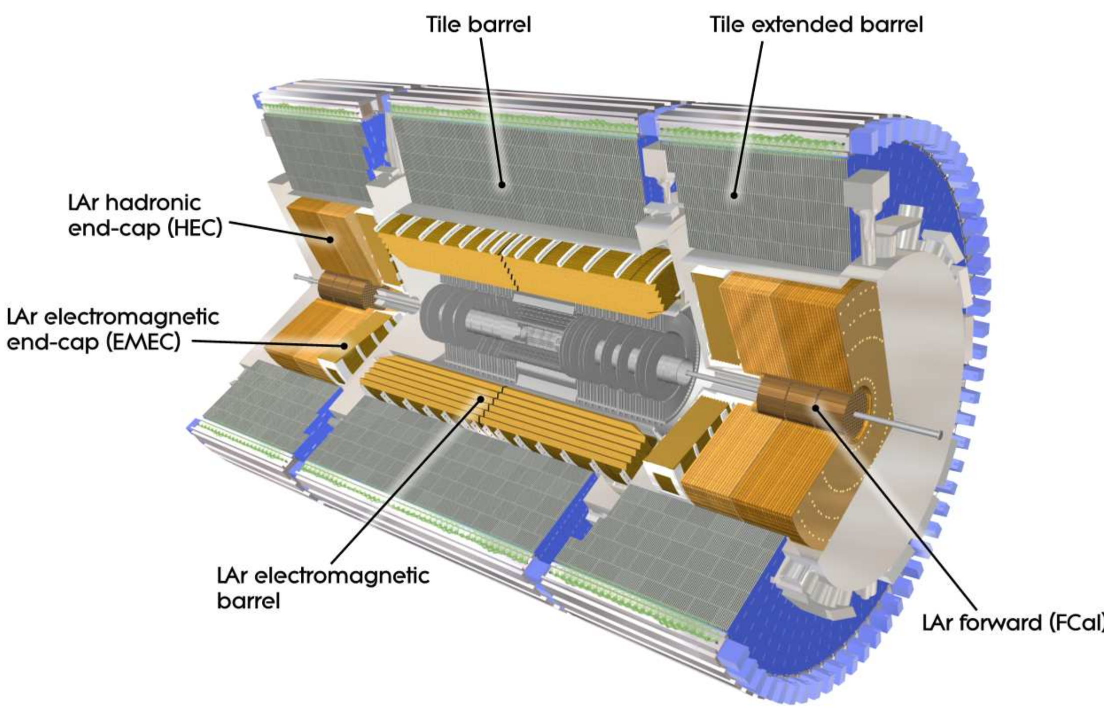

Figure 5.4: The ATLAS calorimeter system.

The EM calorimeters comprise accordion-shaped copper-kapton electrodes positioned between similarly shaped lead absorber plates and kept in position by honeycomb spacers, with the system immersed in LAr (Fig. 5.5). Incident particles shower in the absorber material and subsequently the LAr is ionized. Under the influence of the electric field between the grounded absorber and electrode kept at high voltage, the ions and electrons drift, the latter inducing a triangular pulse (Fig. 5.6) to be collected by the electrodes. With the purpose of redundancy, both sides of the electrodes are powered independently, which allows for the collection of half of the signal should one side lose high voltage. In the EMB, the size of the drift gap on each side of the electrode is 2.1 mm, which corresponds to a total electron drift time [66] of approximately 450 ns for a nominal operating voltage of 2000 V. In the EMEC, the gap is a function of radius and therefore the HV varies with η to provide a uniform detector response.

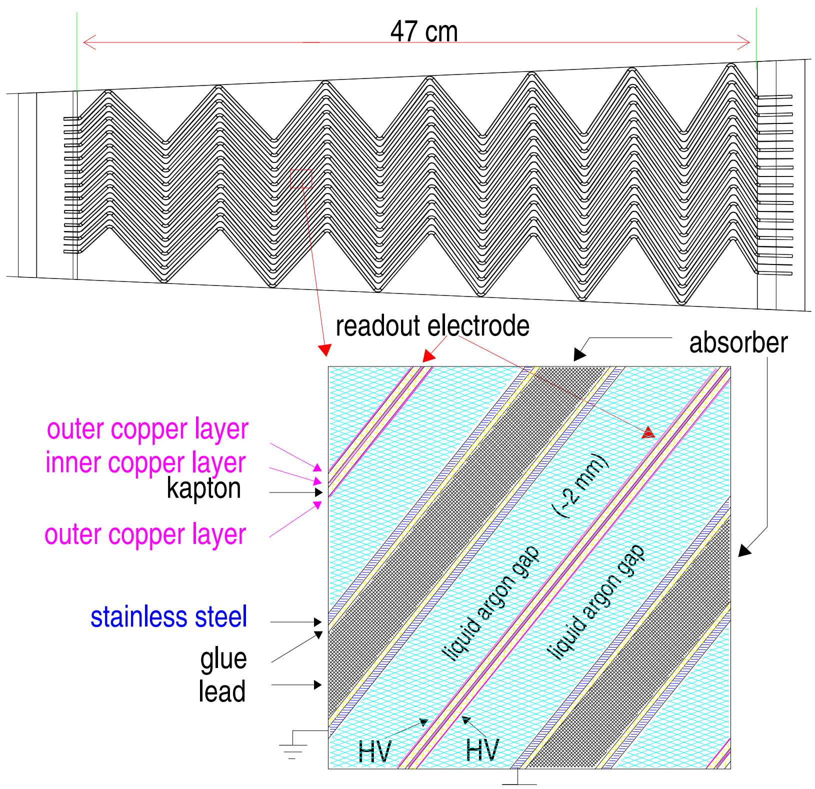

Figure 5.5: Accordion structure of the EM barrel calorimeter. The top figure is a view of a small sector of the barrel calorimeter in a plane transverse to the LHC beams.

For most of the EM calorimeter, EMB and EMEC-OW, each module has three layers in depth with different granularities, as can be seen in Fig. 5.7, while each EMEC-IW module has only two layers. The EM calorimeter is designed so that, for EM objects, the largest fraction of the energy

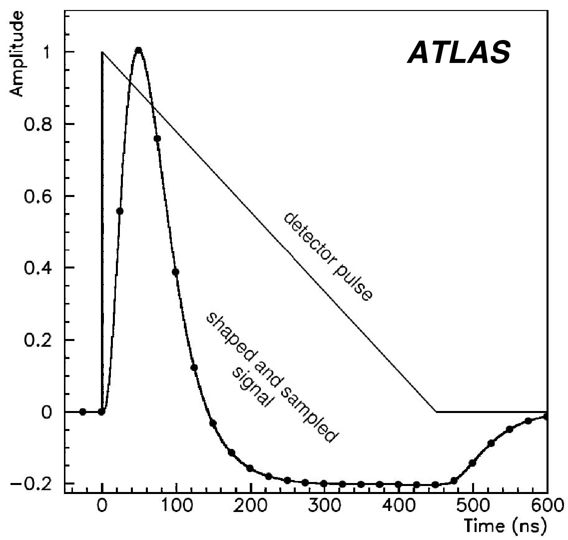

Figure 5.6: Shapes of the LAr calorimeter current pulse in the detector and of the signal output from the shaper chip. The dots indicate an ideal position of samples separated by 25 ns.

is collected in the second (middle) layer, while the back layer collects only the tail of EM showers. The first layer features strip cells with their long edges in the ϕ-direction.

The granularity of the cells in the EM calorimeter depends on the calorimeter layer and $|\eta|$. For most of the EMB (up to approximately $|\eta| = 1.4$) the cell sizes are as indicated in Fig. 5.7: the first layer cells have size $\Delta\eta \times \Delta\phi = 0.0031 \times 0.0245$, while the second layer has a granularity of 0.025×0.0245, and the back layer cells have a larger size of 0.05×0.0245. A similar arrangement is used for the rest of the η-coverage of the EM calorimeter. Using the energy measurement and position for all cells in all layers of the calorimeter contained in the shower, the incident particle energy can be reconstructed and, taking advantage of the fine segmentation of the strips, its direction and characteristics can be inferred. The fine segmentation is also extremely useful in the discrimination between photons and jets with a leading π^0 meson which primarily decays to two photons. In addition, with its novel projective tower geometry, the calorimeter can reconstruct the direction of neutral particles, such as photons, for which the ID cannot be used.

The hadronic calorimetry provided by the tile calorimeter is complemented by two parallel-plate copper/LAr hadronic endcap (HEC) calorimeters [67] that cover the region $1.5 < |\eta| < 3.2$, as well as modules in the forward calorimeter (FCal), described below. Each HEC consists of two independent wheels sharing the same cryostat as the EMEC and FCal modules. Each of the

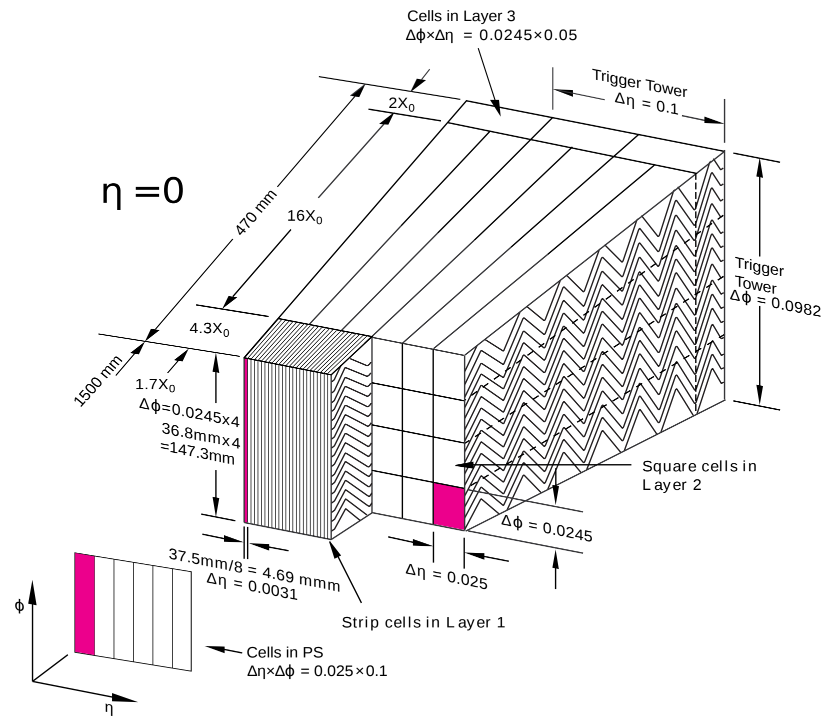

Figure 5.7: Sketch of an EMB section where the different layers are visible. The granularity in η and ϕ of the cells in each of the three layers and of the trigger towers is also shown.

HEC wheels comprises 32 wedge-shaped modules made of copper plates. The HEC wheel outer radius is 2.03 m while the inner radius is 372 mm for the first nine plates of the front wheels and 475 mm for the rest of the HEC. The gaps between the plates are kept at 8.5 mm and three electrodes divide the gap into four separate LAr drift zones of 1.8 mm width each. Readout cells are etched onto the central electrode, while the two other electrodes are kept at high voltage. The two wheels combined provide four longitudinal calorimeter layers with the cells arranged in a semi-projective geometry, with a granularity in $\Delta\eta \times \Delta\phi$ of 0.1×0.1 for $1.5 < |\eta| < 2.5$ and 0.2×0.2 for $2.5 < |\eta| < 3.2$.

The FCal [68] provides coverage over $3.1 < |\eta| < 4.9$. In order to withstand the high particle fluxes in this region, the FCal is based on a novel design that uses cylindrical electrodes consisting of rods positioned concentrically inside tubes parallel to the beam axis, supported by a metal matrix. Very narrow LAr gaps have been chosen to avoid ion buildup at high collision rates and the gap is kept constant with a winding fiber wrapped around the rods. Three cylindrical modules comprise the FCal; the module closest to the IP is optimized for EM measurements and uses mainly copper as absorber and has 269 μm gaps. The two subsequent modules are made mainly of tungsten and are optimized for hadronic measurements, with gaps of 375 and 500 μm, respectively.

5.3.1.1 LAr Calorimeter Readout

The ionization signals from all the LAr calorimeter cells are led outside the cryostats via 114 feedthroughs. Front End Boards (FEBs) [69], housed in crates mounted directly on the feedthroughs, receive the raw signals from up to 128 calorimeter channels, process, digitize and transmit samples via optical link (see Fig. 5.8) to the Back-End electronics housed outside the experimental cavern. The signal for each channel is split into three overlapping linear gain scales (Low, Medium and High) in the approximate ratio 1/9/80, in order to meet the large dynamic range requirements for the expected physics signals. For each gain, the triangular pulse is shaped (see Fig. 5.6) with a bipolar $CR-(RC)^2$ analog filter to optimize the signal-to-noise ratio. The shaped signals are then sampled at the LHC bunch-crossing frequency of 40 MHz and the samples for each gain are stored in a Switched Capacitor Array (SCA) analog memory buffer while waiting for a decision from the first level (L1) of the ATLAS trigger system (see Section 5.5). For events accepted by the L1 trigger, the optimal gain is selected for each channel, and the samples are digitized and transmitted. In 2011 and 2012, typically 5 samples were digitized for each pulse.

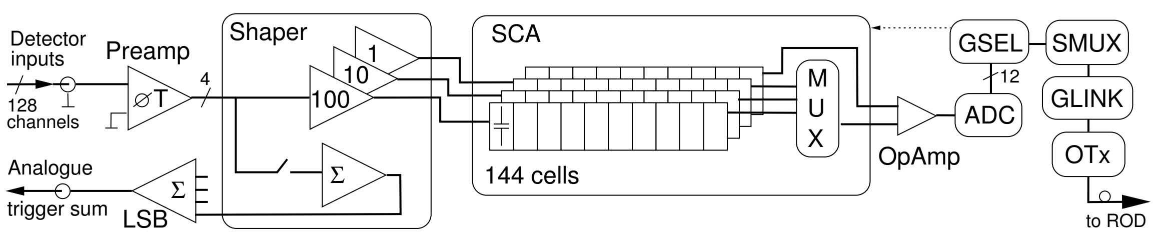

Figure 5.8: Block diagram of the FEB architecture, depicting the dataflow for four of the 128 channels.

In addition to the FEBs, the front end crates house several additional boards [70]. Tower Builder Boards facilitate the propagation of information to the trigger system and Calibration Boards allow the calibration of the electronics by injecting a known exponential pulse to simulate the LAr ionization signal. The calibration signals are then reconstructed through the regular readout chain. Finally, auxiliary boards perform service tasks such as clock distribution, communication and monitoring.

5.3.1.2 Cell Energy and Time Reconstruction

The optimal filtering [71] technique is used to reconstruct the cell energy and peaking time from the samples of a shaped calorimeter pulse. The procedure described here applies to all LAr subsystems, though it differs slightly in the case of the FCal. To calculate the cell energy, E_{cell} in MeV, from the samples s_j in ADC counts, the following formula is used:

$$E_{\text{cell}} = F_{\mu A \to MeV} \cdot F_{DAC \to \mu A} \cdot \frac{1}{\frac{M_{\text{phys}}}{M_{\text{cali}}}} \cdot R \sum_{j=1}^{N_{\text{samples}}} a_j \left(s_j - p \right) \tag{5.3}$$

while to calculate the time a similar formula is used:

$$t_{\text{cell}} = \frac{1}{E_{\text{cell}}} \sum_{j=1}^{N_{\text{samples}}} b_j \left(s_j - p \right) \tag{5.4}$$

where $F_{\mu A \to MeV}$ is a coefficient that is obtained from test beam studies and converts the ionization current values to energy values, $F_{DAC \to \mu A}$ is a property of the calibration board, and $\frac{M_{\text{phys}}}{M_{\text{cali}}}$ is a factor to correct for differences between the physics signal and calibration pulses. R is a factor obtained from calibration, converting the pulse ADC counts to counts of the DAC used to inject the calibration pulses, and p is the pedestal value (electronic baseline), also obtained from calibration. The parameters a_j and b_j are sets of Optimal Filtering Coefficients (OFC), calculated from the knowledge of the pulse shape and the noise autocorrelation function, to give the optimal energy and time resolution. Finally, a *Quality Factor*, Q^2, is calculated for each cell, as an estimate of the quality of the reconstructed pulse. The Quality Factor is similar in nature to a χ^2-value, measuring the difference between the reconstructed pulse shape and the expected physics pulse shape as predicted by the calibration.

5.3.2 The Tile Calorimeter

The tile calorimeter (TileCal) [72] is a sampling calorimeter employing steel as an absorber and scintillating plastic tiles as detecting medium. The TileCal is segmented in three barrel structures placed directly outside the EM calorimeter, with an inner radius of 2.2 m and an outer radius of

4.25 m. The central barrel is 5.8 m long and covers the region $|\eta| < 1.0$. Two extended barrels, each with a length of 2.8 m, cover the range $0.8 < |\eta| < 1.7$. Each barrel comprises 64 wedge-shaped modules in ϕ, each covering a sector with $\Delta\phi \sim 0.1$. As shown in Fig. 5.9, layers of interleaved trapezoidal absorber and scintillator tiles are stacked to form a module. The scintillation light is read by fibers on either side of the scintillator tile and led to photomultipliers housed on the outer radius of the module. The fibers are grouped together to create readout cells, segmenting the tile calorimeter in three layers in depth. The cells have dimensions $\Delta\eta \times \Delta\phi = 0.1 \times 0.1$ in the two innermost layers and 0.2×0.1 in the outer layer.

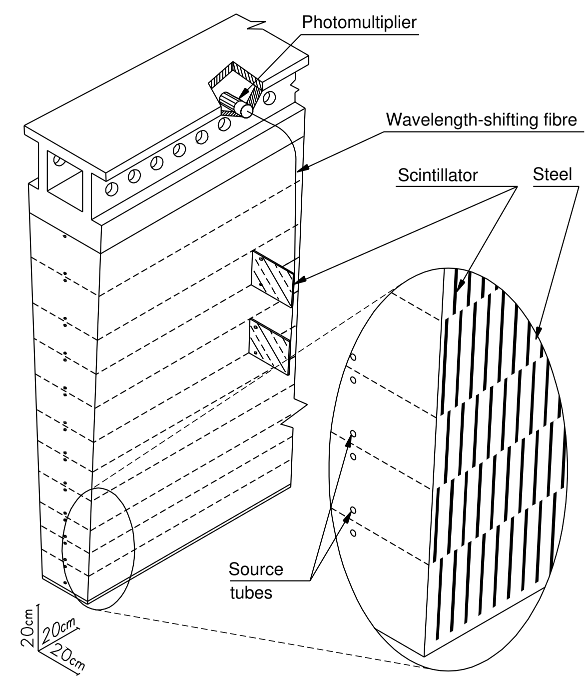

Figure 5.9: Mechanical assembly of a tile calorimeter module showing the absorber and scintillating tiles. The optical readout chain using wavelength-shifting fibers and photomultipliers is also shown.

5.4 Muon Spectrometer

The MS is the outermost subsystem of the ATLAS detector. Roles of the MS include the identification and reconstruction of muon tracks, and the measurement of their momenta, up to $|\eta| < 2.7$, as well as triggering on those events in the range $|\eta| < 2.4$. The MS is designed to measure muon transverse momenta with a resolution of approximately 10% for 1 TeV tracks, which translates into a sagitta along the beam axis of about 500 μm to be measured with a resolution better than 50 μm.

The MS consists of many muon chambers and a large air-core toroidal magnet system, as depicted in Fig. 5.10. The chambers are arranged in several layers: in the barrel, the chambers form three concentric cylindrical cells with approximate radii of 5 m, 7.5 m, and 10 m. In the endcaps, the chambers form large wheels, perpendicular to the beamline and located approximately at points with $|z| = 7.4$ m, 10.8 m, 14 m, and 21.5 m with respect to the IP. The magnet system comprises a toroid consisting of 8 separate coils in the barrel, and two smaller endcap toroids on either side of the detector.

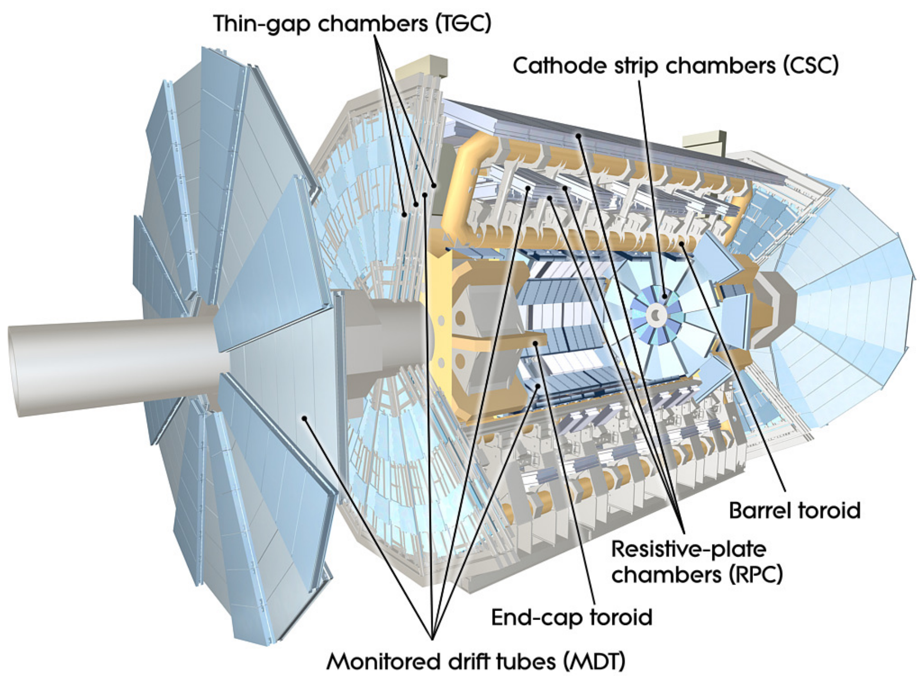

Figure 5.10: Muon instrumentation of the ATLAS experiment.

Four different chamber technologies are employed in the MS. For the high precision measurement of the muon trajectory, 1,150 Monitored Drift Tube (MDT) chambers are used up to $|\eta| < 2.0$ for inner layers and within $|\eta| < 2.4$ for outer layers. For triggering, 606 Resistive Plate Chambers (RPC) and 3,588 Thin Gap Chambers (TGC) are employed in the pseudorapidity ranges $|\eta| < 1.05$ and $1.05 < |\eta| < 2.4$, respectively. The inner barrel layer consists of MDT chambers which are positioned outside the calorimeters. In the middle barrel layer, MDT chambers are placed inside the magnet and are surrounded by two RPC trigger chambers on each side. Finally the third layer consists of MDT chambers paired with an RPC in the outer surface. In addition to providing trigger information, the RPC trigger chambers supply the measurement of the second coordinate of the particle tracks. The endcap scheme is different because it is not possible to install chambers inside the endcap toroids. The inner layers of endcap detectors are placed outside the magnets in the forward region with $2 < |\eta| < 2.7$, and feature 32 Cathode Strip Chambers (CSC) that cope with the higher counting rates. The middle and outer endcap layers consist of MDT chambers supported by TGC trigger chambers, placed on both sides of the middle MDT layer.

Depending on the radius and azimuth, the field provided by the magnets varies from 0.15 T to 2.5 T in the barrel region, and from 0.2 T to 3.5 T in the endcap region. While the magnetic field is highly non-uniform, a detailed magnetic modeling combined with readings by approximately 1,840 B–field sensors allow a high-precision mapping of the field. The field mapping provides bending power measurements with sufficient accuracy to meet the design performance goals.

5.5 Trigger and Data Acquisition

With the LHC operating at the nominal bunch crossing frequency of 40 MHz and at the design luminosity of 10^{34} cm^{-2}s^{-1}, approximately 10^9 interactions per second are expected. While this is desirable to be able to study rare processes, it is not tractable to record at these rates nor to store every event on disk. In ATLAS, the data recording rate is limited to approximately 200-400 Hz. Therefore a system is needed to intelligently select online on average only 1 in $\sim 2 \times 10^5$ bunch crossings, while maximizing the efficiency to record rare and potentially interesting processes for analysis offline. The event selection is accomplished in ATLAS by a trigger system with three successive levels. The first level is called *Level 1* (L1) and is implemented with custom-designed electronics. The two higher levels are named *Level 2* (L2) and *Event filter* (EF), and are collectively called the *High Level Trigger* (HLT). The HLT is implemented in software running on commercially available computing hardware. A block diagram of the trigger and data acquisition systems (TDAQ) is shown in figure 5.11.

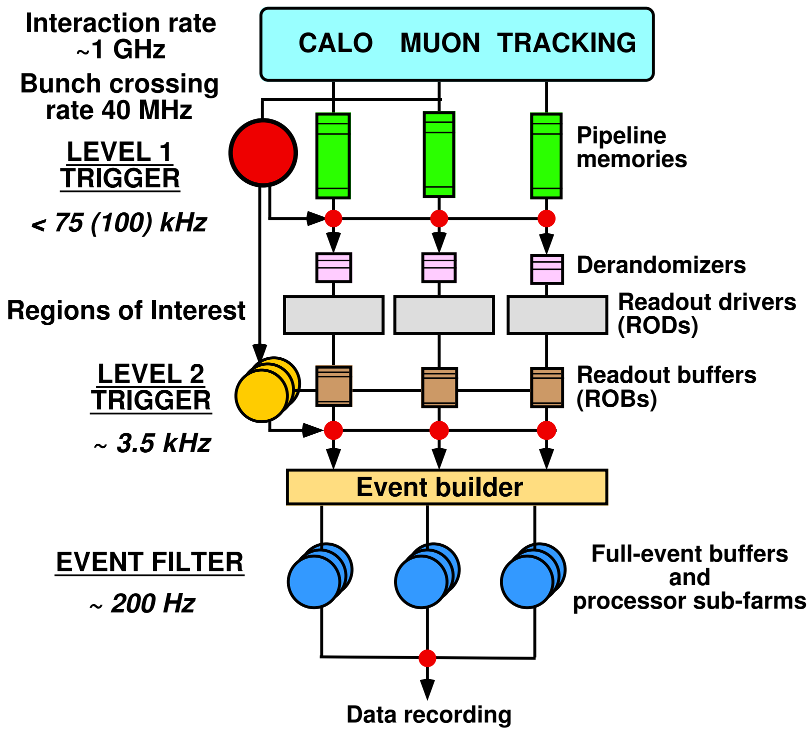

Figure 5.11: Block diagram of the ATLAS Trigger/DAQ system. For more details, see text.

The L1 trigger uses a subset of the available detector information to provide a decision within 2.5 μs, reducing the event rates to a maximum of 75 kHz. Due to the latency limitation, ID and precision muon tracking information is not used in the L1 decision. Instead, the main inputs for L1 come from calorimeter information (L1Calo) and information from the trigger chambers of the muon spectrometer (L1Muon). L1Calo uses energy deposits in all the calorimeters summed in *trigger towers* of typical size $\Delta\eta \times \Delta\phi = 0.1 \times 0.1$, whereas L1Muon employs the RPC and TGC trigger chambers. With these inputs, the L1 trigger searches for particular physics object signatures, such as electrons, photons, jets, τ-leptons decaying hadronically, and high-transverse momentum muons, as well as global event signatures, including large total transverse energy and $E_{\mathrm{T}}^{\mathrm{miss}}$. The *Central Trigger Processor* (CTP) receives the results from L1Calo and L1Muon and makes logical combinations of the decisions based on predefined trigger items that implement a "trigger menu". In the menu, certain trigger items can be configured to be *prescaled*, so that a programmable fraction of the events otherwise passing the selection is discarded at random in order to reduce the trigger rate.

Event information is typically stored in buffers on the detector specific front-end electronics while waiting for a L1 trigger decision. If an event is selected by L1, its information is propagated to the next stages of the front-end electronics and the entire event is read out via Readout Drivers (RODs) over optical links and fed to the DAQ system. The L1 trigger also composes geographical Regions-of-Interest (ROIs) in the detector, where interesting features had been identified, and combines it with information of those particular features. The ROIs are then propagated to the L2 trigger in parallel with the event data and subsequently used to seed the HLT selection process.

The L2 trigger operates with a latency of approximately 40 ms, during which time the event data is stored in Readout Buffers (ROBs). Using the ROIs identified by the L1 trigger, a subset (typically $\sim$ 2%) of the data is transfered to a L2–dedicated processor farm over a high-capacity network infrastructure. Dedicated algorithms run to further refine the event selection, using the full detector granularity, to reduce the selection rate to approximately 3.5 kHz. For events that pass at L2, the event fragments are built into events with the full detector information by the Event Builders and delivered to the EF. This final level of triggering runs high level analysis procedures, similar to offline analysis, on an additional dedicated processor farm to select events with the final recording rate of approximately 200 Hz. The selected events are subsequently stored on disk at the CERN computer center for offline physics analysis. The data is replicated to sites all over the world and processed using the Worldwide LHC Computing Grid [73].

5.6 Forward Detectors and Luminosity Measurement

In addition to the main detector systems described above, ATLAS uses additional smaller systems to provide coverage in the very forward region. LUCID (LUminosity measurement using Cerenkov Integrating Detector) is one of the primary luminosity detectors in ATLAS and consists of two Cerenkov radiation detectors located on either side of the detector at a distance of approximately 17 m from the IP and 10 cm from the beamline. The Zero Degree Calorimeter (ZDC) comprises two modules consisting of layers of alternating quartz rods and tungsten plates and located approximately at $z = \pm 140$ m. The main purpose of ZDC is to detect very forward neutrons ($|\eta| > 8.3$) in heavy-ion collisions. Finally, ALFA (Absolute Luminosity For ATLAS) consists of scintillating-fiber trackers installed very close to the beamline at positions with $z = \pm 240$ m, and measures the absolute luminosity by using elastically scattered protons at small angles.

Even though the ID, and ATLAS in general, has been designed to be able to withstand high levels of radiation during normal operation, it still has to be protected from accidental beam losses near the detector. If proton bunches hit any collimators near the detector, the enormous instantaneous rates can cause significant damage, especially for devices operating close to the beam. The Beam Conditions Monitor (BCM) system is responsible to detect such incidents and transmit the information to the LHC operators so that a beam-abort is triggered and serious damage avoided. The system consists of four modules on each side of the detector at positions $z = \pm 184$ cm and radial distance $R = 5.5$ cm, arranged symmetrically around the beam-pipe. Each module employs two radiation-hard diamond sensors and radiation-tolerant electronics. The modules measure bunch-by-bunch rates independently of the DAQ system and the BCM is also used in the determination of luminosity.

To determine the instantaneous luminosity and calculate the integrated luminosity, ATLAS uses several methods and algorithms, employing dedicated detectors as well as systems for which luminosity measurement is a secondary capability [74]. In 2011, the main detectors used in online luminosity measurements were LUCID and BCM. The currents in the tile calorimeter and the FCal were also used in independent offline calculations of the luminosity. Each detector has different characteristics with respect to acceptance, efficiency and systematic uncertainties, and the results from all the methods are cross-checked and compared in an effort to improve the final luminosity measurement. The different methods are calibrated using absolute luminosity measurements using beam characteristics during van der Meer scans (see Section 4.1).

The instantaneous luminosity varies during the course of an LHC fill and diminishes as the beam is gradually depleted. For this and other reasons, ATLAS runs are divided in *luminosity blocks* (LB), which are short periods of time during which the delivered instantaneous luminosity is considered constant. The begin and end times of each LB are controlled by the ATLAS online DAQ system, and their length was typically 1 or 2 minutes during the 2011 and 2012 data taking periods, respectively. After corrections are applied (for example for data loss due to DAQ dead time or trigger prescales), the total *recorded* integrated luminosity is calculated by summing the contributions from each LB. Fig. 5.12 shows the cumulative integrated luminosity as a function of time delivered and recorded by ATLAS for the 2011 and 2012 data taking periods. In total, during 2011, ATLAS recorded 5.08 fb^{-1} of pp collisions at 7 TeV while, during 2012, ATLAS recorded 21.3 fb^{-1} of pp collisions at 8 TeV.

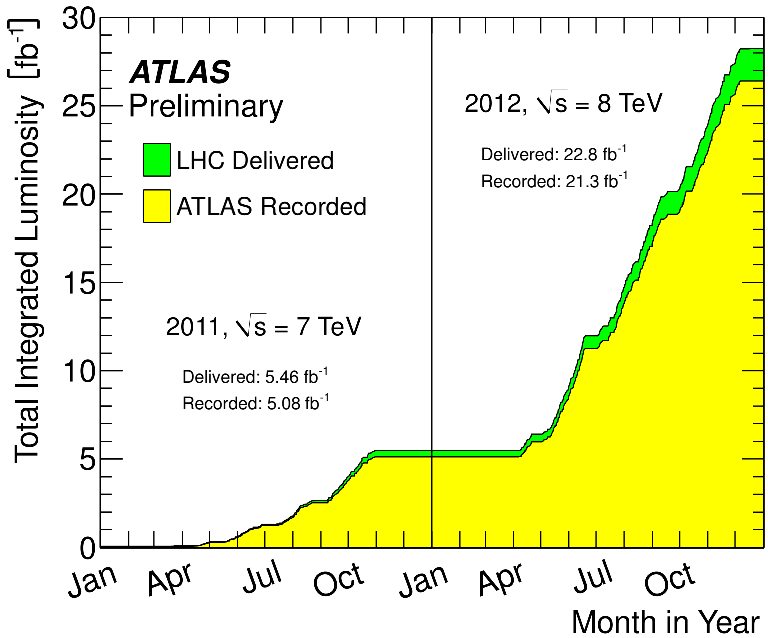

Figure 5.12: Cumulative integrated luminosity versus time delivered to (green) and recorded by ATLAS (yellow) during stable beams for pp collisions at 7 TeV and 8 TeV center-of-mass energy in 2011 and 2012, respectively.

Chapter 6

Physics Object Reconstruction and Identification

In this chapter, we define the various objects that are used to select events of interest. The objects considered are EM objects (photons and electrons, Section 6.1), muons (Section 6.2), and jets (Section 6.3). In addition, we consider the missing transverse energy ($E_{\mathrm{T}}^{\mathrm{miss}}$) of the event (Section 6.4).

6.1 Electron and Photon Reconstruction in ATLAS

Within the ATLAS detector, photons and electrons manifest as EM showers in the calorimeter system. Electrons and photons result in similar EM showers, which translates into similar reconstruction procedures in ATLAS for these two types of objects. In addition to producing an EM shower, electrons can also leave a track in the ID, a characteristic which is typically the main discriminating feature of electrons with respect to photons. However, photons can convert to electron-positron pairs as they interact with the detector material, creating an additional challenge in photon reconstruction and discrimination from electrons.

The LAr calorimeter system is designed so that the EM shower is contained within the EM calorimeter, with typically $\sim 80\%$ of the energy deposited in the middle layer. The reconstruction of electrons and photons therefore begins with the reconstruction of the associated EM showers, as described in Section 6.1.1. The fine segmentation of the LAr calorimeter provides valuable information on the shape and other characteristics of the EM showers, which is employed to obtain an excellent electron and photon identification efficiency and a high jet rejection rate over a broad energy range. Photon and electron reconstruction and identification procedures are described briefly in Sections 6.1.2 and 6.1.3 respectively, followed by the selection criteria applied to select photon and electron candidates in this analysis.

6.1.1 Electromagnetic Cluster Reconstruction

The EM showers that develop in the LAr calorimeter are reconstructed as EM clusters of calorimeter cells using the "sliding-window" algorithm [75]. In this algorithm, the EM calorimeter $\eta \times \phi$ space is divided into a matrix of elements with size $\Delta\eta \times \Delta\phi = 0.025 \times 0.025$ (the size of a cell in the middle EM calorimeter layer). A calorimeter *tower* per element is formed by summing the energies of the cells within that range in all the calorimeter layers. For energy depositions that span different cells, the energy is shared between the relevant towers. Then, a window of size 5×5 towers is moved across the grid to search for a local maximum of the sum of tower transverse energies, E_{T}, within the window. If the total E_{T} is above a certain threshold, a precluster is formed, to be used as a seed for the creation of a cluster. By calculating the barycenter using all the cells in a fixed 3×3 tower window around the central tower of the seed, the seed position in $\eta \times \phi$ space is calculated. A set of seeds is formed and any duplicates (if their position is the same within a 2×2 window) are removed by keeping the one with highest E_{T}.

The next step is to build EM clusters around the seeds by adding cells layer by layer. This is done by adding to the cluster all the cells in a window of size $N_{\eta}^{\mathrm{clus}} \times N_{\phi}^{\mathrm{clus}}$, centered around a position on the seed that depends on the layer. For the middle layer, which is the first to be processed, the centering position used is the seed barycenter calculated in the previous step. The barycenter in that layer is calculated using the cells covered by the window. This position is used as a centering position for the same procedure applied to the back and front layers. Finally, the barycenter in the strips is used as a centering position when the procedure is applied to the presampler layer. As a result of this procedure, a set of EM clusters of fixed size $N_{\eta}^{\mathrm{clus}} \times N_{\phi}^{\mathrm{clus}}$ is created, with the size depending on the particle hypothesized to have created the shower, as well as the location of the shower (barrel or endcap). As shown in Table 6.1, a wider cluster size in ϕ is used in the barrel for electrons and converted photons compared to unconverted photons, due to the bending of the electron/positron trajectory in the transverse plane caused by the solenoidal magnetic field.

Particle Type	$N_\eta^{\text{clus}} \times N_\phi^{\text{clus}}$	
	Barrel	**Endcap**
Electron	3×7	5×5
Converted photon	3×7	5×5
Unconverted photon	3×5	5×5

Table 6.1: Cluster sizes for different particle types in the barrel and endcap regions of the EM calorimeter.

The EM clusters contain a large fraction of the deposited energy for electron and photon candidates. However, some energy is not contained in the fixed-size cluster and some is lost upstream or downstream of the calorimeter, creating the need to apply corrections offline. Calibration constants are calculated from MC simulation as a function of η, energy and shower depth. The overall energy scale is set with reconstructed mass distributions from $Z \to ee$ events (see Fig. 6.1 for an example in the barrel) and cross-checked using the electron E/p distribution in $W \to e\nu$ events. The latter takes advantage of the independent measurements of the electron energy, E, in the calorimeter and its momentum, p, in the ID.

6.1.2 Photon Reconstruction and Identification

Photons are reconstructed in ATLAS as either converted or unconverted photons, as described in Ref. [76]. Converted photons are characterized by the presence of at least one track in the ID that matches the EM cluster in the calorimeter, resulting in an ambiguity in the distinction between converted photons and electrons. In addition, unconverted photons can also be reconstructed as electrons if their EM clusters are erroneously associated with tracks that typically have low momentum. For this reason, a procedure has been established to recover photon candidates from a collection of electron candidates, based on combined information from the ID and the calorimeter (number and momentum of matched tracks, number and position of hits in the ID, E/p ratio). In the calculation of the photon E_{T}, the energy is taken from the calibrated energy of the cluster [77]. If the photon is converted and has a track with more than 3 silicon hits the η measurement of the track is used, otherwise the η value as determined from the reconstruction of

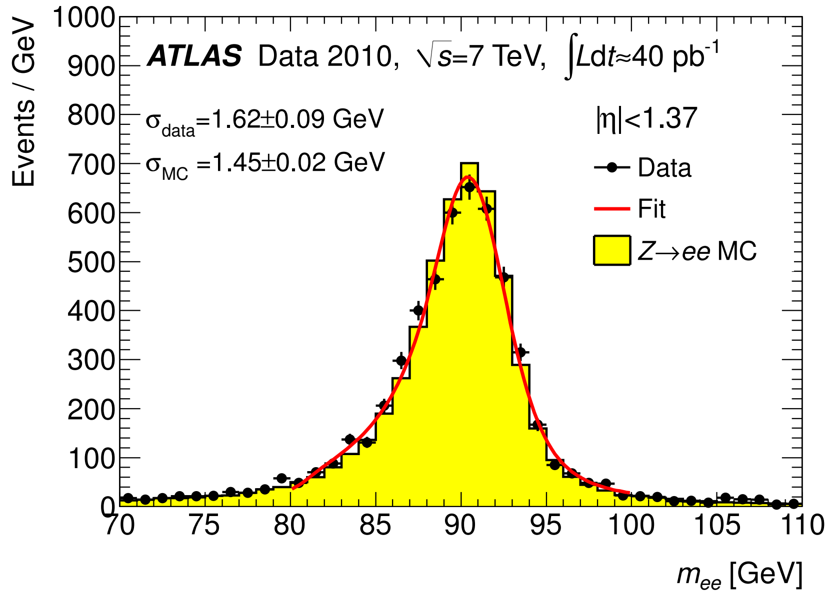

Figure 6.1: Reconstructed dielectron mass distribution for $Z \rightarrow ee$ decays for $|\eta| < 1.37$, and comparison to simulation.

the cluster direction in the calorimeter is used, as discussed later. Finally, the photon energy scale is corrected for data and MC as described in Ref. [78].

The fine granularity of the calorimeter is a significant asset, allowing the separation of photons from jets. As can be seen in Fig. 6.2, the shower shape for a photon is expected to have a narrower profile compared to the shower shape for a jet. For jets with a leading π^0 meson, a distinctive energy deposition with two energy maxima is expected in the first layer of the LAr calorimeter (strips). To efficiently reject background in analyses using photons, photon identification is performed with a cut-based method using the characteristics of their shower shape. Two reference sets of cuts, *loose* and *tight*, are defined. The former set of cuts has a very high efficiency with a modest jet rejection power, while the latter has a rejection power of approximately 5,000 while keeping a relatively high efficiency, approximately 85% for photons with $E_{\mathrm{T}} > 40$ GeV [79]. For the loose and tight categories, two different sets of selections based on the shape of the EM shower in the calorimeter are defined, as described in Table 6.2. The table indicates which shower shape discriminating variables (DVs) are used as part of the loose and tight definitions.

Fig. 6.3 [76] shows distributions obtained in simulation for photons (true photons) and jets

Category	Description	Name	loose	tight
Hadronic leakage	Ratio of E_{T} in the first sampling of the hadronic calorimeter to E_{T} of the EM cluster (used over the range $\lvert\eta\rvert < 0.8$ and $\lvert\eta\rvert > 1.37$)	R_{had1}	✓	✓
	Ratio of E_{T} in all the hadronic calorimeter to E_{T} of the EM cluster (used over the range $0.8 < \lvert\eta\rvert < 1.37$)	R_{had}	✓	✓
EM Middle layer	Ratio in η of cell energies in 3×7 versus 7×7 cells	R_{η}	✓	✓
	Lateral width of the shower	$w_{\eta 2}$	✓	✓
	Ratio in ϕ of cell energies in 3×3 and 3×7 cells	R_{ϕ}		✓
EM Strip layer	Shower width for three strips around maximum strip	w_{s3}		✓
	Total lateral shower width	w_{stot}		✓
	Fraction of energy outside core of three central strips but within seven strips	F_{side}		✓
	Difference between the energy associated with the second maximum in the strip layer, and the energy reconstructed in the strip with the minimal value found between the first and second maxima	ΔE		✓
	Ratio of the energy difference associated with the largest and second largest energy deposits over the sum of these energies	E_{ratio}		✓

Table 6.2: Shower shape discriminating variables used for the loose and tight photon definitions.

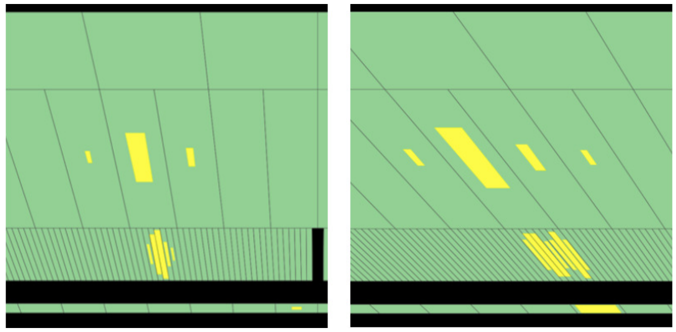

Figure 6.2: Shower shapes for a photon candidate (left) and a candidate for a jet with a leading π^0 (right), in data recorded in pp collisions.

reconstructed as photons (fake photons) in the unconverted and converted categories, before applying any identification requirements. Each individual plot in the figure shows, in overlay, the the mean values of one of the DVs used in photon identification as a function of $|\eta|$, for the two categories of true and fake photons. As can be seen from the distributions, the DVs provide significant separation between photons and jets faking photons across the entire η-coverage of the detector. It can further be concluded that cuts on the DVs can be optimized as a function of η and can be different according to the photon conversion status. Consequently, the DVs are studied in several bins in $|\eta|$. For example, Fig. 6.4 shows the normalized distributions for the DVs, obtained in simulation, for both true and fake photons reconstructed as unconverted photons with $|\eta| < 0.6$. For the purpose of photon identification, cuts parametrized in $|\eta|$ bins are determined from the DV distributions. The loose identification criteria only use cuts on the R_{had1} (or R_{had}), R_η, and $w_{\eta 2}$ DVs and make no distinction between unconverted and converted photons. The tight identification criteria employ all the DVs in Table 6.2 and, in general, have cuts that are more restrictive than the loose criteria. In addition, for the tight identification criteria, two different sets of cuts are used for unconverted and converted photons.

A series of criteria is applied in this analysis to select photon candidates. All photon candidates are required to have $E_{\mathrm{T}} > 50$ GeV and to satisfy at least the loose identification criteria. Photon candidates are required to have $|\eta_{s2}| < 2.37$, excluding the transition region of $1.37 < |\eta_{s2}| < 1.52$ between the barrel and endcap EM calorimeters, where η_{s2} is the η of the cluster in the second layer of the calorimeter, measured with respect to the IP. If a photon satisfies the loose identifica-

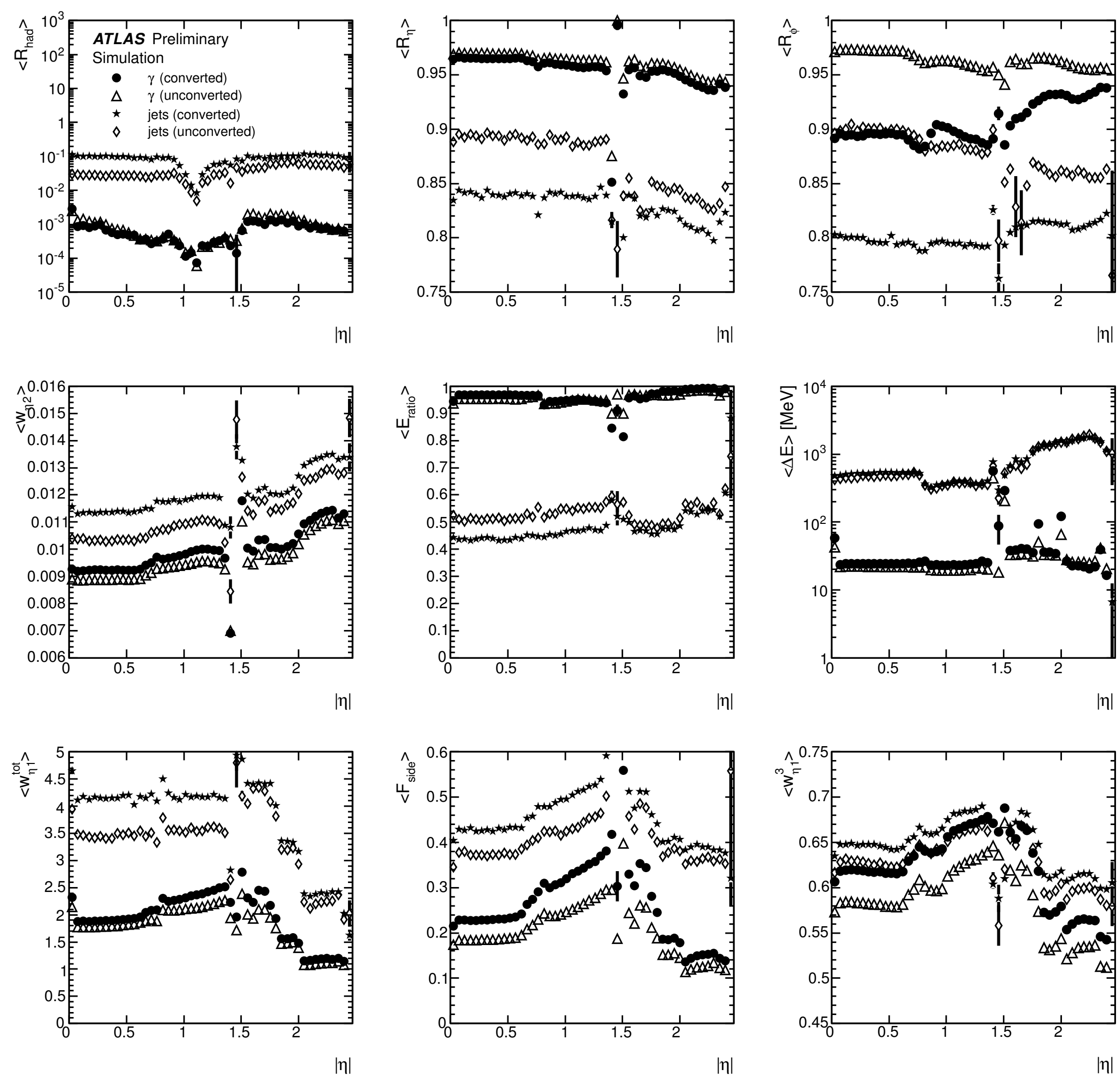

Figure 6.3: Distributions of the means of discriminating variables as a function of $|\eta|$, obtained from simulation, for true and fake photons with $E_{\mathrm{T}} > 20$ GeV, before applying any photon requirements.

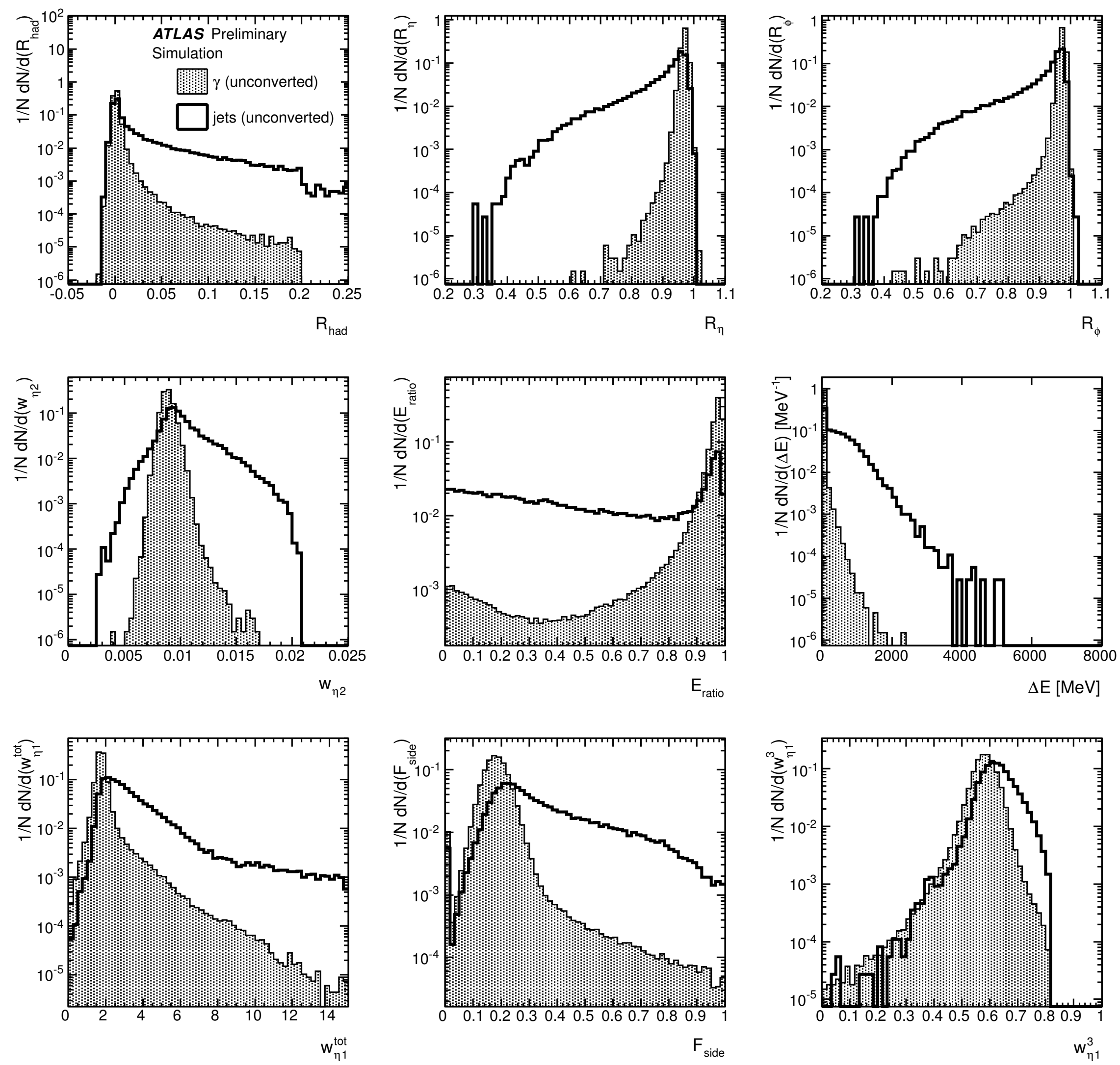

Figure 6.4: Normalized distributions of the discriminating variables in the region $0 < |\eta| < 0.6$ for $E_{\mathrm{T}} > 20$ GeV for true and fake photons reconstructed as unconverted, before applying any photon requirements.

tion criteria with the additional requirement that $|\eta_{s2}| < 1.37$, it is then designated as a "Loose" photon. If a photon satisfies the tight identification criteria, it is then designated as a "Tight" photon, without any further requirements on $|\eta_{s2}|$. If a photon is reconstructed as converted, in order to be designated as a Tight photon, it must not have any pixel hits associated with any associated track, in order to reduce the rate at which electrons are misidentified as converted photons.

The photon candidates are further required to be isolated in order to reduce fake photon contributions from jets. The transverse energy deposited in a cone of $\Delta R < 0.2$ around the photon candidate is required to be less than 5 GeV, following standard ATLAS recommendations [80]. In the calculation of the isolation variable, the photon cluster energy itself is subtracted and corrections for energy leakage and pileup are applied [81].

Additional object quality criteria have been established in ATLAS to remove photons and electrons with a cluster possibly affected by any detector issues [82]. The following requirements apply for the EM cluster associated with a photon candidate, with a similar set of requirements applied for electrons. The core of the photon cluster (defined as the 3×5 cells for unconverted photons, 3×7 cells for converted photons), should not overlap with a missing LAr calorimeter FEB in the first or second layer or a dead high-voltage (HV) region. In addition, it is required that there is a not a dead or disabled cell either in the core of the 3×3 cells cluster in the second layer or in the eight central strips in the first layer of the EM calorimeter. Further, EM clusters are checked for the quality of the LAr signal in the individual cells composing the cluster using the quality factor (Q-factor) for each cell. A photon is rejected if the value:

$$\frac{\sum_{\text{cluster}} E_{\text{cell}}(Q > 4000)}{\sum_{\text{cluster}} E_{\text{cell}}} > 0.8\% \tag{6.1}$$

and either the shower variables $R_\phi > 1.0$ or $R_\eta > 0.98$, as defined in Table 6.2.

Finally, a cluster time cut is applied to reduce the contribution from non-collision backgrounds such as cosmic rays. The photon candidate is therefore rejected if it has a cluster time $|t| > (10 + 2/|E_{\text{clus}}|)$ ns, where the cluster energy, E_{clus}, is measured in GeV.

6.1.3 Electron Reconstruction and Identification

Electrons are reconstructed in ATLAS primarily as EM clusters matched to ID tracks. Electron identification [83] is performed with a cut-based method similar to photon identification, and combines information from the shower shape characteristics in the calorimeter with the information from the ID, where available. Three reference sets of cuts have been defined with increasing background rejection power: *loose++*, *medium++* and *tight++*, with expected jet rejections of approximately 500, 5,000 and 50,000, respectively, based on MC simulation. The selection of shower shape variables used in the loose++ and tight++ definitions is similar to their photon counterparts, loose and tight, respectively, albeit with different cut values optimized for electrons [84].

Only electron candidates satisfying the medium++ identification criteria are considered in this analysis. The medium++ criteria impose requirements on the R_{had1}, R_{had}, R_{η}, w_2, w_{stot}, and E_{ratio} shower variables, with cuts parametrized according to the electron η and E_{T} values. In addition, requirements on the associated ID track are applied. The track is required to have transverse impact parameter $d_0 < 5$ mm and should match the EM cluster within $\Delta\eta < 0.005$. When calculating the p_{T} value of an electron, the energy is always taken to be from the calorimeter cluster, suitably calibrated [77], and the η value is taken from the matched track. The electron energy scale is corrected for data and smeared for Monte Carlo, as specified in Ref. [78].

The electron selection criteria used in this analysis in addition to the medium++ identification requirements are similar in nature to the photon selection criteria. Electrons are required to have $p_{\mathrm{T}} > 25$ GeV and should have $|\eta_{s2}| < 2.37$, excluding the region $1.37 < |\eta_{s2}| < 1.52$. The electrons must also be isolated, with the transverse energy deposited in a cone of $\Delta R < 0.2$ around the electron candidate required to be less than 5 GeV, calculated as described previously for photons. To remove electron candidates affected by any detector issues, it is required that neither the core of the electron cluster (defined as the 3×4 cells in the second layer) nor the cluster edge in the first or second sampling layer is read out by a dead LAr calorimeter FEB. In addition, the core of the electron cluster should not contain any dead HV region or disabled cells. Finally, electron candidates are rejected if $|t| > (10 + 2/|E_{\mathrm{clus}}|)$ ns, where E_{clus} is measured in GeV.

6.2 Muons

ATLAS uses various strategies to identify and reconstruct muons, in order to be sensitive to the broad spectrum of final-state muons produced at the LHC, with p_{T} ranging from a few GeV up to a few TeV. In conjunction with precise MS measurements, information from the ID as well as the calorimeter system is used to improve the muon identification efficiency and momentum resolution. More details on the muon reconstruction and identification can be found in Refs. [8, 85].

In this analysis, muons are not used in the definition of interesting events. However, muon candidates are used to reject events with indications of cosmic ray activity in the detector. Fairly loose requirements are therefore applied in order to ensure efficient identification of muons, translating to a high cosmic background rejection factor.

In ATLAS, four general muon categories are defined, according to what part of the available detector information and which strategy is used to reconstruct them: *Standalone* muons are reconstructed by finding tracks in the MS and extending them to the beam line. So-called *combined* muons are obtained by matching standalone muons to tracks in the ID, and then combining the ID and MS measurements. *Segment-tagged* muons are found by extrapolating ID tracks to the MS and searching for nearby track segments. Finally, *calorimeter–tagged* muons use the presence of a minimum ionizing signal in calorimeter cells to tag ID tracks.

Two distinct reconstruction chains are used to reconstruct muons of the above categories, each using a different set of reconstruction algorithms and resulting in two independent muon candidate collections per event. The two reconstruction chains and associated collections are named *STACO* [86] and *MUID* [87], named after the algorithm used in the reconstruction of combined-category muons. In each collection, special care is taken so as to avoid overlap between the different muon categories. For example, muon candidates that were successfully reconstructed as combined muons are removed from the standalone category.

Only muon candidates from the STACO collection are considered in this analysis. Muons are required to have $p_{\mathrm{T}} > 10$ GeV, with $|\eta| < 2.4$. Any muon candidate is required to satisfy the *loose* quality criteria, as defined by the muon combined performance group [88]. Muon candidates are required to be either combined or segment-tagged muons and should have an associated track in the ID. The ID track must have a B-layer pixel hit, unless it traverses a dead B-layer module.

Further, the sum of the number of pixel hits and crossed dead pixel sensors must be greater than one, while the sum of the number of SCT hits and crossed dead SCT sensors must be at least six. In addition, the sum of the number of crossed dead pixel and SCT modules must be less than three. Finally, if the ID track is within the TRT acceptance ($|\eta| < 2$), the TRT extension of the track is required to satisfy the following:

- Let $n = n_{\text{TRT}}^{\text{hits}} + n_{\text{TRT}}^{\text{outliers}}$, where $n_{\text{TRT}}^{\text{hits}}$ is the number of hits in the TRT that can be associated with the extension and $n_{\text{TRT}}^{\text{outliers}}$ is the number of TRT hits that are in the vicinity of the track but are not crossed by the track or fail to form a smooth track measurement in association with the pixel and SCT measurements.
- Case 1: $|\eta| < 1.9$. Require $n > 5$ and $n_{\text{TRT}}^{\text{outliers}} < 0.9n$.
- Case 2: $|\eta| \geq 1.9$. If $n > 5$, then require $n_{\text{TRT}}^{\text{outliers}} < 0.9n$.

The requirements described above apply for muon identification for the purpose of rejecting events with cosmic muons, as described later. However, any muons in the event are also used in the calculation of the event missing energy, with different identification requirements, as discussed later.

6.3 Jets

By the term *"jets"*, we are referring to the collimated sprays of energetic particles that are typical in high energy particle collisions. In ATLAS, jets are primarily detected by large localized energy depositions in the calorimeter system, which are usually associated with multiple tracks in the ID. As a consequence, the basic ingredients to reconstruct jets are three-dimensional topological calorimeter clusters, known as *TopoClusters*.

6.3.1 Topological Clustering

TopoClusters [75] are formed in the calorimeters by grouping calorimeter energy deposits according to their significance with respect to the noise. Unlike the EM clusters created with the sliding window algorithm discussed before, TopoClusters do not have a fixed size. The algorithm starts by searching for seed cells around which the TopoCluster is built. Cells are considered as seeds if they satisfy $|E_{\text{cell}}|/\sigma_{\text{cell}}^{\text{noise}} > 4$, where $\sigma_{\text{cell}}^{\text{noise}}$ is the total cell-by-cell noise, including contributions from electronics noise and pileup. Each cluster grows by iteratively adding neighboring cells if they satisfy $|E_{\text{cell}}|/\sigma_{\text{cell}}^{\text{noise}} > 2$. At the last step, all the cells immediately adjacent to the created clusters are added, regardless of their significance. This strategy is efficient in finding low energy clusters, while effectively suppressing the calorimeter noise. Finally, the TopoCluster energy is defined to be the sum of the energies of all the included calorimeter cells, while its direction in $\eta - \phi$ is calculated by the sum of the individual cell positions, weighted by their energy.

6.3.2 Jet Reconstruction

Several algorithms exist and can be used for the reconstruction of jets in a hadron collider. In this analysis, the anti-k_t jet algorithm [89] is used, which belongs to the *sequential recombination* family of jet reconstruction algorithms. These algorithms operate iteratively on a set of provided jet constituents (in this case, TopoClusters) to merge them pairwise or declare them as jets, according to certain criteria. An abstract distance measure d_{ij} is introduced which, in the case of the anti-k_t algorithm, is defined as:

$$d_{ij} \equiv \min\left(\frac{1}{p_{\text{T},i}^2}, \frac{1}{p_{\text{T},j}^2}\right)\frac{\Delta\eta_{ij}^2 + \Delta\phi_{ij}^2}{R^2} \tag{6.2}$$

where R is the four-momentum recombination and distance parameter, controlling the size of the jets in $\eta - \phi$ space. In this analysis, jets with $R = 0.4$ are used. In addition, the distance of constituent i with respect to the beam is defined as:

$$d_{i\text{B}} \equiv \frac{1}{p_{\text{T},i}^2}. \tag{6.3}$$

On every iteration, the list of all distances d_{ij} and $d_{i\text{B}}$ is calculated and sorted. If the minimum distance is a d_{ij} the two constituents i and j are merged and replaced in the set by their combined constituent. If the minimum distance is a $d_{i\text{B}}$, the constituent i is called a jet and is removed from the set. The procedure is repeated on the updated set of constituents until empty and all the jets are found.

The jet energy measured in the calorimeter has to be calibrated so that it reflects the energy of the initiating parton. Due to the non-compensating nature of the ATLAS calorimeters, the calorimeter energy response is lower for hadronic compared to EM showers of the same energy. In addition, some energy can be lost in non-active regions or escape the calorimeters. Finally, some energy may not be contained in the calorimeter clusters or may not be included during the reconstruction of the jet. Several calibration methods are used by ATLAS to correct the *Jet Energy Scale* (JES). Jets in this analysis are calibrated using the so called *EM+JES* scheme [90, 91], which is the simplest mode of jet calibration used by ATLAS. In this scheme, the jet energy is measured at the EM scale and then a scale factor is applied to obtain the jet energy. The scale factor is derived from simulation and depends on the energy of the jet at the EM scale as well as its direction. Jets are considered in this analysis if they have a calibrated transverse momentum $p_{\mathrm{T}}^{\mathrm{EM+JES}} > 20$ GeV. For the jets considered, the JES uncertainty is at the level of $1-4\%$ [90] depending on the p_{T} and η of the jet.

Jets are only used in this analysis to establish whether an event has indications of cosmic activity or is affected by any detector issues. The *Very Loose* set of standard ATLAS jet requirements [92, 93] is applied to the selected jet candidates, and the event is rejected if at least one jet candidate is classified as "bad". The criteria employ discriminating variables such as the fraction of the jet energy in individual subsystems, as well as estimators of the quality of the jet using the Q-factor of the cells composing the cluster associated with the jet.

6.4 Missing Transverse Energy

Even though energy and momentum are conserved in a pp collision, it is not possible to determine the momentum exchange between the partons in the direction of the beam. However, since the colliding protons have no momentum in the transverse direction before the collision, the vectorial sum of the transverse momenta of all the particles produced in the collision is expected to vanish. The negative of the vector obtained by the component sum of all particle momenta in the transverse plane is the *missing transverse momentum* and its magnitude is called the *missing transverse energy* ($E_{\mathrm{T}}^{\mathrm{miss}}$). The existence of missing transverse energy is usually used as an indication of a particle (or particles) that has escaped without detection. However, there can also be contributions to $E_{\mathrm{T}}^{\mathrm{miss}}$ from instrumental effects, energy mis-calibration, or due to limitations in the coverage of the detector.

In general in ATLAS, $E_{\mathrm{T}}^{\mathrm{miss}}$ is constructed from energy depositions in the calorimeters, taking into account losses in dead material (DM) and including contributions from any muons summed in components, using the following:

$$\begin{aligned} E_{\mathrm{T}}^{\mathrm{miss}} &\equiv \sqrt{\left(E_{\mathrm{x}}^{\mathrm{miss}}\right)^2 + \left(E_{\mathrm{y}}^{\mathrm{miss}}\right)^2} \\ E_{\mathrm{x(y)}}^{\mathrm{miss}} &\equiv E_{\mathrm{x(y)}}^{\mathrm{miss}}\Big|_{\mathrm{calo}} + E_{\mathrm{x(y)}}^{\mathrm{miss}}\Big|_{\mathrm{DM}} + E_{\mathrm{x(y)}}^{\mathrm{miss}}\Big|_{\mu} \end{aligned} \tag{6.4}$$

The contribution from the calorimeter can be calibrated in several ways to set the measured energy scale. As a result, several $E_{\mathrm{T}}^{\mathrm{miss}}$ flavors are available in ATLAS for use in physics analysis. In this analysis, the *LocHadTopo* flavor is used, which employs the Local Hadron Calibration (LCW) [94] scheme to calibrate the calorimeter contribution to the missing energy determined from the set of TopoClusters reconstructed in the calorimeters. In this scheme, each TopoCluster is classified as EM-like or hadronic-like, using the characteristics of the cluster shape. Different calibration weights, based on MC simulation, are applied to each cluster according to its classification. The calibration weights include corrections for energy lost in dead material as well as energy not contained in the cluster. The sum of the energies deposited in calorimeter cells associated with TopoClusters up to $|\eta| = 4.5$ is calculated in x and y components. The respective components of the missing transverse energy in the calorimeters, including the DM components, are calculated from the corrected cell energies using Eq. 6.5.

$$\begin{aligned} E_{\mathrm{x}}^{\mathrm{miss}}\Big|_{\mathrm{calo+DM}} &\equiv -\sum_{i=1}^{N_{\mathrm{cell}}} E_i^{\mathrm{cell}} \sin\theta_i \cos\phi_i \\ E_{\mathrm{y}}^{\mathrm{miss}}\Big|_{\mathrm{calo+DM}} &\equiv -\sum_{i=1}^{N_{\mathrm{cell}}} E_i^{\mathrm{cell}} \sin\theta_i \sin\phi_i \ . \end{aligned} \tag{6.5}$$

For the muon contribution, only good quality muon candidates with $|\eta| < 2.7$ from the STACO collection are used [95]. To reduce contributions from fake muons, muon candidates in the pseudorapidity range covered by the ID ($|\eta| < 2.5$) are required to be combined muons, while standalone muons are used for $2.5 < |\eta| < 2.7$. The transverse momenta of all the muons considered are added to obtain the muon contribution. The p_{T} measurement considered depends on the category (combined/standalone) and isolation of the muon candidate. For the purposes of this calculation, a muon is considered isolated if it does not overlap with any jet within a cone with $\Delta R < 0.3$. For isolated combined muons, the combined MS and ID p_{T} measurement is used, subtracting a term for any ionization energy deposited in the calorimeters, to avoid double counting the calorimeter contribution. For a non-isolated combined muon, the standalone MS measurement for the p_{T} is used, unless there is a significant mis-match between the p_{T} measurements in the MS and ID. In that case, the combined measurement is used and an estimation of the muon energy loss in the calorimeter is subtracted. Finally, for standalone muons, the MS p_{T} measurement is used, regardless of muon isolation.

A frequently used measure of the performance of the $E_{\mathrm{T}}^{\mathrm{miss}}$ calculation is the $E_{\mathrm{T}}^{\mathrm{miss}}$ resolution. The resolution is often parametrized in terms of the total transverse energy of the event using the function

$$\sigma = k \cdot \sqrt{\Sigma E_{\mathrm{T}}} \quad . \tag{6.6}$$

Fig. 6.5 shows the $E_{\mathrm{T}}^{\mathrm{miss}}$ component resolution as a function of the total transverse energy in the event for $Z \to ee$ and $Z \to \mu\mu$ events in 2011 data, where the fit to the expected form of the $E_{\mathrm{T}}^{\mathrm{miss}}$ resolution yields $k = 0.66\ \mathrm{GeV}^{1/2}$ and $k = 0.67\ \mathrm{GeV}^{1/2}$, respectively [96].

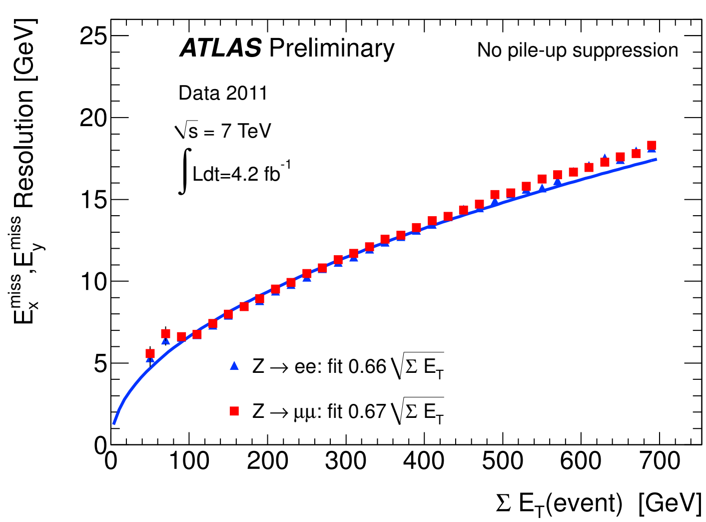

Figure 6.5: $E_{\mathrm{x}}^{\mathrm{miss}}$ and $E_{\mathrm{y}}^{\mathrm{miss}}$ resolution as a function of the total transverse energy in the event. Only the fit for the $Z \to ee$ channel is shown.

6.5 Overlap Removal

Occasionally, the different object reconstruction algorithms can reconstruct different objects sharing the same cluster. In order to prevent double counting, overlap removal rules are applied for each event after the initial object selection, as described below.

First, a check for overlaps between electron and photon candidates is performed. If the clusters of a photon and an electron are found within $\Delta R < 0.01$, the object is interpreted as an electron and the photon is removed from the list of photon candidates. At the next step, jet candidates are checked against the list of electron, photon and muon candidates. If a jet and an electron are found within $\Delta R < 0.2$, the object is interpreted as an electron and the overlapping jet is removed from the event. Similarly, if a jet and a photon are found within $\Delta R < 0.2$, the object is interpreted as a photon and the overlapping jet is removed from the event. If, instead, a jet and an electron or a photon are found within $0.2 < \Delta R < 0.4$, the object is interpreted as a jet and the electron or photon is removed. Finally, if a jet and a muon are found within $\Delta R < 0.4$, the object is interpreted as a jet and the muon is removed. After the overlap removal steps have been completed, the resulting lists of physics object candidates are used in the event selection and calculation of event observables.

Chapter 7

Calorimeter Pointing and Timing

In this chapter, the performance of the LAr calorimeter pointing and timing is discussed. Section 7.1 describes how the direction of EM clusters is determined in general using the EM calorimeter. The relevant variables employed in this analysis are also defined. Section 7.2 discusses the modeling of the pointing performance in simulation and its behavior for non-pointing photons. In Section 7.3, the timing measurement and the calibration procedure used to optimize it are briefly discussed.

7.1 Pointing Measurement

As discussed previsouly, the LAr EM calorimeter is divided, for most of its $|\eta|$ coverage, in three layers in depth. In addition to providing separation between photons and jets, the fine segmentation of the EM calorimeter front layer (strips) allows, in conjunction with the middle layer, for the measurement of the direction of photons.

As shown in Fig. 7.1, the photon direction can be determined by measuring precisely the lateral and the longitudinal positions of the shower in the front and middle layers of the EM calorimeter. The diagram demonstrates the case of a non-pointing photon reconstructed in the EMB, where the angles and dimensions are exaggerated for clarity. From the measurements of the positions of the two barycenters, one can obtain the photon direction in η. Dividing by the lever arm, the z coordinate of the photon at its distance-of-closest-approach to the beamline ($x = y = 0$) is obtained using the equation

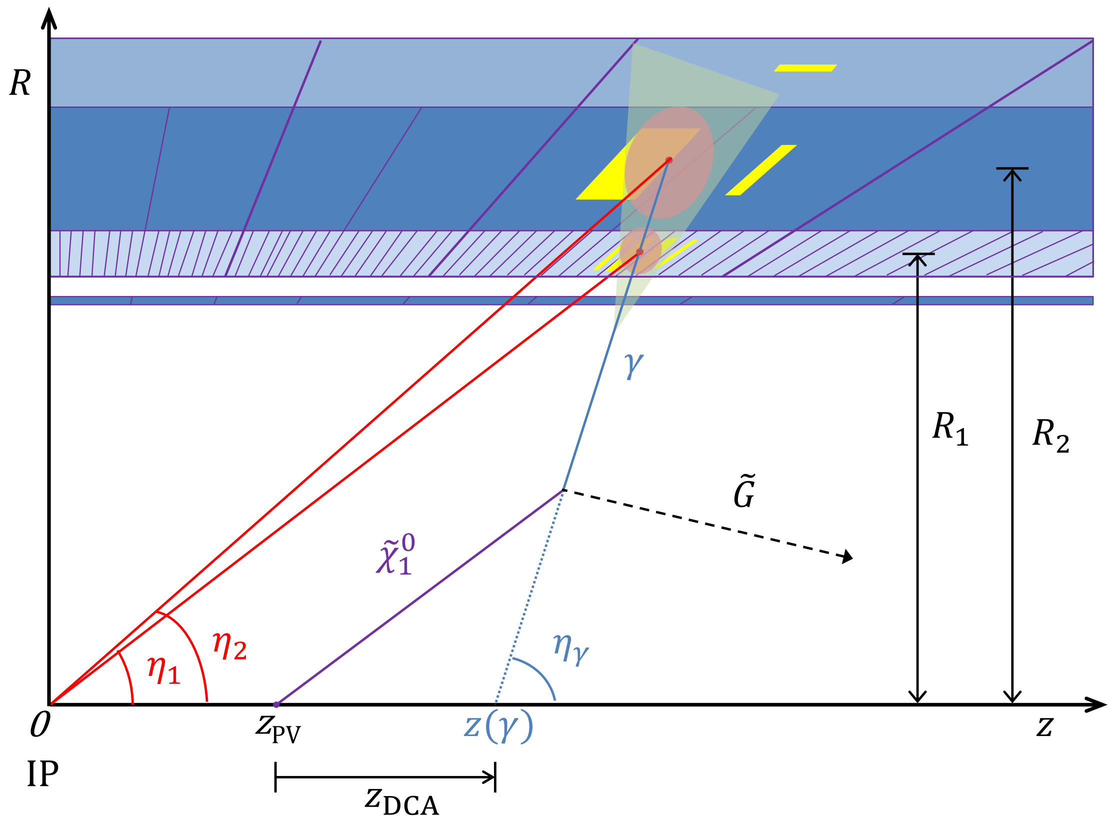

Figure 7.1: Schematic (not to scale) demonstrating the principle for measuring the direction of a photon in the EM barrel calorimeter. The diagram shows the case of a non-pointing photon due to a long-lived $\tilde{\chi}_1^0$ decay to a photon and a Gravitino in a GMSB scenario. The three layers of the EM calorimeter and the presampler are represented by the blue rectangles, while the hatching demonstrates the projective geometry of the calorimeter and the relative sizes of the cells in each layer. The relevant angles and distances used in the measurement of the photon direction are also shown. For more details, see the text.

$$z(\gamma) = \frac{R_1 R_2}{R_2 - R_1}(\sinh \eta_1 - \sinh \eta_2) \tag{7.1}$$

where $z(\gamma)$ is given with respect to the IP ($x = y = z = 0$). Similarly, η_1 and η_2 are the pseudorapidities of the cluster barycenters in the front and middle layers, respectively, calculated with respect to the center of the detector. The radial distances R_1 and R_2 are η- and layer-dependent depth calculations for the cluster barycenters in the front and middle layers, respectively. The longitudinal segmentation of the EM calorimeter layers is not sufficiently fine for a precise measurement of the depth and, therefore, the depths of the barycenters are determined from a parametrization obtained in test-beam and simulation studies.

The calorimeter angular resolution obtained in this way is of the order of 60 mrad/$\sqrt{\mathrm{E}}$ [8], where E is measured in GeV, corresponding in the EMB to a resolution on $z(\gamma)$ of order 15 mm for photons with typical energies in the range of 50 – 100 GeV. Given the geometry, the $z(\gamma)$ resolution is worse in the endcaps, so the use of pointing was restricted in this analysis to photon candidates in the EMB.

The LHC collision region exhibits a finite spread along the beamline. Fig. 7.2 shows an example distribution of the z position of PVs obtained in May 2011 [97]. The typical mean value and width of the z position of the PV (z_{PV}) were observed to be approximately −5 mm and 60 mm, respectively. The spread of the position of the PV is much larger than the intrinsic resolution of the ID. As can be seen in Fig. 7.3, the measured ID resolution for the z-position of the PV is better than $\sim$ 0.2 mm, for vertices with more than 5 associated tracks [98, 99]. In the ATLAS $H \rightarrow \gamma\gamma$ analysis that contributed to the discovery of the Higgs boson [12, 13], calorimeter pointing was used to help choose the PV from which the two photons originated, thereby improving the diphoton invariant mass resolution and sensitivity of the search. The analysis described in this thesis uses the measurement of the photon flight direction to search for photons that do not point back to the PV, and therefore $z(\gamma)$ is corrected for the position of the PV. Henceforth, the main pointing variable used in this analysis, z at the distance-of-closest approach (z_{DCA}), will be defined as:

$$z_{\mathrm{DCA}} = z(\gamma) - z_{\mathrm{PV}} \quad . \tag{7.2}$$

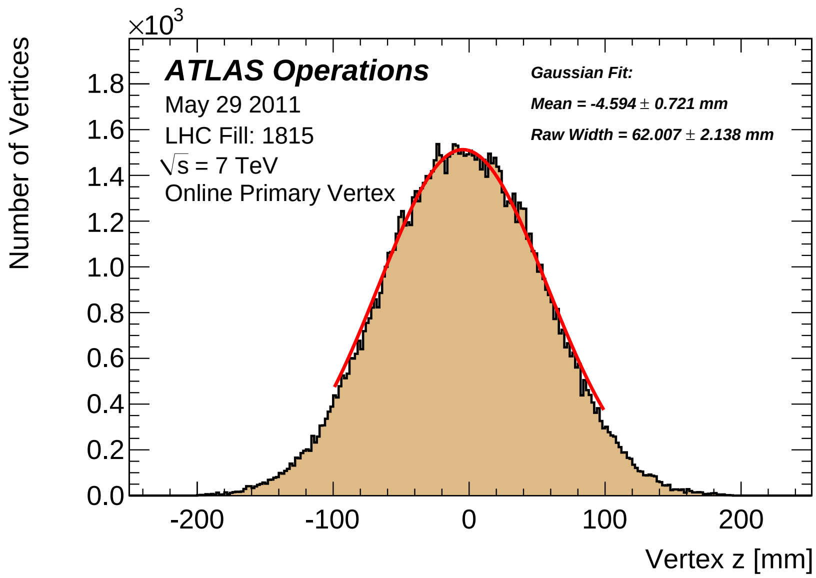

Figure 7.2: Longitudinal distribution of primary vertices reconstructed online in the HLT. The distribution corresponds to 1 minute of data taking. The mean of the distribution reflects the luminous centroid position, while its width shows the luminous length, which is much larger than the intrinsic resolution of the ID.

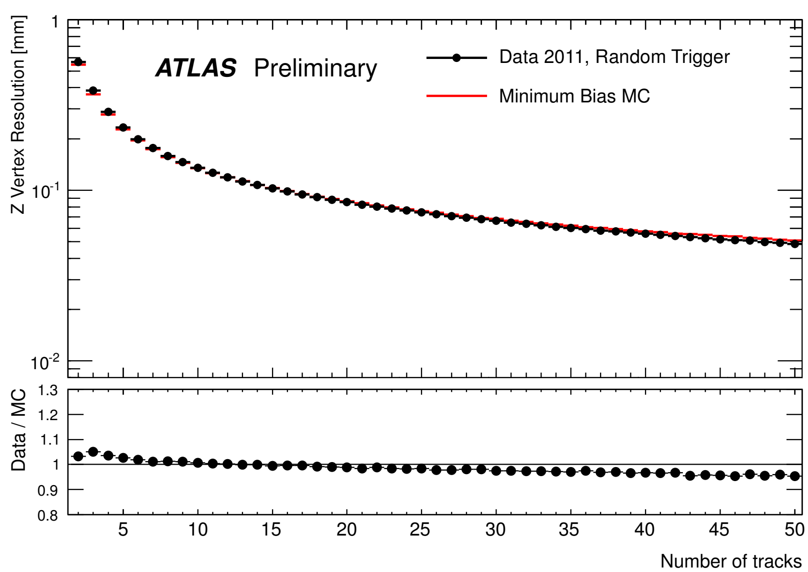

Figure 7.3: Estimated ID vertex z-position resolution, σ_z, in 7 TeV data from 2011 as a function of the number of tracks per vertex.

7.2 Pointing Resolution

Even though the geometry of the EM calorimeter has been optimized for the case of photons which point back to the nominal center of the detector, the fine segmentation allows reasonable angular precision to be achieved over a wide range of photon impact angles. This fact is demonstrated in Fig. 7.4 which shows, as a function of $|z_{\text{DCA}}|$, the expected pointing resolution for simulated signal photons from SPS8 MC. The pointing resolution is obtained by fitting to a Gaussian the difference between the value of z_{DCA} from the calorimeter measurement and the MC generator–level information. As can be seen, while the pointing resolution degrades with increasing $|z_{\text{DCA}}|$, it remains small compared to $|z_{\text{DCA}}|$ over a large range of $|z_{\text{DCA}}|$ values.

The determination of the EM cluster direction using the calorimeter is very useful in the case of photons, which leave no track in the ID. However, the method can readily be used in an independent measurement of the direction of electrons. Using the method described previously, the electron direction in η can be determined, as well as its point of origin along the beamline, $z(e)$. In order to get a source of non-pointing EM clusters in data, the finite spread of the LHC collision region along the beamline is exploited in $Z \rightarrow ee$ events. Superimposed on Fig. 7.4 is the pointing resolution as a function of $|z_{\text{DCA}}|$ obtained using electrons from $Z \rightarrow ee$ events, where z_{PV} serves the role of z_{DCA}. In this case the measure of the resolution is obtained by fitting a Gaussian to the difference between z_{PV}, as determined with high precision from the ID, and the calorimeter measurement of $z(e)$. Fig. 7.4 shows that a very similar pointing performance is observed for photons and for electrons, as expected given their very similar EM shower developments. This similarity allows the pointing performance for prompt photons to be determined from data, using a sample of electrons from $Z \rightarrow ee$ events, as will be discussed in Section 10.2. Also shown superimposed on Fig. 7.4 is the expected pointing performance for electrons in a simulated MC sample of $Z \rightarrow ee$ events, determined in the same way as the data sample. The level of agreement between the data and MC over the $|z_{\text{DCA}}|$ values that can be accessed gives confidence that the pointing performance behavior can be extrapolated with MC to the high $|z_{\text{DCA}}|$ values expected for signal photons.

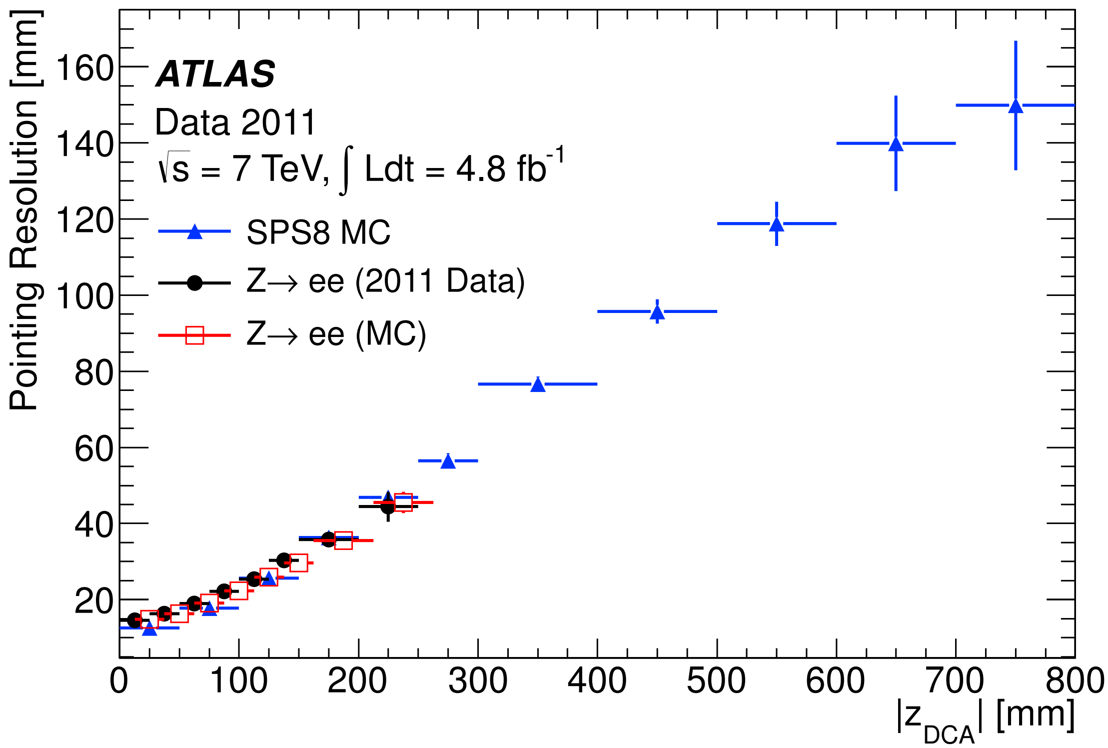

Figure 7.4: Pointing resolution obtained for EM showers in the ATLAS LAr EM barrel calorimeter. The pointing resolution for photons from GMSB signal MC samples is plotted as a function of $|z_{\mathrm{DCA}}|$. The pointing resolution is also shown for $Z \rightarrow ee$ data and MC, for which the primary vertex position, z_{PV}, serves the role of z_{DCA}.

7.3 Timing Performance

The time and energy for each cell that constitutes an EM cluster in the LAr calorimeter are calculated using the Optimal Filtering technique as described previously. The time resolution, $\sigma(t)$, is expected to follow the form

$$\sigma(t) = \frac{a}{E} \oplus b \quad , \tag{7.3}$$

where E is the energy measured in GeV and $\oplus$ indicates addition in quadrature. The coefficients a and b multiply the so-called noise term and constant term, respectively.

For this analysis, the EM cluster time is defined as the time of the cell in the second EM calorimeter layer with the maximum energy deposit. The EM calorimeter, with its novel accordion design, and its readout, which incorporates fast shaping, has excellent timing performance. Quality control tests during production of the electronics required the clock jitter on the LAr FEBs to be less than 20 ps, with typical values of 10 ps [69]. Calibration tests of the overall electronic readout performed *in situ* in the ATLAS cavern show a timing resolution of $\sim$70 ps [100], limited not by the readout but by the jitter of the calibration pulse injection system. Test-beam measurements [101] of production EMB modules demonstrated a time resolution of $\sim$ 100 ps in response to high energy electrons.

During 2011, the various LAr channels were timed in online with a precision of order 1 ns. Extracting the ultimate timing performance requires that a careful calibration process [4] be determined and subsequently applied. A large sample of $W \rightarrow e\nu$ events was used to determine a number of calibration corrections which need to be applied to optimize the time resolution for EM clusters in the EMB. The calibration includes corrections of various offsets in the timing of individual channels, corrections for the energy dependence of the timing, and time-of-flight corrections depending on the position to the PV. The corrections determined using the $W \rightarrow e\nu$ events were subsequently applied to electron candidates in $Z \rightarrow ee$ events to validate the procedure as well as determine the timing performance in an independent data sample. Figure 7.5 shows the time resolution achieved as a function of the energy deposited in the second-layer cell used in the time measurement. Superimposed on Figure 7.5 is the result of a fit of the expected functional form of the time resolution. Using the full 2011 dataset, a time resolution of $\sim$ 290 ps was achieved for a large energy deposit in the EMB. By comparing the timing of the two electrons in $Z \rightarrow ee$ candidate events, this resolution is understood to include a correlated contribution of $\sim$ 220 ps, as expected by the spread in the time of the pp collisions due the lengths of the individual proton bunches along the beamline. Subtracting this beam contribution in quadrature, the obtained timing resolution for the LAr calorimeter is $\sim$ 190 ps. Similar results were achieved over the full η range of the LAr EM calorimeters, when the study was extended to include the EM endcaps.

As discussed previously, the LAr FEBs employ three overlapping linear gain scales, dubbed high, medium, and low. The results in Figure 7.5 are those obtained for electrons where the time was measured using a second-layer cell read out using high gain, for which the $W \rightarrow e\nu$ sample

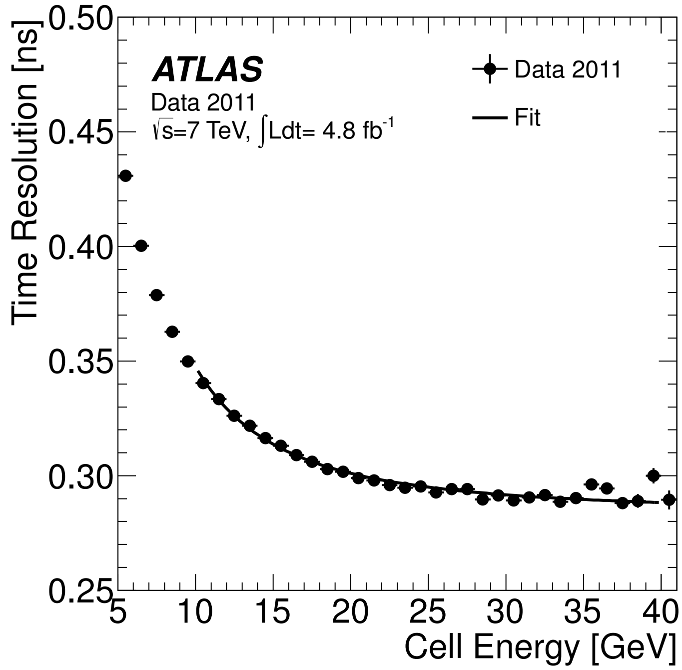

Figure 7.5: Time resolution obtained for EM showers in the ATLAS LAr EMB, as a function of the energy deposited in the second-layer cell with the maximum deposited energy. Superimposed is the result of the fit described in the text. The data are for electrons read out using high gain, and the errors shown are statistical only.

used to calibrate the timing is large. Calibration samples for the medium and low gain scales are smaller, resulting in reduced precision. The time resolutions obtained for data recorded in 2011 are approximately 400 ps for medium gain and approximately 1 ns for low gain.

Chapter 8

Analysis Strategy

This chapter describes the analysis method, which includes the selection of events with two photon candidates, and the use of the missing transverse energy in each event to define a signal region (SR) and various background control regions (CR). Section 8.1 describes the collision data sample used. As described in Section 8.2, an important detail in the analysis event selection is the application of asymmetric identification and pseudorapidity requirements on the two photon candidates that are used to define a "Tight-Loose" (TL) diphoton sample. Section 8.3 describes the procedures used to ensure only high-quality events are selected. Section 8.4 outlines the criteria which select the candidate events populating the signal and control regions defined in Section 8.5. Finally, in Section 8.6, the MC simulation samples used to study the expected SPS8 GMSB signal distributions are described.

8.1 Dataset and Trigger Selection

This analysis is based on the full sample of pp collision events recorded at $\sqrt{s} = 7$ TeV with the ATLAS detector in 2011. Selected events were required to satisfy the *EF_2g20_loose* online trigger, which requires at least two loose photon candidates, each with $E_{\mathrm{T}} > 20$ GeV and $|\eta| < 2.5$. An additional offline requirement for two loose photon candidates, each with $E_{\mathrm{T}} > 46$ GeV and $|\eta| < 2.5$, was applied in anticipation of the analysis selection requirements. This pre-selection defines a set of events on which further offline selection criteria were then applied.

The standard ATLAS Good Run List (GRL)[1] was applied to select events from luminosity blocks during periods when all detector components were working as expected. The collected integrated luminosities are shown in Table 8.1 for each data taking period in 2011, adding up to a total of 4812.3 pb^{-1} for the entire 2011 data taking period.

Period	**Run range**	**Luminosity** $[\mathrm{pb}^{-1}]$
B2	178044–178109	11.7
D	179710–180481	166.7
E	180614–180776	48.8
F	182013–182519	136.1
G	182726–183462	537.5
H	183544–184169	259.5
I	185353–186493	386.2
J	186516–186755	226.4
K	186873–187815	600.1
L	188902–190343	1401.9
M	190503–191933	1037.6
Total	178044–191933	4812.3

Table 8.1: Integrated luminosity used in this analysis. For each data taking period, the run range and the integrated luminosity are given.

8.2 Tight-Loose Diphoton Selection

A key point in the analysis is the selection of a sample of events with two isolated photon candidates, one satisfying the tight identification criteria (hereafter called the "Tight" photon) and the other satisfying at least the loose identification criteria (hereafter called the "Loose" photon). Both photons were required to have $E_{\mathrm{T}} > 50$ GeV. The Tight photon was required to satisfy $|\eta_{s2}| < 2.37$, excluding the transition region of $1.37 < |\eta_{s2}| < 1.52$ between the barrel and endcap

[1] `data11_7TeV.periodAllYear_DetStatus-v36-pro10_CoolRunQuery-00-04-08_Susy_ph_met.xml`.

EM calorimeters, while the Loose photon was restricted to have $|\eta_{s2}| < 1.37$.

Signal MC simulation was used to study properties of signal events and determine the optimal selection requirements. For example, Fig. 8.1 shows the E_{T} and η distributions of the two photons coming from the decay of the NLSP, and also the $E_{\mathrm{T}}^{\mathrm{miss}}$ distribution in signal events, for NLSPs decaying promptly and for a selection of Λ values. Using the prompt signal case to define the selection criteria avoided the introduction of any bias at early stages of the analysis due to the lifetime of the neutralino, for example in the selection of the E_{T} and $E_{\mathrm{T}}^{\mathrm{miss}}$ cuts.

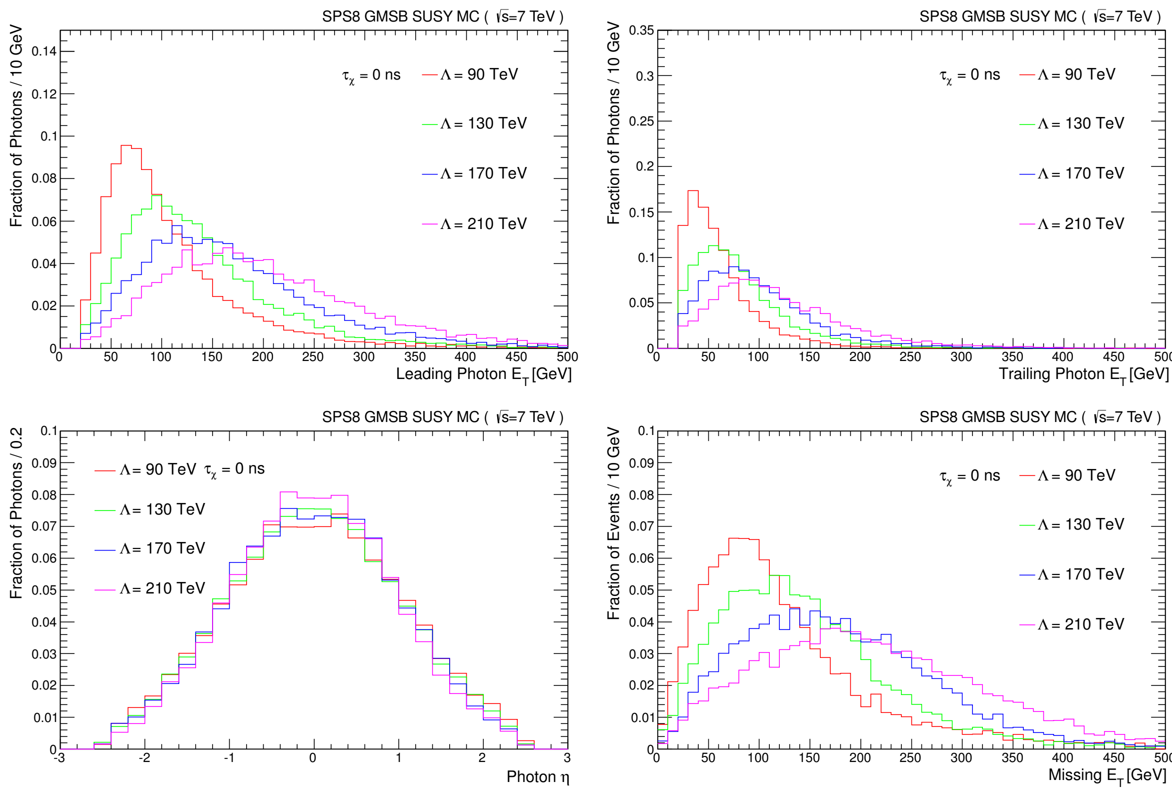

Figure 8.1: Unit-normalized distributions of kinematic variables for various Λ values on the SPS8 GMSB model line. The variables plotted are E_{T} of the leading photon (upper left), E_{T} of the subleading photon (upper right), η of the two photons (lower left), and $E_{\mathrm{T}}^{\mathrm{miss}}$ (lower right).

As seen in the top plots of Fig. 8.1, the requirement that both photons have $E_{\mathrm{T}} > 50$ GeV has a high efficiency for the GMSB signal points under consideration. In addition, this requirement reduces significantly any background contribution from $W \to e\nu$ events with the electron faking a photon. As seen in the bottom right plot of Fig. 8.1, the $E_{\mathrm{T}}^{\mathrm{miss}} > 75$ GeV requirement has a quite high efficiency for the GMSB signal points under consideration. While a somewhat lower $E_{\mathrm{T}}^{\mathrm{miss}}$ cut could provide a modest gain in sensitivity, it was decided that there was more benefit in using events with $20 < E_{\mathrm{T}}^{\mathrm{miss}} < 75$ GeV as an additional control region.

The need for asymmetric photon identification and selection requirements was also demonstrated by using signal MC simulation. Fig. 8.2 shows the photon identification efficiency versus $|z_{\mathrm{DCA}}|$ for signal photons for various levels of photon identification, including container, for which no additional identification criteria are applied, and photons passing the loose and tight criteria. As can be seen, the efficiency for the photon to be reconstructed in the photon container is rather flat out to rather large values of $|z_{\mathrm{DCA}}|$, up to ~ 800 mm. However, at the container level, background levels would be very high. The figure shows that the loose efficiency is roughly flat at $\sim 95\%$ for $|z_{\mathrm{DCA}}|$ values up to ~ 250 mm, and then starts to fall smoothly, reaching values $\sim 55\%$ for $|z_{\mathrm{DCA}}| = 600$ mm. On the other hand, the tight requirement, which includes cuts on the strip variables, has a much stronger dependence on $|z_{\mathrm{DCA}}|$, starting to fall quickly already for values of $|z_{\mathrm{DCA}}|$ above 100 mm.

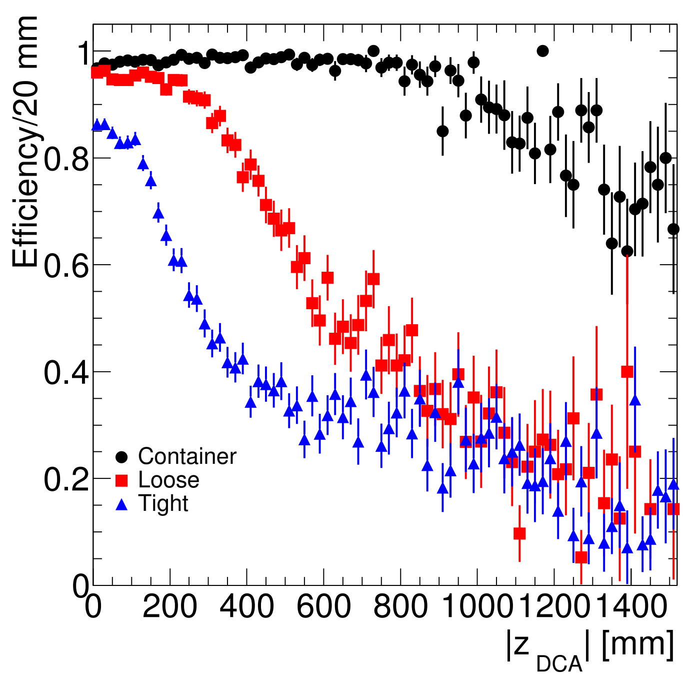

Figure 8.2: Photon reconstruction efficiencies as a function of $|z_{\mathrm{DCA}}|$ for container, loose and tight photons in SPS8 GMSB signal MC samples.

Given the behavior in Fig. 8.2, the Tight-Loose selection is a compromise between achieving a reasonable purity while maintaining reasonable efficiency for the non-pointing, Loose photon. In addition, to reduce the potential bias in the pointing measurement that results from applying the photon identification requirements, only the Loose photon in each event was examined for evidence of non-pointing. Further, given the better expected pointing and timing performance in the EM barrel calorimeter, the Loose photon was further restricted to lie within $|\eta_{s2}| < 1.37$. If two photons in the event passed the tight selection criteria, and both had $|\eta_{s2}| < 1.37$, the highest energy photon was treated as the Tight photon, and the lower energy object was treated as the Loose photon in the event.

8.3 Event Cleaning Procedures

In order to ensure the selection of high-quality events, a set of standard ATLAS procedures were applied. In this section, the procedures established to remove events affected by detector issues or with indications of cosmic ray activity are briefly described.

8.3.1 LAr Error Flag

An event-by-event bitset is available in ATLAS data to flag events affected by problems in the LAr calorimeter system [102]. The most significant example of such a problem is the appearance of bursts of large scale coherent noise, or *noise bursts*, mainly located in the endcaps. This phenomenon manifests itself only in the presence of collisions and was found to scale with instantaneous luminosity. The effect is very short in time, lasting usually less than ~ 5 μs, and during that time a significant percentage of channels exhibit signals which are significantly above the typical electronic noise levels. Noise bursts are identified in triggered empty bunch crossings where no collisions are expected. Taking advantage of the short nature of the phenomenon, neighboring events are vetoed within a conservative time window of 1 s around the identified noise burst.

8.3.2 LAr Calorimeter Hole Veto

The term “LAr hole” refers to a loss of acceptance in the LAr EM calorimeter due to problems in the control of six LAr FEBs, following a power failure on April 30th, 2011. Four of the affected

FEBs service EM calorimeter cells in the middle layer, while the other two service cells in the back layer. As a result, readout from approximately 0.4% of the EM calorimeter cells was lost, covering the $\eta - \phi$ region $(0, 1.4) \times (-0.74, -0.64)$ [103]. The loss of the middle layer severely impacted the capability to reconstruct photons and electrons in the affected region, while for the reconstruction of jets, it resulted in a significant mis-measurement of their EM component. Following an intervention in July 2011, the effects of the problem were significantly alleviated by the recovery of four of the problematic FEBs, restoring readout to the cells in the middle layer. The LAr hole therefore impacts ATLAS data taking periods E through H, after which only the two back-layer FEBs remained non-operational.

The loss of photon acceptance due to the LAr hole is modeled properly in signal MC, which was simulated to represent the detector conditions as closely as possible, and therefore no further treatment is necessary. Any effect on the measurement of $E_{\mathrm{T}}^{\mathrm{miss}}$, due to jets in the LAr hole region, was mitigated by the use of the SUSY LAr hole "smart veto" procedure. This veto procedure does not reject all events with jets in the problematic region, but instead rejects events where those jets contribute significantly to the $E_{\mathrm{T}}^{\mathrm{miss}}$ calculation. The acceptance loss due to the smart veto in SPS8 signal MC has been estimated to be 1.4% [104].

8.3.3 Cosmic Muon Veto

Cosmic muons can affect the $E_{\mathrm{T}}^{\mathrm{miss}}$ reconstruction by being included in the total energy calculation. Further, energy depositions from cosmic muons and overlapping with calorimeter clusters have the potential to distort the cluster shape and disrupt the pointing measurement. Events with muons apparently not related to the collision event were therefore rejected using the standard ATLAS cosmic muon veto procedure. In this procedure, the muon track impact parameters with respect to the event PV were used to classify a muon candidate as a cosmic ray candidate. The event was rejected if any muon selected after overlap removal was found with $|d_0| > 0.2$ mm or $z_0 > 1$ mm, where d_0 and z_0 are the transverse and longitudinal impact parameters, respectively.

8.4 Event Selection

A set of offline selection requirements was applied to the 2011 data sample as well as the signal MC samples, in the following order:

- For both data and signal MC, events were required to satisfy the *EF_2g20_loose* diphoton trigger. Further, the data events also had to satisfy the ATLAS GRL, as described above.
- At least one PV candidate with five or more associated tracks was required. In case of multiple vertices, the PV was chosen as the vertex with the greatest sum of the square of the transverse momenta of all associated tracks.
- Events flagged with a LAr error due to noise bursts or data integrity errors were removed.
- The overlap removal steps from Section 6.5 were applied. At this step no event was rejected.
- The jet cleaning veto was applied.
- The cosmic muon veto was applied.
- The LAr calorimeter hole event veto was applied.
- Events with at least two photons were selected, one satisfying tight and the other loose identification requirements.

At this point in the selection, the Tight-Loose (TL) diphoton sample was formed, from which a signal-rich subset defined by high $E_{\mathrm{T}}^{\mathrm{miss}}$ values was used to probe for new physics, whereas complementary subsets were used for background estimation and supporting studies.

8.5 Signal and Control Region Definitions

The distribution of $E_{\mathrm{T}}^{\mathrm{miss}}$ for the TL diphoton sample obtained from 2011 pp collisions is shown in Fig. 8.3. For comparison, Fig. 8.3 also shows, in overlay, the $E_{\mathrm{T}}^{\mathrm{miss}}$ distribution for some example SPS8 signal MC samples. The TL diphoton sample was divided into exclusive subsamples according to the value of $E_{\mathrm{T}}^{\mathrm{miss}}$. The TL sample with $E_{\mathrm{T}}^{\mathrm{miss}} < 20$ GeV was used to model the prompt backgrounds, as will be discussed later. The TL events with intermediate $E_{\mathrm{T}}^{\mathrm{miss}}$ values, namely 20 GeV $< E_{\mathrm{T}}^{\mathrm{miss}} <$ 75 GeV, were used as a control sample to validate the analysis procedure. The final signal region was defined by applying to the TL diphoton sample the additional requirement that $E_{\mathrm{T}}^{\mathrm{miss}} >$ 75 GeV.

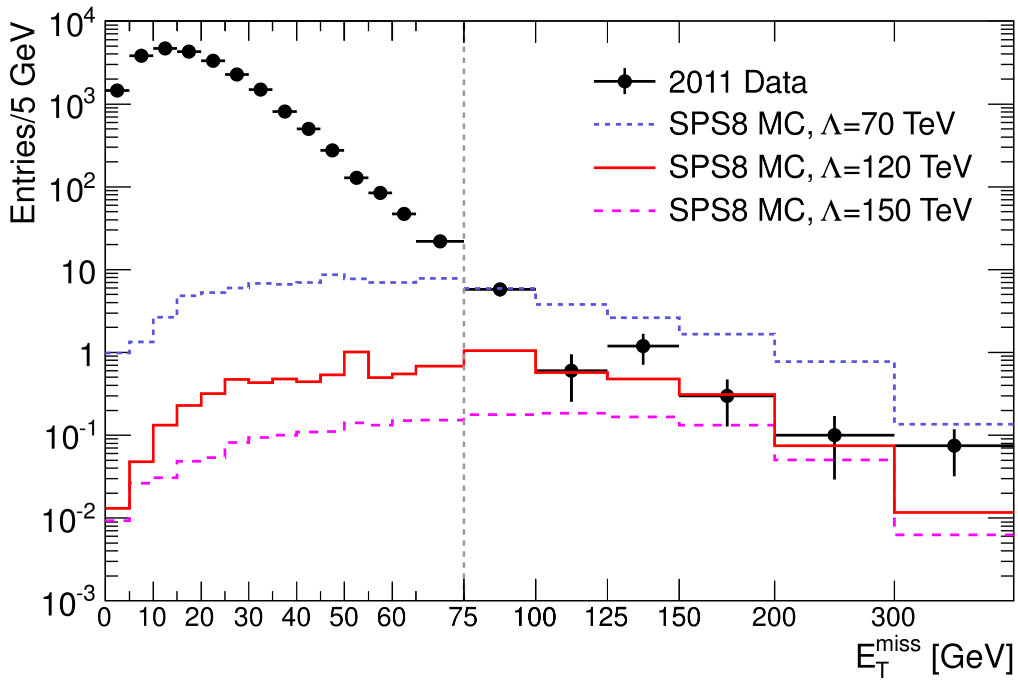

Figure 8.3: The $E_{\mathrm{T}}^{\mathrm{miss}}$ distribution for events in the selected diphoton sample using the full 2011 dataset. The predicted SPS8 signal contributions are shown for three reference signal MC samples. The right-most bin contains all events with values of $E_{\mathrm{T}}^{\mathrm{miss}}$ beyond 300 GeV and the vertical dashed line indicates the $E_{\mathrm{T}}^{\mathrm{miss}} >$ 75 GeV requirement for the signal region.

Initial studies were performed using only the data from period K, which corresponds to approximately 12% of the total integrated luminosity. Subsequently the analysis method and strategy were developed with the data in the signal region for the rest of the periods blinded. The number of events in the SR, as well as their pointing and timing distributions, were probed only after the analysis method was frozen.

The results of applying the selection requirements described above to the full 2011 dataset is presented in Table 8.2, showing the resulting number of selected events after each step of the selection (cutflow). In addition, the cutflow for one of the SPS8 signal MC samples ($\Lambda = 120$ TeV,

$\tau = 2$ ns) is presented. As can be seen in the Table, the final SR for the full 2011 dataset contains 46 selected events, while for the example SPS8 signal sample, 86.2 events are expected in the SR for the same total integrated luminosity.

Selection	**Data**	**SPS8** $\Lambda = 120$ TeV, $\tau = 2$ ns
All events	–	39999 (529.5)
GRL+Trigger	142168	23344 (308.9)
LAr Error	141644	23344 (308.9)
Jet Cleaning	141460	22774 (301.4)
Vertex	141220	22683 (300.2)
Muon veto	141174	22543 (298.3)
LAr veto	140926	22543 (298.3)
1 Loose Photon	103642	19049 (252.1)
TL Diphoton	23284	9155 (121.2)
$E_{\mathrm{T}}^{\mathrm{miss}} > 75$ GeV	46	6512 (86.2)

Table 8.2: Cutflow table for data and a reference MC sample. The numbers shown are the number of events after each selection step. The number in brackets is the number of signal events normalized to the luminosity of the 2011 data taking period.

8.6 Signal Monte Carlo Simulation

MC simulation was used to study SPS8 GMSB signal events. All MC samples used in this analysis were generated at $\sqrt{s} = 7$ TeV, were passed through a `GEANT4` [105] based simulation of the ATLAS detector [106], and were reconstructed with the same algorithms used for the data.

The generated events were produced so as to reflect as closely as possible the conditions observed throughout the 2011 data taking period. Where needed, appropriate corrections and scale factors were applied to the distributions so that simulated observables match the behavior observed in data. For example, in order to simulate in signal MC the presence of additional interaction vertices due to pileup in the signal, simulated minimum bias events were overlaid with the generated signal event. The number of simulated minimum bias events was chosen according to the distribution of the mean number of interactions ($\langle\mu\rangle$) observed in data. However, the $\langle\mu\rangle$ distribution used in the production of the MC may be different than the distribution for the actual selection of data used in an offline analysis. The ATLAS default pileup reweighting tool [107] was used to reweight the MC events in order to model the actual pileup conditions in the data sample.

As discussed in Section 3.4 the only free parameters in the GMSB SPS8 signal scenario considered are the SUSY breaking scale, Λ, and the lifetime of the NLSP, τ. The full mass spectrum, the branching ratios and the width of the decays were calculated from this set of parameters using `ISAJET` [108] version 7.80. The `HERWIG++` generator version 2.4.2 [109] with the MRST 2007 LO* [110] parton distribution functions (PDFs) was used to generate the signal MC samples. In all the generated samples, the branching ratio for the lightest neutralino to decay to a photon and a gravitino was fixed to 100%.

The signal MC points generated cover Λ values in the range of 70 TeV – 210 TeV, in steps of 10 TeV. Each signal point was generated with approximately 20,000 or 40,000 simulated events. In terms of the NLSP lifetime, the majority of the samples was produced with $\tau = 2$ ns, with some samples generated with additional lifetime values, as summarized in Table 8.3.

Several different lifetime points, with a relatively small step in lifetime, are needed for a given Λ. The production of a complete grid spanning all necessary Λ and τ values is neither feasible nor necessary. Instead, a lifetime reweighting technique has been applied to the produced samples to generate, for each Λ value, the appropriate distributions for different lifetime values. The reweighting procedure relies on the exponential form of the proper decay time of the NLSP to determine an event weight, appropriate for a signal sample with target lifetime T', for each event from a source signal sample generated with an NLSP lifetime T. The event weight for a proper decay time t is obtained by using the formula:

$$w(t) = \frac{T}{T'} \exp\left[-t\left(\frac{1}{T'} - \frac{1}{T}\right)\right] \tag{8.1}$$

where $t = L/(c\beta\gamma)$, L is the distance between the NLSP production and decay vertices in the lab frame, $\beta = p/E$ for the NLSP, and $\gamma = (1-\beta^2)^{-1/2}$. More details on the reweighting procedure are given in Appendix A. With the use of the reweighting procedure, signal MC distributions were obtained for lifetimes above 250 ps, which was the lowest lifetime value considered in this analysis.

Sample ID	Λ[TeV]	τ[ns]	σ(LO)[fb]	σ(NLO+NLL)[fb]	Uncert.(%)
164471	210	2	3.30	3.78	5.0
164470	200	2	4.44	5.12	4.9
164469	190	2	6.06	7.17	4.7
164468	180	2	8.30	9.98	4.8
164467	170	2	11.5	14.1	4.7
164466	160	2	16.2	20.2	4.7
157548	150	2	23.2	29.4	4.7
164465	140	2	34.0	44.2	4.9
157549	130	1	51.2	68.4	5.2
157550		2			
157551		4			
157552		6			
157553	120	0	79.5	110	5.5
157554		1			
157555		2			
157556		4			
157557		6			
157558		10			
157559	110	1	129	184	5.8
157560		2			
157561		4			
157562		6			
157563	100	1	221	324	6.1
157564		2			
157565		4			
157566		6			
157567	90	1	403	609	6.3
157568		2			
157569		4			
157570		6			
164464	80	2	794	1230	6.4
157571	70	2	1710	2690	6.3

Table 8.3: The total LO and NLO (+NLL for strong production) cross sections for the SPS8 signal points generated for this analysis, together with their PDF and scale uncertainties.

The signal MC events were generated at leading order (LO) using HERWIG++. The GMSB signal cross sections were calculated at NLO using PROSPINO [46] version 2.1. Table 8.3 shows the calculated LO cross section for each generated sample, along with the calculated NLO cross section, which includes the NLL terms for the strong production processes, as discussed previously. For each different production process contributing to the cross section, a weight (also known as a k-factor) was applied to correct for the difference between the LO cross section used at the generator level and the calculation in the NLO+NLL scheme.

Table 8.3 also quotes the uncertainty on the calculated NLO+NLL cross section, obtained by using the uncertainty on the PDF and renormalization and factorization scales. For the cross section calculation, the CTEQ6.6 [111] and MSTW2008 [112] PDF sets were used, applying the procedure documented in Ref. [47]. In this procedure, an envelope is formed by using the 68% CL ranges of the two PDF sets, with the addition in quadrature of a term due to the uncertainty on the renormalization and factorization scales. The scale uncertainty was obtained by a factor of two change of the nominal scale values. In addition, for the CTEQ6.6 sets, the uncertainty on the strong coupling constant, α_S, was added in quadrature. The extend of the envelope was determined by the maximum and minimum variations of the two PDF sets and the additional uncertainties. For the nominal value of the PDF used in the cross section calculation, the mid-point of the envelope was used and, for its uncertainty, a symmetric uncertainty was obtained by using the half-width of the envelope.

Chapter 9

Signal Efficiencies and Expected Event Yields

In this chapter, the signal selection efficiencies and expected yields are discussed. Studies performed to determine the effect that non-pointing photons have on the selection efficiency are described first. Studies on the modeling of the efficiency in simulation are also discussed. Sections 9.1 and 9.2 cover the trigger efficiency and identification efficiency studies, respectively. Finally, a summary of the selection efficiencies and yields of all the signal MC samples considered is provided in Section 9.3.

9.1 Trigger Efficiency

Several methods were used to determine the overall trigger efficiency and to check for a possible dependence on the degree of non-pointing. A standard *Bootstrap* method [113] using Minimum Bias events was used to determine the overall trigger efficiency of the `2g20_loose` diphoton trigger. In the Bootstrap method, the efficiency of a higher threshold trigger can be measured for events selected by a lower threshold trigger, in a p_{T} region where the lower trigger operates with maximum efficiency. The efficiency of the diphoton trigger is calculated from the individual `g20_loose` single photon trigger efficiencies in selecting the selected diphoton events using the leading and sub-leading photon. The single photon trigger efficiency is calculated relative to the L1 trigger providing the seed for the `g20_loose` trigger. The L1 seed of `g20_loose` changed from

L1_EM14 (periods D to K) to L1_EM12 (periods L to M). Therefore, the 2011 dataset is divided into these two sub-periods. The L1 seed efficiency is calculated relative to a sample of Minimum Bias triggered events. The results for the two sub-periods are very similar and are very close to 100%, as summarized in Table 9.1. In addition to determining the overall trigger efficiency, the efficiency was studied with the Bootstrap method as a function of $|z(\gamma)|$. As shown in Fig. 9.1, no evidence was observed for any dependence of the trigger efficiency as a function of $|z(\gamma)|$.

A second approach to calculating the trigger efficiency used a sample of $Z \to ee$ events that were selected with a pre-scaled single-electron trigger instead of the standard 2g20_loose trigger. The trigger efficiency can be calculated as the fraction of such events that also pass the 2g20_loose trigger. This efficiency is plotted in Fig. 9.2 as a function of z_{PV}. Superimposed is the prediction from MC. As can be seen, the efficiency is high ($\sim$ 94%) and is rather flat as a function of z_{PV} for values up to $|z_{\mathrm{PV}}| \approx 300$ mm accessible due to the beam spread. Furthermore, there is reasonable agreement between data and MC over the available z_{PV} range.

In order to extend the reach to higher z_{DCA} values, trigger object emulation in signal MC was used to study the effect of highly non-pointing photons on the trigger efficiency. While the loose photon requirements applied in the HLT are similar to those applied offline, and therefore can be included in the photon reconstruction and identification efficiency studies, it is important to check for any possible impact on the L1 trigger sums and algorithms due to the non-pointing nature of the Loose signal photon. Given the EM calorimeter design, the L1 trigger sum primitives of $\Delta\eta \times \Delta\phi = 0.1 \times 0.1$ are projective in nature, pointing back to the nominal interaction

Dataset Considered	**Efficiency (%) for First Photon**	**Efficiency (%) for Second Photon**	**Combined Trigger Efficiency (%)**
Data: Periods D-K	$100 +0 -0.4$	$100 +0 -0.5$	$100 +0 -1$
Data: Periods L-M	$99.7 +0.2 -0.5$	$99.5 +0.3 -0.6$	$99.3 +0.5 -1.0$
Signal MC	$99.6 \; +0.1 \; -0.1$	$94.7 \; +0.2 \; -0.2$	$94.4 \; +0.3 \; -0.3$

Table 9.1: Trigger efficiencies of the 2g20_loose trigger, as determined via the Bootstrap method, for collision data in 2011 as well as MC simulation. The 2011 dataset is divided into two distinct periods according to the L1 trigger seeding the 2g20_loose trigger.

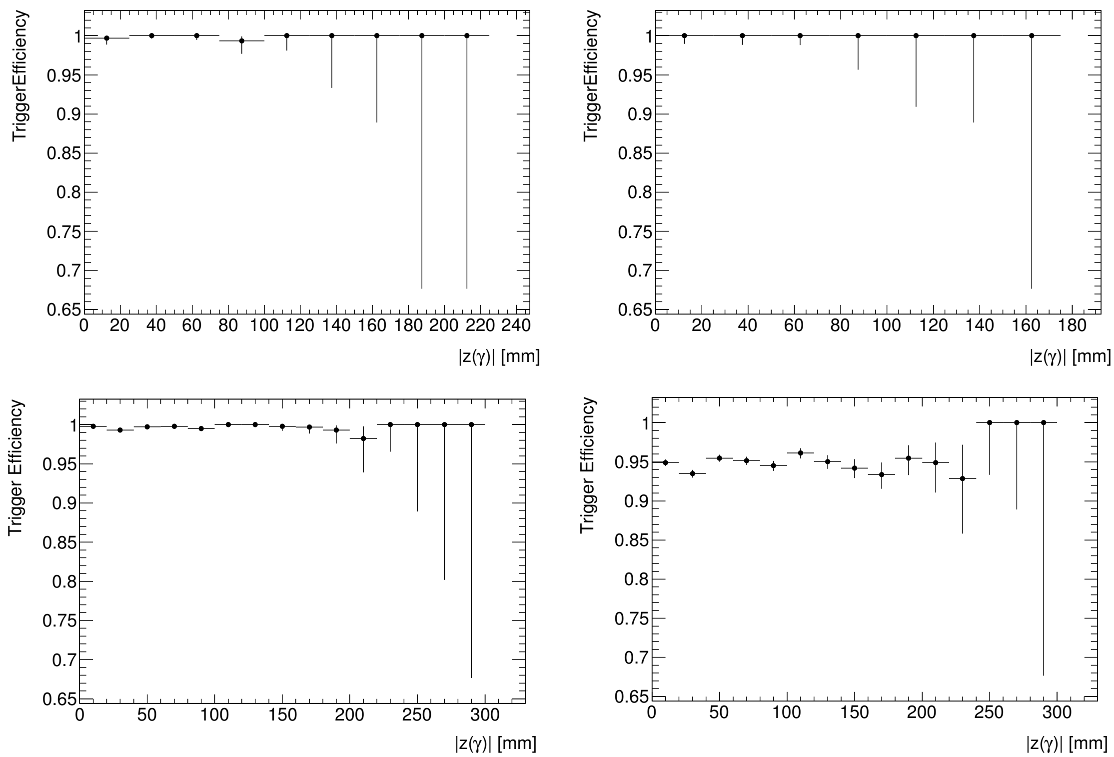

Figure 9.1: Trigger efficiency as a function of $|z(\gamma)|$, as determined with the Bootstrap method. The upper plots show the results for the leading photon in data for periods (left) D-K and (right) L-M. The bottom plots show the signal MC results for the (left) leading photon and (right) sub-leading photon.

point at the center of the detector. A study has therefore been performed to determine the degree of energy containment in the L1 EM Cluster energy sums for highly non-pointing EM showers. Loose photons in the signal region are matched to emulated L1 trigger objects within a cone with $\Delta R < 0.015$. The L1 trigger efficiency is defined as the fraction of the number of signal region photons that are matched to emulated L1 trigger objects with EM Cluster energy sums over the nominal 50 GeV photon E_{T} requirement. The efficiency was studied as a function of the extrapolated photon point of origin on the beam axis, $z(\gamma)$, and is plotted in Fig. 9.3. As can be seen, the efficiency is high and consistent with flat as a function of $z(\gamma)$. This leads to the conclusion that there is no trigger bias or loss of efficiency as a function of the degree of non-pointing. A flat systematic uncertainty of $\pm 2\%$ was assigned to the L1 trigger efficiency to account for any possible deviation of the L1 trigger efficiency, as shown in Fig. 9.3, from flat versus the degree of non-pointing.

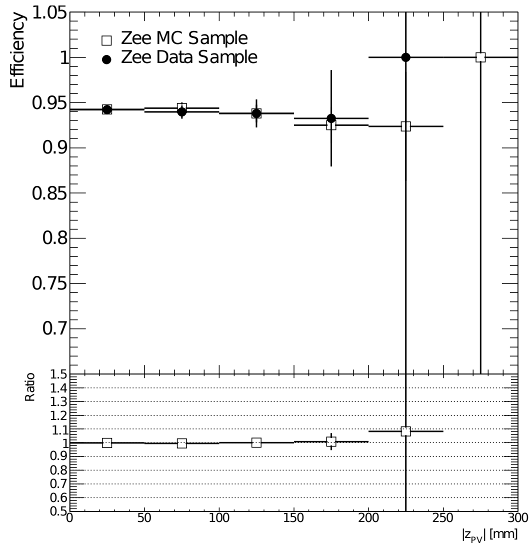

Figure 9.2: Trigger efficiency, defined as the fraction of $Z \rightarrow ee$ events selected via a pre-scaled single electron trigger that also pass the `2g20_loose` trigger requirements, as a function of the z_{PV}, for data and MC. The bottom panel shows the ratio of the data over the MC.

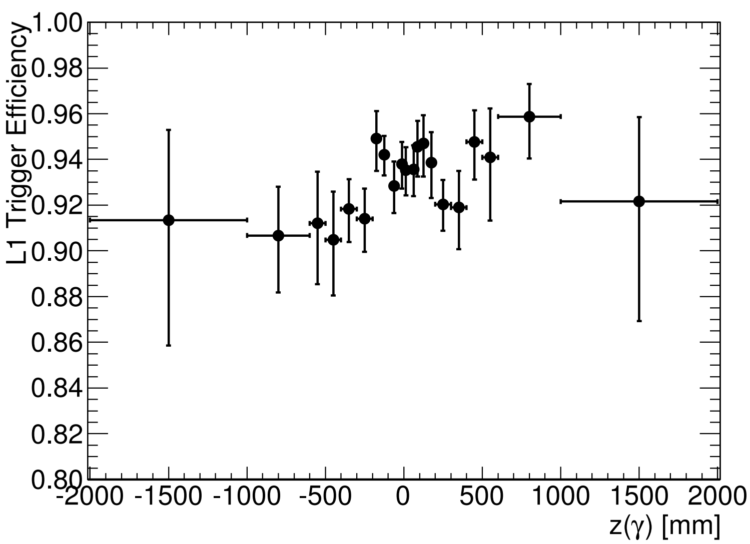

Figure 9.3: L1 Trigger efficiency in signal MC for Loose photons in the signal region matched to emulated L1 Trigger objects, versus the extrapolated photon point of origin on the beam axis.

9.2 Non-Pointing Photon Identification Efficiency

Two methods were implemented in order to study the efficiency of the reconstruction and identification of non-prompt photons. A data-driven technique using a standard tag-and-probe method using $Z \to ee$ events is described in 9.2.1. A MC-based study of the impact of the efficiency of variations of the shower shape variables is described in Section 9.2.2.

9.2.1 Tag-and-Probe Studies

The first set of photon identification efficiency results were obtained by applying a modified version of the standard tag-and-probe method to samples of MC and data electrons from $Z \to ee$ events. As in the trigger efficiency tag-and-probe study described previously, to avoid a trigger bias, the $Z \to ee$ events were selected with a single electron trigger. All electrons must have $p_{\mathrm{T}} > 25$ GeV, must pass the medium++ identification requirements, and must have $|\eta| < 2.37$, excluding the transition region between the barrel and endcap EM calorimeters. Events must contain two electron candidates that meet the requirements, and, to ensure good quality electrons, they must be produced at the same PV, be oppositely charged, and have a dielectron invariant mass between 81 GeV and 101 GeV. Further, events are selected only if at least one of the two electrons satisfies additionally the tight++ electron identification requirements.

If only one electron passes the tight++ electron identification requirements, it is assigned the tag electron label and the second electron the probe. However, if both electrons pass the tight++ requirements, to remove any bias, one is randomly selected to be the tag and the other the probe. The probe electron shower shape discriminating variables are used to study the efficiency of the electron satisfying the loose and tight identification requirements for photons. The efficiency is plotted against z_{PV} for the tight photon identification requirements and, if the electron is detected with $|\eta| < 1.37$, the loose photon identification requirements.

Fig. 9.4 shows comparisons of the data and MC values of the efficiencies, as a function of z_{PV}, for the loose photon identification requirements. Fig. 9.4 shows the $Z \to ee$ data and MC efficiencies are in reasonable agreement for loose photons, though the statistical error bars become significant for large values of z_{PV}. Also shown in the figure is the comparison to signal MC, demonstrating a good agreement between signal MC and the tag-and-probe results for the loose identification efficiency.

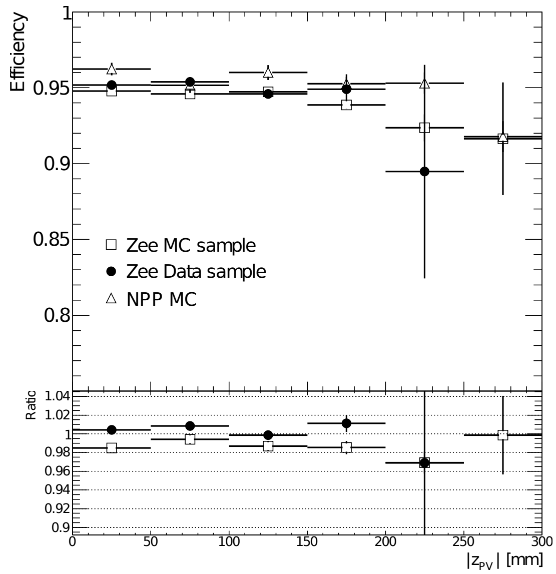

Figure 9.4: The efficiency, as a function of z_{PV}, of the probe electron passing the loose shower shape variable requirements for photons, measured with a tag-and-probe analysis using a $Z \to ee$ selection on both data and MC. The efficiency of non-pointing photons (NPP) passing the photon loose identification requirements is shown superimposed. The ratio plots are calculated relative to the non-pointing photon values.

Fig. 9.5 shows similar results for tight photon identification requirements. The left plot shows the results when the tight++ requirements appropriate for electrons are applied. While there is good agreement between the $Z \to ee$ data and MC results, there are differences when comparing with the signal MC photons. The reason is that, for the tight identification requirements, which use additional variables compared to the loose identification, there are differences in selection criteria for converted and unconverted photons, due to the wider shower profiles in the ϕ-direction for converted photons because of the impact of the magnetic field. This means that, for the tight identification efficiency, it is more meaningful to compare the tight identification efficiency for the $Z \to ee$ sample to converted photons in the signal MC. Such a comparison is shown in the right plot of Fig. 9.5, and shows similar shapes for the $Z \to ee$ and signal MC samples. With the tag-and-probe studies it was therefore verified that the MC describes well the EM shower shape variations and the consequent changes in identification efficiency for non-pointing EM objects.

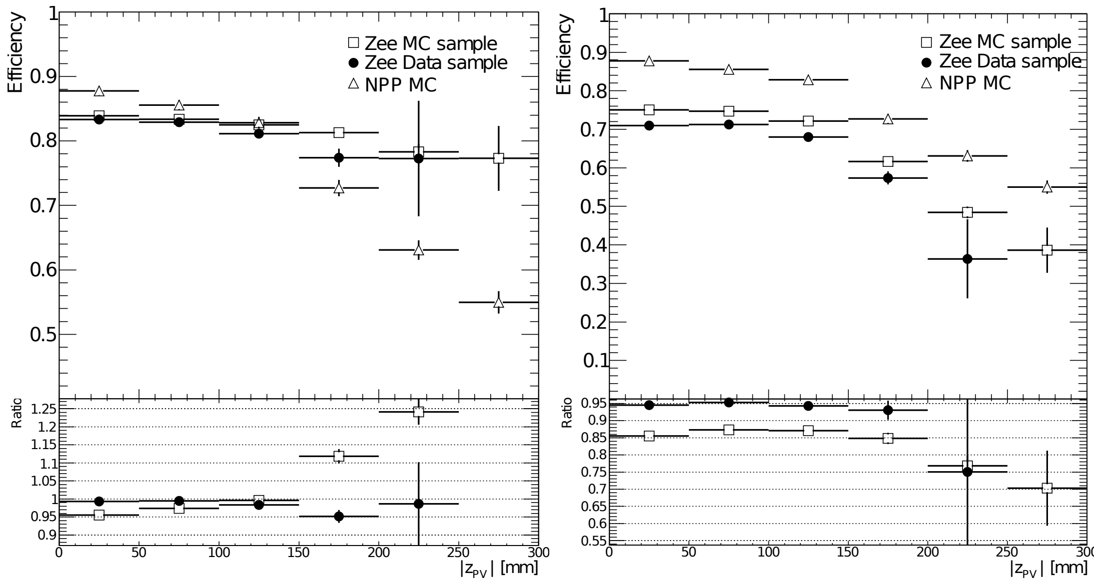

Figure 9.5: The efficiency, as a function of z_{PV}, of the probe electron passing the tight shower shape variable requirements for electrons (left) and converted photons (right), measured with a tag-and-probe analysis using a $Z \to ee$ selection in both data and MC, plotted on the same graph as the efficiency of non-pointing photons (NPP) passing the photon tight requirements. The ratio plots are calculated relative to the non-pointing photon values.

9.2.2 Shower Shape Studies

As shown in Fig. 9.6, the shower shape distributions of signal photons vary as a function of z_{DCA}, which leads to a dependence of photon efficiency on z_{DCA}. Any uncertainty in these shifts would result in a z_{DCA}-dependent uncertainty of the photon efficiency.

It is well known that discrepancies between data and MC distributions exist for some of the shower shape variables used in electron/photon identification [114]. The discrepancies between data and MC in the DVs are parametrized as shifts [115], also known as "fudge factors", and are applied to the simulated values in order to match the distributions observed in data. In order to match the photon identification efficiency in signal MC to the one observed in data, an ATLAS official tool [116] is used to apply the appropriate fudge factors to each simulated photon candidate. Subsequently, the photon identification criteria are re-applied using the corrected DVs. The fudge factor approach is typically used in ATLAS analyses involving photons.

For this analysis, it is necessary to determine whether the observed shifts are dependent upon

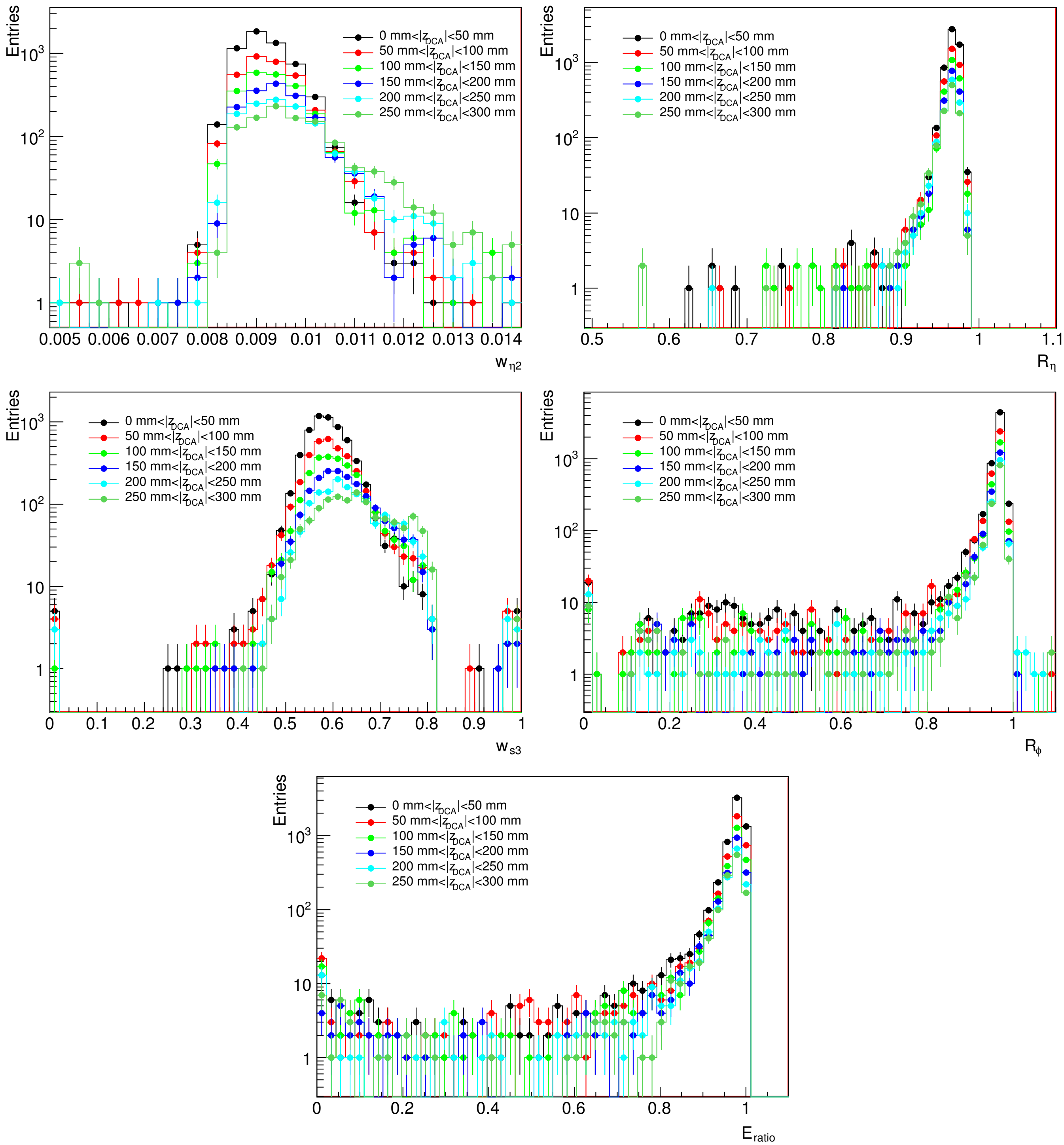

Figure 9.6: Shower shape variables for photons with different $|z_{\mathrm{DCA}}|$ ranges. The top two plots show variables used in the loose identification requirements, while the other three show variables used in the tight identification. Details of the shower shape variables can be found in table 6.2.

the value of z_{DCA}. Therefore, data and MC distributions for shower shape variables for $Z \to ee$ electrons have been compared as a function of $|z_{\mathrm{PV}}|$, once again using the beam spread as a source of electrons which do not originate at the center of the detector. For example, Fig. 9.7 shows, versus $|z_{\mathrm{PV}}|$, the differences between data and MC in the mean values for the variables $w_{\eta 2}$ (used in loose identification) and w_{s3} (used in tight identification). These variables were chosen since, as seen in Fig. 9.6, they demonstrate the largest variations with z_{DCA}. As can be seen in the top plots of Fig. 9.7, while there are differences between data and MC in the mean values of these shower shape variables, the differences are roughly constant, independent of $|z_{\mathrm{PV}}|$. The bottom plots of Fig. 9.7 show the differences in the RMS values of these variables. For $w_{\eta 2}$, the RMS differences are roughly constant, independent of $|z_{\mathrm{PV}}|$. However, the RMS of the w_{s3} distribution grows faster with $|z_{\mathrm{PV}}|$ in MC than in data. Extrapolating out to $|z_{\mathrm{PV}}|$ values of ~ 500 mm, which is approximately how far out the tight photon can be efficiently identified, the RMS difference could be as large as $\sim 40\%$. As a simple check of the impact of such a mis-modeling, an additional 40% smearing of w_{s3} was applied and the tight efficiency remeasured. The results are shown in Fig. 9.8, and show that the resultant changes are at or below the level of a few percent. Furthermore this study overestimates the impact for small z, where the data-MC discrepancy is much smaller than 40%. In the high z range, the impact is less than $\sim \pm 2\%$, and is therefore negligible.

Summarizing the shower shape studies, the MC describes the effects observed in data fairly well. The exception is the RMS of w_{s3}, but this has a negligible impact on the tight efficiency. There is, therefore, no indication of any need for an identification efficiency uncertainty which depends on z_{DCA}. Instead, the overall photon identification uncertainty can be obtained using the "fudge factor" approach in the same way as other ATLAS analyses involving photons.

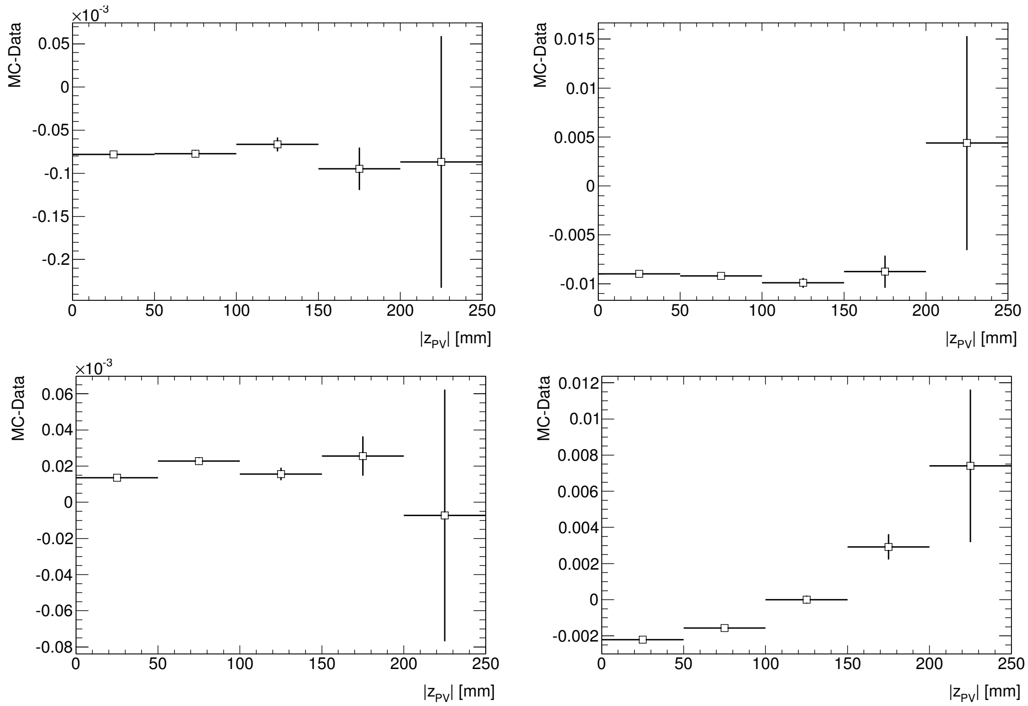

Figure 9.7: The difference between data and MC in the (top row) mean values and (bottom row) RMS values of the shower shape variables (left) $w_{\eta 2}$ (used in loose identification) and (right) w_{s3} (used in tight identification), as a function of $|z_{\mathrm{PV}}|$.

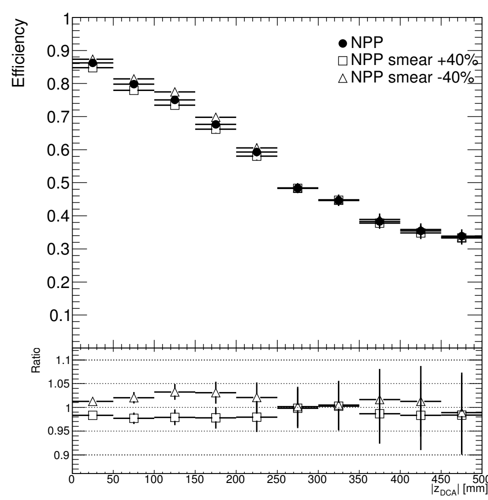

Figure 9.8: Comparisons of the tight photon efficiency in the non-pointing photon signal selection, with and without the additional smearing, described in the text, applied to the w_{s3} shower shape variable.

9.3 Summary of Signal Efficiencies and Expected Event Yields

The total signal selection efficiencies, including the acceptance, for each signal MC sample to pass the Tight-Loose selection and have $E_{\mathrm{T}}^{\mathrm{miss}}$ greater than 75 GeV are presented in Table 9.2. The results are plotted in Fig. 9.9 as a function of NLSP lifetime for some representative Λ values. The predicted NLO signal yields after the same requirements are presented in Table 9.3. For fixed Λ, the acceptance falls approximately exponentially with increasing τ, dominated by the requirement that both NLSPs decay inside the ATLAS tracking detector so that the decay photons are detected by the EM calorimeters. For fixed τ, the acceptance increases with increasing Λ, since the SUSY particle masses increase, leading the decay cascades to produce, on average, higher $E_{\mathrm{T}}^{\mathrm{miss}}$ and also higher E_{T} values of the decay photons.

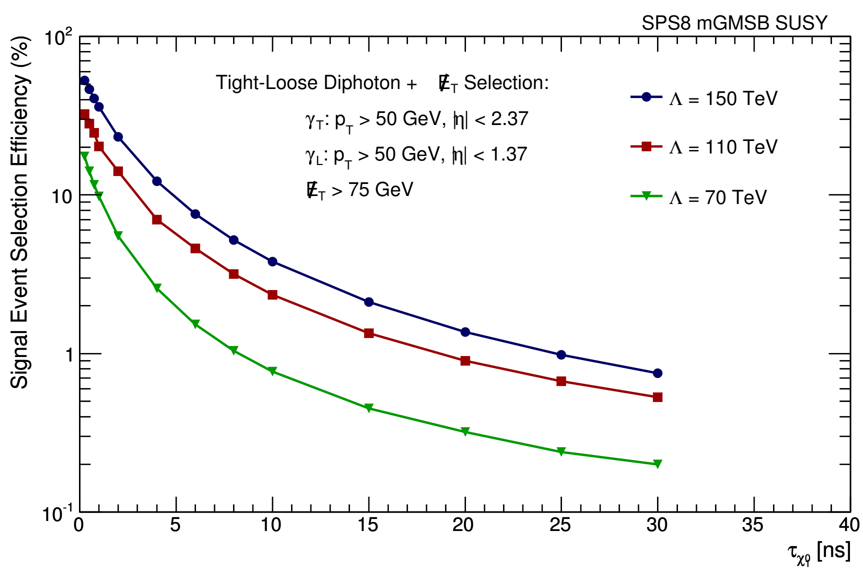

Figure 9.9: Signal acceptance times efficiency versus NLSP lifetime for several Λ values on the SPS8 GMSB model line.

Λ [TeV]	NLSP lifetime [ns] 0	0.25	0.5	0.75	1	2	4	6	8	10	15	20	25	30	40	60	80	100
210	-	58.6 ±0.6	54.6 ±0.5	50.9 ±0.5	50.0 ±0.5	33.0 ±0.3	17.6 ±0.2	10.8 ±0.1	7.3 ±0.07	5.3 ±0.05	3.1 0.02	1.9 ±0.02	1.4 ±0.01	0.99 ±0.01	-	-	-	-
200	-	56.3 ±0.4	52.0 ±0.4	48.2 ±0.3	44.3 ±0.3	31.1 ±0.2	16.8 ±0.1	10.4 ±0.07	7.1 ±0.05	5.2 ±0.04	2.9 ±0.02	1.8 ±0.02	1.3 ±0.01	1.0 ±0.007	-	-	-	-
190	-	52.0 ±0.2	50.9 ±0.3	47.8 ±0.4	44.0 ±0.4	30.4 ±0.3	16.1 ±0.2	9.9 ±0.2	6.8 ±0.1	4.9 ±0.1	2.7 0.07	1.8 ±0.05	1.3 ±0.04	0.97 ±0.04	-	-	-	-
180	-	48.6 ±0.5	47.7 ±0.4	44.8 ±0.4	41.3 ±0.4	28.6 ±0.3	15.1 ±0.2	9.3 ±0.2	6.3 ±0.1	4.6 ±0.1	2.5 ±0.06	1.6 ±0.05	1.1 ±0.03	0.86 ±0.03	-	-	-	-
170	-	52.4 ±0.4	47.8 ±0.3	43.6 ±0.3	39.6 ±0.3	27.0 ±0.2	14.4 ±0.1	9.0 ±0.06	6.2 ±0.04	4.5 ±0.03	2.5 ±0.02	1.6 ±0.01	1.2 ±0.01	0.90 ±0.006	-	-	-	-
160	-	45.1 ±0.3	42.0 ±0.3	39.1 ±0.3	35.9 ±0.3	24.8 ±0.2	13.1 ±0.09	8.06 ±0.06	5.50 ±0.03	4.01 ±0.03	2.2 ±0.02	1.43 ±0.01	1.0 ±0.007	0.772 0.006	0.510 ±0.004	0.287 ±0.002	0.196 ±0.002	-
150	-	42.5 ±0.2	40.4 ±0.2	37.3 ±0.2	34.0 ±0.2	23.1 ±0.1	12.13 ±0.06	7.45 ±0.04	5.07 ±0.03	3.69 ±0.02	2.11 ±0.06	1.311 ±0.007	0.98 ±0.03	0.715 ±0.004	0.473 ±0.003	0.276 ±0.001	0.189 ±0.001	-
140	-	38.5 ±0.3	37.1 ±0.3	34.4 ±0.2	31.3 ±0.2	21.1 ±0.2	11.1 ±0.08	6.82 ±0.05	4.68 ±0.2	3.44 ±0.03	1.9 ±0.9	1.25 ±0.01	0.9 ±0.05	0.682 ±0.005	0.448 ±0.003	0.255 ±0.002	0.176 ±0.001	-
130	-	36.1 ±0.2	34.2 ±0.2	31.5 ±0.2	27.3 ±0.2	19.2 ±0.1	10.04 ±0.07	6.39 ±0.03	4.40 ±0.02	3.25 ±0.02	1.9 ±0.04	1.235 ±0.006	0.92 ±0.02	0.712 ±0.004	0.493 ±0.003	0.309 ±0.002	0.231 ±0.001	-
120	29.6 ±0.3	30.2 ±0.2	29.2 ±0.2	27.0 ±0.2	23.9 ±0.1	16.3 ±0.06	8.73 ±0.03	5.38 ±0.02	3.68 ±0.02	2.71 ±0.02	1.54 ±0.04	1.006 ±0.005	0.74 ±0.02	0.568 ±0.003	0.384 ±0.002	0.230 ±0.001	0.164 ±0.001	-
110	-	28.1 ±0.2	26.2 ±0.1	24.0 ±0.1	20.1 ±0.2	14.30 ±0.07	6.83 ±0.05	4.55 ±0.02	3.15 ±0.02	2.33 ±0.01	1.34 ±0.03	0.900 ±0.005	0.67 ±0.02	0.525 ±0.003	0.366 ±0.002	0.230 ±0.001	0.172 ±0.001	0.1470 ±0.0007
100	-	22.9 ±0.1	21.8 ±0.1	19.7 ±0.1	16.6 ±0.1	11.34 ±0.06	5.84 ±0.04	3.51 ±0.02	2.42 ±0.01	1.79 ±0.01	1.03 ±0.03	0.688 ±0.004	0.51 ±0.02	0.399 ±0.002	0.277 ±0.002	0.172 ±0.001	0.128 ±0.001	0.1040 ±0.0006
90	-	19.1 ±0.1	17.9 ±0.1	16.1 ±0.1	13.9 ±0.1	9.06 ±0.05	4.72 ±0.04	2.91 ±0.01	1.96 ±0.01	1.447 ±0.008	0.85 ±0.01	0.563 ±0.003	0.43 ±0.02	0.333 ±0.002	0.235 ±0.002	0.151 ±0.001	0.115 ±0.001	0.095 ±0.001
80	-	15.3 ±0.3	14.1 ±0.2	12.6 ±0.2	11.1 ±0.1	6.90 ±0.07	3.34 ±0.04	2.01 ±0.02	1.37 ±0.02	1.01 ±0.02	0.6 ±0.01	0.39 ±0.01	0.3 ±0.01	0.24 ±0.01	0.175 ±0.005	0.116 ±0.004	0.090 ±0.004	0.076 ±0.004
70	-	14.2 ±0.2	12.4 ±0.2	10.8 ±0.1	9.32 ±0.08	5.49 ±0.05	2.57 ±0.02	1.53 ±0.02	1.04 ±0.01	0.77 ±0.01	0.46 ±0.02	0.311 ±0.005	0.24 ±0.01	0.194 ±0.004	0.144 ±0.003	0.101 ±0.003	0.082 ±0.003	0.072 ±0.003

Table 9.2: The efficiency in percent of the Tight-Loose photon selection and $E_{\mathrm{T}}^{\mathrm{miss}}$ requirement for the generated SPS8 GMSB signal MC samples. The errors indicated are statistical only.

Λ	Neutralino lifetime [ns]																
[TeV]	**0.25**	**0.5**	**0.75**	**1**	**2**	**4**	**6**	**8**	10	**15**	**20**	**25**	**30**	**40**	**60**	**80**	**100**
210	10	9.7	9.2	8.5	6	3.2	2	1.4	1	0.55	0.34	0.25	0.19	-	-	-	-
200	13.9	12.8	11.9	10.9	7.7	4.1	2.6	1.8	1.3	0.71	0.46	0.32	0.25	-	-	-	-
190	17.9	17.6	16.5	15.2	10.5	5.6	3.4	2.3	1.7	0.94	0.61	0.44	0.33	-	-	-	-
180	23.4	22.9	21.5	19.9	13.7	7.3	4.5	3	2.2	1.2	0.77	0.55	0.41	-	-	-	-
170	35.6	32.4	29.6	26.9	18.3	9.7	6.1	4.2	3.1	1.7	1.1	0.8	0.61	-	-	-	-
160	45.1	42.1	39.3	36.1	25	13.2	8.2	5.6	4.1	2.2	1.4	1	0.78	0.5	0.28	0.19	-
150	60.2	57.3	53	48.4	33	17.4	10.7	7.3	5.4	2.99	1.95	1.39	1.06	0.68	0.39	0.28	-
140	82.2	79.4	73.8	67.3	45.4	23.8	14.7	10.1	7.4	4.1	2.7	1.9	1.5	0.96	0.55	0.38	-
130	118.7	112.3	104.2	90.4	63.7	33.3	21.3	14.7	10.8	6.2	4.1	3.02	2.37	1.6	1	0.77	-
120	199.6	176.7	155.5	127.7	86.9	46.6	28.8	19.6	14.7	8.16	5.4	3.93	3.05	2.1	1.2	0.88	-
110	242.4	221.6	203.7	179.3	124.7	61.6	41	28.1	20.8	11.9	8	5.92	4.67	3.3	2.1	1.6	1.3
100	359	340.9	308.7	261.2	178.9	92.1	55.3	37.9	28.3	16.2	10.9	8.03	6.31	4.4	2.7	2	1.6
90	563.1	526.5	474	411.6	268.1	139.8	85.4	58.6	43.4	25	16.9	12.64	10.03	7.1	4.6	3.5	2.9
80	909.8	835.8	747.8	661.9	411.4	199.4	119.9	81.7	60.3	34.7	23.7	17.9	14.3	10.3	6.9	5.4	4.5
70	1844.1	1618.8	1404.3	1214.1	717.5	336.9	200.8	136.7	101.2	59.1	41.2	31.6	25.9	19.4	13.8	11.3	10.0

Table 9.3: The predicted NLO signal yield (in events), for 4.8 fb^{-1}, after the Tight-Loose photon selection and $E_{\mathrm{T}}^{\mathrm{miss}}$ requirement for the generated SPS8 GMSB signal MC samples.

Chapter 10

Signal and Background Modeling

In this chapter, the modeling of SPS8 GMSB signal photons (Section 10.1) and the modeling of sources of background (Section 10.2) are described. The shapes of the z_{DCA} distributions for signal and background, alternately denoted hereafter as the pointing distributions, are defined. The expected collision background composition in the TL diphoton sample is described in Section 10.2, dominated by two contributions with different pointing behavior. All the background contributions are studied in collision data using either control regions in the TL sample, or $Z \to ee$ events. With the purpose of using the photon arrival times as an additional cross-check, photon timing distributions for signal, as well as the two identified background sources, are described in Section 10.3. Finally, Section 10.4 discusses the possibility for background contributions from other sources, not originating from the main collision events.

10.1 SPS8 GMSB Signal Modeling

The pointing distribution expected for photons from NLSP decays in events passing the selection cuts is determined using the SPS8 GMSB MC signal samples, for various values of Λ and τ. The signal pointing distributions, normalized to unit area, are used as signal templates, hereafter referred to as T_{sig}.

Since the T_{sig} shape is determined using MC simulation, systematic uncertainties in the shape are included to account for possible differences in pointing performance between MC simulation and data. In particular, the presence of pileup could impact the pointing resolution, due both to energy deposits in the calorimeter from additional minimum bias collisions and to the possibility of misidentifying the PV. As discussed previously, the signal MC samples were reweighted, using a standard ATLAS tool, to match the pileup distribution observed in the entire 2011 dataset. To examine the influence of pileup, for each signal MC sample, the T_{sig} shapes for the entire MC sample were compared with subsamples chosen with differing levels of pileup. The pp collision dataset collected in 2011 has roughly equal numbers of events with less than six and with greater than or equal to six reconstructed PV candidates. Therefore, six was chosen as the boundary between "lower pileup" and "higher pileup" subsamples. Fig. 10.1 shows the Loose photon z_{DCA} distribution for all TL events of the MC sample generated with $\Lambda = 120$ TeV and neutralino lifetime of 2 ns, compared to the shapes for the lower and higher pileup subsamples. The bottom panel shows the ratio of each of the lower/higher pileup subsamples, divided in each case by the result for the full MC dataset. The three templates agree quite well with each other, with the observed variations being at the level of less than or about 15%. Figures for other MC data samples show similar variations. The three templates shown in Fig. 10.1 are included in the template fitting procedure, as possible systematic variations on the signal template shape due to pileup.

An additional source of uncertainty on the shape of the T_{sig} template could potentially arise from differences in the fraction of unconverted photons expected for non-prompt MC signal samples compared to the fraction observed in the data. For example, for a simulation sample with a neutralino lifetime of 2 ns, the fraction of photons reconstructed as unconverted was $85.7 \pm 0.4\%$. As discussed later, the fraction of photons reconstructed as unconverted in data, for the signal region as well as the control regions, was determined to be of the order of 60%. However, as shown in Fig. 10.2, the number of photons identified in signal MC as converted drops sharply for large values of $|z_{\mathrm{DCA}}|$. As a result, it was concluded that the differences in the fraction of photons reconstructed as unconverted in MC and data does not originate from actual differences in conversion rates. Instead, the lower fraction of conversions results from a lower efficiency of correctly associating tracker hits and finding the corresponding conversion tracks for converted photons which are strongly non-pointing. It is expected, therefore, that the signal MC describes sufficiently well the EM showers of the signal photons, irrespective of the drop in the efficiency of identifying conversions.

Potential mis-modeling of the detector material in simulation could also affect the shape of the

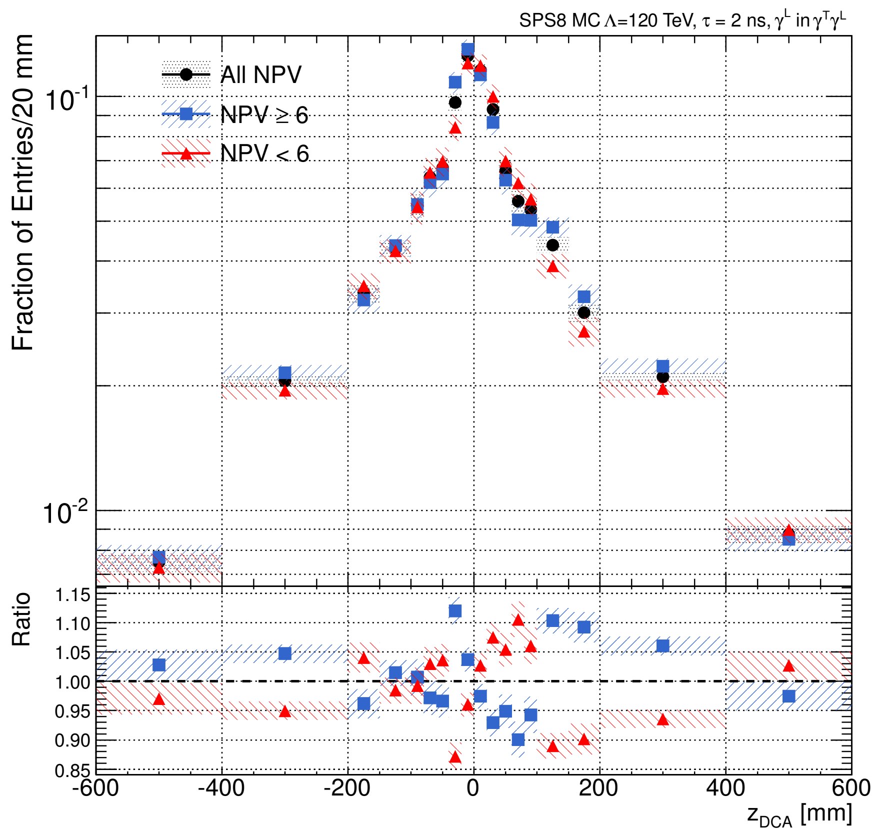

Figure 10.1: The shape of the unit-normalized Loose photon z_{DCA} distribution for a TL selection of the signal MC dataset with $\Lambda = 120$ TeV and NLSP lifetime of 2 ns, and for low/high pileup subsamples as defined in the text.

T_{sig} template. To allow a study of the impact of the uncertainty on the material distribution of the inner detector, one of the signal MC samples, namely that with $\Lambda = 120$ TeV and $\tau = 6$ ns, was simulated with both the nominal detector geometry and one with additional material. Fig. 10.3 shows the pointing distribution for both the nominal and additional material samples. Within the statistical uncertainties, the two distributions are very similar: the overall normalizations are the same within less than 0.5%, they both have means consistent with zero, and their RMS values, reflecting the impact of their finite widths and their tails, are also consistent. Given their similarities, it was concluded that the material uncertainties have a negligible impact on the results.

Given the studies described above, it was concluded that the only systematic uncertainty relevant for the T_{sig} templates is the contribution from pileup. The shape obtained from signal MC

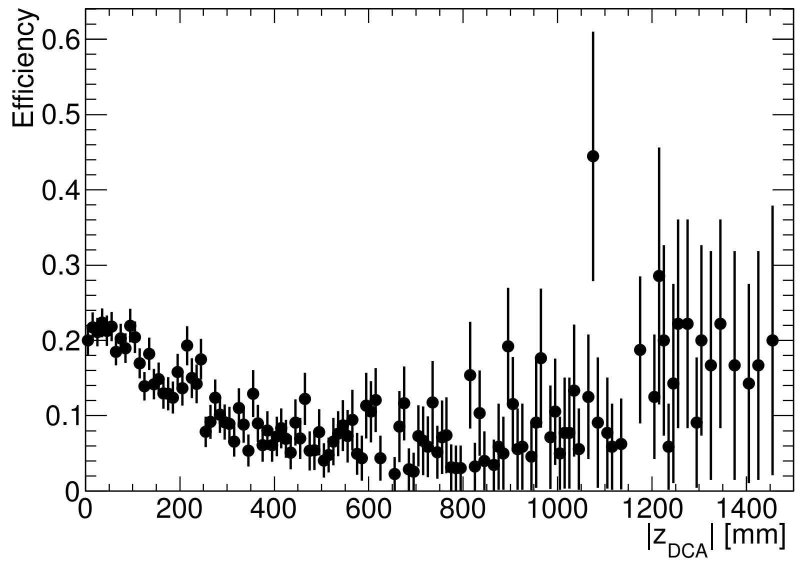

Figure 10.2: Efficiency in identifying photon conversions in signal MC, as a function of z_{DCA}.

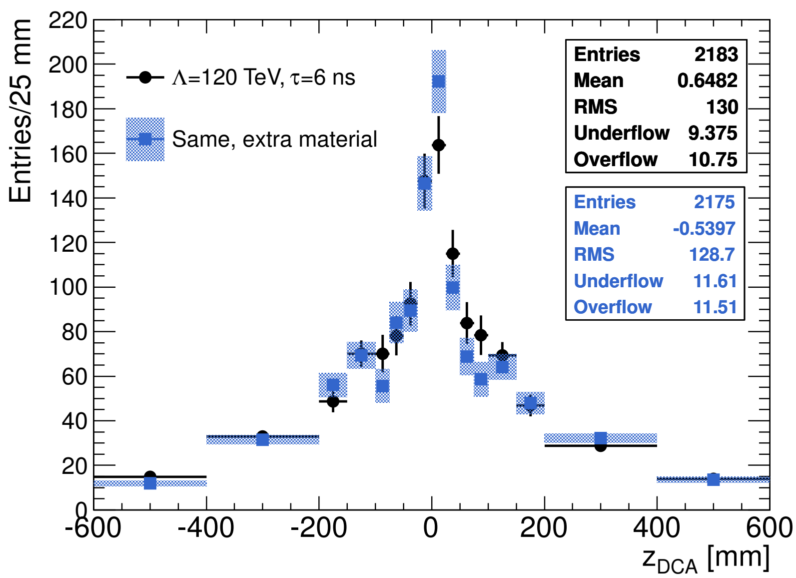

Figure 10.3: The pointing distribution for the nominal signal MC sample with $\Lambda = 120$ TeV and $\tau = 6$ ns, and for the sample with the same signal parameters but with additional material in the inner detector.

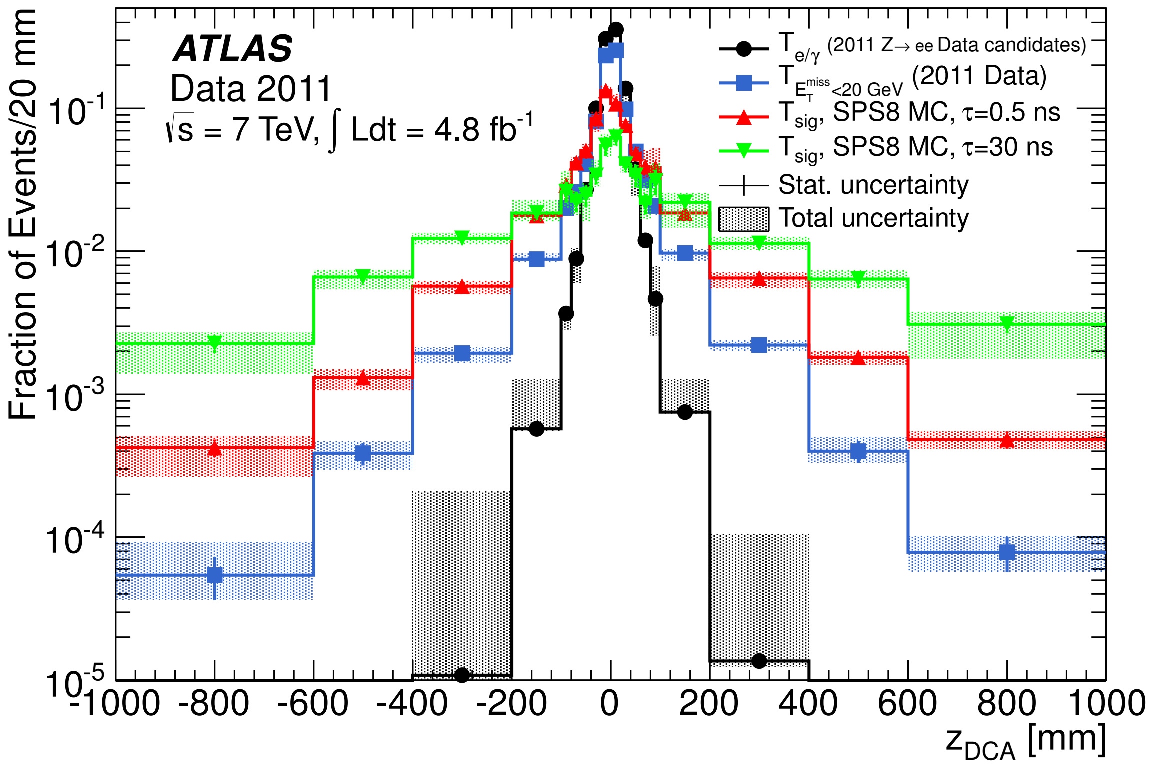

Figure 10.4: The z_{DCA} templates from $Z \rightarrow ee$ events, from the TL control sample with $E_{\mathrm{T}}^{\mathrm{miss}} < 20\,\mathrm{GeV}$, and for MC simulation of GMSB signals with $\Lambda = 120$ TeV and values for the NLSP lifetime of $\tau = 0.5$ and 30 ns. The data points show the statistical errors, while the shaded bands show the total uncertainties, with statistical and systematic contributions added in quadrature. The first (last) bin includes the contribution from underflows (overflows).

simulation for each signal point is therefore used as the central value, with the low and pileup sub-samples in each signal point defining their systematic variations. The T_{sig} distributions, along with their statistical and total uncertainties, are shown in Fig. 10.4 for $\Lambda = 120$ TeV and for NLSP lifetime values of $\tau = 0.5$ and 30 ns.

10.2 Background Modeling

The background is expected to be completely dominated by pp collision events. The contribution from pileup, satellite collisions, or non-collision sources such as cosmic rays or beam halo events, is expected to be negligible, as discussed later. The dominant background contributions are not categorized in terms of their production processes, but instead are organized according to their pointing and timing behavior.

The source of the Loose photon in background events contributing to the selected TL sample is expected to be either a prompt photon, an electron misidentified as a photon, or a jet misidentified as a photon. In each case, the object providing the Loose photon signature originates from the PV. However, differences in the shower shapes of these objects give rise to different z_{DCA} distributions. It is difficult to obtain an *a priori* prediction of the relative contributions from these sources, since the relevant misidentification rates are not described in MC with sufficient accuracy. For the same reason, an absolute prediction of the total background contribution in the TL sample is also infeasible. Instead, we utilize the differences in the pointing distribution shape between the main sources of background to determine the total background composition.

The pointing and timing distributions expected for the above background sources are determined using data control samples. Due to the similarities in the EM cascade produced by electrons and photons, the pointing resolution is similar for these two objects. As a result, the contribution to background from electrons and prompt photons is considered as a single source of background, modeled as discussed in Section 10.2.1. The contribution from jets constitutes the second component of the background and its modeling is described in Section 10.2.2.

10.2.1 Contribution from Prompt Photons and Electrons

The z_{DCA} distribution for prompt electrons and photons is obtained from a selection of $Z \to ee$ events with a ”tag-and-probe“ selection independent of, but similar to, the TL diphoton selection described previously. To avoid any bias, the pointing resolution for electrons is determined using the distribution measured for the probe electrons. The pointing distribution determined from $Z \to ee$ events, normalized to unit area, is used as the pointing template for prompt photons and electrons, and is referred to hereafter as $T_{e/\gamma}$. The $T_{e/\gamma}$ distribution, along with its statistical and total uncertainties, discussed briefly below, is shown superimposed on Fig. 10.4.

While the EM showers of electrons and photons are similar, there are some differences. In particular, electrons traversing the material of the ID may emit bremsstrahlung photons, widening the resulting EM shower. In addition, photons can convert into electron-positron pairs in the material of the ID. In general, the EM showers of unconverted photons are slightly narrower than those of electrons, which are in turn slightly narrower than those of converted photons. The EM component of the background in the signal region includes an unknown mixture of electrons, converted photons, and unconverted photons. Therefore, using electrons from $Z \to ee$ events to model the EM showers of the Loose photon candidates in the signal region can slightly underestimate the pointing resolution in some cases, and slightly overestimate it in others. The pointing distribution from $Z \to ee$ events is taken as the nominal $T_{e/\gamma}$ shape and the expected distributions from MC samples of unconverted and converted photons are separately taken to provide conservative estimates of the possible variations in the $T_{e/\gamma}$ shape which could result from not separating these various contributions. Fig. 10.5 shows the differences between electrons as opposed to converted or unconverted photons, in each case selected with similar energy distributions. As expected, the converted photon pointing distribution is wider than that of electrons, while the unconverted photon pointing distribution is narrower than that of electrons.

The different kinematic distributions, namely that the $Z \to ee$ sample is selected with $p_{\mathrm{T}}(e) > 25$ GeV while signal region photons must have $E_{\mathrm{T}}(\gamma) > 50$ GeV, also have an impact. Fig. 10.6 plots the normalized pointing distributions for electrons from $Z \to ee$ data and MC events, with $p_{\mathrm{T}}(e) > 25$ GeV, showing good agreement between data and MC. Superimposed are the distributions for unconverted and converted photons passing the signal region cut of $E_{\mathrm{T}} > 50$ GeV. As expected, the converted photon pointing distribution is still wider than that of unconverted photons, and the electron distribution has a width between those of the two categories of photons. However, the differences are more modest than in Fig. 10.5, since the higher E_{T} values for the photons has led to a narrowing of the photon pointing distributions. The similarities among the electron pointing distribution and the converted and unconverted photon pointing distributions indicate that the $T_{e/\gamma}$ template determined with $Z \to ee$ electrons models reasonably well the z_{DCA} distribution for background from prompt electrons and photons in the signal region.

The $T_{e/\gamma}$ template is much narrower than both the distributions for signal and for background which is dominated by jets and therefore has an important impact only on the core of the final pointing distribution for signal events. The main systematic concern, therefore, is how much the width of the core of the $T_{e/\gamma}$ template could vary. While Figures 10.5 and 10.6 show rather large ratios for values of $|z_{\mathrm{DCA}}|$ near 100 mm, these uncertainties are not very important in the final result since the template fit is dominated for large $|z_{\mathrm{DCA}}|$ by the $T_{E_{\mathrm{T}}^{\mathrm{miss}}<20\ \mathrm{GeV}}$ and signal templates.

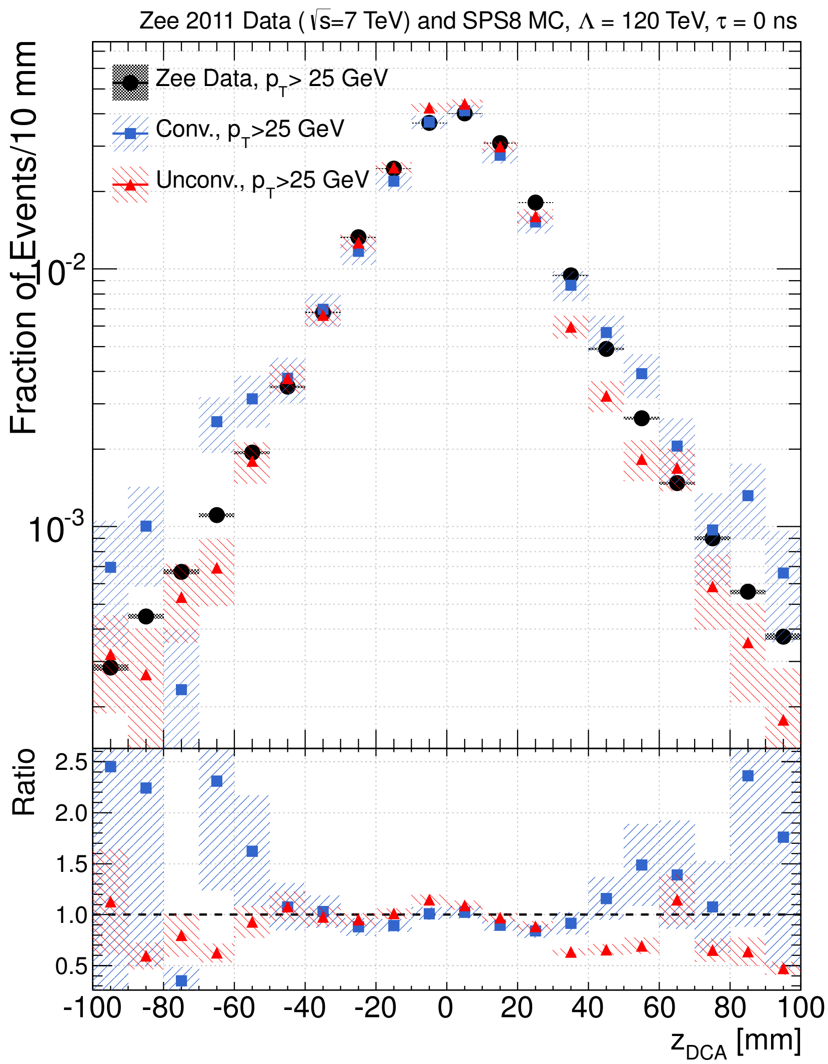

Figure 10.5: Normalized pointing distributions for electrons from $Z \rightarrow ee$ data events and for unconverted and converted photons, selected from a prompt SPS8 GMSB sample ($\Lambda = 120$ TeV, $\tau = 0$ ns), with similar kinematics.

As described previously, we take as the central estimate of the $T_{e/\gamma}$ template shape the distribution determined from $Z \rightarrow ee$ data events. As the widest (narrowest) reasonable distribution, we take the distribution for converted (unconverted) photons with $E_T > 25$ GeV, namely the photon distributions also shown superimposed on Fig. 10.5. The lower E_T photon distributions, rather than the distributions with higher photon E_T shown in Fig. 10.6, are used as a more conservative estimate of the systematic uncertainty.

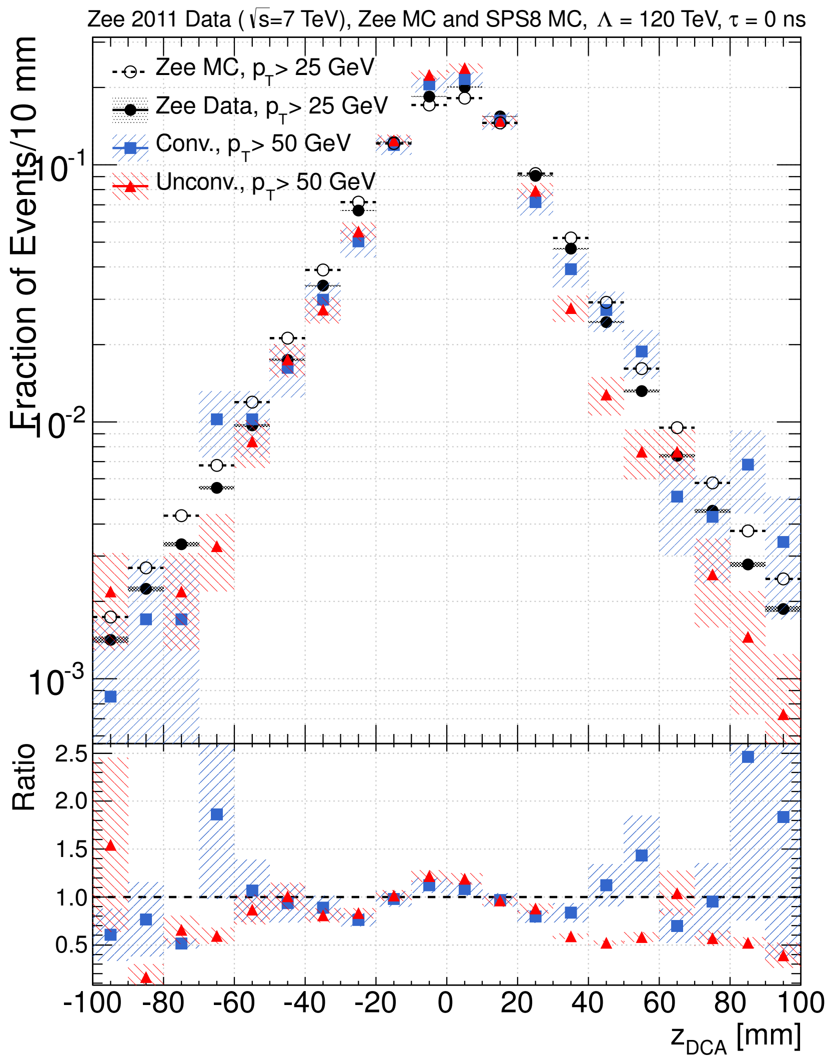

Figure 10.6: Normalized pointing distributions for electrons from $Z \to ee$ data and MC events, with $E_{\mathrm{T}}(e) > 25$ GeV. Superimposed are the distributions for unconverted and converted photons, selected from sample 157553 ($\Lambda = 120$ TeV, $\tau = 0$ ns), passing the analysis requirement $E_{\mathrm{T}} > 50$ GeV.

10.2.2 Contribution from Jets

The sample of events passing the TL selection, but with the additional requirement that $E_{\mathrm{T}}^{\mathrm{miss}} <$ 20 GeV, is used as a data control sample that includes jets with properties similar to the background contributions expected in the signal region. The $E_{\mathrm{T}}^{\mathrm{miss}}$ requirement serves to render negligible any possible signal contribution in this control sample. The shape of the z_{DCA} distribution for the Loose photon in these events, normalized to unit area, is used as a template, referred to hereafter as $T_{E_{\mathrm{T}}^{\mathrm{miss}}<20\ \mathrm{GeV}}$, in the final fit to the signal region.

The TL sample with $E_{\mathrm{T}}^{\mathrm{miss}} < 20$ GeV should be dominated by jet-jet, jet-γ and $\gamma\gamma$ events. Therefore, the $T_{E_{\mathrm{T}}^{\mathrm{miss}}<20\ \mathrm{GeV}}$ template includes contributions from photons as well as from jets faking the Loose photon signature. When using the template in the fit to extract the final results, it is not necessary to separate the photon and jet contributions. Instead, the relative fraction of the two background templates is treated as a nuisance parameter in the fitting procedure, as discussed later.

The shape of the $T_{E_{\mathrm{T}}^{\mathrm{miss}}<20\ \mathrm{GeV}}$ is determined entirely using data, and should therefore already correctly account for the impacts of pileup and material. To verify the modest effect of pileup, the pointing distribution in data control regions were compared to low and high pileup subsamples in the same regions. Fig. 10.7 show the pointing distributions in TL diphoton events with $E_{\mathrm{T}}^{\mathrm{miss}} <$ 20 GeV and $20 < E_{\mathrm{T}}^{\mathrm{miss}} < 75$ GeV. Very small variations are observed, indicating that pileup has a very small effect on the pointing shape.

The $T_{E_{\mathrm{T}}^{\mathrm{miss}}<20\ \mathrm{GeV}}$ template is also expected to model correctly the impact of the pointing resolution. However, it is known that the pointing resolution depends on E_{T}. Applying the shape of the $T_{E_{\mathrm{T}}^{\mathrm{miss}}<20\ \mathrm{GeV}}$ template to describe events in the signal region, defined with $E_{\mathrm{T}}^{\mathrm{miss}} > 75$ GeV, therefore implicitly relies on the assumption that the E_{T} distributions for photons are similar in the signal region and low $E_{\mathrm{T}}^{\mathrm{miss}}$ control region. However, since $E_{\mathrm{T}}^{\mathrm{miss}}$ is essentially a negative vector sum of the E_{T} values of the energy depositions in the calorimeter, it is expected that there should be a correlation between the value of $E_{\mathrm{T}}^{\mathrm{miss}}$ and the E_{T} distributions of the physics objects in the event. This correlation is observed in the TL control region samples, as illustrated in Table 10.1.

Increasing to 60 GeV the minimum E_{T} requirement on the photons in the $E_{\mathrm{T}}^{\mathrm{miss}} < 20$ GeV control sample provides events with more similar kinematic properties to the events in the signal region. Fig. 10.8 shows the Loose photon z_{DCA} distribution for TL events with $E_{\mathrm{T}}^{\mathrm{miss}} < 20$ GeV, obtained with various E_{T} requirements on the photon candidates. The bottom panel shows the ratio of each of the 50 and 70 GeV results, divided in each case by the 60 GeV result. The three templates agree quite well with each other, with the observed variations being at the level of less than or about 15%. As a cross-check, the right panel of Fig. 10.8 shows the results for the control

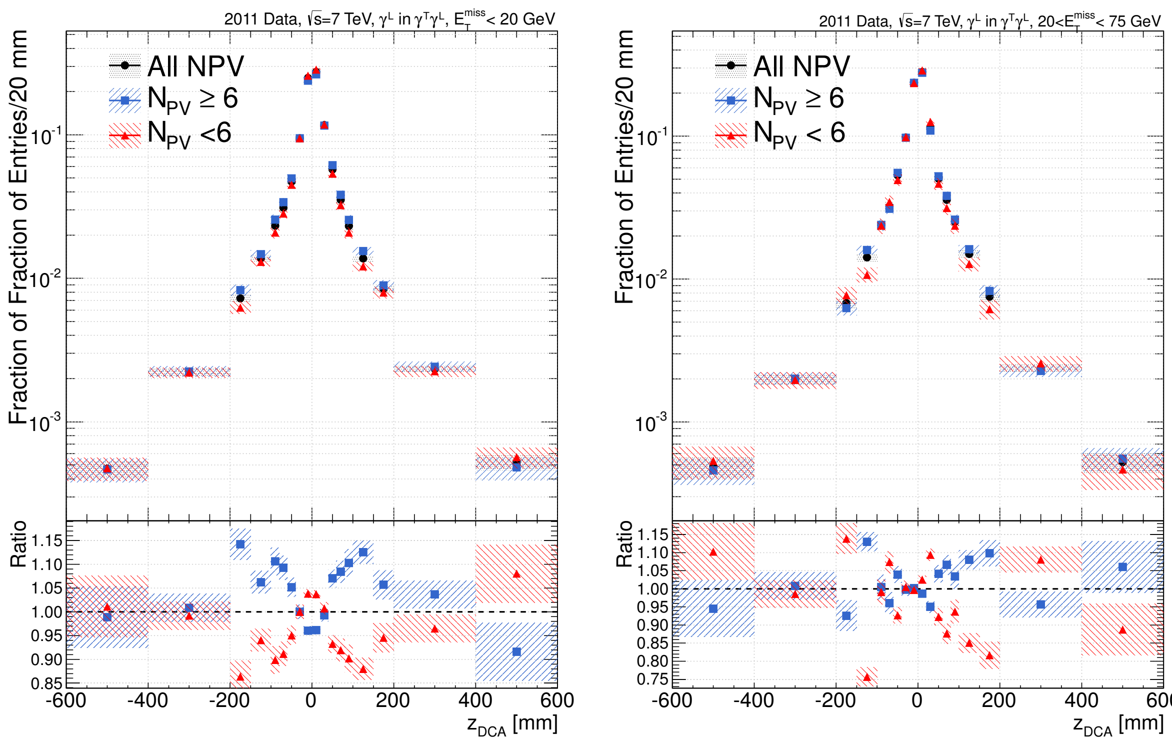

Figure 10.7: Data templates for the entire dataset in two data control regions and for low/high pileup subsamples. Shown are the control regions with (left) $E_{\mathrm{T}}^{\mathrm{miss}} < 20\,\mathrm{GeV}$ and (right) $20 < E_{\mathrm{T}}^{\mathrm{miss}} < 75\,\mathrm{GeV}$.

region with $20 < E_{\mathrm{T}}^{\mathrm{miss}} < 75$ GeV, showing similar variations. The three templates shown in the left panel of Fig. 10.8 will be included in the final template fitting: the 60 GeV shape will be used as the central value, and the others as possible systematic variations on the $T_{E_{\mathrm{T}}^{\mathrm{miss}}<20\,\mathrm{GeV}}$ template shape due to the dependence on the E_{T} of the photons.

As discussed in Section 10.2.1, it is expected that the pointing resolution will be worse for converted photons than for unconverted photons. This behavior is indeed observed in the $T_{E_{\mathrm{T}}^{\mathrm{miss}}<20\,\mathrm{GeV}}$ template, as shown in the left plot of Fig. 10.9. The ratio plot at the bottom panel shows that converted photons contribute more strongly to the tails of the z_{DCA} distribution (and less strongly to the core) compared to unconverted photons. As shown in the right plot of Fig. 10.9, similar behavior is observed for the TL control sample with $20 < E_{\mathrm{T}}^{\mathrm{miss}} < 75\,\mathrm{GeV}$. Of the photons in the TL control sample with $E_{\mathrm{T}}^{\mathrm{miss}} < 20$ GeV, which are used to determine the shape of the $T_{E_{\mathrm{T}}^{\mathrm{miss}}<20\,\mathrm{GeV}}$ template, the fraction that was identified as unconverted is $62.1 \pm 0.4\%$, in good agreement with

$E_{\mathrm{T}}^{\mathrm{miss}}$ **Range of Control Region**	**Photon E_{T} Cut [GeV]**	**Mean Photon E_{T} [GeV]**
0 – 20 GeV	50	70.0
	65	88.1
50 – 75 GeV	50	79.7

Table 10.1: The mean value of the photon E_{T}, listed for a variety of TL control samples defined according to their $E_{\mathrm{T}}^{\mathrm{miss}}$ range and minimum photon E_{T} requirement.

the corresponding value of $60.9 \pm 0.5\%$ for the TL control sample with $20 < E_{\mathrm{T}}^{\mathrm{miss}} < 75$ GeV. The value for the signal region with $E_{\mathrm{T}}^{\mathrm{miss}} > 75$ GeV is $67.4 \pm 6.9\%$, which is also in good agreement, albeit with a sizable statistical error. Given the consistency of these numbers, and the fact that the template is determined from data, no systematic uncertainty is needed to account for the possible impact of differences between converted and unconverted photons on the shape of the $T_{E_{\mathrm{T}}^{\mathrm{miss}}<20\ \mathrm{GeV}}$ template.

The $T_{E_{\mathrm{T}}^{\mathrm{miss}}<20\ \mathrm{GeV}}$ template, along with its statistical and total uncertainties, is shown superimposed on Fig. 10.4.

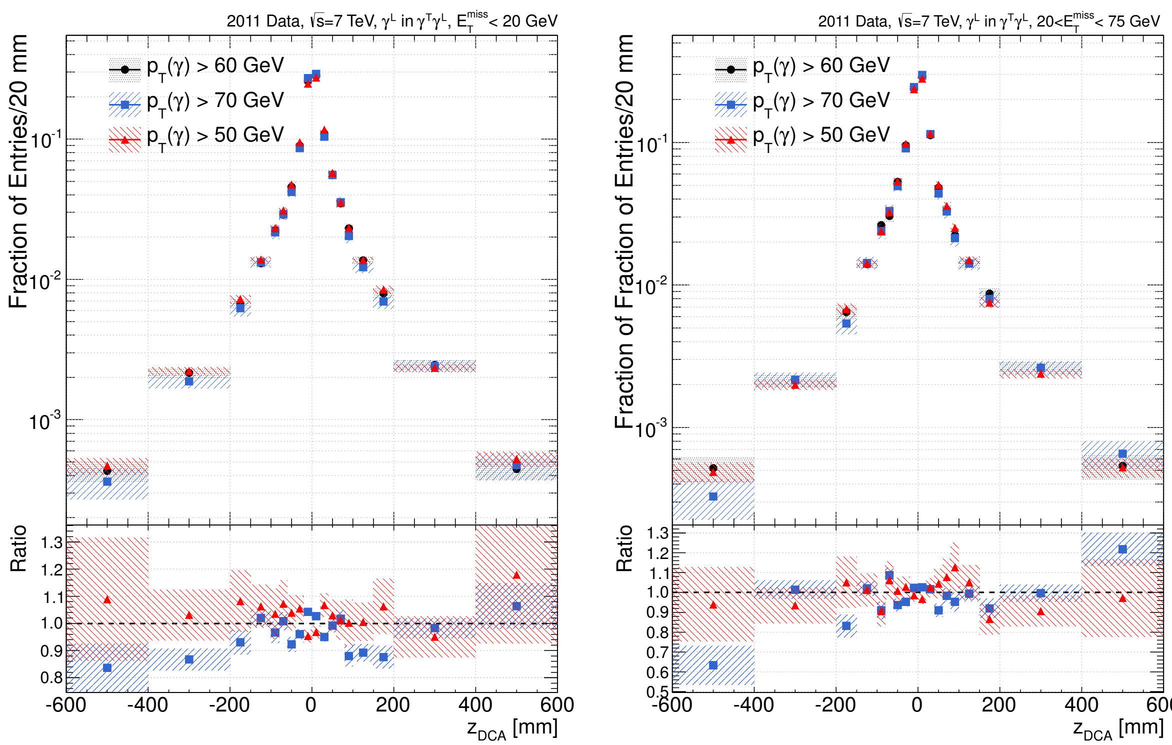

Figure 10.8: The shape of the unit-normalized $T_{E_{\mathrm{T}}^{\mathrm{miss}}<20\ \mathrm{GeV}}$ template with minimum E_{T} requirements on the photons of 50, 60 and 70 GeV. The $E_{\mathrm{T}}^{\mathrm{miss}} < 20$ GeV control sample is shown on the left, and the results for the $20 < E_{\mathrm{T}}^{\mathrm{miss}} < 75$ GeV control sample is shown on the right.

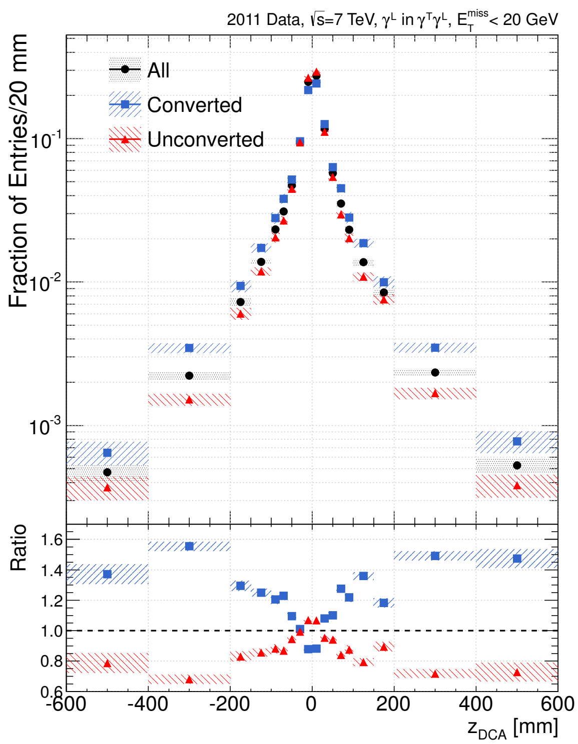

Figure 10.9: Unit-normalized z_{DCA} template for the TL control sample with (left) $E_{\mathrm{T}}^{\mathrm{miss}} < 20\,\mathrm{GeV}$ and (right) $20 < E_{\mathrm{T}}^{\mathrm{miss}} < 75\,\mathrm{GeV}$, as well as the results showing separately the contributions from converted and from unconverted photons. The bottom panel shows the ratio of the converted and unconverted distributions, divided in each case by the distribution over all photons, independent of conversion status.

10.3 Timing Templates

Photons from NLSP decays in GMSB signal events would reach the LAr calorimeter with a slight delay compared to prompt photons produced directly in the hard scatter. This delay results mostly from the flight time of the heavy NLSP, as well as some effect due to the longer geometric path of a non-pointing photon produced in the NLSP decay. The excellent timing performance of the LAr calorimeter can therefore be employed to discriminate between the prompt background and any signal photons. In this analysis, the timing measurement is used to cross-check the results obtained by using the pointing measurement.

The LAr timing performance is not simulated properly in MC, and it is necessary to apply additional smearing to the MC in order to match the resolution observed in the data. Fig. 10.10 shows the timing distribution for electrons in $Z \to ee$ data, with an RMS of approximately 340 ps and a mean of the order of 10 ps. Superimposed are several MC timing distributions. The raw timing distribution for a prompt GMSB sample is shown, demonstrating that the time for prompt electrons in MC with an RMS of $\sim$ 160 ps does not have the spread expected in data. Applying additional smearing to the prompt sample leads to a result which reproduces well the $Z \to ee$ timing performance, with a smeared distribution RMS of $\sim$ 350 ps and mean of $\sim$ 15 ps. This additional smearing is subsequently applied to MC signal samples with finite NLSP lifetimes, illustrating the level of separation possible between prompt and delayed photons. As can be seen in Fig. 10.10, the distributions for the non-prompt samples with $\tau(\tilde{\chi}_1^0) = 1$ ns and 6 ns are clearly asymmetric with large positive tails, with mean values of $\sim$ 470 ps and $\sim$ 1 ns, respectively, while the RMS of the distributions are 590 ps and 1 ns, respectively, significantly deviating from what is expected for prompt background.

The expectations for the backgrounds are determined using the same data control samples described previously. It is expected that the performance of the calorimeter timing measurement, as determined using the second-layer cell with the maximum deposited energy, should be rather insensitive to the details of the EM shower development. As shown in Fig. 10.11, it was verified that the timing distribution of electrons in $Z \to ee$ events is very similar to that of Loose photon candidates in the TL control sample with $E_{\mathrm{T}}^{\mathrm{miss}} < 20$ GeV. Therefore, the timing distribution determined with the larger $Z \to ee$ sample is characteristic of the timing performance expected for all prompt backgrounds, and is shown on Fig. 10.12. Superimposed in Fig. 10.12, are the

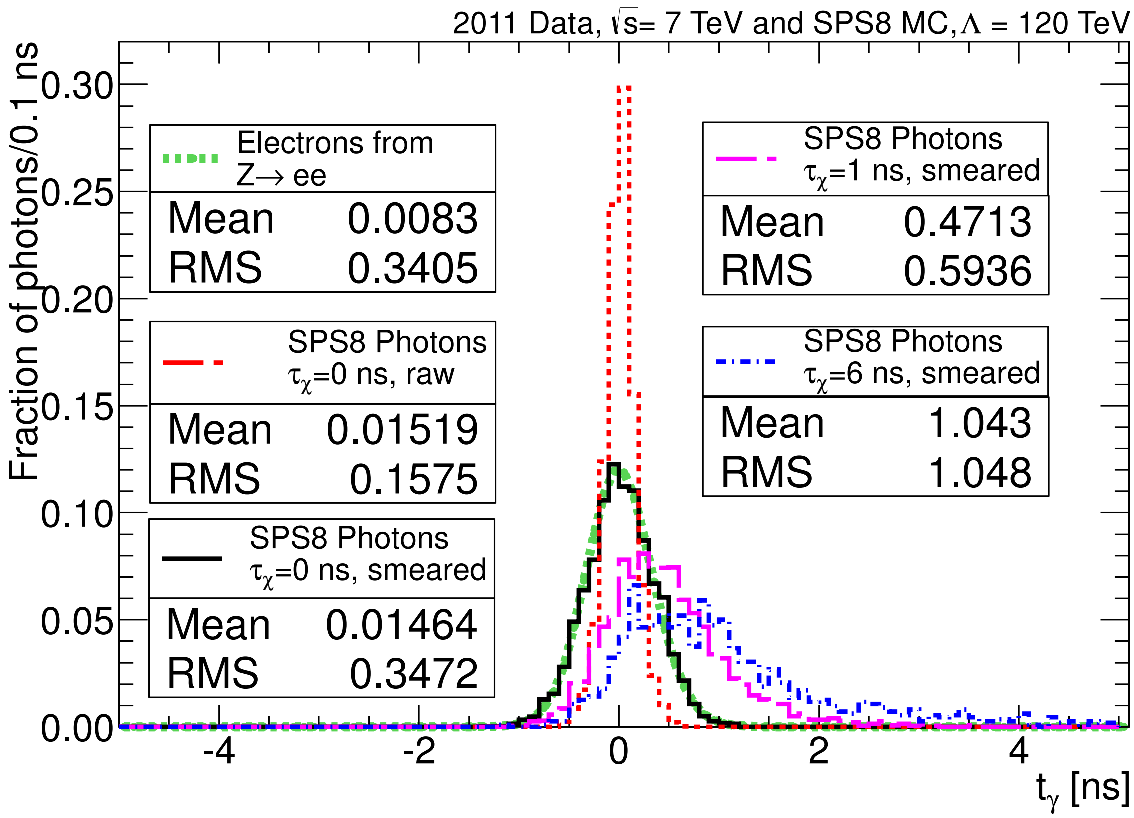

Figure 10.10: Timing distribution for $Z \rightarrow ee$ events (green points), for a prompt MC sample before (red) and after (black) applying additional smearing, and for two MC signal samples (magenta and dark blue) with finite neutralino lifetimes. For more details, see text.

timing distributions expected for selected signal events, for $\Lambda = 120$ TeV and for NLSP lifetime values of $\tau = 0.5$ and 30 ns.

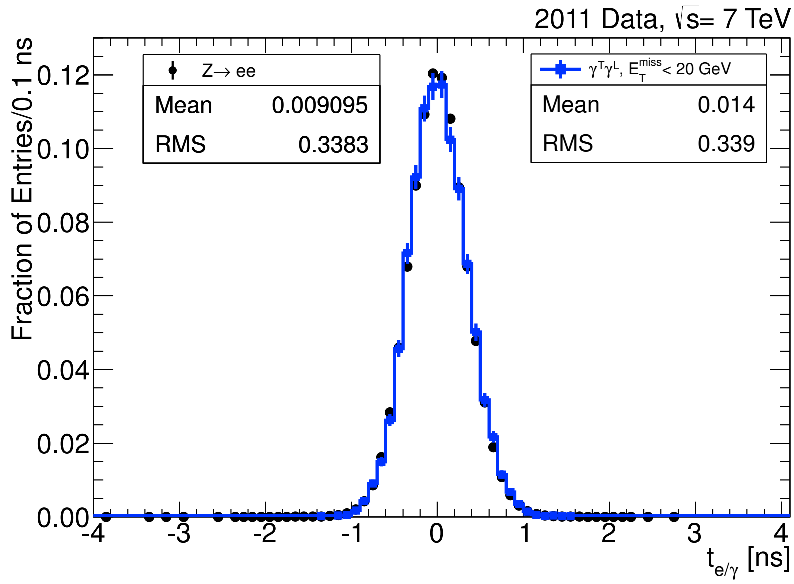

Figure 10.11: The timing templates as determined for prompt electrons/photons from two data samples: a $Z \rightarrow ee$ sample (points) and the TL sample (blue) with $E_{\mathrm{T}}^{\mathrm{miss}} < 20$ GeV.

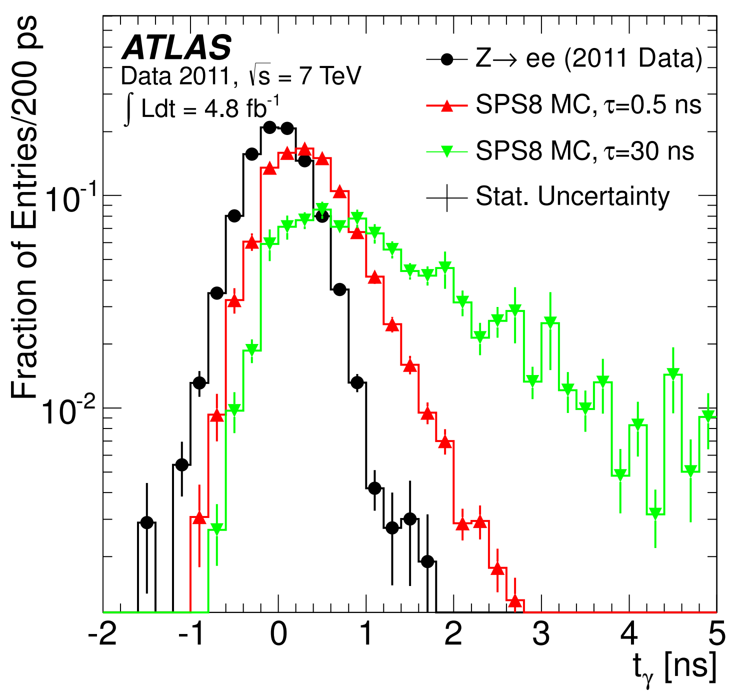

Figure 10.12: The distribution of photon arrival times (t_{γ}) expected for SPS8 GMSB signal models with $\Lambda = 120$ TeV and for NLSP lifetime values of $\tau = 0.5$ and 30 ns. Superimposed is the expectation for prompt backgrounds, as determined using electrons from $Z \rightarrow ee$ events. The uncertainties shown are statistical only.

10.4 Other Backgrounds

Backgrounds could arise from situations in which the Loose photon candidate does not originate from the PV due to, for example, an overlap of two separate events due to pileup or an overlap of an event with a satellite collision. These two scenarios are discussed briefly below.

Events overlapping with a beam halo [117] event are expected to be rejected [93] by the very loose criteria for rejecting events with "bad" jets, as introduced in Section 6.3, which provide a fake-jet rejection factor better than approximately 50% while maintaining an efficiency above 99.8% [118]. The bad jet rejection criteria also contribute to the rejection of events overlapping with cosmic ray activity. Such events are further rejected by the use of the cosmic muon veto (see Section 8.3.3) and the standard EM cluster time cut applied to electrons and photons, as described in Section 6.1.2 and 6.1.3. A previous ATLAS analysis [119] with similar event selection criteria, has shown that non-collision backgrounds are negligible.

To estimate the level of the background contribution from multiple events overlapping in the same bunch crossing, we consider the example of a $W \to e\nu$ event overlapping with a separate event producing a high E_{T} photon. This situation could mimic the final signature of a tight photon (the electron faking a photon), $E_{\mathrm{T}}^{\mathrm{miss}}$ (due to the neutrino), and a photon that does not point back to the PV (of the W boson event). An estimate of the rate of such overlaps can be obtained using ATLAS measurements of the relevant cross sections, as described below.

The total inelastic cross section at $\sqrt{s} = 7$ TeV has been measured [120] by ATLAS to be (60.3 ± 2.1) mb. The full 2011 dataset of ~ 5 fb^{-1} therefore corresponds to $\sim 3 \times 10^{14}$ inelastic collisions. The fiducial $W \to e\nu$ cross section has been measured to be (4.791 ± 0.0186) nb [121], where the fiducial region requires $E_{\mathrm{T}}(e) > 20$ GeV, $E_{\mathrm{T}}^{\mathrm{miss}} > 25$ GeV, and transverse mass $M_{\mathrm{T}} >$ 40 GeV. The probability per collision to produce such a $W \to e\nu$ event is therefore $\sim 8 \times 10^{-8}$. The ATLAS measurement of the inclusive photon cross section is approximately (5.88 ± 0.21) nb for $E_{\mathrm{T}}(\gamma) > 45$ GeV [122]. Therefore, the probability per collision to produce such a photon is $\sim 10^{-7}$.

Given these probabilities, we can calculate the rate of overlaps of $W \to e\nu$ events with prompt photon events in the full 2011 dataset of $\sim 3 \times 10^{14}$ inelastic collisions, which were produced with an average pileup rate of ~ 10 collisions per bunch crossing. The result is a prediction of ~ 24 bunch crossings with these overlapping events produced.

The selection requirements would provide additional suppression of these events. The probability for an electron to be misidentified as a tight photon, as estimated by the prompt diphoton analysis [48], varies between 2.5% and 7.0%. Requiring that the electron from the W decay be misidentified as a Tight photon would, therefore, provide a reduction by a factor of $\sim 15-40$. In addition, both photon candidates are required to have $E_{\mathrm{T}} > 50$ GeV and $E_{\mathrm{T}}^{\mathrm{miss}} > 75$ GeV. While the $E_{\mathrm{T}}(\gamma)$ requirement is only slightly higher than the 45 GeV requirement used in the measured photon cross section, raising the E_{T} cut on the electron and the $E_{\mathrm{T}}^{\mathrm{miss}}$ cut would reduce the expected rate of $W \rightarrow e\nu$ events by an additional significant factor, estimated to be ~ 25. Even neglecting any further suppression factors arising from inefficiencies in our selection, a prediction of a small fraction of one overlap event in the final signal sample is obtained.

Due to the LHC bunch structure, an additional source of background not originating from the PV can arise from any interactions between the proton bunches that are not nominally colliding. The LHC operates an RF system with a 2.5 ns bucket spacing, where nominally every 10th bucket is filled for 25 ns bunch spacing operation. For various reasons, the empty buckets adjacent to the nominally filled bucket can capture protons, leading to the formation of so-called satellite bunches. Satellite collisions can occur when the nominal bunch collides with a satellite bunch, producing interactions at positions $z = \pm k \cdot 37.5$ cm and delayed by $k \cdot 1.25$ ns, where $k = 1, 2, \ldots$. Collisions between the satellite bunches can also occur, producing interactions approximately centered at $z = 0$ and at a time early or delayed by multiples of 2.5 ns.

Based on measurements in Van der Meer scans performed in 2010, the estimated fraction of protons in satellite collisions with respect to the nominal bunch is approximately 10^{-3} [123]. This suggests that collisions between satellite and nominal bunches are suppressed by three orders of magnitude, whereas collisions between satellite bunches are suppressed by a factor of 10^{6}. Taking into account the satellite bunch populations and the LHC parameters in 2011, overlaps of a main collision event with an event from satellite collision would be extremely rare and, therefore, this potential source of background is negligible.

Chapter 11

Systematic Uncertainties

This chapter discusses the systematic uncertainties that affect this analysis. In general, the various systematic uncertainties are divided into two types, namely "flat" uncertainties that are not a function of z_{DCA}, and "shape" uncertainties modifying the shapes of the background and signal pointing templates. Flat uncertainties contribute to uncertainties in the signal yield and are discussed in Section 11.1. Sources of systematic uncertainties that can affect the shape of the templates were described in Chapter 10 and are not repeated in this chapter. A summary of all the relevant systematic uncertainties is given in Section 11.2.

11.1 Flat Systematic Uncertainties

For the uncertainty in the measurement of the total integrated luminosity, the standard ATLAS value is used. The luminosity uncertainty for the 2011 dataset used in this analysis was measured to be ±1.8% [124, 74].

For the determination of the diphoton trigger efficiency, the bootstrap method was used for prompt photons, with an associated uncertainty estimated at ±0.5%. As described in Section 9.1, no evidence was observed for a dependence of the L1 trigger efficiency on z_{DCA}. However, a conservative flat uncertainty of ±2% is assigned to account for any possible such variations. Adding these two contributions in quadrature, a total uncertainty on the trigger efficiency of ±2.1% is obtained.

As described in Section 9.2.2, the differences between data and MC for the various shower shape variables were observed to be independent of z_{DCA}. Therefore, it is sufficient to use the "fudge factor" strategy to correct those differences and estimate the resulting systematic uncertainty. The photon ID requirements are applied with and without the shifts on the shower shape variables to obtain the systematic uncertainties on the photon ID resulting from the disagreement between data and MC. An uncertainty of ±4.4% per event is used, which includes effects of the photon E_{T} scale and resolution as well as the identification of both photons.

The systematic uncertainty due to the photon isolation requirement was determined by shifting the cut by the difference in mean of the photon isolation variable distributions between data and MC, as described in Ref. [125, 48]. From this analysis, it was determined that the mean of the `etcone20` distributions of electrons in $Z \rightarrow ee$ data and MC samples are shifted by 0.4 GeV. To assess the impact of the isolation uncertainty on the signal efficiency, the photon isolation selection cut was changed from 5 GeV to 4.6 GeV and 5.4 GeV, and the result on the change in signal efficiency was assessed for a sample of the signal grid points, as shown in Table 11.1. The largest deviation in Table 11.1 was taken as a conservative and symmetric uncertainty of ±1.4%.

Λ [TeV]	τ [ns]	**Efficiency difference (%) when lowering isolation cut to 4.6 GeV**	**Efficiency difference (%) when raising isolation cut to 5.4 GeV**
90	2	-0.8	+0.8
90	6	-1.4	+0.6
100	2	-1.0	+0.7
100	6	-0.8	+0.9
120	2	-0.7	+0.6
120	10	-1.1	+0.9
150	2	-0.9	+0.6
200	2	-0.9	+0.6

Table 11.1: Change in signal efficiency for a sample of SPS8 GMSB signal MC points as the isolation cut is changed by ±0.4 GeV.

In analyses involving photons, a selection has to be applied to reject bad quality clusters or fake clusters originating from calorimeter problems, using the Object Quality (OQ) flags, as discussed in Section 6.1.2. Further, as discussed in Section 8.4, the event selection takes into account any detector issues and pathologies. However, the ATLAS MC samples used in this analysis have been simulated to reflect the detector features found in the data as closely as possible. For 2011 data and MC, a systematic uncertainty on the usage of the OQ flag has been calculated [126]. This uncertainty is taken as the difference of efficiency between data and MC, and was found to be 0.1% per photon. Since the signal has two photons, this systematic uncertainty is ±0.2%, assuming 100% correlation between the two photons.

11.1.1 $E_{\mathrm{T}}^{\mathrm{miss}}$ Uncertainties

Given the definition of $E_{\mathrm{T}}^{\mathrm{miss}}$ used in this analysis, two main sources of systematic uncertainty were considered: the uncertainty on the TopoCluster energy scale, and the uncertainty on the $E_{\mathrm{T}}^{\mathrm{miss}}$ resolution. Any effects from the muon corrections to the $E_{\mathrm{T}}^{\mathrm{miss}}$ were previously shown to be negligible [125, 48]. Contributions from pileup were not considered, since they are included in the overall treatment of the impact of pileup on the event selection.

The uncertainty on $E_{\mathrm{T}}^{\mathrm{miss}}$ due to the TopoCluster energy scale was estimated by varying the energies of the TopoClusters using the TopoCluster energy scale uncertainty. The TopoCluster energy scale can be estimated by comparing the momentum and energy measurements of charged particles [127, 128], and its uncertainty has been determined from comparisons between data and MC simulation to vary from ±20% for $p_{\mathrm{T}} \approx 500$ MeV to ±5% at high p_{T} [129, 130]. Subsequently, the difference in the signal acceptance due to the changes in the $E_{\mathrm{T}}^{\mathrm{miss}}$ measurement was used as the systematic uncertainty and was found to vary between $\pm(1.0-6.4)\%$ across the set of generated signal MC points.

Similarly, the uncertainty on the $E_{\mathrm{T}}^{\mathrm{miss}}$ resolution [131] was used to vary the measurement of $E_{\mathrm{T}}^{\mathrm{miss}}$. The resolution for each component of $E_{\mathrm{T}}^{\mathrm{miss}}$ was parametrized as a function of the total transverse energy of the event, ΣE_{T}, as $\sigma = k \cdot \sqrt{\Sigma E_{\mathrm{T}}}$. The parameter k was measured to be $k = 0.49$ for minimum bias events at $\sqrt{s} = 7$ TeV. With the requirement of at least one jet with $p_{\mathrm{T}} > 20$ GeV, the resolution parameter was measured to be $k = 0.53$ [130]. Further, it was determined that, in events with at least two photons with $p_{\mathrm{T}} > 20$ GeV satisfying the loose identification criteria, the $E_{\mathrm{T}}^{\mathrm{miss}}$ resolution parameters in data and SPS8 MC simulation agree within 14% [125]. Subsequently, for each signal MC point, the $E_{\mathrm{T}}^{\mathrm{miss}}$ resolution parameter was varied with Δk in the range $[-0.16, 0.16]$ with respect to the nominal measured value of k, and the change in the efficiency of the $E_{\mathrm{T}}^{\mathrm{miss}}$ requirement was determined. The change of the efficiency of the $E_{\mathrm{T}}^{\mathrm{miss}}$ requirement was then studied as a function of Δk and fitted to a first-order polynomial. The result of the fit was used to estimate the change in efficiency of the $E_{\mathrm{T}}^{\mathrm{miss}}$ requirement resulting from a change in k of 14%. The resulting acceptance differences were used as the systematic uncertainty on the $E_{\mathrm{T}}^{\mathrm{miss}}$ requirement due to the $E_{\mathrm{T}}^{\mathrm{miss}}$ resolution uncertainty, and were found to vary between 0 and ±4.9% for different signal MC points.

11.1.2 Signal MC Statistics

For the majority of our signal MC samples, each point was generated with approximately 20,000 events, with some points having increased statistics with approximately 40,000 events. The uncertainty on the signal efficiency due to MC statistics lies typically in the range of $\pm(0.7-5.0)\%$. For the signal MC efficiency and its associated uncertainty per point, see Table 9.2.

11.1.3 Signal PDF and Scale Uncertainties

The uncertainties on the calculated SPS8 GMSB signal cross section due to uncertainties on the PDFs, as well as uncertainties on the factorization and renormalization scales, are computed as described in Section 8.6. The resulting uncertainties are presented in Table 8.3, and vary between $\pm(4.7-6.4)\%$ for different signal MC points. The quoted values include both the PDF and scale uncertainties.

11.2 Summary of Systematic Uncertainties

The various flat systematic uncertainties are summarized in Table 11.2. As discussed previously, the flat systematic uncertainties are treated as symmetric and uncorrelated, and contribute collectively to a total uncertainty in the signal yield. The total systematic uncertainty on the signal yield, obtained by adding the individual uncertainties in quadrature, lies in the range $\pm(7.2-11.7)\%$, which does not include the contribution of $\pm(0.7-5.0)\%$ due to statistical uncertainties in the signal MC predictions. Uncertainties affecting the shape of the pointing distributions are also considered, as described in Chapter 10.

Impact	Source of Uncertainty	Value	Comment
Signal Yield	Integrated Luminosity	±1.8%	Section 11.1
	L1 Trigger Efficiency	±2%	Section 11.1
	HLT Efficiency	±0.5%	
	Photon E_{T} Scale/Resolution and Photon Identification	±4.4%	Section 11.1
	Photon Isolation	±1.4%	
	Object Quality and LAr Hole Flags	±0.2%	
	$E_{\mathrm{T}}^{\mathrm{miss}}$: Topocluster Energy Scale	$\pm(1.0-6.4)\%$	Section 11.1.1
	$E_{\mathrm{T}}^{\mathrm{miss}}$ Resolution	$\pm(0-4.9)\%$	
	Signal PDF and Scale Uncertainties	$\pm(4.7-6.4)\%$	Section 11.1.3
	Total Flat Systematic Uncertainty	$\pm(7.2-11.7)\%$	Does not Include Signal MC Statistics
	Signal MC Statistics	$\pm(0.7-5)\%$	Table 9.2
	Signal Template	Shape	Section 10.1
Background	e/γ Template	Shape	Section 10.2.1
	$E_{\mathrm{T}}^{\mathrm{miss}} < 20$ GeV Template	Shape	Section 10.2.2

Table 11.2: Summary of systematic uncertainties.

Chapter 12

Template Fitting and Limit Setting Procedures

In this chapter, the procedure used to fit the pointing distributions is described. From the results of the fit, limits are set on the number of observed signal events, with a procedure that is also described briefly. Finally, tests performed to validate the fitting procedure are discussed.

12.1 Description of the Template Fitting Procedure

An absolute background prediction is neither provided, nor needed, in this analysis. Instead, the number of signal (N_{sig}) and background events (N_{bkg}) is normalized to the sum of the number of events observed in the data and used as a constraint in the fitting procedure described below. To determine the contribution from signal, as well as the separate contributions from the backgrounds due to jets and to prompt photons/electrons, the z_{DCA} templates are fitted to the z_{DCA} distribution observed for the Loose photon.

Let T_{sig} be the signal pointing template for a given pair of (Λ, τ) values, obtained using signal MC simulation. The background contribution can be modeled as a weighted sum of the $T_{e/\gamma}$ template, and a template describing the pointing distribution of jets, T_{jet}, with a factor f_{jet}, dubbed the "jet fraction", controlling the relative weighting of the two background sources. The T_{sig}, $T_{e/\gamma}$ and T_{jet} templates can be fitted to the z_{DCA} data distribution, with N_{sig}, N_{bkg}, and f_{jet} used as fit parameters. Denoting by Z^i_{data} the content in bin i of the z_{DCA} distribution observed in data, one can write the following expression:

$$Z^i_{\text{data}} = N_{\text{bkg}} \cdot \left[f_{\text{jet}} \cdot T^i_{\text{jet}} + \left(1 - f_{\text{jet}}\right) \cdot T^i_{e/\gamma} \right] + N_{\text{sig}} \cdot T^i_{\text{sig}} \quad . \tag{12.1}$$

As discussed previously, the prompt electron/photon template, $T_{e/\gamma}$, is measured using $Z \to ee$ events. However, the jet template, T_{jet}, is not measured directly; instead, what is measured is $T_{E_{\text{T}}^{\text{miss}}<20\text{ GeV}}$, the template of TL events in the control sample with $E_{\text{T}}^{\text{miss}} < 20$ GeV. This control sample is a sample of jets which could be contaminated by a fraction $f_{e/\gamma}^{E_{\text{T}}^{\text{miss}}<20\text{ GeV}}$ of prompt electrons/photons. Taking the contamination into consideration, T^i_{jet} can be rewritten as

$$T^i_{\text{jet}} = \frac{\left(T^i_{E_{\text{T}}^{\text{miss}}<20\text{ GeV}} - f_{e/\gamma}^{E_{\text{T}}^{\text{miss}}<20\text{ GeV}} \cdot T^i_{e/\gamma} \right)}{\left(1 - f_{e/\gamma}^{E_{\text{T}}^{\text{miss}}<20\text{ GeV}} \right)} \quad . \tag{12.2}$$

Replacing T^i_{jet} in Eq. 12.1 with the right hand side of Eq. 12.2 and re-arranging, one obtains the following:

$$Z^i_{\text{data}} = N_{\text{bkg}} \cdot \left[F_{\text{jet}} \cdot T^i_{E_{\text{T}}^{\text{miss}}<20\text{ GeV}} + \left(1 - F_{\text{jet}}\right) \cdot T^i_{e/\gamma} \right] + N_{\text{sig}} \cdot T^i_{\text{sig}} \tag{12.3}$$

where the symbol F_{jet}, denoted as the "modified jet fraction", has been defined as shorthand for

$$F_{\text{jet}} = \frac{f_{\text{jet}}}{\left(1 - f_{e/\gamma}^{E_{\text{T}}^{\text{miss}}<20\text{ GeV}} \right)} \quad . \tag{12.4}$$

Therefore, the distribution observed in the TL signal sample with $E_{\text{T}}^{\text{miss}} > 75$ GeV can be fitted using Eq. 12.3 with an appropriately weighted combination of the z_{DCA} template of the TL sample with $E_{\text{T}}^{\text{miss}} < 20$ GeV, the prompt electron/photon template from $Z \to ee$ events, and the signal template. The normalized templates and their shape uncertainties are provided as inputs to the fitting procedure, which returns the best-fit results for N_{sig} and N_{bkg}, with F_{jet} treated as a nuisance parameter.

12.2 Limit Setting Procedure

Background-only fits were performed to determine the compatibility of the observed pointing distribution with the background-only hypothesis. For each signal MC point, signal-plus-background fits were performed to obtain the best-fit results under the signal-plus-background hypothesis. The final limits were determined by performing a binned profile likelihood fit using the RooStats framework [132]. Using the CLs method [133], 95% CL limits were set on the signal strength, μ, defined as the number of fitted signal events divided by the SPS8 expectation for the signal yield. Limits on the observed number of signal events were obtained by fitting the z_{DCA} distribution observed in data, while the expected limits were obtained by performing the same procedure over ensembles of pseudo-experiments generated according to the background-only hypothesis.

12.3 Validation of the Fitting Procedure

Before inspecting the pointing distribution for events in the signal region, the template fitting procedure was validated on different control samples. A validation method performed with generated pseudo-data is described in the next section, followed by the results of performing the procedure over control regions in the TL diphoton sample.

12.3.1 Results for Generated Pseudo-data

Using pseudo-data generated according to the $T_{e/\gamma}$ and $T_{E_{\mathrm{T}}^{\mathrm{miss}}<20\ \mathrm{GeV}}$ templates obtained from data, a number of checks of the fitting procedure were performed. For example, Fig. 12.1(left) shows the results obtained by fitting pseudo-data datasets with varying fractions due to jets, and with the total number of background and signal events fixed to 46. As can be seen, the fit returned on average a jet fraction which agreed with the input jet fraction, verifying that the fitting procedure is linear against variations of this fit parameter.

The right plot of Fig. 12.1 shows the expected 95% CL limit on the number of signal events, as returned by the fitting procedure applied to the same pseudo experiments, using an example SPS8 GMSB signal MC sample with $\Lambda = 130$ TeV and $\tau = 10$ ns. Note that the expected limit depends on the jet fraction of the pseudo-data. This result is expected, since the jet template is significantly wider than the template for electrons/photons, and more closely resembles the template for signal.

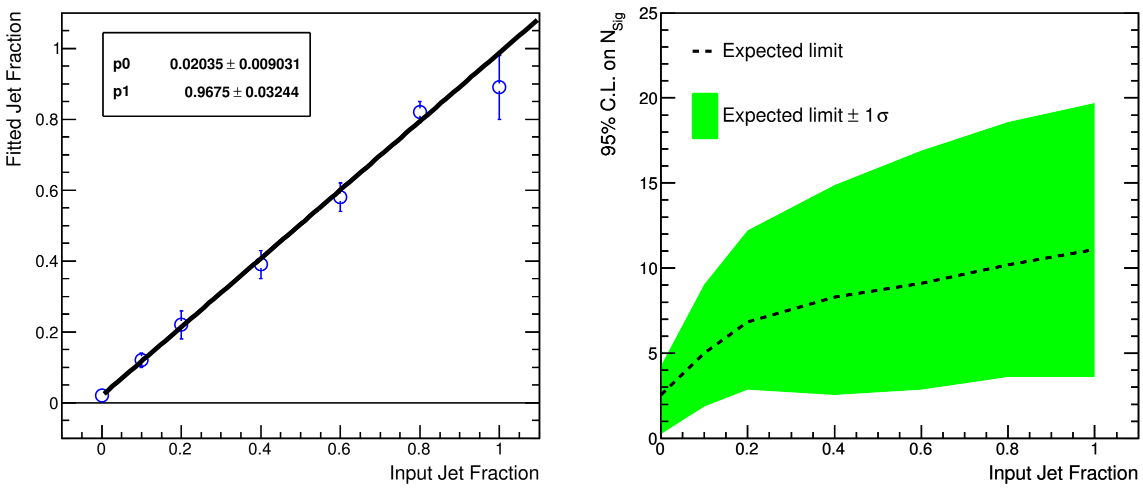

Figure 12.1: (Left) The jet fraction returned by the fitting procedure when applied to pseudo-data datasets with varying input jet fractions. The data points correspond to the mean value and spread, averaged over sets of $\sim$ 10 pseudo-experiments. (Right) The expected 95% CL limit on the number of signal events, as returned by the fitting procedure applied to the same pseudo experiments.

Therefore, pseudo-data generated with low jet fractions contain very few events in the large z_{DCA} tails, and result in more stringent limits than pseudo-data generated with large jet fraction.

12.3.2 Results in Tight-Loose Diphoton Control Samples

The signal region is defined as the TL sample with $E_{\mathrm{T}}^{\mathrm{miss}} > 75$ GeV so the TL sample with $E_{\mathrm{T}}^{\mathrm{miss}} < 75$ GeV, where signal contamination is expected to be negligible, can be used as a control sample. The TL sample with lower $E_{\mathrm{T}}^{\mathrm{miss}}$ is expected to have a background composition similar to that in the signal region, with the possibility that the jet fraction may differ slightly. Since the TL sample with $E_{\mathrm{T}}^{\mathrm{miss}} < 20$ GeV is used to generate the $T_{E_{\mathrm{T}}^{\mathrm{miss}}<20\ \mathrm{GeV}}$ template, the TL sample with values of $E_{\mathrm{T}}^{\mathrm{miss}}$ in the range $20 < E_{\mathrm{T}}^{\mathrm{miss}} < 75$ GeV is available for cross-checks. Given the available statistics, it was decided to divide these data into two exclusive control samples, the TL sample with $20 < E_{\mathrm{T}}^{\mathrm{miss}} < 50$ GeV and the TL sample with $50 < E_{\mathrm{T}}^{\mathrm{miss}} < 75$ GeV. Comparing the results of the two TL control samples also provides some indication of the variation of the background composition with $E_{\mathrm{T}}^{\mathrm{miss}}$.

To investigate the composition of the TL control samples and obtain an independent estimate of the jet fraction, isolation template fits were performed. Results of the fits indicate that the TL samples with $20 < E_{\mathrm{T}}^{\mathrm{miss}} < 50$ GeV and with $50 < E_{\mathrm{T}}^{\mathrm{miss}} < 75$ GeV have jet fractions of the order of 46% and 32%, respectively. More details on the isolation template fit procedure, including plots of the isolation distributions and the fits, are available in Appendix B.

Fig. 12.2 shows the z_{DCA} distribution for the TL control sample with $20 < E_{\mathrm{T}}^{\mathrm{miss}} < 50$ GeV, which contains 8,568 events. Superimposed is the result of fitting the distribution employing the formalism of Eq. 12.3, using the signal MC sample with $\Lambda = 150$ TeV and $\tau = 8$ ns. The fit returns a value of the modified jet fraction, F_{jet}, of 0.92 ± 0.02, which corresponds to a fraction of jets of $\sim 41\%$, in reasonable agreement with the $\sim 46\%$ estimate from the isolation fit. The $\pm 1\sigma$ variations of the background, due to the uncertainty on the fitted jet fraction, are also shown superimposed in Fig. 12.2. The fit returns a 95% CL expected limit on the number of signal events of 270, with $\pm 1\sigma$ values of 210 and 330. As an indication, a curve showing the fitted background combined with 270 signal events is included in Fig. 12.2. The central value of the exclusion corresponds to $\sim 3.1\%$ of the total events in the control sample.

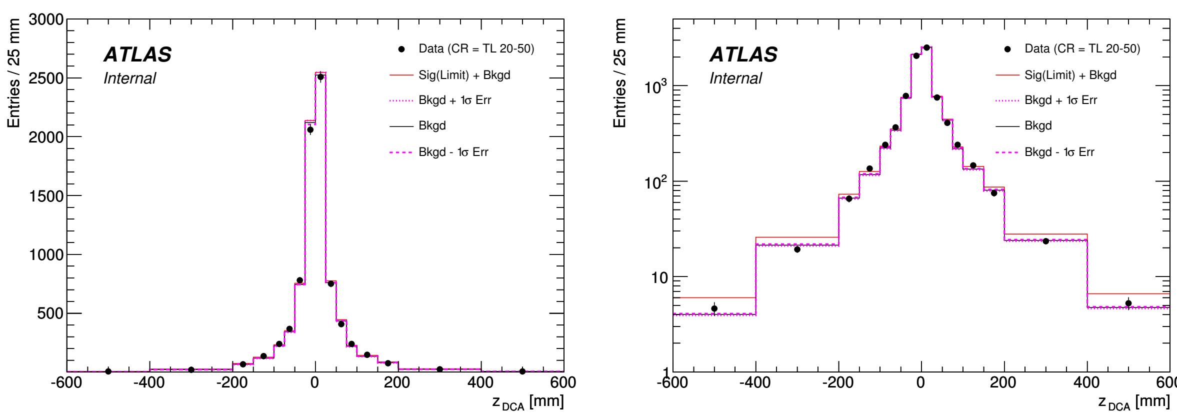

Figure 12.2: The z_{DCA} distribution for the TL control sample with $20 < E_{\mathrm{T}}^{\mathrm{miss}} < 50$ GeV, on (left) linear and (right) log scales. Superimposed are the results of the fit, including the best-fit background curve, the $\pm 1\sigma$ variations on the background due to the uncertainty on the jet fraction, and a curve showing the best-fit background plus the number of signal events equal to the 95% CL limit.

Fig. 12.3 shows the z_{DCA} distribution for the TL control sample with $50 < E_{\mathrm{T}}^{\mathrm{miss}} < 75$ GeV, which contains 303 events. Superimposed is the result of fitting the distribution using the formalism of Eq. 12.3 and the signal MC sample with $\Lambda = 150$ TeV and $\tau = 8$ ns. The fit returns a value of the modified jet fraction, F_{jet}, of 0.88 ± 0.10, which corresponds to a fraction of jets of $\sim 38\%$, in reasonable agreement with the $\sim 32\%$ estimate from the isolation fit. The $\pm 1\sigma$ variations of the background, due to the uncertainty on the fitted jet fraction, are also shown superimposed in Fig. 12.3. The fit returns a 95% CL expected limit on the number of signal events of 31, with $\pm 1\sigma$ values of 17 and 43. As an indication, a curve showing the fitted background combined with 31 signal events is included in Fig. 12.3. The central value of the expected exclusion corresponds to $\sim 10.2\%$ of the total events in the control sample. There appears in Fig. 12.3 to be some asymmetry in the tails of the z_{DCA} distribution, with fewer events on the right side of the plot compared to the left. This small deficit leads to an observed limit which is slightly lower than the expected limit, though the significance of the deficit is less than 1σ. No such asymmetry is apparent in Fig. 12.2 showing the distribution for the higher statistics TL sample with $20 < E_{\mathrm{T}}^{\mathrm{miss}} < 50$ GeV, suggesting the asymmetry could be a statistical fluctuation.

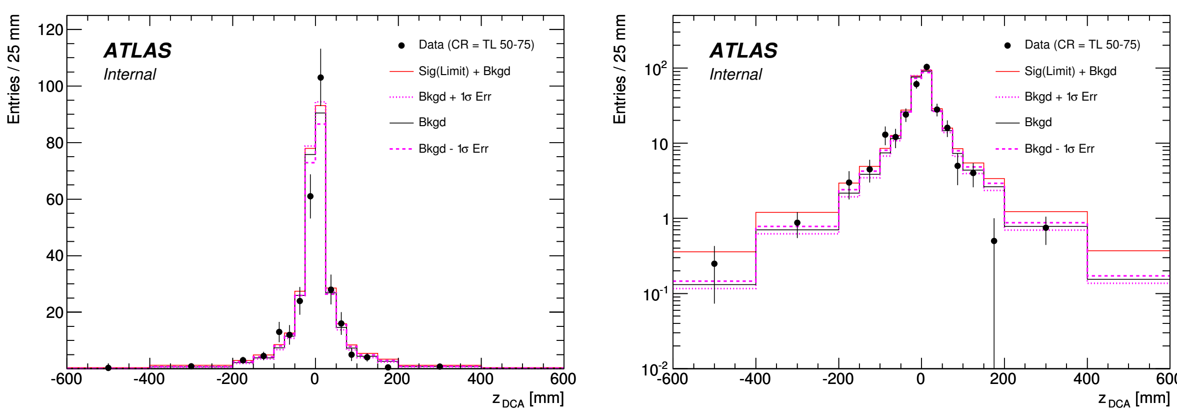

Figure 12.3: The z_{DCA} distribution for the TL control sample with $50 < E_{\mathrm{T}}^{\mathrm{miss}} < 75$ GeV, on (left) linear and (right) log scales. Superimposed are the results of the fit, including the best-fit background curve, the $\pm 1\sigma$ variations on the background due to the uncertainty on the jet fraction, and a curve showing the best-fit background plus the number of signal events equal to the 95% CL limit.

For completeness, the Loose photon timing distributions for TL events in the control samples with $20 < E_{\mathrm{T}}^{\mathrm{miss}} < 50$ GeV and $50 < E_{\mathrm{T}}^{\mathrm{miss}} < 75$ GeV are shown superimposed in Fig. 12.4. The timing distributions are narrow, with very limited tails, as expected for prompt backgrounds. The mean value and RMS of the timing distribution in the control sample with $20 < E_{\mathrm{T}}^{\mathrm{miss}} < 50$ GeV are approximately 3 ps and 370 ps, respectively, while in the control sample with $50 < E_{\mathrm{T}}^{\mathrm{miss}} < 75$ GeV, the mean value and RMS of the timing distribution are approximately −4 ps and 380 ps, respectively. These values are consistent with what would be expected for prompt backgrounds, given the timing resolution.

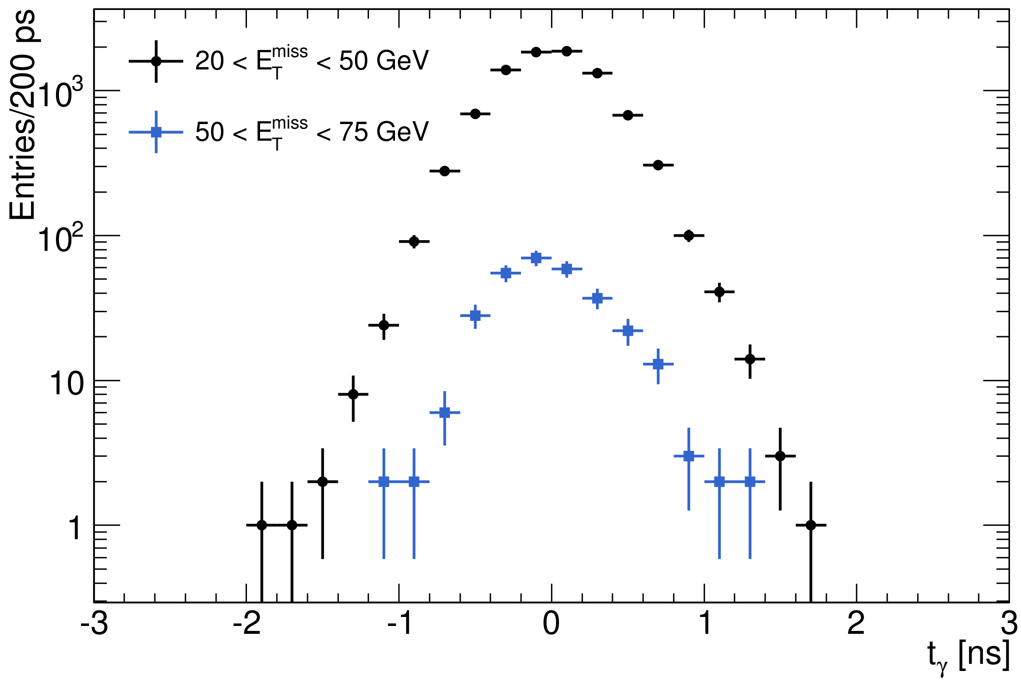

Figure 12.4: The Loose photon timing distributions for the control samples, defined as the TL events with $20 < E_{\mathrm{T}}^{\mathrm{miss}} < 50$ GeV and $50 < E_{\mathrm{T}}^{\mathrm{miss}} < 75$ GeV.

Chapter 13

Results and Interpretation

In this chapter, the results of the investigations of the pointing and timing in the SR are discussed. In Section 13.1, the Loose photon pointing and timing distributions are described and compared with the expectation for background and SPS8 GMSB signal. Subsequently, in Section 13.2, the limits obtained for SPS8 GMSB signal models are discussed.

13.1 Pointing and Timing Distributions in the Signal Region

Once the analysis method and selection criteria were frozen and the expected sensitivity determined, the SR was unblinded and investigated for evidence on non-pointing photons. The z_{DCA} distribution for the 46 events in the SR with $E_{\mathrm{T}}^{\mathrm{miss}} > 75$ GeV is shown in Fig. 13.1. As expected for SM backgrounds, the distribution is rather narrow, and there is no obvious sign of a significant excess in the tails that would be expected for GMSB signal photons originating from decays of long-lived NLSPs. There are three events with $|z_{\mathrm{DCA}}| > 200$ mm, including one far outlier with a value of $z_{\mathrm{DCA}} = +752$ mm. The properties of these three events were studied extensively and are briefly discussed below.

The timing distribution for the 46 events in the SR is shown in Fig. 13.2. The distribution is rather narrow, in agreement with the background-only expectation which is shown superimposed. There is also a slight outlier in the timing distribution, with a value of $t \approx 1.2$ ns. Fig. 13.3 shows the two-dimensional plot of z_{DCA} versus t for the 46 signal events. As can be seen, the timing outlier corresponds to one of the three events with $|z_{\mathrm{DCA}}| > 200$ mm, mentioned above, but not to the most extreme pointing outlier. For the timing outlier, the Loose photon time is measured using a channel which was read out with medium gain, for which the timing uncertainty is larger than for high gain, due to the limited statistics available in the $W \rightarrow e\nu$ sample used to calibrate the calorimeter timing, which results in a timing resolution for the medium gain of ~ 400 ps.

Some additional information about the three events with $|z_{\mathrm{DCA}}| > 200$ mm is summarized in Table 13.1. For two of the events, the timing is in good agreement with the hypothesis that the photon is in-time, while the third corresponds to the timing outlier mentioned above. As can also be seen in the Table, the $E_{\mathrm{T}}^{\mathrm{miss}}$ measurement for all three outlier events is very close to the threshold of the $E_{\mathrm{T}}^{\mathrm{miss}} > 75$ GeV requirement for the SR, as expected for background, which has a sharply falling $E_{\mathrm{T}}^{\mathrm{miss}}$ spectrum.

Run	**Event**	$E_{\mathrm{T}}^{\mathrm{miss}}$	**Loose Photon**			**Tight Photon**		
Number	**Number**	**[GeV]**	E_{T} **[GeV]**	z_{DCA} **[mm]**	t **[ns]**	E_{T} **[GeV]**	z_{DCA} **[mm]**	t **[ns]**
186721	30399675	77.11	75.87	-274.0	0.360	71.96	21.5	0.575
187552	14929851	77.28	59.42	-261.8	1.207	87.21	-118.4	0.242
191920	14157929	77.86	56.61	751.6	0.002	54.17	4.5	-0.197

Table 13.1: Some relevant parameters of the three "outlier" events mentioned in the text.

Fig. 13.4 shows the event display for run number 191920, event number 14157929, which is the event with the farthest non-pointing outlier, with $z_{\mathrm{DCA}} = 752$ mm. The lego plot in the upper right shows the energy deposits of the two photon candidates in yellow, those of identified jets in white, and $E_{\mathrm{T}}^{\mathrm{miss}}$ in red; the same colour scheme is used in the other views. The non-pointing photon candidate is the photon in the upper left in both the $x - y$ view (in the upper left corner of the display) and in the $r - z$ view (lower left corner). The rightmost bottom panel shows details of the EM shower of the photon that passes the tight photon ID requirements, and which has values of z_{DCA} and t of 5 mm and -200 ps, respectively, in agreement with the photon having been produced promptly in the primary collision. The central bottom panel shows details of the EM shower of the non-pointing photon candidate, with $z_{\mathrm{DCA}} = 752$ mm. This photon candidate passes loose but fails tight photon ID requirements. The shower is rather wide in the

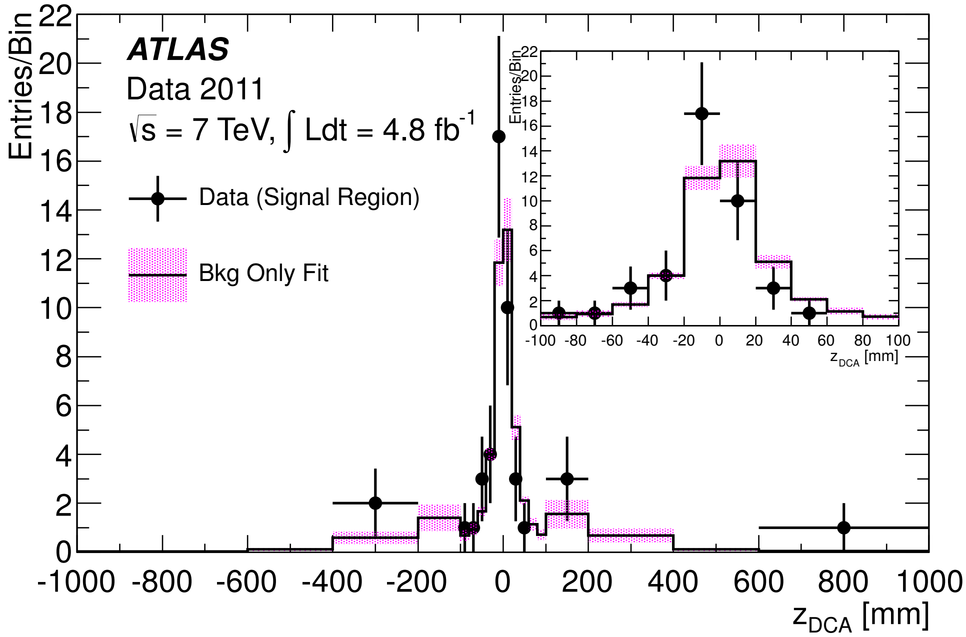

Figure 13.1: The z_{DCA} distribution for the 46 Loose photon candidates of the events in the SR. Superimposed are the results of the background-only fit. The hatching shows the uncertainty in each bin due to the uncertainty on the determined modified jet fraction. The inlay shows an expanded view of the central region, near $z_{\mathrm{DCA}} = 0$.

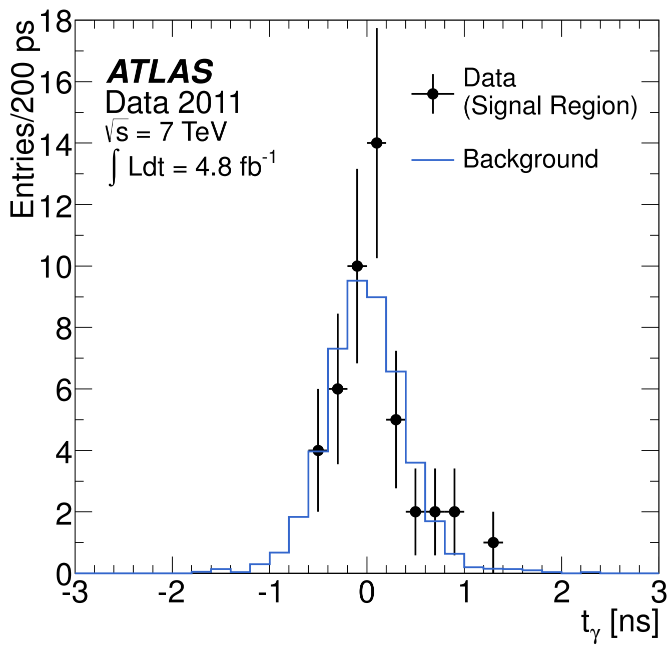

Figure 13.2: The distribution of arrival times (t_γ) for the 46 Loose photon candidates of the events in the SR. Superimposed for comparison is the shape of the timing distribution expected for background only, normalized to 46 total events.

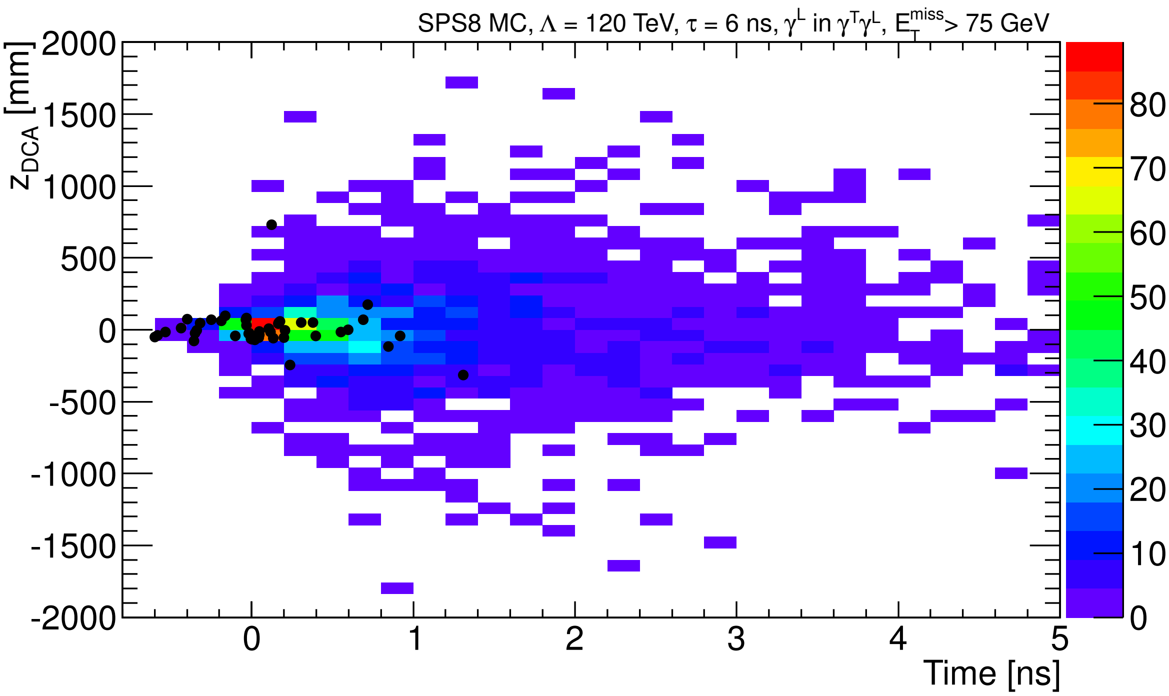

Figure 13.3: The distribution (black points) of z_{DCA} versus time for the Loose photons in the SR. Superimposed (shaded boxes) is the distribution expected for a signal with $\Lambda = 120$ TeV and a neutralino lifetime value of 6 ns.

strip layer, and has an indication of two separate maxima in the strips, characteristic of what would be expected for a jet (for example with a leading π^0 meson) faking the loose photon signature. The interpretation as jet background is also supported by the measured value of 2 ps for this photon candidate's arrival time, consistent with prompt production in the primary collision.

To quantify the compatibility of the observed z_{DCA} distribution with the background-only hypothesis, a background-only template fit was performed. The result of the background-only fit is shown superimposed in Fig. 13.1, which indicates the binning used in the fitting procedure. The modified jet fraction in the background-only hypothesis was determined by the fit to be 0.68 ± 0.28. The uncertainty on the modified jet fraction translates to an uncertainty on the background-only fit shape which is represented by the hatching in Fig. 13.1. To facilitate comparison, the first two rows in Table 13.2 show, in various $|z_{\mathrm{DCA}}|$ regions, the observed number of data events and the results of the background-only fit. respectively. As can be seen, the background-

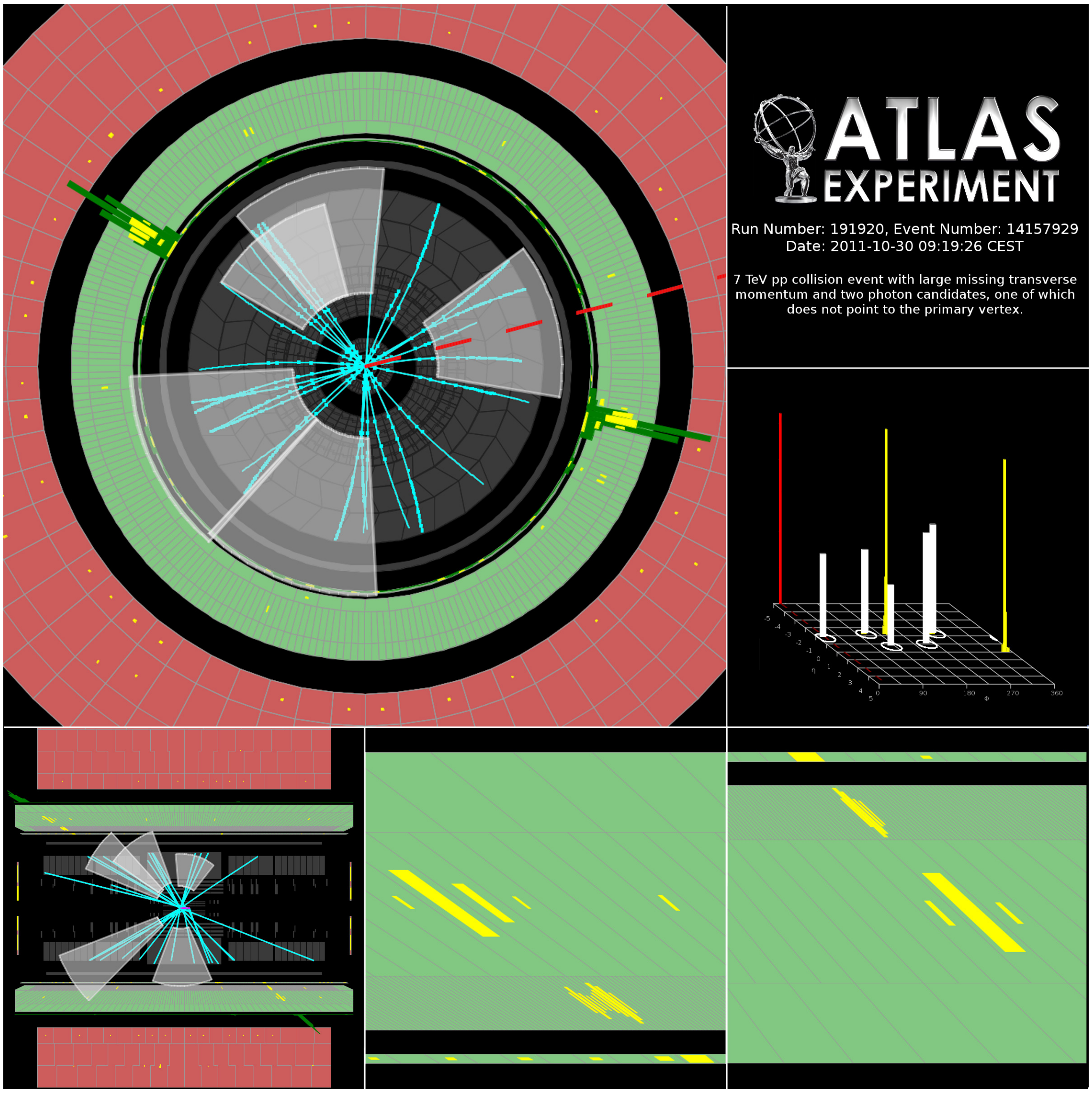

Figure 13.4: Event display for run number 191920, event number 14157929. For more details, see the text.

only fit agrees reasonably well with the data, although some excess is observed in the data for large $|z_{\text{DCA}}|$ values. The probability, p_0, to obtain a distribution at least as incompatible with the background-only hypothesis, assuming the latter is true, is estimated at ~ 0.060, indicating that the slight excess has a significance with a gaussian equivalent of $\sim 1.5\sigma$, understood to be driven largely by the outlier photon candidate with $z_{\text{DCA}} = +752$ mm. To investigate this assumption, a simple test was performed by removing this event from the distribution and performing a new fit, which returned a p_0-value of ~ 0.30, indicating in this case a much better agreement with the background-only model.

To test the signal-plus-background hypothesis, fits using a weighted sum of the background templates and the signal template were performed for each signal MC sample. The best signal-plus-background template fit to the observed z_{DCA} distribution is shown in Fig. 13.5, for the case of $\Lambda = 120$ TeV and $\tau = 6$ ns, superimposed to the observed distribution. The fitting procedure returned a fitted signal strength of $\mu = 0.20 \pm 0.19$, corresponding to a signal contribution of 5.7 ± 5.1 events in the 46 observed events in the SR. No significant excess was observed that can be attributed to this signal MC sample, or to a sample with any other $\Lambda - \tau$ combination. The hatching in Fig. 13.5 indicates the total bin-by-bin uncertainty for the best signal-plus-background fit. The background component in the signal-plus-background fit is also shown superimposed on Fig. 13.5. For this particular signal MC example, the signal-plus-background fit determined the modified jet fraction to be 0.32 ± 0.38. The last three rows in Table 13.2 show the total number of fitted events in each $|z_{\text{DCA}}|$ bin for the signal-plus-background fit, as well as the separate contributions from signal and background.

Fit Type	Event Type	Range of $\lvert z_{\mathrm{DCA}}\rvert$ Values [mm]								
		0 – 20	20 – 40	40 – 60	60 – 80	80 – 100	100 – 200	200 – 400	400 – 600	> 600
-	Data	27	7	4	1	1	3	2	0	1
Bkg Only	Bkg	25.0±2.2	9.1±0.8	3.8±0.3	2.1±0.5	1.4±0.4	3.0±1.1	1.3±0.5	0.2±0.1	0. 08±0.03
Signal	Total	25.1±4.2	9.3±1.5	3.3±0.7	1.6±0.6	1.1±0.4	2.6±1.0	1.8±0.8	0.7±0.5	0. 5±0.4
Plus	Sig	0.7±0.6	0.5±0.5	0.4±0.3	0.3±0.3	0.3±0.3	1.2±1.1	1.3±1.2	0.6±0.5	0.4±0.4
Bkg	Bkg	24.4±4.2	8.8±1.5	2.9±0.8	1.3±0.7	0.8±0.6	1.4±1.5	0.5±0.7	0.1±0.1	0. 03±0.04

Table 13.2: Integrals over various $\lvert z_{\mathrm{DCA}}\rvert$ ranges of the distributions shown in Fig. 13.5 for the 46 Loose photons in the SR. The numbers of events observed in data are shown, as well as the results of a background-only fit and a signal-plus-background fit for the case of $\Lambda = 120$ TeV and $\tau = 6$ ns. The total fitted number of signal events is 5.7 ± 5.1, corresponding to a signal strength $\mu = 0.20 \pm 0.19$. The errors shown correspond to the sum of both statistical and systematic uncertainties. Note that the numbers of signal and background events from the signal-plus-background fit are negatively correlated.

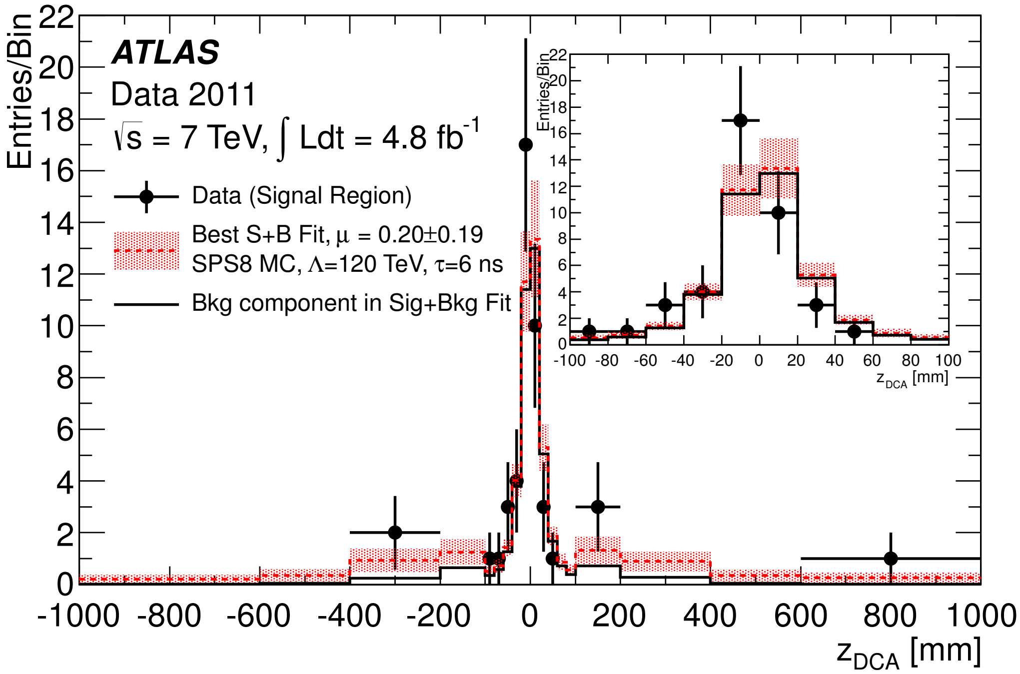

Figure 13.5: The z_{DCA} distribution for the 46 Loose photons of the events in the SR. Superimposed are the results of the signal-plus-background fit (for the case of $\Lambda = 120$ TeV and $\tau = 6$ ns), as well as the contribution from the background to that fit. The hatching shows the total uncertainties in each bin for the signal-plus-background fit. The inlay shows an expanded view of the central region, near $z_{\mathrm{DCA}} = 0$.

13.2 Limits on SPS8 GMSB Models

Given the lack of a significant excess attributed to signal, the fit results were used to set 95% CL limits on the number of SPS8 GMSB signal events. To determine the final exclusion limits, signal-plus-background fits were performed for the various Λ and τ values considered. Fig. 13.6 (left) shows an example result where the 95% CL limits on the number of signal events are shown versus τ, for a fixed value of $\Lambda = 120$ TeV. Similar plots for all fixed Λ values between 70 TeV and 210 TeV are included for reference in Appendix D.

As shown in Fig. 13.6 (right), the results can also be rendered as limits on the allowed cross section. Both plots show, as a function of lifetime, the expected limits (dashed black lines), the observed limit (solid black lines), and the SPS8 GMSB theory prediction (solid red lines). The

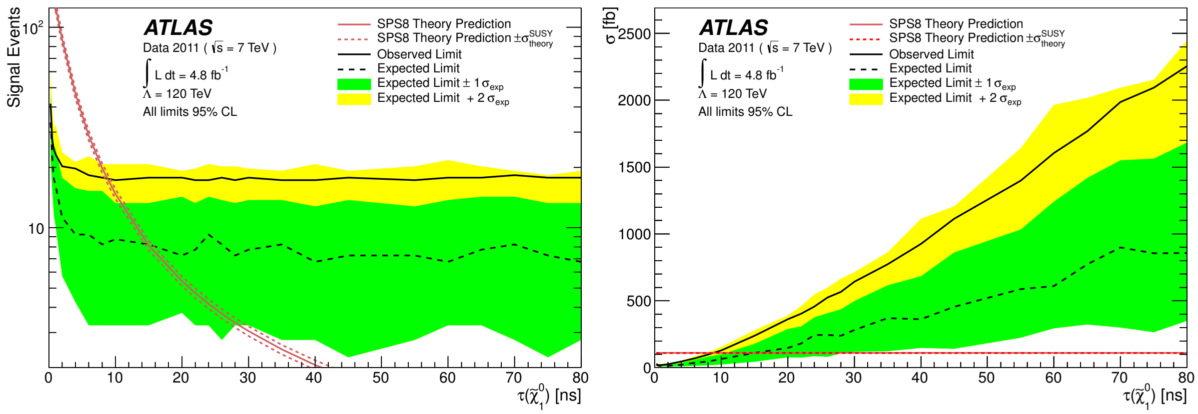

Figure 13.6: 95% CL limits on (left) the number of signal events and (right) the SPS8 signal cross section, as a function of NLSP lifetime, for the case of $\Lambda = 120$ TeV. The region below the limit curve is excluded at 95% CL. For more details, see the text.

green and yellow bands associated with the expected limit lines indicate the limits after variations by $\pm 1\sigma_{\text{exp}}$ and $+2\sigma_{\text{exp}}$, respectively, where σ_{exp} is the total uncertainty excluding the theoretical uncertainties (PDF and scale uncertainties). The $-2\sigma_{\text{exp}}$ band is not shown, since it would yield a negative limit on the expected number of events, which is not physical. The dashed red lines indicate the effect of the theoretical uncertainty, $\sigma^{\text{SUSY}}_{\text{theory}}$, on the theoretical yield prediction. The intersections, in Fig. 13.6, where the limits cross the theory prediction show that, for $\Lambda = 120$ TeV, values of τ below 8.7 ns are excluded at 95% CL, whereas the expected limit would exclude values of τ below 14.6 ns.

Comparing with the theoretical cross section of the SPS8 GMSB model, the results are converted into an exclusion region in the two-dimensional plane of τ versus Λ, as shown in Fig. 13.7. For example, for $\Lambda = 70$ TeV (160 TeV), NLSP lifetimes between 0.25 ns and 50.7 ns (2.7 ns) were excluded at 95% CL. Also shown in the figure are corresponding limits on the lifetime versus the masses of the lightest neutralino and lightest charginos, where the relation between Λ and sparticle masses is taken from theory. It can be seen that, due mostly to the three events with $|z_{\text{DCA}}| > 200$ mm, the observed limit is somewhat less restrictive than the expected limit, but does lie within less than 2σ of the expected limit.

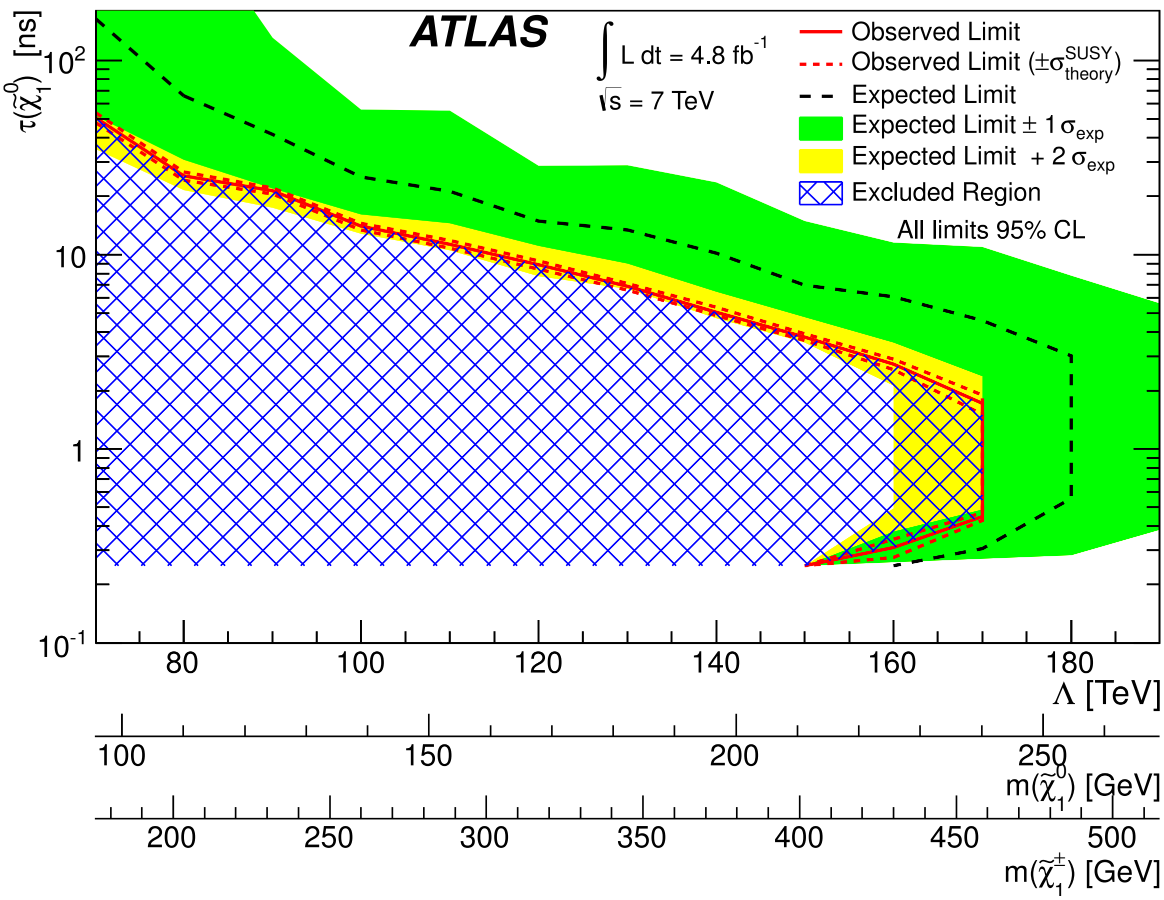

Figure 13.7: The expected and observed limits in the plane of NLSP lifetime versus Λ (and also versus the $\tilde{\chi}_1^0$ or $\tilde{\chi}_1^\pm$ masses), for the SPS8 model. Linear interpolations are shown to connect between Λ values, separated by 10 TeV, for which MC signal samples are available. The region excluded at 95% CL is shown as the blue hatched area. The limit is not shown below an NLSP lifetime of 0.25 ns, which, due to the MC signal samples available, is the smallest value considered in the analysis.

Chapter 14

Conclusions and Outlook

A search has been performed for non-pointing photons in the diphoton plus $E_{\mathrm{T}}^{\mathrm{miss}}$ final state, using the full data sample of 4.8 fb^{-1} of 7 TeV proton–proton collisions recorded in 2011 with the ATLAS detector at the LHC. To perform the search, the analysis exploits the capability of the ATLAS LAr calorimeter to measure the flight direction of photons. The precision measurement of the arrival time of photons is used as a cross-check of the results and for this reason an extensive study of calorimeter timing performance was undertaken. Several sets of corrections were determined and applied and as a result of this study, the timing performance of the LAr EMB was improved to attain a timing resolution of ~ 300 ps, which includes a contribution of ~ 220 ps due to the LHC beam spread. No significant evidence for non-pointing photons was observed and the results were interpreted in the context of Gauge Mediated Supersymmetry Breaking (GMSB) using the SPS8 benchmark model. Exclusion limits at 95% CL were set in the two-dimensional plane of τ (the lifetime of the lightest neutralino) versus Λ (the effective scale of SUSY breaking) or, alternatively, versus the mass of the lightest neutralino. For example, for $\Lambda = 70$ TeV (160 TeV), NLSP lifetimes between 0.25 ns and 50.7 ns (2.7 ns) were excluded at 95% CL. This analysis investigated a scenario to which most previous ATLAS analyses are not sensitive, filling the gap left by direct searches for prompt photons from GMSB decays. With the analysis of the full 2011 dataset, a significant expansion of the excluded SPS8 GMSB parameter space was achieved.

A further enlargement of the explored parameter space can be achieved by exploiting the 20 fb^{-1} of pp collisions at a center of mass energy of 8 TeV, collected by ATLAS in 2012. The search for non-pointing photons in the data sample collected by ATLAS in 2012 is already underway. Simply performing the same analysis using the full 2012 dataset is expected to increase the analysis sensitivity manyfold, due to the increased statistics as well as the increase in signal production cross sections. However, various different analysis strategies and methods are being explored to further increase the analysis sensitivity, armed with the experience from the analysis of the 2011 data.

The most important change in the 2012 data analysis is the development of a two-dimensional search technique, using both the calorimeter timing and pointing. Using the increased size of the 2012 dataset, the timing calibration procedure was further refined compared to 2011, resulting in an even better LAr timing performance. Further, with the latest timing calibration, preliminary studies show that the calorimeter timing has more signal discriminating power compared to the calorimeter pointing. Consequently, having already studied the calorimeter timing extensively, the photon arrival time is intended to be used in a more leading role in the search method currently envisioned.

Improvements are also being investigated in the selection efficiency. Since the background and signal modeling has been shown to work well, it is envisioned to relax the photon identification requirements, moving from a Tight-Loose (TL) analysis to a Loose-Loose (LL) analysis. Preliminary results show an increase in signal selection efficiency of approximately 10-20%. An additional gain in efficiency of approximately 5% is expected if the photon selection is expanded to include the endcaps. While the above efficiency gains appear to be modest, in a symmetric diphoton selection, a significant increase of a factor of two in statistics can be expected by using both photons as “probes”. Hence, the possibility of moving from an “event-based” analysis to an “object-based” analysis is being considered. With the larger dataset and analysis improvements, the reach in $\Lambda - \tau$ is expected to be extended significantly.

Even more accessible exclusion region and discovery potential lies in exploiting the anticipated wealth of pp collision data at unprecedented center of mass energies between 13 TeV and 14 TeV, expected during the upcoming LHC Run 2, beginning in 2015. With the LHC operating at its design luminosity, a total integrated luminosity of ~ 100 fb^{-1} of pp collisions is projected to be collected during Run 2, which will result in an estimated increase by a factor of five in statistics compared to the 2012 dataset. Coupled with a significant increase in the production cross section, a substantial further expansion of the reach of the analysis can be expected.

Bibliography

[1] J. Ban et al., Tech. Rep. ATL-COM-UPGRADE-2010-020, CERN, Geneva, Oct, 2010.

[2] N. Nikiforou and J. Montejo Berlingen, Tech. Rep. ATL-PHYS-SLIDE-2012-154, CERN, Geneva, May, 2012.

[3] N. Nikiforou, arXiv:1306.6756 [physics.ins-det].

[4] N. Nikiforou and J. Parsons, Tech. Rep. ATL-LARG-INT-2012-003, CERN, Geneva, May, 2012.

[5] R. Bhandari et al., Tech. Rep. ATL-PHYS-INT-2013-020, CERN, Geneva, Oct, 2013.

[6] ATLAS Collaboration, Phys. Rev. **D88** (2013) 012001.

[7] N. Nikiforou and J. Parsons, Tech. Rep. ATL-COM-LARG-2014-*** (In preparation), CERN, Geneva, Feb, 2014.

[8] ATLAS Collaboration, JINST **3** (2008) S08003.

[9] L. Evans and P. Bryant, JINST **3** (2008) S08001.

[10] Brüning et al., Tech. Rep. CERN-2004-003-V-1 and CERN-2004-003-V-2, Geneva, 2004.

[11] CMS Collaboration, JINST **3** (2008) S08004.

[12] ATLAS Collaboration, Phys. Lett. **B716** (2012) 1.

[13] ATLAS Collaboration, Phys. Lett. **B726** (2013) 88.

[14] G. 't Hooft and M. Veltman, Nucl. Phys. **B44** (1972) 189.

[15] M. Gell-Mann, Phys. Lett. **8** (1964) 214.

[16] G. Zweig, Tech. Rep. CERN-TH-401, CERN, Geneva, Jan, 1964.

[17] G. Zweig, Tech. Rep. CERN-TH-412, CERN, Geneva, Feb, 1964.

[18] S. P. Martin, `arXiv:hep-ph/9709356 [hep-ph]`, and references therein.

[19] Particle Data Group Collaboration, Phys. Rev. **D86** (2012) 010001.

[20] J. R. Ellis, `arXiv:hep-ph/9812235 [hep-ph]`.

[21] H. Miyazawa, Prog. Theor. Phys. **36 (6)** (1966) 1266.

[22] P. Ramond, Phys. Rev. **D3** (1971) 2415.

[23] Y. A. Golfand and E. P. Likhtman, JETP Lett. **13** (1971) 323.

[24] A. Neveu and J. H. Schwarz, Nucl. Phys. **B31** (1971) 86.

[25] A. Neveu and J. H. Schwarz, Phys. Rev. **D4** (1971) 1109.

[26] J.-L. Gervais and B. Sakita, Nucl. Phys. **B34** (1971) 632.

[27] D. V. Volkov and V. P. Akulov, Phys. Lett. **B46** (1973) 109.

[28] J. Wess and B. Zumino, Phys. Lett. **B49** (1974) 52.

[29] J. Wess and B. Zumino, Nucl. Phys. **B70** (1974) 39.

[30] R. Haag, J. T. Lopuszanski, and M. Sohnius, Nucl. Phys. **B88** (1975) 257.

[31] S. R. Coleman and J. Mandula, Phys. Rev. **159** (1967) 1251.

[32] A. Djouadi, Phys. Rept. **459** (2008) 1.

[33] P. Fayet, Phys. Lett. **B64** (1976) 159.

[34] P. Fayet, Phys. Lett. **B69** (1977) 489.

[35] G. R. Farrar and P. Fayet, Phys. Lett. **B76** (1978) 575.

[36] P. Fayet, Phys. Lett. **B84** (1979) 416.

[37] S. Dimopoulos and H. Georgi, Nucl. Phys. **B193** (1981) 150.

[38] A. Djouadi, `arXiv:1311.0720 [hep-ph]`.

[39] M. Dine and W. Fischler, Phys. Lett. **B110** (1982) 227.

[40] L. Alvarez-Gaum, M. Claudson, and M. B. Wise, Nucl. Phys. **B207** (1982) 96.

[41] C. R. Nappi and B. A. Ovrut, Phys. Lett. **B113** (1982) 175.

[42] M. Dine and A. Nelson, Phys. Rev. **D48** (1993) 1277.

[43] M. Dine, A. Nelson, and Y. Shirman, Phys. Rev. **D51** (1995) 1362.

[44] M. Dine, A. Nelson, Y.Nir, and Y. Shirman, Phys. Rev. **D53** (1996) 2658.

[45] B. C. Allanach et al., Eur. Phys. J. **C25** (2002) 113.

[46] W. Beenakker, R. Hopker, and M. Spira, `arXiv:hep-ph/9611232`.

[47] M. Kramer et al., `arXiv:1206.2892 [hep-ph]`.

[48] ATLAS Collaboration, Phys. Lett. **B718** (2012) 411.

[49] D0 Collaboration, Phys. Rev. Lett. **105** (2010) 221802.

[50] CMS Collaboration, JHEP **1303** (2013) 111.

[51] CMS Collaboration, Phys. Lett. **B722** (2013) 273.

[52] CDF Collaboration, Phys. Rev. Lett. **104** (2010) 011801.

[53] LHCb Collaboration, JINST **3** (2008) S08005.

[54] ALICE Collaboration, JINST **3** (2008) S08002.

[55] S. Baird, Tech. Rep. CERN-AB-Note-2007-014, CERN, Geneva, 2007.

[56] S. van der Meer, Tech. Rep. CERN-ISR-PO-68-31, CERN, Geneva, 1968.

[57] E. Courant and H. Snyder, Annals Phys. **3** (1958) 1.

[58] A. W. Chao, ed., *Handbook of accelerator physics and engineering*. World Scientific, Singapore, 2013.

[59] R. R. Wilson, Phys. Today **30N10** (1977) 23.

[60] C. Lefevre, Tech. Rep. CERN-Brochure-2009-003-Eng, CERN, Geneva, 2009.

[61] M. Bajko et al., Tech. Rep. CERN-LHC-PROJECT-Report-1168, CERN, Geneva, 2009.

[62] B. Aubert et al., Nucl. Instrum. Meth. **A558** (2006) 388.

[63] ATLAS Collaboration, Tech. Rep. ATLAS-TDR-4, CERN, Geneva, 1997.

[64] ATLAS Collaboration, Tech. Rep. ATLAS-TDR-5, CERN, Geneva, 1997.

[65] ATLAS Collaboration, JINST **3** (2008) P06002.

[66] ATLAS Collaboration, Eur. Phys. J. **C70** (2010) 755.

[67] D. Gingrich et al., JINST **2** (2007) P05005.

[68] A. Artamonov et al., JINST **3** (2008) P02010.

[69] N. Buchanan et al., JINST **3** (2008) P03004.

[70] N. Buchanan et al., JINST **3** (2008) P09003.

[71] W. E. Cleland and E. G. Stern, Nucl. Instrum. Meth. **A338** (1994) 467.

[72] ATLAS Collaboration, Tech. Rep. ATLAS-TDR-3, CERN, Geneva, 1996.

[73] C. Eck et al., Tech. Rep. CERN-LHCC-2005-024, CERN, Geneva, 2005.

[74] ATLAS Collaboration, Eur. Phys. J. **C73** (2013) 2518.

[75] W. Lampl et al., Tech. Rep. ATL-LARG-PUB-2008-002, CERN, Geneva, 2008.

[76] ATLAS Collaboration, Tech. Rep. ATL-PHYS-PUB-2011-007, CERN, Geneva, Apr, 2011.

[77] D. Banfi et al., Tech. Rep. ATL-PHYS-INT-2010-038, CERN, Geneva, Apr, 2010.

[78] https://twiki.cern.ch/twiki/bin/view/AtlasProtected/EnergyScaleResolutionRecommendations.

[79] ATLAS Collaboration, Tech. Rep. ATLAS-CONF-2012-123, CERN, Geneva, Aug, 2012.

[80] https://twiki.cern.ch/twiki/bin/view/AtlasProtected/CaloIsolationCorrections.

[81] M. Hance, D. Olivito, and H. Williams, Tech. Rep. ATL-COM-PHYS-2011-1186, CERN, Geneva, Sep, 2011.

[82] https://twiki.cern.ch/twiki/bin/viewauth/AtlasProtected/LArCleaningAndObjectQuality.

[83] ATLAS Collaboration, Tech. Rep. ATL-PHYS-PUB-2011-006, CERN, Geneva, Apr, 2011.

[84] https://twiki.cern.ch/twiki/bin/viewauth/AtlasProtected/TechnicalitiesForMedium1.

[85] ATLAS Collaboration, arXiv:0901.0512 [hep-ex].

[86] S. Hassani et al., Nucl. Instrum. Meth. **A572** (2007) 77.

[87] T. Lagouri et al., IEEE Trans. Nucl. Sci. **51** (2004) 3030.

[88] https://twiki.cern.ch/twiki/bin/viewauth/AtlasProtected/MCPAnalysisGuidelinesRel17MC11a.

[89] M. Cacciari, G. Salam, and G. Soyez, JHEP **04** (2008) 063.

[90] ATLAS Collaboration, Tech. Rep. ATLAS-CONF-2013-004, CERN, Geneva, Jan, 2013.

[91] ATLAS Collaboration, Eur. Phys. J. **C73** (2013) 2304.

[92] ATLAS Collaboration, Tech. Rep. ATLAS-CONF-2010-038, CERN, Geneva, Jul, 2010.

[93] ATLAS Collaboration, Tech. Rep. ATLAS-CONF-2012-020, CERN, Geneva, Mar, 2012.

[94] T. Barillari et al., Tech. Rep. ATL-LARG-PUB-2009-001-2, CERN, Geneva, Jun, 2008.

[95] ATLAS Collaboration, Eur. Phys. J. **C72** (2012) 1844.

[96] ATLAS Collaboration, Tech. Rep. ATLAS-CONF-2012-101, CERN, Geneva, Jul, 2012.

[97] `https://twiki.cern.ch/twiki/bin/view/AtlasPublic/OnlineBeamSpotPublicResults`.

[98] ATLAS Collaboration, Tech. Rep. ATLAS-CONF-2010-069, CERN, Geneva, Jul, 2010.

[99] `https://twiki.cern.ch/twiki/bin/view/AtlasPublic/InDetTrackingPerformanceApprovedPlots`.

[100] H. Abreu et al., JINST **5** (2010) P09003.

[101] M. Aharrouche et al., Nucl. Instrum. Meth. **A597** (2008) 178.

[102] `https://twiki.cern.ch/twiki/bin/viewauth/AtlasProtected/LArCleaningAndObjectQuality`.

[103] S. Asai et al., Tech. Rep. ATL-PHYS-INT-2011-082, CERN, Geneva, Oct, 2011.

[104] J. Alasia et al., Tech. Rep. ATL-PHYS-INT-2011-095, CERN, Geneva, Nov, 2011.

[105] GEANT4 Collaboration, Nucl. Instrum. Meth. **A506** (2003) 250.

[106] ATLAS Collaboration, Eur. Phys. J. **C70** (2010) 823.

[107] `https://twiki.cern.ch/twiki/bin/viewauth/AtlasProtected/ExtendedPileupReweighting`.

[108] F. E. Paige, S. D. Protopopescu, H. Baer, and X. Tata, `arXiv:hep-ph/0312045`.

[109] M. Bahr et al., Eur. Phys. J. **C58** (2008) 639.

[110] A. Sherstnev and R. S. Thorne, Eur. Phys. J. **C55** (2008) 553.

[111] P. M. Nadolsky et al., Phys. Rev. **D78** (2008) 013004.

[112] A. Martin, W. Stirling, R. Thorne, and G. Watt, Eur. Phys. J. **C63** (2009) 189.

[113] ATLAS Collaboration, Eur. Phys. J. **C72** (2012) 1849.

[114] ATLAS Collaboration, Eur. Phys. J. **C72** (2012) 1909.

[115] L. Carminati et al., Tech. Rep. ATL-PHYS-INT-2011-014, CERN, Geneva, Mar, 2011.

[116] `https://twiki.cern.ch/twiki/bin/viewauth/AtlasProtected/PhotonFudgeFactors`.

[117] ATLAS Collaboration, Tech. Rep. ATLAS-CONF-2011-137, CERN, Geneva, Sep, 2011.

[118] ATLAS Collaboration, JINST **8** (2013) P07004.

[119] ATLAS Collaboration, Phys. Rev. Lett. **110** (2013) 011802.

[120] ATLAS Collaboration, Nature Commun. **2** (2011) 463.

[121] ATLAS Collaboration, Phys. Rev. **D85** (2012) 072004.

[122] ATLAS Collaboration, Phys. Lett. **B706** (2011) 150.

[123] ATLAS Collaboration, Tech. Rep. ATLAS-CONF-2010-102, CERN, Geneva, Dec, 2010.

[124] ATLAS Collaboration, Tech. Rep. ATLAS-CONF-2011-116, CERN, Geneva, Aug, 2011.

[125] F. Alonso et al., Tech. Rep. ATL-COM-PHYS-2012-463, CERN, Geneva, Apr, 2012.

[126] ATLAS Collaboration, Phys. Lett. **B717** (2012) 49.

[127] ATLAS Collaboration, Tech. Rep. ATLAS-CONF-2010-052, CERN, Geneva, Jul, 2010.

[128] ATLAS Collaboration, Tech. Rep. ATLAS-CONF-2011-028, CERN, Geneva, Mar, 2011.

[129] ATLAS Collaboration, JHEP **1012** (2010) 060.

[130] M. Schott et al., Tech. Rep. ATL-PHYS-INT-2010-125, CERN, Geneva, Nov, 2010.

[131] ATLAS Collaboration, Eur. Phys. J. **C72** (2012) 1844.

[132] L. Moneta et al., PoS **ACAT2010** (2010) 057, `arXiv:1009.1003 [physics.data-an]`.

[133] A. L. Read, J. Phys. G **G28** (2002) 2693.

Appendices

Appendix A

Lifetime Reweighting of Signal Monte Carlo Samples

Although a grid of signal samples has been produced, the production of a complete grid spanning all necessary Λ and τ values is neither feasible nor necessary. Instead, a reweighting technique is employed utilizing the MC samples produced with a particular Λ and τ, to obtain simulated distributions for additional neutralino lifetimes.

The distribution of the proper decay times of a neutralino, t, with a lifetime of $\tau_\chi = T$, is given by the probability distribution function

$$p(t) = \frac{1}{T} \exp\left(-\frac{t}{T}\right).$$

The proper decay time of a neutralino in a given simulated event can be calculated with the formula $t = L/(c\beta\gamma)$, where L is the distance between the neutralino production and decay vertices in the lab frame, $\beta = p/E$, and $\gamma = (1-\beta^2)^{-1/2}$. Figure A.1 shows distributions of the proper decay times for neutralinos in the SPS8 model ($\Lambda = 120$ TeV) with different values of the neutralino lifetime.

A given neutralino decay in a simulated event produced with a neutralino lifetime of T (reference sample) can be assigned a weight

$$w(t) = \frac{p'(t)}{p(t)} = \frac{T}{T'} \exp\left[-t\left(\frac{1}{T'} - \frac{1}{T}\right)\right]$$

in order to simulate a neutralino decay when the lifetime is T' (target sample). Figure A.2 (left)

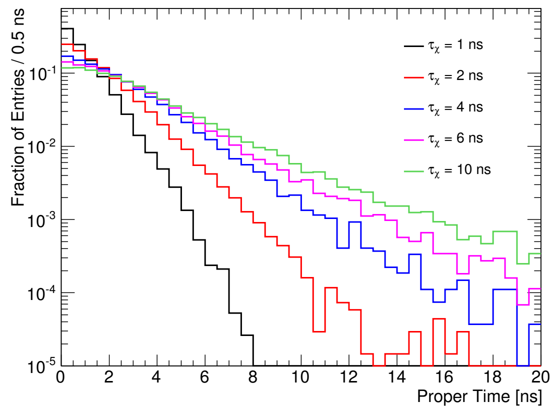

Figure A.1: Distributions of the proper decay times for NLSPs in the SPS8 model ($\Lambda = 120$ TeV) with different values of the NLSP lifetime.

shows the value of the weight as a function of the proper time for a reference sample lifetime of $T = 2$ ns and several target sample lifetime values, T'. Figure A.2 (right) shows distributions of weights calculated with the proper time values from the SPS8 $\Lambda = 120$ TeV MC with $\tau = 2$ ns (shown in Figure A.1) and for the same target sample lifetime values shown in the figure on the left.

Figure A.3 presents a validation of this re-weighting method on reconstruction level variables after final event selection. The variable distributions are shown for two existing samples at $\Lambda = 120$ TeV, one with $\tau = 2$ ns and the other with $\tau = 6$ ns. A third distribution is also shown, which uses $\tau = 2$ ns simulated events (reference sample) reweighted to simulate $\tau = 6$ ns events. Good agreement is observed between the distribution re-weighted to simulate $\tau = 6$ ns events and the one actually produced with $\tau = 6$ ns lifetime.

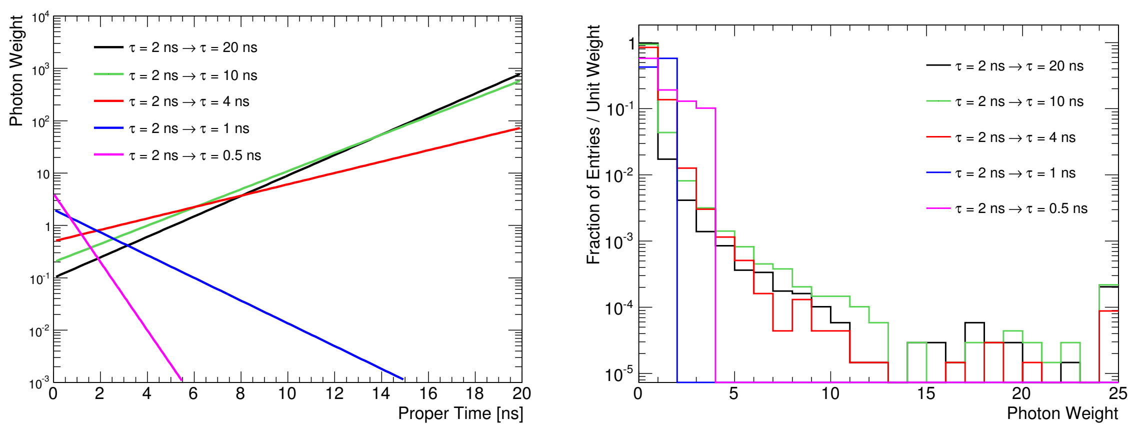

Figure A.2: (Left) Value of the weight as a function of the proper time for a reference sample lifetime of $T = 2$ ns and several target sample lifetime values, T'. (Right) Distributions of weights calculated with the proper time values from the SPS8 $\Lambda = 120$ TeV MC with $\tau = 2$ ns and for the same target sample lifetime values shown in the figure on the left. The last bin contains any overflow entries.

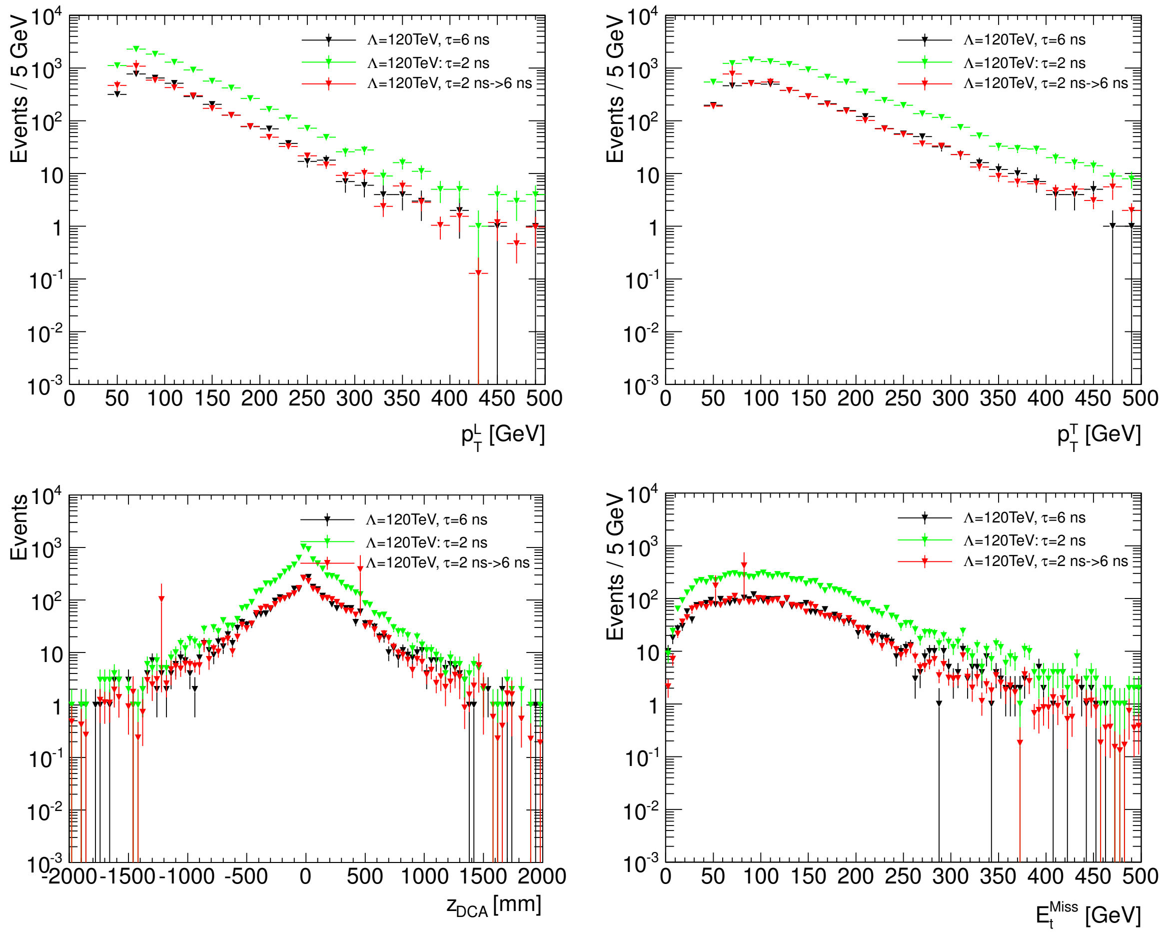

Figure A.3: Loose photon E_{T} distributions (top-left), Tight photon E_{T} distributions (top-right), Loose photon z_{DCA} distributions (bottom-left), and $E_{\mathrm{T}}^{\mathrm{miss}}$ distributions (bottom-right) for events in the $\tau = 2$ ns and $\tau = 6$ ns MC samples with $\Lambda = 120$ TeV, as well as for $\tau = 2$ ns MC events reweighted to simulate $\tau = 6$ ns MC events.

Appendix B

Isolation Template Fits to the Tight-Loose Control Samples

The TL sample with $E_{\mathrm{T}}^{\mathrm{miss}} < 20$ GeV sample should be dominated by QCD events, including jet-jet, jet-γ and $\gamma\gamma$ processes. Therefore, the $T_{MET<20GeV}$ template includes contributions from photons as well as from jets faking the Loose photon signature. For using the template in the fit, as will be discussed in Section 12.2, it is not necessary to separate the photon and jet contributions. However, it is interesting to do so in order to be able to isolate the pointing distribution due to jets, in order to perform some cross-checks of the overall method.

The fraction of photons in the $T_{MET<20GeV}$ sample will be referred to as $f_{e/\gamma}^{MET<20GeV}$. In order to estimate the value of $f_{e/\gamma}^{MET<20GeV}$, fits to isolation distributions were applied, as described below:

In the one-dimensional template fit method, the proportions of prompt photons and jets composing the reconstructed Loose photon object were extracted from an extended likelihood fit to the one-dimensional distribution of the transverse isolation energies. Templates of the prompt photon and jet isolation templates were obtained by two data samples with similar kinematic properties but orthogonal to the control sample. In order to achieve this, an *anti-tight* photon object is defined as a reconstructed photon that passes the loose requirements, but fails the F_{side} or w_{s3} cut (see table 6.2). An anti-tight photon should consist of mainly jets.

- Photon Isolation Template: A control sample form the full 2011 dataset is selected by requiring events with one anti-tight and one tight photon and with $E_{\mathrm{T}}^{\mathrm{miss}}$ less than 20 GeV. This sample should consist of jet-γ events where the jet and γ are identified as the anti-tight and tight objects respectively. The isolation distribution of the tight photon is used as the isolation distribution of a prompt photon.

- Jet Isolation Template: A control sample form the full 2011 dataset is selected by requiring two anti-tight photons and with $E_{\mathrm{T}}^{\mathrm{miss}}$ less than 20 GeV. This sample should be dominated by jet-jet events. The isolation distribution of one of the antitight photons (selected randomly) is used as the isolation distribution of a prompt jet.

Fig. B.1 presents the isolation distribution of the Loose photon from the TL with $E_{\mathrm{T}}^{\mathrm{miss}} <$ 20 GeV. The photon and jet isolation templates are fitted to this distribution using TFractionFitter from the ROOT package. The figure also shows the agreement between the resultant fit and the TL sample. From this fit, it is estimated that $f_{e/\gamma}^{MET<20GeV}$ is $\approx 57\%$ once the default isolation cut of 5 GeV is applied.

The isolation template method was applied to the TL control samples with $20 < E_{\mathrm{T}}^{\mathrm{miss}} <$ 50 GeV and $50 < E_{\mathrm{T}}^{\mathrm{miss}} < 75$ GeV. The isolation distributions for the Loose photon in these two control samples are shown in Figure B.2, with the isolation template fits superimposed. Results of the fits indicate that the TL samples with $20 < E_{\mathrm{T}}^{\mathrm{miss}} < 50$ GeV and with $50 < E_{\mathrm{T}}^{\mathrm{miss}} < 75$ GeV have jet fractions of about 46% and 32%, respectively.

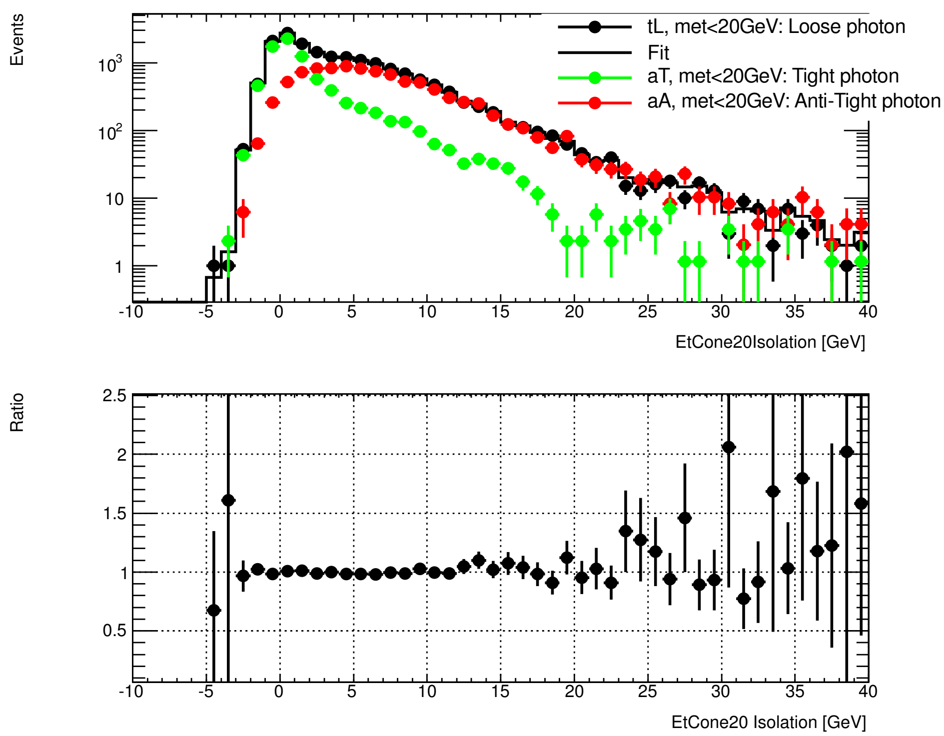

Figure B.1: The one-dimensional photonand jet isolation distributions, together with their fit to the Loose photon from the TL sample with $E_{\mathrm{T}}^{\mathrm{miss}}$ less than 20 GeV.

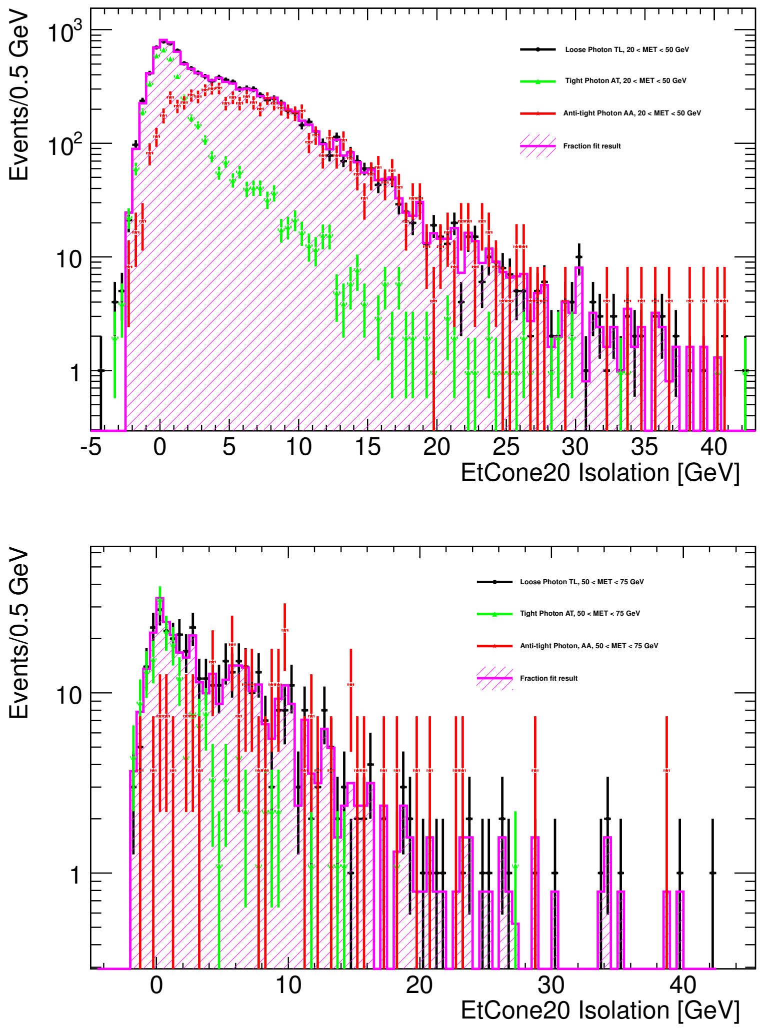

Figure B.2: Isolation distribution for the Loose photon candidate in the TL control sample with (left) $20 < E_{\mathrm{T}}^{\mathrm{miss}} < 50$ GeV and (right) $50 < E_{\mathrm{T}}^{\mathrm{miss}} < 75$ GeV. Superimposed is the result of the isolation template fit.

Appendix C

$E_{\mathrm{T}}^{\mathrm{miss}}$ Systematic Errors per Signal MC Point

The following pages contain tables summarizing the uncertainties in signal efficiency due to uncertainties on the $E_{\mathrm{T}}^{\mathrm{miss}}$ measurement, for each $\Lambda - \tau$ pair considered. As discussed previously, the two major sources of uncertainty considered for the $E_{\mathrm{T}}^{\mathrm{miss}}$ measurement are the uncertainty on the $E_{\mathrm{T}}^{\mathrm{miss}}$ scale and the uncertainty on the $E_{\mathrm{T}}^{\mathrm{miss}}$ resolution. The fractional uncertainties due to these two sources are quoted separately and are treated as uncorrelated, with the total uncertainty obtained by their addition in quadrature.

Lambda [TeV]	τ [ps]	Fractional Error due to: E_T^{miss} Scale	E_T^{miss} Res.	Lambda [TeV]	τ [ps]	Fractional Error due to: E_T^{miss} Scale	E_T^{miss} Res.
70	250	0.042	0.030	80	250	0.055	0.048
70	500	0.045	0.020	80	500	0.050	0.038
70	750	0.046	0.022	80	750	0.049	0.031
70	1000	0.048	0.020	80	1000	0.049	0.027
70	2000	0.053	0.020	80	2000	0.051	0.023
70	3000	0.057	0.020	80	3000	0.052	0.023
70	4000	0.059	0.020	80	4000	0.052	0.023
70	5000	0.061	0.017	80	5000	0.052	0.024
70	6000	0.062	0.020	80	6000	0.052	0.025
70	7000	0.062	0.015	80	7000	0.052	0.026
70	8000	0.062	0.014	80	8000	0.052	0.026
70	9000	0.062	0.0.13	80	9000	0.051	0.027
70	10000	0.061	0.120	80	10000	0.051	0.028
70	12000	0.060	0.010	80	12000	0.050	0.029
70	14000	0.059	0.009	80	14000	0.049	0.030
70	16000	0.058	0.008	80	16000	0.049	0.031
70	18000	0.056	0.007	80	18000	0.048	0.032
70	20000	0.055	0.006	80	20000	0.047	0.032
70	22000	0.053	0.005	80	22000	0.047	0.033
70	24000	0.052	0.004	80	24000	0.046	0.033
70	26000	0.050	0.004	80	26000	0.045	0.034
70	30000	0.047	0.003	80	30000	0.044	0.034
70	35000	0.044	0.001	80	35000	0.042	0.035
70	40000	0.042	0.000	80	40000	0.041	0.035
70	45000	0.039	0.001	80	45000	0.040	0.035
70	55000	0.035	0.002	80	55000	0.037	0.034
70	60000	0.033	0.002	80	60000	0.036	0.034
70	65000	0.031	0.002	80	65000	0.035	0.034
70	70000	0.030	0.002	80	70000	0.034	0.033
70	75000	0.028	0.003	80	75000	0.033	0.033
70	80000	0.027	0.003	80	80000	0.032	0.032
70	90000	0.025	0.003	80	90000	0.030	0.031
70	100000	0.023	0.003	80	100000	0.029	0.030

Table C.1: Signal MC systematic errors due to the E_T^{miss} scale and resolution uncertainties, for $\Lambda = 70$ and 80 TeV.

Lambda [TeV]	τ [ps]	Fractional Error due to: E_T^{miss} Scale	E_T^{miss} Res.	Lambda [TeV]	τ [ps]	Fractional Error due to: E_T^{miss} Scale	E_T^{miss} Res.
90	250	0.030	0.016	100	250	0.004	0.000
90	500	0.040	0.023	100	500	0.020	0.002
90	750	0.043	0.022	100	750	0.026	0.005
90	1000	0.053	0.014	100	1000	0.042	0.018
90	2000	0.051	0.012	100	2000	0.039	0.016
90	4000	0.046	0.016	100	4000	0.048	0.009
90	6000	0.042	0.020	100	6000	0.054	0.013
90	8000	0.044	0.020	100	8000	0.055	0.013
90	10000	0.045	0.020	100	10000	0.056	0.013
90	12000	0.047	0.020	100	12000	0.057	0.013
90	14000	0.048	0.020	100	14000	0.057	0.014
90	16000	0.049	0.020	100	16000	0.057	0.015
90	18000	0.050	0.020	100	18000	0.058	0.015
90	20000	0.051	0.021	100	20000	0.058	0.016
90	22000	0.052	0.021	100	22000	0.058	0.016
90	24000	0.052	0.021	100	24000	0.058	0.017
90	26000	0.053	0.022	100	26000	0.059	0.018
90	30000	0.054	0.022	100	30000	0.059	0.019
90	35000	0.055	0.023	100	35000	0.060	0.020
90	40000	0.056	0.024	100	40000	0.060	0.021
90	45000	0.057	0.025	100	45000	0.060	0.023
90	55000	0.058	0.027	100	55000	0.061	0.025
90	60000	0.059	0.028	100	60000	0.062	0.027
90	65000	0.059	0.029	100	65000	0.062	0.028
90	70000	0.060	0.030	100	70000	0.063	0.029
90	75000	0.060	0.031	100	75000	0.063	0.030
90	80000	0.060	0.031	100	80000	0.063	0.031
90	90000	0.061	0.033	100	90000	0.064	0.033
90	100000	0.062	0.034	100	100000	0.065	0.035

Table C.2: Signal MC systematic errors due to the E_T^{miss} scale and resolution uncertainties, for $\Lambda = 90$ and 100 TeV.

Lambda [TeV]	τ [ps]	Fractional Error due to: E_T^{miss} Scale	E_T^{miss} Res.	Lambda [TeV]	τ [ps]	Fractional Error due to: E_T^{miss} Scale	E_T^{miss} Res.
110	250	0.036	0.011	120	250	0.035	0.028
110	500	0.035	0.009	120	500	0.033	0.019
110	750	0.035	0.010	120	750	0.033	0.016
110	1000	0.037	0.014	120	1000	0.027	0.012
110	2000	0.038	0.013	120	2000	0.034	0.011
110	4000	0.038	0.021	120	4000	0.036	0.019
110	6000	0.045	0.004	120	6000	0.028	0.016
110	8000	0.044	0.001	120	8000	0.028	0.016
110	10000	0.045	0.002	120	10000	0.039	0.006
110	12000	0.046	0.002	120	15000	0.028	0.015
110	14000	0.046	0.002	120	20000	0.027	0.015
110	16000	0.046	0.001	120	22000	0.027	0.015
110	18000	0.046	0.001	120	24000	0.027	0.015
110	20000	0.046	0.001	120	26000	0.027	0.015
110	22000	0.046	0.000	120	28000	0.027	0.015
110	24000	0.046	0.000	120	30000	0.027	0.014
110	26000	0.046	0.000	120	35000	0.026	0.014
110	30000	0.046	0.000	120	40000	0.026	0.014
110	35000	0.046	0.000	120	45000	0.026	0.014
110	40000	0.046	0.000	120	55000	0.025	0.013
110	45000	0.046	0.000	120	60000	0.025	0.013
110	55000	0.046	0.000	120	65000	0.024	0.013
110	60000	0.046	0.000	120	70000	0.024	0.013
110	65000	0.046	0.000	120	75000	0.024	0.012
110	70000	0.046	0.000	120	80000	0.023	0.012
110	75000	0.046	0.000				
110	80000	0.046	0.000				
110	90000	0.046	0.000				
110	100000	0.047	0.000				

Table C.3: Signal MC systematic errors due to the E_T^{miss} scale and resolution uncertainties, for $\Lambda = 110$ and 120 TeV.

Lambda [TeV]	τ [ps]	Fractional Error due to: E_T^{miss} Scale	E_T^{miss} Res.	Lambda [TeV]	τ [ps]	Fractional Error due to: E_T^{miss} Scale	E_T^{miss} Res.
130	250	0.022	0.005	140	250	0.016	0.01
130	500	0.024	0.007	140	500	0.022	0.01
130	750	0.025	0.007	140	750	0.025	0.01
130	1000	0.031	0.016	140	1000	0.027	0.01
130	2000	0.029	0.006	140	2000	0.032	0.011
130	4000	0.030	0.014	140	3000	0.034	0.012
130	6000	0.036	0.009	140	4000	0.035	0.012
130	8000	0.037	0.008	140	5000	0.035	0.012
130	10000	0.038	0.008	140	6000	0.036	0.012
130	12000	0.038	0.007	140	7000	0.036	0.012
130	14000	0.039	0.007	140	8000	0.036	0.012
130	16000	0.040	0.006	140	9000	0.036	0.011
130	18000	0.040	0.006	140	10000	0.036	0.011
130	20000	0.041	0.005	140	12000	0.036	0.011
130	22000	0.042	0.005	140	14000	0.036	0.010
130	24000	0.042	0.005	140	16000	0.036	0.010
130	26000	0.043	0.004	140	18000	0.036	0.009
130	28000	0.043	0.004	140	20000	0.036	0.009
130	30000	0.044	0.004	140	22000	0.036	0.009
130	35000	0.045	0.003	140	24000	0.036	0.008
130	40000	0.046	0.003	140	26000	0.036	0.008
130	45000	0.047	0.002	140	30000	0.036	0.007
130	55000	0.049	0.002	140	35000	0.036	0.007
130	60000	0.050	0.001	140	40000	0.035	0.006
130	65000	0.051	0.001	140	45000	0.035	0.006
130	70000	0.052	0.001	140	55000	0.035	0.005
130	75000	0.053	0.001	140	60000	0.035	0.004
130	80000	0.053	0.001	140	65000	0.035	0.004
				140	70000	0.034	0.004
				140	75000	0.034	0.003
				140	80000	0.034	0.003

Table C.4: Signal MC systematic errors due to the E_T^{miss} scale and resolution uncertainties, for $\Lambda = 130$ TeV and 140 TeV.

Lambda [TeV]	τ [ps]	Fractional Error due to: E_T^{miss} Scale	E_T^{miss} Res.	Lambda [TeV]	τ [ps]	Fractional Error due to: E_T^{miss} Scale	E_T^{miss} Res.
150	250	0.016	0.007	160	250	0.024	0.010
150	500	0.020	0.008	160	500	0.019	0.000
150	750	0.022	0.008	160	750	0.018	0.000
150	1000	0.023	0.008	160	1000	0.018	0.002
150	2000	0.025	0.009	160	2000	0.018	0.005
150	3000	0.027	0.011	160	3000	0.018	0.006
150	4000	0.028	0.012	160	4000	0.018	0.007
150	5000	0.029	0.013	160	5000	0.017	0.008
150	6000	0.029	0.014	160	6000	0.017	0.008
150	7000	0.030	0.015	160	7000	0.017	0.009
150	8000	0.031	0.016	160	8000	0.018	0.009
150	9000	0.031	0.016	160	9000	0.018	0.009
150	10000	0.031	0.017	160	10000	0.018	0.009
150	12000	0.032	0.018	160	12000	0.018	0.010
150	14000	0.032	0.018	160	14000	0.019	0.010
150	16000	0.032	0.019	160	16000	0.019	0.010
150	18000	0.033	0.019	160	18000	0.020	0.010
150	20000	0.033	0.019	160	20000	0.020	0.010
150	22000	0.033	0.019	160	22000	0.021	0.010
150	24000	0.033	0.019	160	24000	0.022	0.010
150	26000	0.033	0.019	160	26000	0.023	0.010
150	30000	0.033	0.019	160	30000	0.024	0.010
150	35000	0.033	0.019	160	35000	0.026	0.010
150	40000	0.032	0.019	160	40000	0.028	0.010
150	45000	0.032	0.018	160	45000	0.030	0.010
150	55000	0.031	0.018	160	55000	0.034	0.009
150	60000	0.031	0.017	160	60000	0.036	0.009
150	65000	0.030	0.017	160	65000	0.039	0.009
150	70000	0.030	0.017	160	70000	0.041	0.009
150	75000	0.030	0.016	160	75000	0.043	0.009
150	80000	0.029	0.016	160	80000	0.045	0.009

Table C.5: Signal MC systematic errors due to the E_T^{miss} scale and resolution uncertainties, for $\Lambda = 150$ TeV and 160 TeV.

Lambda [TeV]	τ [ps]	Fractional Error due to: $E_{\mathrm{T}}^{\mathrm{miss}}$ Scale	$E_{\mathrm{T}}^{\mathrm{miss}}$ Res.	Lambda [TeV]	τ [ps]	Fractional Error due to: $E_{\mathrm{T}}^{\mathrm{miss}}$ Scale	$E_{\mathrm{T}}^{\mathrm{miss}}$ Res.
170	250	0.020	0.008	180	250	0.020	0.010
170	500	0.020	0.012	180	500	0.019	0.009
170	750	0.019	0.011	180	750	0.018	0.008
170	1000	0.018	0.011	180	1000	0.018	0.008
170	2000	0.017	0.010	180	2000	0.018	0.008
170	3000	0.017	0.010	180	3000	0.018	0.008
170	4000	0.017	0.011	180	4000	0.018	0.007
170	5000	0.017	0.011	180	5000	0.017	0.006
170	6000	0.017	0.011	180	6000	0.017	0.005
170	7000	0.017	0.012	180	7000	0.017	0.004
170	8000	0.017	0.012	180	8000	0.017	0.003
170	9000	0.017	0.012	180	9000	0.017	0.003
170	10000	0.017	0.012	180	10000	0.017	0.002
170	12000	0.017	0.013	180	12000	0.017	0.001
170	14000	0.017	0.013	180	14000	0.016	0.000
170	16000	0.018	0.013	180	16000	0.016	0.000
170	18000	0.018	0.013	180	18000	0.016	0.000
170	20000	0.018	0.013	180	20000	0.016	0.000
170	22000	0.019	0.013	180	22000	0.016	0.000
170	24000	0.019	0.013	180	24000	0.016	0.000
170	26000	0.020	0.013	180	26000	0.016	0.000
170	30000	0.021	0.013	180	30000	0.016	0.000

Table C.6: Signal MC systematic errors due to the $E_{\mathrm{T}}^{\mathrm{miss}}$ scale and resolution uncertainties, for $\Lambda = 170$ TeV and 180 TeV.

Lambda [TeV]	τ [ps]	Fractional Error due to: $E_{\mathrm{T}}^{\mathrm{miss}}$ Scale	$E_{\mathrm{T}}^{\mathrm{miss}}$ Res.	Lambda [TeV]	τ [ps]	Fractional Error due to: $E_{\mathrm{T}}^{\mathrm{miss}}$ Scale	$E_{\mathrm{T}}^{\mathrm{miss}}$ Res.
190	250	0.013	0.000	200	9000	0.019	0.001
190	500	0.013	0.004	200	10000	0.019	0.000
190	750	0.014	0.006	200	12000	0.019	0.000
190	1000	0.015	0.006	200	14000	0.019	0.000
190	2000	0.017	0.007	200	16000	0.019	0.000
190	3000	0.018	0.006	200	18000	0.018	0.000
190	4000	0.018	0.006	200	20000	0.018	0.000
190	5000	0.019	0.005	200	22000	0.018	0.010
190	6000	0.019	0.005	200	24000	0.018	0.010
190	7000	0.019	0.004	200	26000	0.018	0.010
190	8000	0.019	0.004	200	30000	0.018	0.010
190	9000	0.019	0.004	210	250	0.010	0.001
190	10000	0.019	0.004	210	500	0.014	0.004
190	12000	0.019	0.004	210	750	0.015	0.005
190	14000	0.019	0.004	210	1000	0.015	0.006
190	16000	0.019	0.004	210	2000	0.014	0.005
190	18000	0.019	0.005	210	3000	0.014	0.005
190	20000	0.019	0.005	210	4000	0.013	0.004
190	22000	0.019	0.006	210	5000	0.013	0.004
190	24000	0.018	0.006	210	6000	0.013	0.004
190	26000	0.018	0.007	210	7000	0.013	0.003
190	30000	0.018	0.008	210	8000	0.013	0.003
200	250	0.011	0.000	210	9000	0.012	0.003
200	500	0.012	0.001	210	10000	0.012	0.003
200	750	0.013	0.003	210	12000	0.012	0.003
200	1000	0.014	0.004	210	14000	0.012	0.002
200	2000	0.017	0.007	210	16000	0.012	0.002
200	3000	0.018	0.007	210	18000	0.012	0.002
200	4000	0.018	0.006	210	20000	0.012	0.002
200	5000	0.019	0.005	210	22000	0.012	0.002
200	6000	0.019	0.004	210	24000	0.012	0.002
200	7000	0.019	0.003	210	26000	0.012	0.002
200	8000	0.019	0.002	210	30000	0.012	0.002

Table C.7: Signal MC systematic errors due to the $E_{\mathrm{T}}^{\mathrm{miss}}$ scale and resolution uncertainties, for $\Lambda = 190,\ 200$, and 210 TeV.

Appendix D

Limit Plots for Different Λ Values

In the following pages several one-dimensional limit plots are shown. Each plot shows, as a function of the NLSP lifetime, tau, the expected and observed 95% CL limit obtained for the number of signal events for each Λ value investigated. The theory prediction for SPS8 is also shown.

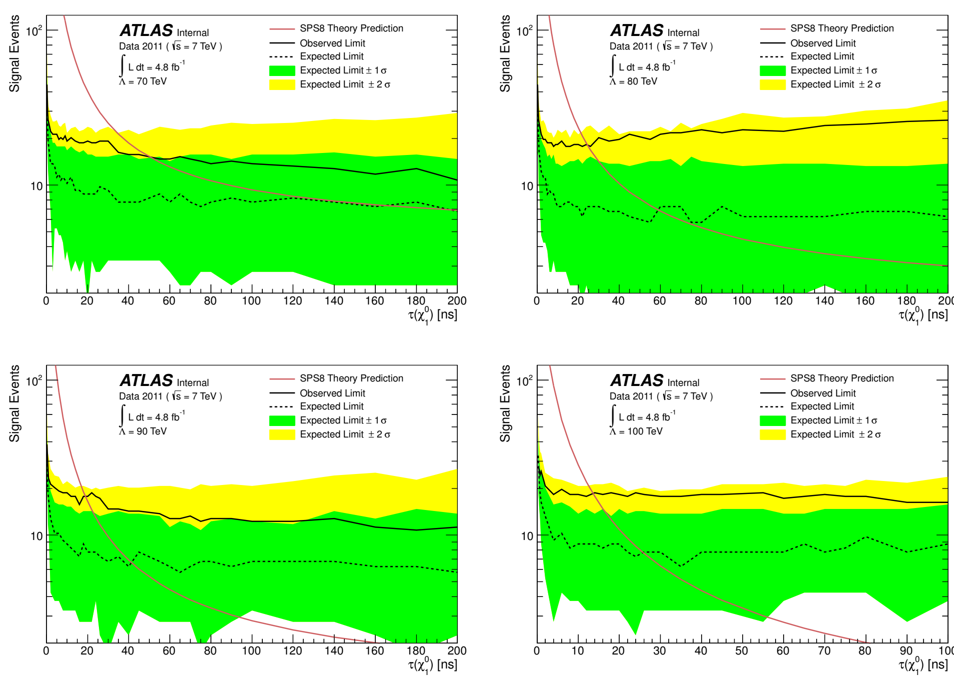

Figure D.1: 95% CL limits on the number of signal events, as a function of τ, for $\Lambda = 70$, 80, 90, and 100 TeV.

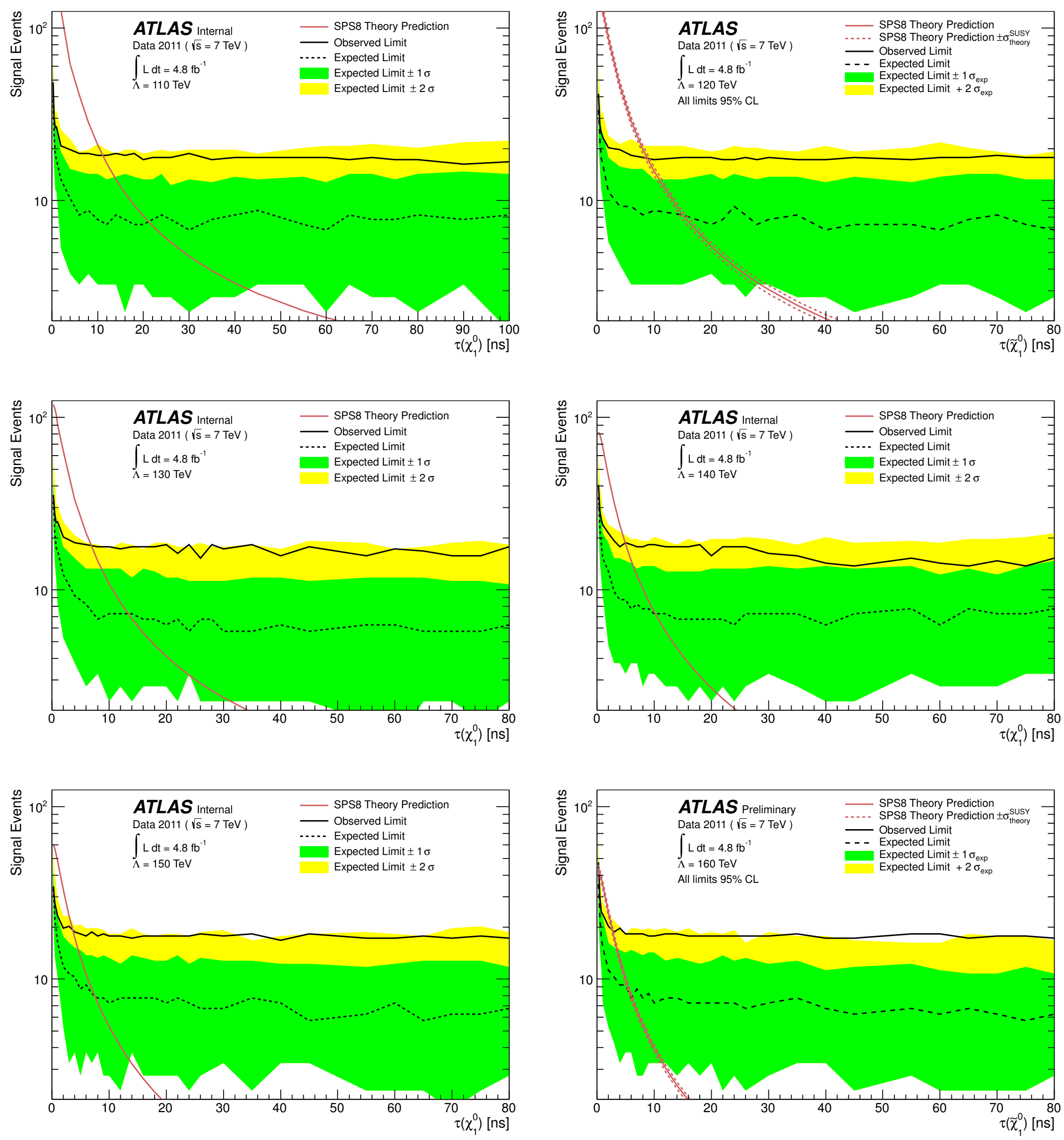

Figure D.2: 95% CL limits on the number of signal events, as a function of τ, for $\Lambda = 110$, 120, 130, 140, 150, and 160 TeV.

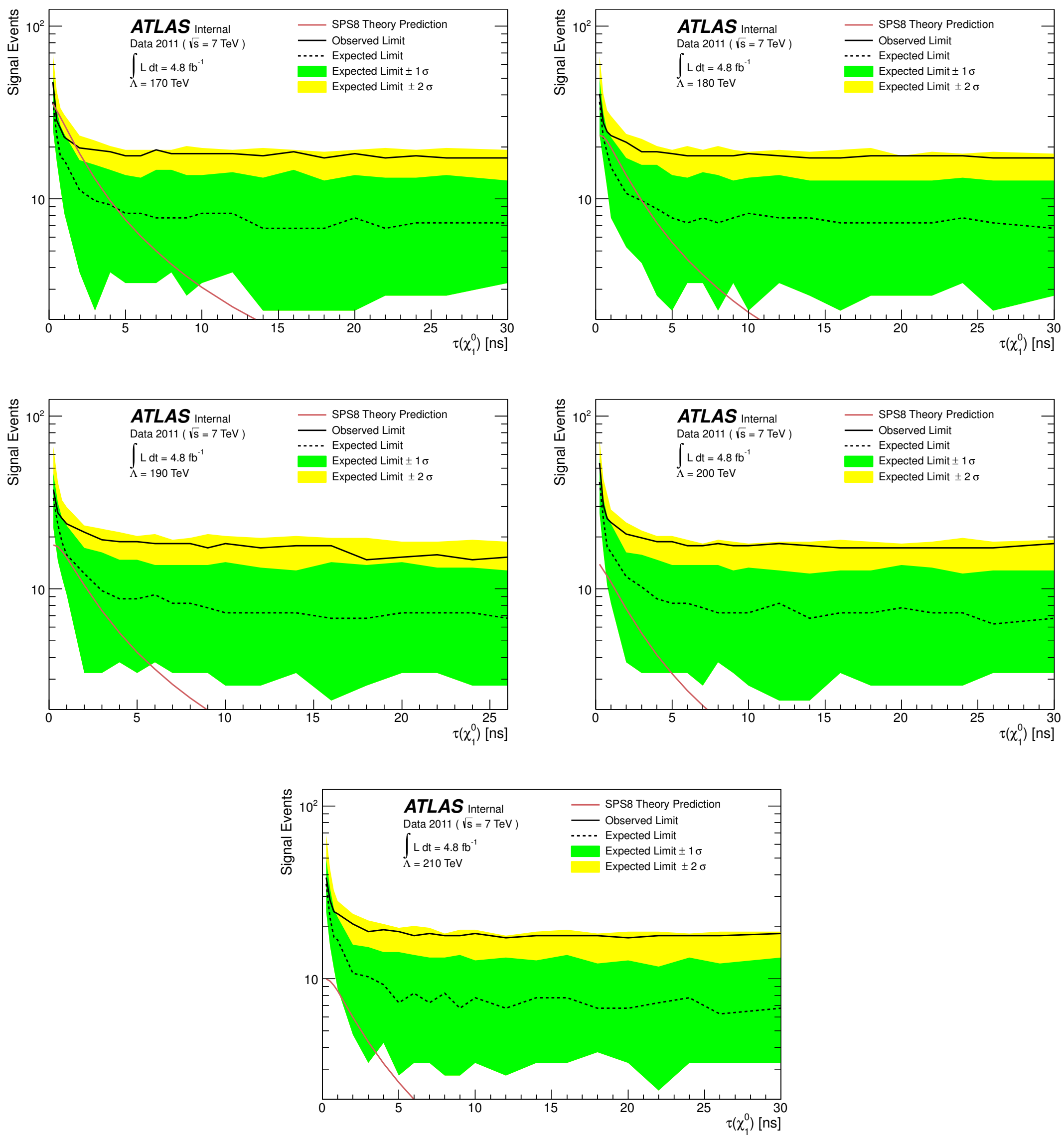

Figure D.3: 95% CL limits on the number of signal events, as a function of τ, for $\Lambda = 170$, 180, 190, 200 and 210 TeV.